

# Search for relativistic magnetic monopoles with the AMANDA-II detector

Von der Fakultät für Mathematik, Informatik und Naturwissenschaften der RWTH Aachen University zur  
Erlangung des akademischen Grades einer Doktorin der Naturwissenschaften genehmigte Dissertation

vorgelegt von

Diplom Physikerin

**Henrike Wissing**

aus

Hattingen

Berichter: Universitätsprofessor Christopher Wiebusch  
Dr. Christian Spiering

Tag der mündlichen Prüfung: 25. 02. 2009

Diese Dissertation ist auf den Internetseiten der Hochschulbibliothek online uverfügbar.



# Zusammenfassung

Das *Antarctic Muon And Neutrino Detection Array* (AMANDA) ist ein Neutrino-teleskop, das in der antarktischen Eiskappe in unmittelbarer Nähe des geographischen Poles installiert ist. Mittels eines dreidimensionalen Gitters aus rund 680 Sekundärelektronenvervielfachern in druckfesten Glaskugeln, die in Tiefen zwischen 1500 m und 2000 m im südpolaren Gletscher eingefroren sind, werden die Spuren elektrisch geladener relativistischer Teilchen anhand ihrer Čerenkov Strahlung detektiert. Neben dem primären Ziel, der Detektion von elektrisch geladenen Leptonen aus Wechselwirkungen von hochenergetischen Neutrinos, bietet AMANDA die Möglichkeit, nach bisher unentdeckten, *magnetisch* geladenen Teilchen zu suchen.

Die elektromagnetische Wechselwirkung solcher magnetischer Monopole wäre aus Symmetriegründen der Wechselwirkung elektrisch geladener Teilchen sehr ähnlich, zeichnete sich jedoch durch eine erheblich größere Kopplungskonstante aus. Daher überträfe die Intensität der Čerenkovstrahlung eines relativistischen Monopols in Eis die eines elektrisch geladenen Teilchens gleicher Geschwindigkeit um mehrere Größenordnungen.

Die vorliegende Arbeit beschreibt die Suche nach Čerenkov-Signaturen magnetischer Monopole in den im Jahr 2000 mit AMANDA aufgezeichneten Daten. Der zur Analyse bereitstehende experimentelle Datensatz entspricht, nach Totzeitkorrektur, einer Datennahmezeit von rund 155 Tagen.

Der dominante Untergrund für die Suche nach magnetischen Monopolen sind Bündel hochenergetischer atmosphärischer Myonen. Zur Unterdrückung dieses Untergrundes wird anhand von simulierten Untergrund- und Signalereignissen eine schrittweise Datenselektion entwickelt. Selektionskriterien sind zum einen die während eines Ereignisses im Detektor deponierte Lichtmenge, und zum anderen die mittels einer *Maximum-Likelihood* Rekonstruktion ermittelte Spurrichtung.

Der Untergrund atmosphärischer Myonen besteht ausschliesslich aus Teilchenspuren mit Einfallrichtungen oberhalb des Horizontes. Nach einer ersten Vorselektion, werden die Ereignisse in Datensätze mit jeweils aufwärtslaufenden Teilchen (Einfallrichtung unterhalb des Horizonts) und abwärtslaufenden Teilchen (Einfallrichtung oberhalb des Horizonts) geteilt, und die weiteren Selektionskriterien werden für aufwärts- und abwärtslaufende Teilchen getrennt optimiert. Für die Suche nach magnetischen Monopolen unterhalb des Horizonts verbleibt nur ein geringer Untergrund derjenigen atmosphärischen Myonen, die als aufwärtslaufend misrekonstruiert wurden. Daher erreicht die Suche nach magnetischen Monopolen unterhalb des Horizonts eine wesentlich bessere Sensitivität als die Suche oberhalb des Horizonts. Letztere ist aber dadurch motiviert, dass die abgeleiteten Flussgrenzen für einen größeren Massenbereich magnetischer Monopole gültig sind.

Die nach der Anwendung aller Selektionskriterien im experimentellen Datensatz verbleibenden Ereignisse sind konsistent mit dem zu erwartenden verbleibenden Untergrund. Unter Berücksichtigung systematischer und statistischer Fehler in den Signal- und Untergrunderwartungen werden, abhängig von der Monopolgeschwindigkeit, obere Flussgrenzen bestimmt. Bei einem 90% Konfidenzniveau liegen die Flussgrenzen für aufwärtslaufende Monopole zwischen  $3.8 \times 10^{-17} \text{ cm}^{-2} \text{ s}^{-1} \text{ sr}^{-1}$  ( $v = c$ ,  $c = \text{Vakuumlichtgeschwindigkeit}$ ) und  $8.8 \times 10^{-16} \text{ cm}^{-2} \text{ s}^{-1} \text{ sr}^{-1}$  ( $v = 0.76 c$ ). Diese Flussgrenzen sind für Monopole mit Massen oberhalb von  $10^{11} \text{ GeV}$  uneingeschränkt gültig und sind die besten momentan vorliegenden experimentellen Grenzen. Die Flussgrenzen für abwärtslaufende Monopole liegen etwa eine Größenordnung höher, gelten jedoch für auch leichtere Monopole mit Massen ab  $10^8 \text{ GeV}$ . Für diesen Massenbereich sind die hier abgeleiteten Flussgrenzen vergleichbar mit den momentan besten experimentellen Grenzen.



## Abstract

Cherenkov emissions of magnetically charged particles passing through a transparent medium will exceed those of electrically charged particles by several orders of magnitude. The *Antarctic Muon And Neutrino Detector Array* (AMANDA), a neutrino telescope utilizing the glacial ice at the geographic South Pole as Cherenkov medium, is capable of efficiently detecting relativistic magnetic monopoles that may pass through its sensitive volume. This thesis presents the search for Cherenkov signatures from relativistic magnetic monopoles in data taken with AMANDA during the 2000. No such signal is observed in the data, and the analysis allows to place upper limits on the flux of relativistic magnetic monopoles.

The limit obtained for monopoles reaching the detector from below the horizon, *i.e.*, those monopoles that are capable of crossing the Earth, is the most stringent experimental constraint on the flux of magnetic monopoles to date: Dependent on the monopole speed, the flux limit (at 90% confidence level) varies between  $3.8 \times 10^{-17} \text{ cm}^{-2} \text{ s}^{-1} \text{ sr}^{-1}$  (for monopoles moving at the vacuum speed of light) and  $8.8 \times 10^{-16} \text{ cm}^{-2} \text{ s}^{-1} \text{ sr}^{-1}$  (for monopoles moving at a speed just above the Cherenkov threshold). The limit obtained for monopoles reaching the detector from above the horizon is less stringent by roughly an order of magnitude, owing to the much larger background from down-going atmospheric muons. This looser limit is valid for a larger class of magnetic monopoles, since the monopole's capability to pass through the Earth is not a requirement.



# Contents

<b>1</b>	<b>Introduction</b>	<b>1</b>
<b>2</b>	<b>Magnetic Monopoles</b>	<b>3</b>
2.1	Theory of magnetic monopoles . . . . .	3
2.2	Monopole creation in the early universe . . . . .	6
2.3	Acceleration of cosmic monopoles . . . . .	6
2.4	The Parker Bound . . . . .	7
2.5	Interaction with matter . . . . .	7
2.6	Experimental bounds . . . . .	9
<b>3</b>	<b>Monopole search with neutrino telescopes</b>	<b>11</b>
3.1	The science objective of neutrino telescopes: Neutrino Astrophysics . . . . .	11
3.2	The concept of a neutrino telescope . . . . .	13
3.3	Event classes in a neutrino telescope . . . . .	14
3.4	Monopole searches . . . . .	16
3.5	Experimental bounds . . . . .	19
<b>4</b>	<b>The AMANDA-II neutrino telescope</b>	<b>21</b>
4.1	The detection medium: South Polar ice . . . . .	21
4.2	Deployment and detector geometry . . . . .	23
4.3	The optical module . . . . .	24
4.4	Surface electronics . . . . .	25
4.5	Calibration . . . . .	29
4.6	Trigger rate . . . . .	30
4.7	Detector monitoring . . . . .	31
4.8	Removing electronic noise . . . . .	31
4.9	Recent results from AMANDA . . . . .	34
<b>5</b>	<b>Simulation of particles in AMANDA-II</b>	<b>36</b>
5.1	The detector simulation . . . . .	36
5.2	Simulation of magnetic monopoles . . . . .	41
5.3	Simulation of atmospheric muons . . . . .	43

<b>6</b>	<b>Data Pre-processing and first level data selection</b>	<b>48</b>
6.1	Experimental and simulated data sets . . . . .	48
6.2	Retriggering . . . . .	51
6.3	Analysis Level 1 . . . . .	54
6.4	Conclusions . . . . .	56
<b>7</b>	<b>Higher level data selection</b>	<b>58</b>
7.1	Processing and data selection strategy . . . . .	58
7.2	Analysis Level 2 . . . . .	63
7.3	Analysis Level 3 . . . . .	68
7.4	Conclusions . . . . .	72
<b>8</b>	<b>Up-going monopoles</b>	<b>74</b>
8.1	Rejection of misreconstructed atmospheric muon bundles . . . . .	74
8.2	Final light yield criterion . . . . .	76
8.3	Unblinding result . . . . .	78
<b>9</b>	<b>Down-going monopoles</b>	<b>79</b>
9.1	Further background rejection . . . . .	79
9.2	Final light yield criterion . . . . .	81
9.3	Unblinding results . . . . .	83
<b>10</b>	<b>Limit on the flux of relativistic magnetic monopoles</b>	<b>86</b>
10.1	Systematic uncertainties . . . . .	86
10.2	Flux limits including systematic and statistical errors . . . . .	89
10.3	Discussion . . . . .	90
<b>11</b>	<b>Summary and outlook</b>	<b>92</b>
<b>A</b>	<b>Seasonal variations of the event rate</b>	<b>95</b>
A.1	The AMANDA-II trigger rate and the <i>effective</i> atmospheric temperature . . . . .	95
A.2	Sudden stratospheric warming in 2002 . . . . .	96
<b>B</b>	<b>Tagging events caused by electronic noise</b>	<b>100</b>
B.1	The flare indicators . . . . .	100
B.2	File selection using flare indicators . . . . .	106

B.3	Indicator stability for high multiplicity events . . . . .	107
<b>C</b>	<b>The extended OM selection</b>	<b>110</b>
C.1	The impact of the hit cleaning . . . . .	111
C.2	Noise contributions . . . . .	112
C.3	ADC-TDC inconsistencies in strings other than string13 . .	117
C.4	Depth distribution of hits . . . . .	126
C.5	OM selection for the likelihood reconstruction . . . . .	128
<b>D</b>	<b>Cut optimization using the Model Rejection Factor and limit calculation</b>	<b>130</b>
D.1	Hypotheses Testing . . . . .	130
D.2	Constructing Confidence Belts . . . . .	131
D.3	The Average Upper Limit . . . . .	132
D.4	The Model Rejection Factor . . . . .	132
D.5	Confidence belt construction in presence of systematic un- certainties . . . . .	133
<b>E</b>	<b>Event #4731980</b>	<b>135</b>
<b>F</b>	<b>Primary cosmic ray composition and energy spectra used for the background simulation</b>	<b>141</b>



# 1 Introduction

With the advent of electrodynamics, electricity and magnetism are considered as two manifestations of one and the same underlying physical phenomenon. Electromagnetism possesses a symmetry between electric and magnetic fields; it is however disymmetric with respect to the sources of the fields. Only electric charges are observed in nature as isolated sources of electromagnetic fields, whereas “*magnetic charges*” are only observed as dipoles. From a theoretical point of view, there is no obvious intrinsic reason for this asymmetry, and it seems natural to conjecture the existence of isolated magnetic poles.

While electrodynamics could in principle accommodate magnetic monopoles without restraint, quantum mechanics allows the existence of monopoles only on one condition: Both electric and magnetic charge have to be quantized. Electric charge quantization, however, is an observational fact, for which no explanation was known until the emergence of Grand Unified Theories. So, the quantization condition actually supports the existence of magnetic monopoles. In Grand Unified Theories finally, the existence of monopoles is an incontrovertible necessity.

The monopoles predicted by Grand Unified Theories have extremely large masses, far beyond the energies reached by any operated or foreseen accelerator. In fact, the only environment that provides enough energy to produce these “grand unified” monopoles is the early universe. Fortunately, monopoles are predicted to be stable. So, monopoles that may have been produced shortly after the Big Bang should have survived until the present day and should still be abundant in cosmic radiation. Over the past three decades, these relic monopoles have been searched for by various experiments, but so far, there is no experimental proof for their existence. Today, the flux of magnetic monopoles is experimentally constrained to a level of  $\mathcal{O}(10^{-16}) \text{ cm}^{-2} \text{ s}^{-1} \text{ sr}^{-1}$ , meaning that only extremely large detectors have the potential to either detect a monopole or to further improve existing flux limits.

Large scale Cherenkov telescopes deployed in open naturally occurring transparent media like sea water or glacial ice, which were originally constructed to detect Cherenkov light from secondary electrically charged particles produced in rare interactions of high energy extraterrestrial neutrinos with the surrounding matter, could detect magnetic monopoles with specific properties: (1) Relativistic monopoles moving at a speed above the Cherenkov threshold of the utilized medium could efficiently be detected, because the intensity of their Cherenkov emissions is enhanced by several orders of magnitude compared to the emissions from electrically charged particles. (2) Monopoles that catalyze the decay of nucleons in the target matter, a property that is predicted within several Grand Unified Theories, could be detected via the Cherenkov emissions from relativistic secondary particles produced in consecutive nucleon decays along the monopole trajectory.

This thesis concerns the search for relativistic magnetic monopoles using data taken with the AMANDA-II detector, a neutrino telescope embedded in the glacial ice at the South Pole. The outline of this work is as follows: Chapter 2 gives a brief overview of the significance of magnetic monopoles in various theoretical contexts from classical electrodynamics to Grand Unified Theories and Big Bang Cosmology, and treats those monopole interaction mechanisms that are essential for their detection. Chapter 3

explains the basic functionality of neutrino telescopes and how such detectors can be used (and have been used in the past) to search for magnetic monopoles. Particularities of the AMANDA-II neutrino telescope are explained in chapter 4. By convention, all data taken with AMANDA-II are analyzed in a “blind” manner, meaning that data selection strategies have to be optimized based on simulations. Thus, the simulation of the detector response to both relativistic magnetic monopoles and background atmospheric muons formed an integral part of this work. Chapter 5 explains the simulation software and the strategies that were used to establish a basis for a blind analysis. Chapter 6 summarizes the properties of both experimental and simulated data sets and describes the handling and filtering of the data. The progression of the data selection is described in chapter 7 to chapter 9. The ultimate analysis result, a limit on the flux of magnetic monopoles, is derived in chapter 10. A summary of the analysis results and a brief outlook on the future IceCube neutrino telescope are presented in chapter 11.

## 2 Magnetic Monopoles

Modern particle physics suggest that extremely massive, stable particles carrying magnetic charge ought to exist. If Big Bang cosmology is correct, such magnetic monopoles should have been produced during symmetry breaking phase transitions in the early universe. Most of the monopoles produced shortly after the Big Bang should have survived until the present day, but their density will have been strongly diluted during the inflationary phase of the Universe. Recent searches for relic monopoles rely on their electromagnetic interaction with matter or on their potential ability to catalyze nucleon decay.

### 2.1 Theory of magnetic monopoles

The idea that magnetically charged particles should exist has a long history in theoretical physics. While magnetic monopoles are formally permitted by classical electro dynamics and quantum mechanics, they are mandatory in Grand Unified Theories.

#### 2.1.1 Monopoles in classical electro dynamics

The introduction of magnetic charges to classical electrodynamics cancels the asymmetry between electricity and magnetism, which is apparent in the Maxwell equations [1]. The Maxwell equations in presence of matter take the form:

$$\nabla \cdot \vec{D} = 4\pi\rho_e \quad (1)$$

$$\nabla \cdot \vec{B} = 0 \quad (2)$$

$$\nabla \times \vec{H} - \frac{1}{c} \frac{\partial \vec{D}}{\partial t} = \frac{4\pi}{c} \vec{j}_e \quad (3)$$

$$-\nabla \times \vec{E} - \frac{1}{c} \frac{\partial \vec{B}}{\partial t} = 0, \quad (4)$$

where

$$\vec{D} = \epsilon \vec{E} \quad \text{and} \quad \vec{B} = \mu \vec{H}, \quad (5)$$

with  $\vec{E}$  and  $\vec{B}$  being the electric and magnetic field, and  $\epsilon$  and  $\mu$  being the permittivity and permeability.

The electric charge and current densities  $\rho_e$  and  $j_e$  appear as source terms in the Maxwell equations (1) and (3), while equations (2) and (4) are homogeneous, accounting for the experimental fact that neither magnetic monopoles nor magnetic currents have ever been observed in nature. Magnetic charges and currents can however simply be added to the theory. The two initially homogeneous equations would then take the form

$$\nabla \cdot \vec{B} = 4\pi\rho_m \quad (6)$$

$$-\nabla \times \vec{E} - \frac{1}{c} \frac{\partial \vec{B}}{\partial t} = \frac{4\pi}{c} \vec{j}_m, \quad (7)$$

where  $\rho_m$  and  $\vec{j}_m$  denote the magnetic charge and current densities. The modified Maxwell equations (1-4) and the constitutive equations (5) are then invariant under the substitutions [2]:

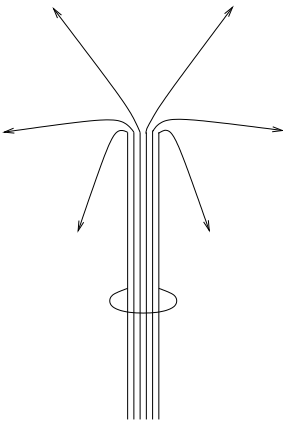
$$\begin{aligned} (\vec{E}, \vec{H}) &\mapsto (\vec{H}, -\vec{E}), & (\vec{D}, \vec{B}) &\mapsto (\vec{B}, -\vec{D}) \\ (\rho_e, \rho_m) &\mapsto (\rho_m, -\rho_e), & (\vec{j}_e, \vec{j}_m) &\mapsto (\vec{j}_m, -\vec{j}_e) \\ \epsilon &\mapsto \mu, & \mu &\mapsto \epsilon. \end{aligned} \quad (8)$$

For symmetry reasons, classical magnetic charges would look very similar to electrical charges. They would give rise to a radial magnetic field and interact via a  $1/r$  potential, with likes repelling and opposites attracting. In fact, the descriptions of electromagnetic phenomena, as for instance ionization or Cherenkov radiation, remain largely form-invariant when evaluated for magnetic instead of electric charges (see section 2.5).

### 2.1.2 Monopoles and Quantum Mechanics

A persuasive argument for the existence of magnetic monopoles was put forward by Dirac, when he studied the consequences of the existence of magnetic monopoles in a quantum mechanical context. He found that quantum mechanics allows magnetic monopoles only, if magnetic charges occur as multiples of an elementary magnetic charge  $g_D$  (the *Dirac Charge*), which relates to the electric elementary charge  $e$  as

$$g_D = \frac{\hbar c}{2e}. \quad (9)$$



Classically, charged particles couple to electromagnetic fields solely via the electric and magnetic fields, but quantum-mechanically, they couple to the scalar and vector potentials  $\Phi$  and  $\vec{A}$ .<sup>1</sup> At first glance, magnetic monopoles seem to conflict with quantum mechanics, for if we define  $\nabla \cdot \vec{B} \propto \rho_m$  there is no well defined vector potential such that  $\vec{B} = \nabla \times \vec{A}$ . Dirac showed that the monopole field can consistently be described with a vector potential which is well defined everywhere except for a line extending from the monopole to infinity (the celebrated *Dirac String*). In his 1931 paper [3], Dirac demonstrated that the string-singularity had no physical meaning, only if the quantization condition (9) was obeyed.

Dirac's result becomes more plausible if we envisage a magnetic monopole as an semi-infinitely long infinitesimally thin solenoid, as sketched in Figure 2.1 [4, 5, 6]. Classically, there is not much difference between the solenoid and a monopole: The magnetic field at the end of such a solenoid would look like an isolated magnetic charge. Quantum-mechanically, however, the solenoid can be identified with a monopole only, if it remains undetected in an electron interference experiment via the Aharanov-Bohm effect [7]. The condition for the phase picked up by the wave function of an electron when moved around the solenoid to be trivial is exactly the Dirac Quantization Condition (9).

One of the most attractive features of Dirac's monopole theory when it was first proposed was that it explained charge quantization. If there were at least one monopole in the universe, all electric charge must be a multiple of a common unit, the inverse of twice the Dirac Charge. The numerical value of Dirac Charge follows from the fine structure constant  $\alpha = e^2/\hbar c$ :

$$g_D = \frac{e}{2\alpha} \approx \frac{137}{2}e. \quad (10)$$

The magnetic elementary charge, and consequently the coupling constant, is obviously much larger than the electric one.

<sup>1</sup>Recall, for instance, the Schrödinger Equation for a particle in an electromagnetic field:  $\left[ -\frac{1}{2m}(\nabla - ie\vec{A})^2 + \Phi \right] \Psi = E\Psi$ .

**Figure 2.1** – The magnetic field at the end of a semi-infinite solenoid is indistinguishable from a magnetic monopole [4]. An Aharanov-Bohm-like experiment would fail to detect the solenoid only, if Dirac's quantization condition is obeyed.

### 2.1.3 Monopoles in Grand Unified Theories

In 1974, magnetic monopoles reappeared as integral part of Grand Unified Theories (GUTs). GUTs are based on the hypothesis that at some sufficiently high energy scale  $\Lambda$ , all fundamental interactions (except gravity) can be described with a single gauge group  $G$ , in which only one gauge coupling appears [8]. At lower energies, the symmetry of  $G$  is spontaneously broken to the symmetries of the standard model. 't Hooft and Polyakov discovered that in non-abelian gauge theories spontaneously broken down to some  $U(1)$  subgroup, monopoles appear as solitons, *i.e.*, as regular, finite energy solutions to the field equations [9, 10].

Loosely speaking, a GUT monopole is a region in space where the vacuum remains in the  $G$ -symmetric state (also referred to as the *false vacuum*), and asymptotically approaches its “true” vacuum configuration at large distances. Contrary to the Dirac monopole, the GUT monopoles does not require the introduction of magnetic charge “by hand”. The radial magnetic field of the GUT monopole arises from the configuration of the gauge fields in the monopole solution. Remarkably, the total magnetic flux emerging from the GUT monopole is quantized exactly as demanded by Dirac’s quantization condition. Unlike the point-like Dirac monopole, a GUT monopole has a rather complicated structure (Figure 2.2). In the innermost region, extending to a radius of order  $\Lambda^{-1}$  [11, 4], the full symmetry of the unified gauge group  $G$  is restored. Further outward, the monopole is surrounded by cloud of gauge bosons and virtual pairs of elementary particles. Interactions of particles with the monopole inner core can involve the exchange of gauge bosons associated with the unified gauge group. Such interactions might, for instance, violate the conservation of baryon number. This is the reason why monopoles might be able to “catalyze” nucleon decay (see section 2.5.4).

Monopole solutions are a general property of gauge theories which unify electromagnetism with the other fundamental forces. The precise monopole properties, like mass and charge, vary for different unified gauge groups, but are precise and unambiguous predictions of each theory. The monopole mass is related to the unification energy scale as

$$M \gtrsim \frac{\Lambda}{\alpha}, \quad (11)$$

where  $\alpha = e^2/\hbar c$  is the running coupling constant renormalized at the energy scale  $\Lambda$ .

The simplest group that can accommodate the symmetries of the standard model is  $SU(5)$ . As determined from the running of the low-energy coupling constants,  $\Lambda$  and  $\alpha$  should be of the order of  $10^{15}$  GeV and  $10^{-2}$  respectively. An  $SU(5)$  monopole should consequently have a mass around  $10^{17}$  GeV, and it would carry one Dirac Charge [13, 14]. The group  $SO(10)$  is the next simplest realistic GUT. Associated with the symmetry breaking of  $SO(10)$  are two types of monopoles [11, 4]: One monopole is very heavy ( $M > 10^{16}$  GeV) and is minimally charged. The other one is lighter, with a mass somewhere between  $10^{10}$  and  $10^{16}$  GeV, and multiply charged [15, 11]. Monopoles with masses around  $10^8$  GeV appear in an  $SU(15)$  GUT [16, 17]. Some supersymmetric models predict multiply charged monopoles with masses as low as  $10^7$  GeV [18, 19]

Although predictions for GUT monopole masses span many orders of magnitude, none of the predicted monopoles is light enough to be produced at

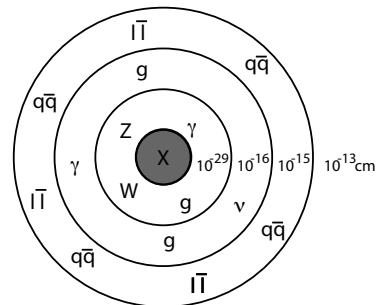


**Figure 2.2** – Possible structure of a GUT monopole. In the center of the monopole, out to  $\Lambda^{-1}$  ( $\approx 10^{-29}$  cm for the most common GUTs) there is a GUT symmetric vacuum (labeled X). From [12].

man-made accelerators. Any monopoles abundant today must be relics of an epoch shortly after the “Big Bang”, when the universe was extremely hot.

## 2.2 Monopole creation in the early universe

According to the Big Bang theory, the universe started from a tremendously hot and dense state and has been cooling and expanding ever since. In the concept of Grand Unification, the full unified gauge symmetry was fulfilled when the temperature exceeded the unification energy scale  $\Lambda$ .

As the universe further expanded and cooled, it underwent several phase transitions associated with the GUT Higgs fields acquiring some non-vanishing expectation value, thereby breaking the unified symmetry [20, 21]. At the time of the phase transition, the Higgs fields must have necessarily been uncorrelated at distances larger than the horizon distance (the furthest distance that light could have traveled since the Big Bang), and the particular vacuum configuration taken by the Higgs fields should have been different in causally disconnected domains. With further evolution of the universe, the horizon size continuously grew. When the causal domains coalesced, monopoles were formed at the intersection points of several domains via the so-called *Kibble mechanism* [22]. According to [22], the density of monopoles created in the early universe is about one per horizon-volume at the time of the phase transition.

It is commonly believed that shortly after the Big Bang the universe underwent a phase of exponential expansion (a so-called *inflationary* phase) [23, 24]. Without this inflationary phase, relic monopoles should be so abundant today that their mass density would exceed the mass density of the observable universe by many orders of magnitude [25].<sup>2</sup> Inflation solves this inconsistency, as the monopole density is drastically reduced during inflation. The issue of inflation is however not settled theoretically. Monopoles may have been produced either during inflation, at the end of inflation, or even afterwards [26, 27, 28, 4, 29]. Some scenarios allow monopole fluxes close to present experimental limits [30, 31, 32]. As of today, cosmology seems to make no firm prediction about the relic monopole abundance.

## 2.3 Acceleration of cosmic monopoles

During the lifetime of the universe, relic monopoles should have acquired kinetic energy in long range cosmic magnetic fields. Like electric charges are accelerated along electric field lines, magnetic monopoles are accelerated along magnetic field lines. The kinetic energy gained by a monopole of charge  $g$  on traversing a magnetic field  $\vec{B}$  along a particular path is [33, 34]

$$T = g \int_{\text{path}} \vec{B} \cdot d\vec{l} \sim gB\xi, \quad (12)$$

where  $B$  is the magnetic field strength, and  $\xi$  is the coherence length of the field. In the magnetic field of our galaxy for instance, which has a strength of  $\sim 3 \times 10^{-6}$  G and a coherence length  $\xi \sim 300$  pc, a monopole with one Dirac charge can gain up to  $6 \times 10^{10}$  GeV. Typical magnetic field strengths and spatial extensions of even more powerful monopole accelerators and the corresponding maximum energy gain for a singly charged magnetic

---

<sup>2</sup>This is known as the “monopole problem”.

monopole are listed in Table 1.

According to [33], magnetic monopoles should have encountered a sufficiently large number of cosmic accelerators to gain kinetic energies of  $\sim 10^{14}$  GeV. Monopoles with masses smaller than  $\sim 10^{14}$  GeV should hence be relativistic

Accelerator	$B/\mu\text{G}$	$L/\text{Mpc}$	$g_{\text{D}}B\xi/\text{GeV}$	Ref.
normal galaxies	3-10	$10^{-2}$	$(0.3 - 1) \cdot 10^{12}$	[35]
star-burst galaxies	10-50	$10^{-3}$	$(1.7 - 8) \cdot 10^{11}$	[36]
AGN jets	$\sim 100$	$10^{-4} - 10^{-2}$	$1.7 \cdot (10^{11} - 10^{13})$	[37]
galaxy clusters	2-30	$10^{-4} - 1$	$3 \cdot 10^9 - 5 \cdot 10^{16}$	[38]
extragal. sheets	0.1-1	1-30	$1.7 \cdot 10^{13} - 5 \cdot 10^{14}$	[39]

**Table 1** – Magnetic field strength  $B$ , coherence length  $\xi$  of various cosmic objects, and the maximum kinetic energy acquired by a singly charged magnetic monopole on traversing such a magnetic field [33].

## 2.4 The Parker Bound

The acceleration of monopoles in magnetic fields also implies a severe theoretical constraint on the monopole abundance: Monopoles residing in our Galaxy would gain kinetic Energy at the expense of the Galactic magnetic field. The requirement that the magnetic field be not depleted faster than it is regenerated by the Dynamo effect [40] constraints the monopole flux to be less than

$$\Phi = 10^{-15} \text{ cm}^2 \text{ sr}^{-1} \text{ s}^{-1}. \quad (13)$$

This is the well known *Parker Bound* [41]. The bound is valid for monopoles with masses smaller than  $10^{17}$  GeV.

## 2.5 Interaction with matter

The essence of the energy loss of electrically charged particles passing through matter can be described by classical electrodynamics. The same holds for magnetic monopoles. Electromagnetic interactions (and hence the energy loss) of magnetic monopoles is calculated using the Maxwell equations with the substitutions given in equation (8) [42, 43], in analogy to electrically charged particles.

### 2.5.1 Ionization

Electrically charged particles passing through matter lose energy mainly by ionization or excitation of atoms in the target matter via electromagnetic interactions. The mean energy loss per path length  $\frac{dE}{dx}$  of a particle with charge  $ze$ , speed  $\beta$ , and boost factor  $\gamma = E/M$  (with  $M$  the mass of the particle) can be calculated with the Bethe-Bloch formula [44, 45, 46],

$$\frac{dE}{dx} = \frac{4\pi N_e z^2 e^4}{m_e c^2} \cdot \frac{1}{\beta^2} \left[ \ln \left( \frac{2m_e c^2 \beta^2 \gamma^2}{I} \right) - \beta^2 \right], \quad (14)$$

where  $N_e$  and  $I$  are the electron density and mean ionization potential of the target material, and  $m_e$  is the electron mass.

A similar formula holds for the energy loss of magnetic monopoles [43]. From the substitutions for the Maxwell equations given in (8), one might conclude that any factor  $ze$  in the Bethe-Bloch formula describing the energy loss of a particle with (electric) charge  $ze$  had to be replaced with the magnetic charge  $g$  to describe a monopole. A monopole with one Dirac Charge  $g_{\text{D}} = 137/2e$  would then mimic a heavy ion with charge  $z \approx 69$ .

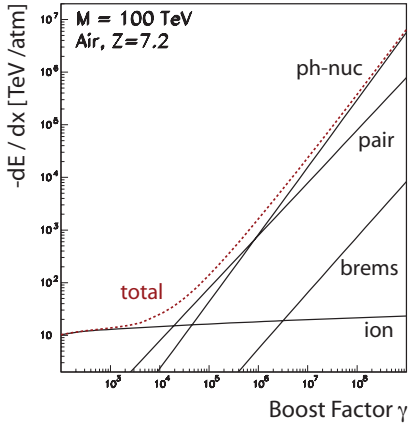


**Figure 2.3** – Energy losses of 100 TeV monopoles in air [47]. Losses due to photo-nuclear interactions and direct pair-production dominate for boost-factors  $\gamma > 10^4$ . Bremsstrahlung is suppressed by a factor  $1/M$ , and is hence less important.

This is indeed a valid approximation for monopoles with speeds close to the speed of light ( $\beta = v/c \approx 1$ ). The correct substitution, however, is

$$ze \mapsto g\beta, \quad (15)$$

where  $\beta$  is the speed of the monopole. The additional factor  $\beta$  arises, because the electric field from a moving magnetic monopole as seen by an atomic electron is proportional to  $\beta$  [43]. As a consequence, there is no rise in ionization loss for monopoles towards lower velocities. A monopole with one Dirac Charge and speed  $\beta \approx 1$  would lose  $(g/e)^2 \approx 4700$  times more energy than a particle which one unit electric charge.

### 2.5.2 Radiative energy losses

The Bethe-Bloch formula does not include the energy loss due to direct pair production, bremsstrahlung and photo-nuclear interactions. The probability for these so-called *radiative energy losses* rises with the particle energy. For ultra relativistic particles, radiative processes dominate the total energy loss.

The radiative energy loss of magnetic monopoles is discussed in detail in [47]. Photo-nuclear interactions and direct pair-production dominate for Lorentz boosts  $\gamma > 10^4$ . Bremsstrahlung is inversely proportional to the monopole mass and hence negligible for massive magnetic monopoles. Boost factors of  $10^4$  and higher are expected only for relatively light monopoles. Radiative processes are negligible over a wide range of predicted monopole masses. Figure 2.3 shows a comparison of radiative and ionization energy loss processes for 100 TeV monopoles in air.

### 2.5.3 Cherenkov light from relativistic monopoles

A fraction of the energy lost by charged relativistic particles traversing a dielectric medium is emitted from excited atoms in the medium as coherent radiation, so-called Cherenkov radiation [48]. Cherenkov radiation is emitted if the particle's speed  $\beta c$  exceeds the speed of light in the medium  $c/n$  (where  $n$  denotes the index of refraction). The radiation is emitted at a specific angle  $\theta_C$ , such that

$$\cos(\theta_C) = \frac{1}{\beta n}. \quad (16)$$

From the Huygens construction in Figure 2.4, one can see that the wavefront forms a cone around the particle track. Cherenkov radiation has a continuous frequency spectrum. In dissipative media,  $n$  and  $\theta_C$  are functions of the frequency  $\nu$ . For a particle with electric charge  $ze$ , the radiated energy per unit track length is

$$\frac{dE}{dx} = \frac{4\pi^2 z^2 e^2}{c^2} \int \left(1 - \frac{1}{\beta^2 n^2}\right) \nu d\nu. \quad (17)$$

The number of photons of a certain frequency or wavelength is proportional to  $d\nu$  or  $d\lambda/\lambda^2$ , meaning that short wavelengths dominate the Cherenkov spectrum.

Like electrically charged particles, relativistic magnetic monopoles will lose energy due to Cherenkov radiation. The intensity of the radiation is proportional to the square of the magnetic charge  $g$ . From substituting  $g$  for the electric charge  $ze$  in the energy loss calculation (equation

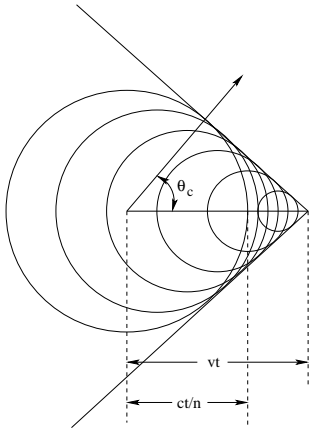


**Figure 2.4** – Huygens construction of the Cherenkov light cone.

(17)), one would conclude that monopoles with one Dirac Charge emit  $(g_D/e)^2 \approx 4700$  times more Cherenkov photons than particles with one unit electric charge. This is true for monopoles traversing a medium refractive index  $n = 1$ . For other media the correct substitution is

$$ze \mapsto ng. \quad (18)$$

The refractive index enters because not only the magnetic and electric charge have to be interchanged, but also the permeability  $\mu$  (assumed to be 1) and the permittivity  $\epsilon$  (see equation (8)), which are related through the refractive index  $n$ . For a minimally charged monopole traveling through water or ice, ( $n = 1.33$ ), the Cherenkov radiation is enhanced by a factor  $(g_D n/e)^2 \approx 8300$ , compared to an electrically charged particle with the same speed. The geometry and frequency spectrum of the emission, however, will be exactly the same [49].

#### 2.5.4 Catalysis of nucleon decay

Interactions of particles with the innermost core of a GUT magnetic monopoles might involve exchanges of the heavy gauge bosons associated with the unified gauge group. Such interactions can violate baryon number conservation (Figure 2.5). As a consequence, GUT monopoles passing through matter might catalyze nucleon decays along their trajectories (Figure 2.6). As the core size of a typical GUT monopole is  $\Lambda^{-1} \approx 10^{-29}$  cm, one would, on geometric grounds, expect the catalysis cross section to be of the order  $\sigma_{\text{cat}} \propto \Lambda^{-2} \approx 10^{-58}$  cm<sup>2</sup>. Callan and Rubakov however found that, due to monopole structure outside its core, the catalysis cross section should be enhanced to values similar to typical strong interaction cross sections [51, 52]. The cross section depends on the monopole speed as

$$\sigma_{\text{cat}} = \frac{\sigma_0}{\beta}, \quad (19)$$

where the constant  $\sigma_0$  should roughly be of the order of  $10^{-28}$  cm<sup>2</sup> [53].

The exact cross section depends on particularities of the monopole structure, which in turn varies for different GUTs and symmetry breaking patterns. Some GUT monopoles, as for instance the lighter monopoles arising from  $SO(10)$  symmetry breaking, will not catalyze nucleon decay at all [11, 4]. Other theoretical uncertainties are related to the properties of the target material. For certain materials and monopole velocities,  $\sigma_0$  might be smaller by two to six orders of magnitudes [54]. Also, the velocity dependence might be  $\beta^{-2}$  rather than  $\beta^{-1}$  [54, 53]. Although the theoretical description is exceedingly difficult, nucleon decay catalysis is very interesting for monopole searches, because it permits detection of extremely heavy, sub-relativistic monopoles.

## 2.6 Experimental bounds

Ever since monopoles were predicted, they have been searched for with a variety of experimental set-ups (see [56] for a review). Over decades of monopole search, the experimental constraints on the monopole abundance became progressively more stringent. Today, the flux of magnetic monopoles is experimentally constrained to a level well below the Parker Bound.

The most stringent flux limit resulted from monopole searches with the *Monopole Astrophysics and Cosmic Ray Observatory* (MACRO). The MACRO

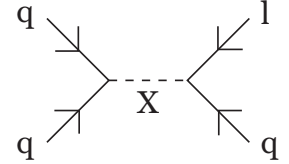


**Figure 2.5** – Example diagram for the exchange of a heavy gauge boson ( $X$ ) associated with the unified gauge group that violates baryon number conservation. Such processes could be catalyzed by magnetic monopoles. From [50].

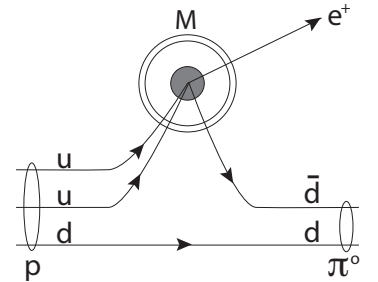


**Figure 2.6** – The process  $p \rightarrow \pi^0 e^+$  is an example of nucleon decay that could be catalyzed by GUT magnetic monopoles. From [55]

detector consisted of three types of sub-detectors: Liquid scintillators, streamer tubes, and nuclear track etch material [57]. More than five years of experimental data have been searched for signatures of magnetic monopoles in various velocity intervals between  $\beta = v/c = 4 \times 10^{-5}$  and  $\beta \approx 1$  [58]. The non-observation of any monopole candidate implies a limit on the flux magnetic monopoles at a level of  $\sim 1.4 \times 10^{-16} \text{ cm}^{-2}\text{s}^{-1}\text{sr}^{-1}$  (Figure 2.7).

The MACRO limit is superseded by results from other experiments only under certain conditions:

- (a) *If* magnetic monopoles catalyze nucleon decay, observations of the luminosity distribution of neutron stars imply a stringent bound on the monopole flux [59, 60]: Nucleon decays catalyzed by monopoles which were gravitationally captured inside neutron stars would cause the stars to heat up and emit ultra-violet and x-ray photons. The bound on the monopole flux inferred from on observational limits on ultra-violet and x-ray emissions from neutron stars lies at least six orders of magnitude below the Parker Bound.
- (b) In the velocity range near  $\beta = 10^{-3}$  [61], bound states of magnetic monopoles and nuclei would leave an etchable track in ancient Mica [61]. With an exposure time close to 500 Myr, the absence of such tracks in nearly 1000 m<sup>2</sup> of scanned Mica implies a flux limit two to three orders of magnitude below the Parker bound [61, 56].
- (c) For monopoles moving at relativistic speeds ( $\beta > 0.8$ ), the MACRO limit is superseded by monopole searches performed with neutrino telescopes.

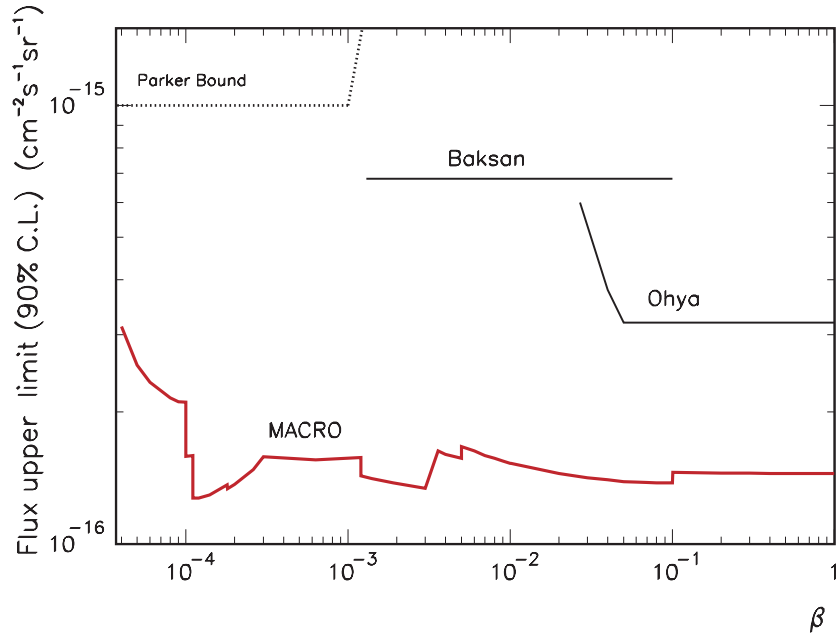


**Figure 2.7** – Limit on the flux of magnetic monopoles set by the MACRO collaboration. The limit is a result of the combination of different analyses using the various sub-detectors of the observatory. Individual analyses were optimized on the detection of monopoles in a certain velocity range (hence the rather complicated structure of the overall limit). Also shown are the limits set by the Ohya [62] and Baksan [63] experiments.

t

### 3 Monopole search with neutrino telescopes

The immense amount of Cherenkov light expected from a relativistic magnetic monopole traversing a transparent medium suggests to search for monopoles with Cherenkov detectors. Neutrino telescopes are presently the only Cherenkov detectors operated that are large enough to reach sensitivities to fluxes below the Parker Bound. Several neutrino telescopes are currently in operation [64, 65]. Others are under construction [66, 67, 68] or planned [69, 70]. The main science objective of these experiments is the identification of the sources of high energy cosmic rays via neutrino detection. Nevertheless, data from neutrino telescopes are also routinely searched for signatures of monopoles.

#### 3.1 The science objective of neutrino telescopes: Neutrino Astrophysics

Neutrino Astrophysics is a relatively young discipline, which attempts to use neutrinos as messenger particles to probe physics processes in extremely energetic cosmic environments such as galaxy centers and Gamma Ray Bursts, or super-nova remnants and micro quasars. The main mission of neutrino astrophysics is to identify such objects as sources of high energy cosmic rays. Cosmic ray physics is of general importance to any science objective involving neutrino telescopes, because secondary cosmic rays are an inevitable background to both the search for astrophysical neutrinos and the search for exotic particles. The background to magnetic monopole searches in particular, originates from interactions of cosmic rays of highest energies.

##### 3.1.1 Primary cosmic rays

Primary cosmic rays consist mostly of protons ( $\sim 90\%$ ), and a smaller fraction of helium nuclei ( $\sim 9\%$ ) and heavier nuclei ( $\sim 1\%$ ) [71]. Their flux at the top of the atmosphere is about 1000 nuclei per square meter per second. The energy spectrum extends from a few hundreds of MeV to above  $10^{20}$  eV. Over this wide range of energy, the spectrum appears relatively structureless, and can be well approximated by broken power laws as  $dN/dE \propto E^{-\gamma}$ . Two (perhaps three) changes of the slope are the only known features [72, 73, 46]: Around  $3 \cdot 10^{15}$  eV, the slope steepens from  $\gamma \approx 2.7$  to  $\gamma \approx 3.1$ . This bend in the spectrum is referred to as the *knee* (Figure 3.1). Around  $10^{18}$  eV the slope flattens again to  $\gamma \approx 2.7$  at what is called the *ankle*. Between the knee and the ankle, around  $5 \cdot 10^{17}$  eV, a third break in the spectrum has been observed (the *second knee*), where the slope steepens to  $\gamma \approx 3.3$  [74, 75, 76]. (Figure 3.2 shows a blowup of the cosmic ray spectrum in the region between the knee and the ankle, exposing the second knee.)

The broken power law spectrum as well as the chemical composition of cosmic ray particles is believed to be a result of shock acceleration (first order Fermi mechanism [77, 78]) and subsequent diffusion through the interstellar medium (*leaky-box* model, see *e.g.* [71]). Fermi acceleration naturally produces an energy spectrum close to  $E^{-2}$ . The observed energy spectrum is steeper than the one at the acceleration site, because (according to the leaky-box model) the typical residence time  $\tau$  of cosmic rays in our galaxy decreases with energy as  $\tau \propto E^{-\delta}$ , with  $\delta \approx 0.6$ . The limiting factor to both the maximum energy achieved by shock acceleration and the resi-

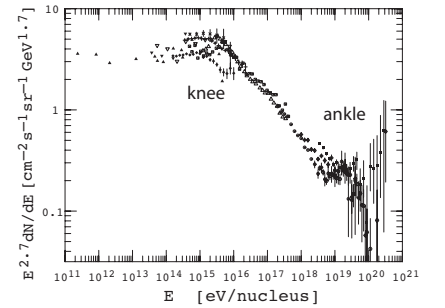
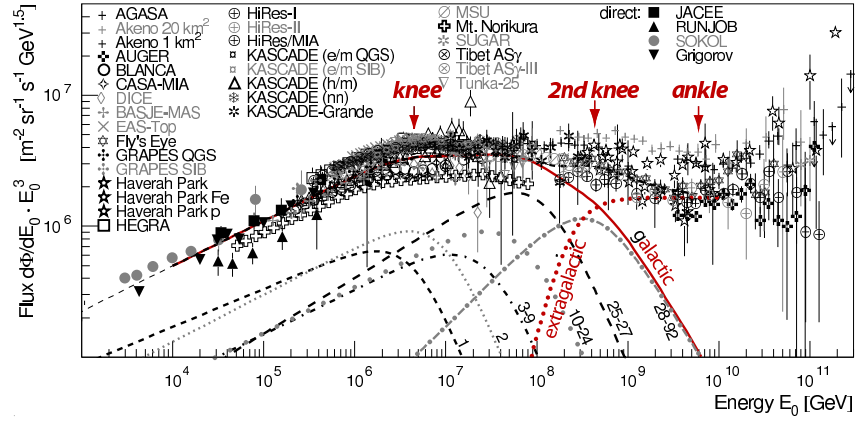


**Figure 3.1** – Observed energy spectrum of primary cosmic rays. Between  $10^{11}$  and  $10^{20}$  eV, the spectrum follows a power-law with changes in the slope at  $\sim 3 \cdot 10^{15}$  eV (knee), and  $\sim 10^{18}$  eV (ankle) [73]. For a better exposure of the features in the slope, the spectrum is weighted by  $E^{2.7}$ . The slope change around  $\sim 5 \cdot 10^{17}$  eV (referred to as second knee) is less exposed in this presentation. The integral flux of cosmic ray particles above the knee and the ankle are approximately 1 per square meter and one per square kilometer per year, respectively [72].

**Figure 3.2** – Available cosmic ray data at the end of the cosmic ray spectrum (the measured is flux weighted by  $E^3$ ). One possible explanation for the smooth continuation of the energy spectrum up to the second knee is a significant contribution from elements heavier than iron [84]. The flux of the “trans-iron” elements is labeled 28-92. From [85].



dence time in our galaxy is magnetic confinement: Cosmic ray nuclei with higher nuclear charge  $Z$  gain more energy in cosmic accelerators and are more efficiently confined in the galactic magnetic field.

In the traditional interpretation of the observed broken power law spectrum, particles with energies below the knee are accelerated within our galaxy. The most common environment in which shock acceleration can take place are super-nova shocks expanding into the inter-stellar medium. Galactic super-nova explosions can account for the bulk of cosmic rays, provided about 10% of the kinetic energy of their ejecta is converted into relativistic cosmic rays. One therefore identifies the knee in the cosmic ray spectrum with the cut-off energy of protons accelerated in galactic super-novae. Since the maximum energy that cosmic ray particles can acquire in super-nova shocks is proportional to  $Z$  [79, 80, 81], the steepening of the slope above the knee is believed to reflect the consecutive cut-offs of progressively heavier elements,<sup>3</sup> and to some extent, the charge dependent leakage of cosmic rays from the galaxy.

The ankle is traditionally believed to mark the transition from galactic to extra-galactic cosmic rays. Particles with energies of  $10^{18}$  and beyond have gyro radii larger than than the extensions of the galactic disk, and are hence believed to be of extragalactic origin. The ankle structure could be due to cosmic rays from more powerful extragalactic accelerators that penetrate into the galaxy and dominate the observed flux above  $10^{18}$  eV. The cosmic ray spectrum is expected to break off above  $\sim 5 \cdot 10^{19}$  eV, where protons are absorbed through pion production with the 2.7-K microwave background photons ( $p\gamma \rightarrow \Delta^+ \rightarrow n\pi^+(p\pi^0)$ ), an effect referred to as *Greisen-Zatsepin-Kuz'min* (GZK) cut off [83].

The interpretation of the cosmic ray spectrum is however not free of debate. Detailed examinations of the energies achievable in standard galactic super-nova shocks suggest that the maximum energy is limited to  $E/Z \sim 10^{14}$  eV [81, 80]. Then, galactic super-novae were not sufficient to account for the smooth continuation of the cosmic ray spectrum all the way up to the ankle. Several scenarios have been suggested to explain observations:

- A significant contribution of extremely heavy elements (*poly-gonato*<sup>4</sup> model): The heaviest common nucleus abundant in cosmic radiation

<sup>3</sup>Recent measurements indeed indicate a composition transition from light to heavier elements above the knee [82].

<sup>4</sup>poly gonato (Greek): “many knees”

is iron ( $Z = 26$ ). As the knee positions of individual elements scale with nuclear charge  $Z$ , a galactic component of super-heavy elements with  $Z > 26$  could explain the all particle spectrum up to the second knee [85, 84] (see Figure 3.2).

- The presence of a second class of galactic cosmic ray accelerators, which are rarer than supernova remnants but accelerate cosmic ray nuclei to higher energies [86, 87, 88].
- An onset of the extragalactic component already around  $10^{17}$  eV [89, 90]: Extragalactic protons would suffer, besides the GZK effect, from energy loss associated with the photo-production of  $e^+e^-$  pairs on the cosmic micro wave background. This would result in a “pair-production dip” between  $10^{18}$  and  $10^{19}$  eV, which would mimic the ankle, *if* extragalactic cosmic rays predominantly consisted of protons and started dominating the spectrum at energies much lower than previously assumed (Figure 3.3).

Much speculation surrounds the origin of cosmic rays above the ankle. Active galactic nuclei or gamma ray bursts might provide enough power to accelerate cosmic rays up to the highest energies observed. The observation of high energy neutrinos from these candidate sources would provide inevitable evidence for hadron acceleration in these sources.

### 3.1.2 Cosmic messengers

Source tracing of cosmic rays is restricted to highest the energies. Protons with energies below  $10^{19}$  eV will be deflected in galactic magnetic fields and thus lose all directional information. Particles above this energy will travel in straight lines through galactic and intergalactic magnetic fields, but will be absorbed in the inter-stellar photon background. The acceleration of cosmic rays, however, is always connected with the emission of gamma rays and neutrinos. This correlation *must* exist, because some fraction of the the accelerated particles will interact in their sources with ambient matter or photons (This mechanism is referred to as “*astrophysical beam dump*”, see Figure 3.4). The interaction will result in the production of pions. The neutral pions will decay into photons as  $\pi^0 \rightarrow \gamma\gamma$ , while the charged pions decay as  $\pi^\pm \rightarrow \mu^\pm\nu_\mu$ ,  $\mu^\pm \rightarrow e^\pm\nu_\mu\nu_e$ . Apart from protons, also photons and neutrinos can be used as messenger particles from cosmic accelerators. The (neutral) photons are not affected by magnetic fields. However, high energy gamma rays will be absorbed when interacting with the photon background via Pair-production ( $\gamma\gamma \rightarrow e^+e^-$ ). As a consequence, the universe is opaque to high energy gamma rays.

Neutrinos in contrast, do not suffer deflection or absorption during propagation. Their great penetrating power allows them to escape from dense sources that may be opaque to other particles, and reach the Earth from the most distant cosmic objects. However, their small interaction probability poses the greatest challenge to neutrino astrophysics: Extremely large detectors are needed to address the small fluxes predicted for cosmic neutrinos.

## 3.2 The concept of a neutrino telescope

Fundamentally, a neutrino telescope maps the Cherenkov light generated by charged particles with a three dimensional grid of optical sensors embedded in a transparent medium which acts as target and Cherenkov medium

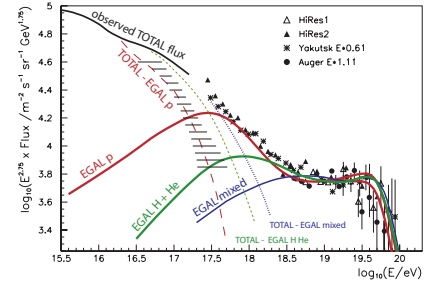


**Figure 3.3** – The upper end of the cosmic ray spectrum. The hatched area shows the probable fall off of the galactic component, as inferred from measurements of the KASCADE experiment [82]. The thick colored lines represent models for the flux of extragalactic cosmic rays. The dashed lines of same color represent the amount of cosmic rays that must, within these models, be due to galactic sources. An extragalactic component consisting predominantly of protons which dominates the overall spectrum just above  $\sim 10^{17}$  eV (red line labeled “EGAL p”) would allow a steeply falling galactic component as suggested by KASCADE. From [86].

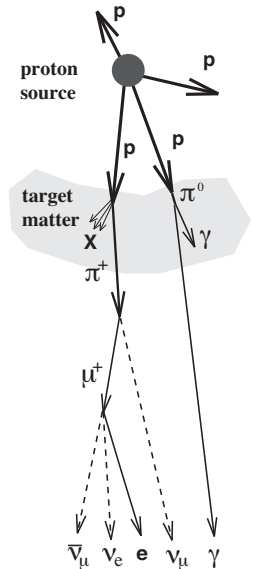


**Figure 3.4** – Astrophysical beam dump. From [91].

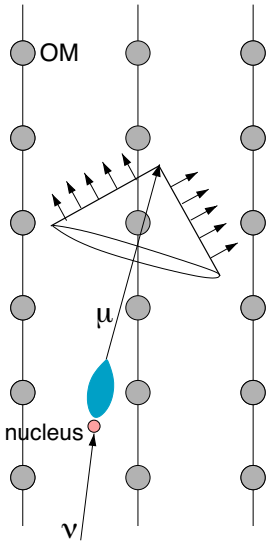


**Figure 3.5** – Principle of a neutrino telescope: The Cherenkov light cone from charged leptons, produced in neutrino nucleon interactions, is mapped with a matrix of optical sensors (labeled OM).

(Figure 3.5). Neutrinos can only be detected through the Cherenkov light emitted by secondary charged leptons that are created in charged current interactions with nuclei in the target matter as

$$\nu_l(\bar{\nu}_l) + N \rightarrow l^-(l^+) + X, \quad (20)$$

where  $l$  is one of the lepton flavors ( $e, \mu, \tau$ ),  $N$  is a nucleon, and  $X$  is a hadronic cascade. The exact Cherenkov signature of the daughter lepton depends on its flavor. Relativistic muons from  $\nu_\mu$ -interactions travel over large enough distances to leave an elongated track-like signature that permits accurate inference of the direction of the initial neutrino. Electrons in contrast, cascade quickly in the target material via bremsstrahlung and pair production, resulting in a spherical light pattern. Extremely short-lived tau leptons travel only short distances in the detector before they decay. The signature of ultra high energy  $\nu_\tau$  are two bright cascades at the production and the decay vertex, respectively (the so-called *double bang* signature).

As neutrinos interact only weakly, their probability to interact in the vicinity of a detector is extremely small. One way to construct a detector large enough to reach astrophysical sensitivity at reasonable cost is to utilize a naturally abundant medium for detection. Sufficiently transparent media are deep oceans, lakes or the thick ice layer at the South Pole. Photomultiplier tubes (PMTs) are used as light sensors, since they are relatively inexpensive and robust, have large collection areas, and are highly sensitive to visible and ultraviolet light. The PMTs are deployed at depth, typically one to two kilometers below the surface, in order to shield the detector from charged particles created in cosmic ray interactions in the atmosphere above the detector.

The preferred detection channel for cosmic neutrinos is the muon channel, because the elongated muon tracks provide the best directional information. At TeV energies, the direction of the initial muon can be reconstructed from the time and spatial pattern of detected Cherenkov photons with degree accuracy or better. The simplest criterion to suppress the cosmic ray induced background, then, is to consider only those muons which enter the detector from below the horizon. Since the neutrino is presently the only known particle capable of crossing the entire Earth, muons from below the horizon are assumed to be neutrino induced. Apart from the small fraction of cosmic ray induced muons for which the direction reconstruction fails, the only remaining background are muons induced by atmospheric neutrinos, which were created in cosmic ray interactions in the atmosphere on the opposite hemisphere (Figure 3.6).

### 3.3 Event classes in a neutrino telescope

The “beam dump” mechanism (*c.f.* Figure 3.4) applies for meson cascades not only in stellar environments but also in the Earth’s atmosphere. Collisions of primary cosmic rays with atmospheric air nuclei produce cascades of high energy secondary particles. The most penetrating components of these secondary cosmic rays are highly relativistic muons and neutrinos. They are created as decay products of charged mesons, mostly pions. Both atmospheric neutrinos and atmospheric muons are capable of reaching detectors located several kilometers underground and form the principal background to all particle searches performed with neutrino telescopes.

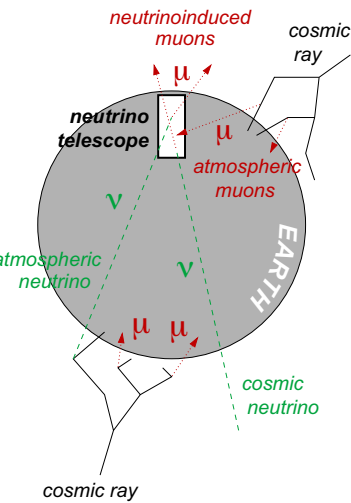


**Figure 3.6** – In a standard cosmic neutrino search, the Earth acts as a filter against the background of cosmic ray induced muons. Only particles that arrive from the hemisphere opposite the detector are considered. Atmospheric neutrinos constitute the remaining background.

### 3.3.1 Atmospheric muons

Muons are the most numerous charged secondary cosmic rays reaching the Earth’s surface. Their energy and angular spectrum is a convolution of the primary cosmic ray spectrum, their production probability, their energy loss and their decay. Atmospheric muons with energies of some hundreds of GeV at the surface are capable of reaching depths at which neutrino telescopes are typically located. At these energies, the muon energy spectrum is steeper than the spectrum of primary cosmic rays (asymptotically by one power in energy), because mother pions with energies greater than  $\sim 115$  GeV tend to interact in the atmosphere (*i.e.*, lose energy) before they decay [92].

Although neutrino telescopes are shielded by several kilometers of water or ice, the bulk of detected particles are atmospheric muons. Figure 3.7 shows the depth dependence of atmospheric muon flux underground. The AMANDA-II telescope, for instance, is covered with  $\sim 1.5$  km of South Polar ice, and atmospheric muons cause an event rate around 90 per second, outweighing the rate of detected atmospheric neutrinos by a factor  $> 10^6$  [93].

As atmospheric muons are created in the atmosphere above the detector, they will always enter the detector from above the horizon (Figure 3.8). Therefore, the most efficient way to eliminate the atmospheric muon background is to discard *down-going* particles.

Some neutrino searches (those that are designed to detect cosmic neutrinos of extremely high energies), and searches for monopoles and some other exotic particles, extend their search region above the horizon. The discriminating criterion against atmospheric muons in these searches can be based on the amount of energy deposited in the detector as Cherenkov radiation. Searches above the horizon are less efficient than those restricted to only one hemisphere. Despite their steep energy spectrum, atmospheric muons can mimic the Cherenkov signature of extremely highly energetic particles: In interactions of very energetic cosmic rays in the atmosphere, muons are produced in bundles of many nearly parallel muons. Although the individual muons are of relatively low energy, the total Cherenkov light yield can be comparable to that expected in signatures of ultra-high energetic (cosmic) neutrinos or relativistic magnetic monopoles.

### 3.3.2 Atmospheric neutrinos

Like atmospheric muons, atmospheric neutrinos occur as decay products of charged mesons that were produced in collisions with cosmic ray particles in the upper atmosphere. In the energy range of interest, that is for neutrino energies above  $\sim 100$  GeV, the energy spectrum of atmospheric muon neutrinos is steeper than the spectrum of primary cosmic rays by one power in energy, *i.e.*,  $dN/dE_\nu \propto E^{-3.7}$ .<sup>5</sup> In contrast, the spectrum of neutrinos created in astrophysical beam dumps in cosmic accelerators is expected to parallel the hard energy spectrum of accelerated nuclei (typically  $\sim E^{-2}$ ), because the mother mesons decay in free flight in the low density environment.

<sup>5</sup>The flux of atmospheric electron neutrinos (decay products of atmospheric muons) is substantially smaller than that of muon neutrinos, because most muons at GeV energies and above reach the ground before they decay. In fact, most  $\nu_e$  originate from the decay of charged kaons.

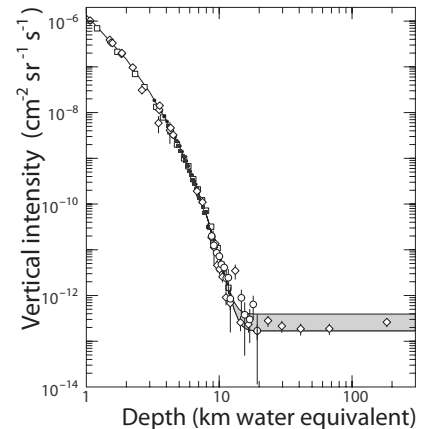


**Figure 3.7** – Vertical muon flux vs depth. The shaded area at depths greater than 10 km w.e. represents the neutrino-induced muons. From [46].

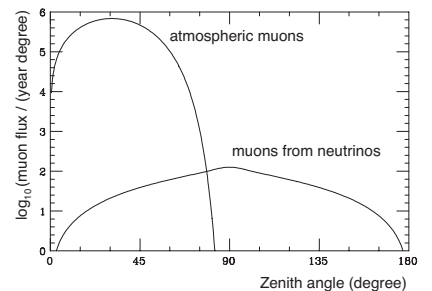


**Figure 3.8** – Zenith angle distribution of atmospheric muons and neutrino induced muons in a neutrino telescope. A zenith angle of  $0^\circ$  corresponds to a muon track that is vertically down-going. The atmospheric muon background vanishes for zenith angles greater than  $85^\circ$ . From [94].

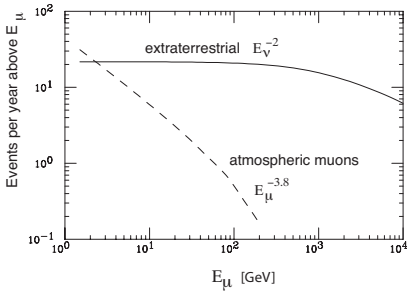


**Figure 3.9** – Expected number of muons detected in a neutrino telescope above a certain threshold  $E_\mu$ . The flux of cosmic neutrinos following a hard energy spectrum as  $E_\nu^{-2}$  can be identified as excess of events at high energies. From [94].

Figure 3.9 shows the energy depended integral muon flux in a neutrino telescope for muons induced by atmospheric neutrinos and muons induced by cosmic neutrinos with an energy spectrum as  $E^{-2}$ .

Atmospheric neutrinos are the principal background to searches for cosmic neutrinos of (in an astrophysical context) relatively low energies. For searches for ultra high energy neutrinos or relativistic magnetic monopoles, atmospheric muon bundles are the dominant background, compared to which atmospheric neutrinos are entirely negligible.

### 3.4 Monopole searches

The most obvious way to search for monopoles with a neutrino telescope is to look for monopole Cherenkov signatures. This of course, requires the monopoles to have a speed above the Cherenkov threshold, which in turn implies that only lighter mass monopoles can be detected, as only those would be relativistic. Heavy, slowly moving monopoles could be detected via nucleon decay catalysis. Strictly speaking, the catalysis signature is also a Cherenkov signature, as the monopoles are detected via Cherenkov emissions of the nucleon decay products. Therefore, the detection of sub-relativistic monopoles requires the monopoles to be capable of catalyzing nucleon decay, which is however only the case within certain unified gauge theories.

The search strategies for relativistic monopoles and super heavy, sub-relativistic monopoles differ. The signal of relativistic magnetic monopoles stand out due to their enormous Cherenkov emission, whereas super-heavy monopoles stand out due to their sub-relativistic velocity. Dominant background to both searches are specific categories of atmospheric muon events: To relativistic monopole searches, large atmospheric muon bundles are the most severe background. To searches for slowly moving monopoles, coincident atmospheric muons from independent air-showers, which enter the detector with a time difference of several micro-seconds relative to each other, pose the most challenging background, as the light flow in the detector can mimic a sub-relativistic particle crossing.

#### 3.4.1 Cherenkov signature of background atmospheric muons

Muons detected in a neutrino telescope are ultra-relativistic ( $\beta \approx 1$ ) and have velocities well above the Cherenkov threshold ( $E_{\text{thresh}} = 160 \text{ MeV}$ , for muons in ice or water). Cherenkov radiation is emitted at an angle  $\theta_C \approx 41^\circ$  relative to the muon track. Light sensors used in neutrino telescopes are sensitive to optical photons, with wavelengths between 350 to 650 nanometers. Within this wavelength interval, the refractive index is approximately constant. The number of photons emitted per path length  $dx$  and wavelength interval  $d\lambda$  is given by the Franck-Tamm Formula

$$\frac{d^2 N_\gamma}{dx d\lambda} = \frac{2\pi\alpha}{\lambda^2} \left( 1 - \frac{1}{\beta^2 n^2} \right), \quad (21)$$

where  $\alpha$  denotes the Finestructure constant. In the relevant wavelength interval, a muon will emit about 200 Cherenkov photons per centimeter. The total energy loss of a relativistic muon due to Cherenkov radiation is about 400 eV per centimeter, which is marginal compared to the energy loss due to ionization ( $\approx 2 \text{ MeV}$  per centimeter track, for a minimally ionizing muon) [46]. In addition to Cherenkov radiation and ionization, muons will lose energy in radiative processes like bremsstrahlung, pair produc-

tion, and photo nuclear interactions. The ionization loss shows only small fluctuations and is practically independent of the muon energy. The other processes are highly stochastic in nature.

The total average energy loss per unit length can be parameterized as

$$-\left\langle \frac{dE_\mu}{dx} \right\rangle = \alpha(E_\mu) + \beta(E_\mu)E_\mu. \quad (22)$$

The coefficient  $\alpha$  represents the ionization loss and can be described by the Bethe-Bloch formula (see for example [46]).  $\beta$  accounts for the stochastic fraction. A first order approximation can be made by considering  $\alpha$  and  $\beta$  to be constant. Assuming the muon minimum-ionizing  $\alpha$  is about  $0.2 \text{ GeV m}^{-1}$ . The value of  $\beta$  is about  $3.4 \cdot 10^{-4} \text{ m}^{-1}$  in ice, so that the stochastic processes start to dominate over the continuous ones at about  $600 \text{ GeV}$  (Figure 3.10). Secondary particles have momenta aligned with the muon track. Their Cherenkov light is therefore peaked at the Cherenkov angle of the muon, preserving the conical geometry of the emission. The resulting enhancement of the Cherenkov light intensity permits estimates of the muon energy.

### 3.4.2 Arrival directions of magnetic monopoles

The energy loss that monopoles suffer during their passage through matter dictate the mass range to which monopole searches with underground detectors are sensitive. Like neutrinos, magnetic monopoles are predicted to be extremely penetrating. Unlike neutrinos, this penetrating power rises with the monopole mass. Super heavy GUT monopoles with masses around  $10^{17} \text{ GeV}$  can pass through the entire Earth without being absorbed and could hence reach a neutrino telescope from all directions. Lighter monopoles are expected to be relativistic but are, below a certain mass threshold, absorbed in the Earth. Hence, they can reach a neutrino telescope only from above the horizon.

Magnetic monopoles traversing matter lose energy mostly through ionization. The full Bethe-Bloch formula adapted for monopoles is discussed in [43]. Including all corrections, it has the form

$$\frac{dE}{dx} = \frac{4\pi N_e g^2 e^2}{m_e c^2} \left[ \ln \left( \frac{2m_e c^2 \beta^2 \gamma^2}{I} \right) - \frac{1}{2} + \frac{K(|g|)}{2} - \frac{\delta}{2} - B(|g|) \right], \quad (23)$$

where  $N_e$  density of electrons,  $m_e$  is the electron mass,  $I$  mean ionization potential,  $\delta$  density effect correction [96], and  $K(|g|)$  is the *Kazama-Yang-Goldhaber* (KYG) cross section correction [97], which takes the values

$$K(|g|) = \begin{cases} 0.406 & \text{for } |g| = 137e/2, \\ 0.346 & \text{for } |g| = 137e, \end{cases} \quad (24)$$

for monopoles carrying one or two Dirac charges, respectively.  $B(|g|)$  is the Bloch correction, taking the values

$$B(|g|) = \begin{cases} 0.248 & \text{for } |g| = 137e/2, \\ 0.672 & \text{for } |g| = 137e. \end{cases} \quad (25)$$

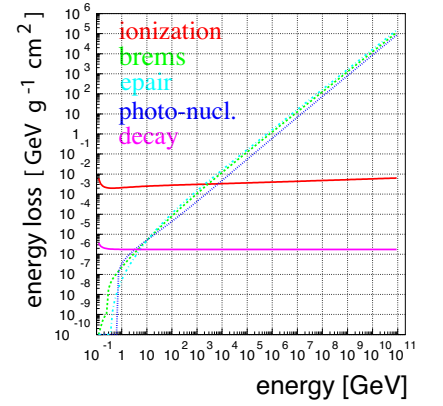


**Figure 3.10** – Energy dependence of energy loss processes (ionization, bremsstrahlung, pair-production, and photo-nuclear interactions) of relativistic muons traversing matter. The loss processes were simulated with the *Muon Monte Carlo mmc*. From [95].

Formula (24) holds for moderate Lorentz boosts  $\gamma = E/M < 100$  [43]. For such Lorentz boosts, radiative energy losses are negligible, and the ionization loss of a minimally charged monopole passing through ice or water is of the order of 10 GeV per centimeter. In the Earth's mantle (consisting mostly of silicon) and the Earth's core (consisting mostly of iron) the ionization loss is three to ten times higher. On traversing the full diameter of the Earth, a relativistic monopole would lose  $\mathcal{O}(10^{11})$  GeV [98]. Since the monopole kinetic energy acquired in cosmic magnetic fields is of the order of  $10^{12}$  to  $10^{15}$  GeV, monopoles may reach neutrino telescopes from below.

In order to be detectable via direct Cherenkov emissions, monopoles must have a velocity above the Cherenkov threshold when reaching the detector. For ice or water this requires a minimum Lorentz boost of  $\gamma \sim 1.5$ . With an initial kinetic energy of  $10^{14}$  GeV, monopoles with masses up to  $\sim 10^{14}$  GeV are fast enough to be detected by their direct Cherenkov emissions.

For very light monopoles ( $M < 10^7$  GeV), the initial Lorentz boost will be high and radiative energy losses are dominant. The passage of light monopoles through the Earth is treated in detail in [33]. Figure 3.11 Shows the Lorentz boost of light magnetic monopoles with initial kinetic energies between  $10^{11}$  and  $10^{14}$  GeV after traversing the Earth. With these initial kinetic energies, monopoles with masses down to  $10^7$  GeV can traverse the full diameter of the Earth.

### 3.4.3 The Monopole Cherenkov signature

The total number of Cherenkov photons per track length  $dx$  and wavelength interval  $d\lambda$  emitted by a monopole is calculable with the Franck-Tamm formula adapted for magnetic monopoles [49]:

$$\frac{d^2N}{dx d\lambda} = \frac{2\pi\alpha}{\lambda^2} \left(\frac{gn}{e}\right)^2 \left(1 - \frac{1}{\beta^2 n^2}\right), \quad (26)$$

where  $g$  denotes the magnetic charge and  $n$  is the refractive index. A minimally charged monopole traversing ice will lose about 300 MeV per centimeter due to Cherenkov radiation. The number of emitted Cherenkov photons is of the order  $10^6$  per centimeter in the wavelength interval between 400 nm and 600 nm.

For monopole with a speed  $\beta \approx 1$ , the total amount of Cherenkov light due to the bare magnetic charge equals the amount of light emitted by a muon with an energy of  $\sim 14$  PeV. If the monopole is extremely relativistic, this amount of Cherenkov light is enhanced by the emissions from secondary particles.

Monopoles which are detectable with a neutrino telescope are not necessarily *ultra*-relativistic. Monopoles with  $\beta < 1$  emit Cherenkov light at smaller angles  $\theta_C$  and with smaller intensities (see equation (26)). The Cherenkov threshold in water or ice is  $\beta \approx 0.75$ . Monopoles with velocities below this threshold can still be detected via the Cherenkov emission of secondary electrons ( $\delta$ -electrons). With a speed of  $\beta \approx 0.5$  or greater, a monopole can produce  $\delta$ -electrons with sufficient kinetic energy to emit Cherenkov radiation. Figure 3.12 shows the number of Cherenkov photons emitted by monopoles and secondary  $\delta$ -electrons as a function of the monopole velocity.

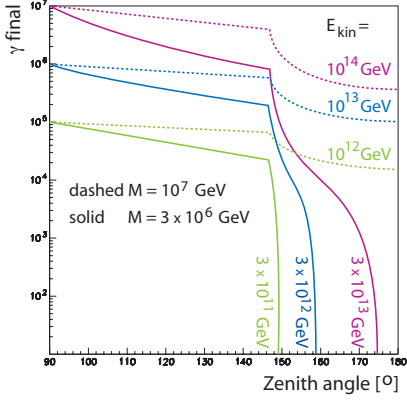


**Figure 3.11** – Lorentz boost of light magnetic monopoles at a detector as a function of their arrival direction. A zenith angle of  $90^\circ$  corresponds to a horizontal track,  $180^\circ$  corresponds to a vertically up-going track. From [33].

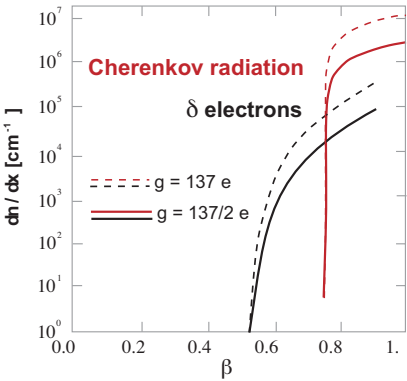


**Figure 3.12** – Number of Cherenkov photons emitted per centimeter path length by monopoles carrying a Dirac charge  $g = g_D = 137/2 e$  and  $g = 137 e$ . The threshold for direct Cherenkov radiation is  $\beta \approx 0.75$ . Monopoles with  $\beta > 0.52$  can produce  $\delta$ -electrons with enough kinetic energy to emit Cherenkov light.

The search for relativistic magnetic monopoles arriving from the opposite hemisphere *i.e.*, those which would be detected as *up-going* particles in a neutrino telescope, is almost background-free. Background events from atmospheric neutrinos have only a small Cherenkov light yield compared to relativistic monopoles and are easily rejected. Large atmospheric muon bundles in contrast can illuminate large areas of the detector. Bundles induced by cosmic rays of highest energies can contain up to tens of thousands of muons, spread over a cross sectional area as large hundreds of square meters [99]. Track reconstructions are more probable to fail on bundle events, since the cone geometry of the Cherenkov emission is less regular than the geometry of the emission from only a single track. The background of mis-reconstructed muon bundles is rejected using criteria sensitive to the Cherenkov light intensity rather than to the timing of the detected Cherenkov photons. Such criteria have enough rejection power to extend the search to the angular region above the horizon.

### 3.4.4 Catalysis signature

Super-heavy monopoles ( $M > 10^{16}$  GeV) are expected to have velocities around  $10^{-3}c$  [56]. Monopole passing through a neutrino telescope at such sub-relativistic speeds might catalyze the decay of protons and neutrons in the target matter, mainly as [100]

$$\begin{aligned} p &\rightarrow e^+\pi^0 & \text{and} & & p &\rightarrow \mu^+K^0, \\ n &\rightarrow e^+\pi^- & \text{and} & & n &\rightarrow \mu^+K^-. \end{aligned} \tag{27}$$

The signature of a nucleon decay catalyzing monopole would be a series of closely spaced bursts of Cherenkov light, emitted from the decay products, along the monopole trajectory. The mean free path of the interaction depends on the catalysis cross section, for which there is no firm theoretical prediction (see section 2.5.4). It may lie in the sub-millimeter range, but could also exceed meters (in which case neutrino telescopes cease to be sensitive [101]).

In a search for sub-relativistic monopoles, the main distinctive feature is the event duration (*i.e.*, the time span over which Cherenkov light is collected) rather than the light yield. A challenging background to this kind of analysis are overlapping atmospheric muon events. If muons from independent air showers coincide within tens of micro seconds they may fake the time characteristics of slowly moving particle [101].

## 3.5 Experimental bounds

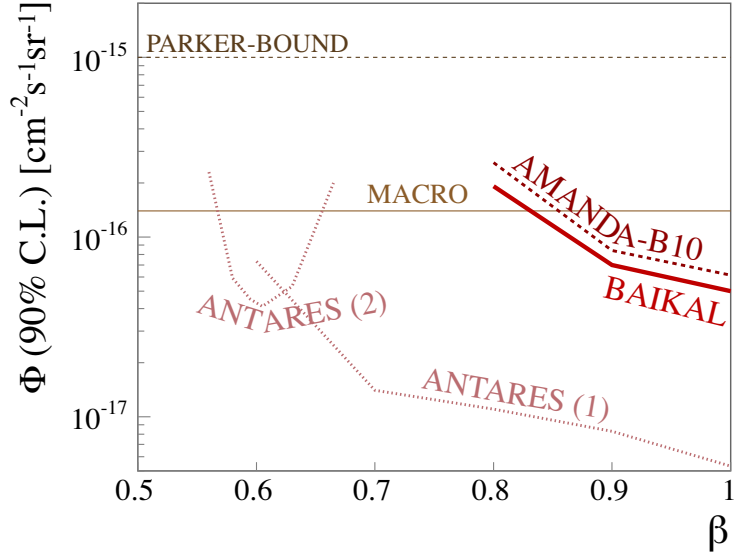
Searches for relativistic monopoles have been carried out with the BAIKAL neutrino telescope [102, 65], and with AMANDA-II's predecessor AMANDA-B10<sup>6</sup> [103]. Neither experiment has observed a monopole signal, and both analyses yielded upper flux limits (Figure 3.13). Both experiments have considered monopoles carrying one Dirac charge and monopole speeds greater than  $\beta = v/c > 0.8$ . As these analyses were restricted to monopoles from below the horizon, the limits apply to monopoles with masses roughly between  $10^7$  and  $10^{14}$  GeV.

Strategies for monopoles search with the ANTARES underwater neutrino telescope, which is presently under construction in the Mediterranean, have

---

<sup>6</sup>The AMANDA-B10 detector is a sub-array of AMANDA-II. It corresponds to an earlier construction stage, when only about half the number of optical sensors were deployed. The AMANDA-B10 detector was operated during the year 1997.

**Figure 3.13** – Existing flux limits and expected ANTARES sensitivity to the flux of relativistic magnetic monopoles. The limit by BAIKAL was obtained from the analysis of data taken during 994 days on which the detector was operational [102, 65]. The AMANDA-B10 [103] was obtained from 179 days effective detector livetime, taken during 1997. The sensitivities of the future ANTARES detector to monopoles above the Cherenkov threshold (labeled “ANTARES (1)”) and below the Cherenkov threshold (labeled “ANTARES (2)”) are expected after 365 days of operation.



already been developed. Based on simulations, the ANTARES collaboration has investigated the feasibility to detect monopoles via their direct Cherenkov emissions [104] and via the emissions from secondary  $\delta$ -electrons [105, 106]. The latter search would be sensitive to monopole velocities down to  $\beta=0.51$  (corresponding to the threshold velocity in sea water, above which monopoles can produce Cherenkov light by  $\delta$ -electrons). The expected sensitivity of the ANTARES analyses is shown in Figure 3.13, along with the existing AMANDA-B10 and BAIKAL limits.

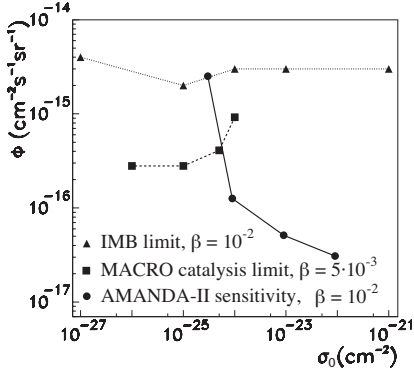


**Figure 3.14** – Expected sensitivity of the AMANDA-II detector to sub-relativistic monopoles ( $\beta = 10^{-2}$ ) [101] compared to limits set by the IMB [108] ( $\beta = 10^{-2}$ ) and MACRO ( $\beta = 5 \cdot 10^{-3}$ ) [100].

Sub-relativistic monopoles have been searched for with the SUPER-KAMIOKANDE [107], IMB [108], BAIKAL [109], and MACRO [100] experiments. No candidate events have been observed so far. Due to large theoretical uncertainties in the catalysis cross section, the non observations of a signal are difficult to translate into a flux limits. Flux limits are usually quoted dependent on the monopole velocity  $\beta$  and the catalysis cross section  $\sigma_0$  (see equation (19)).

Figure 3.14 shows the limits obtained by MACRO and IMB for an assumed monopole velocity of  $\beta = 5^{-3}$  and  $\beta = 10^{-2}$ , respectively. A search for sub-relativistic monopoles with AMANDA-II data is presently being performed [101]. The AMANDA-II sensitivity expected for the analysis of one year of experimental data shown in Figure 3.14 for comparison.

## 4 The AMANDA-II neutrino telescope

The *Antarctic Muon And Neutrino Detector Array* (AMANDA) [64] is a neutrino telescope that is deployed and operated on the Antarctic continent at the geographic South Pole (Figure 4.1). The almost three kilometers-thick ice sheet covering the continental bedrock serves as Cherenkov medium. Because of its purity and low temperature<sup>7</sup>, the Polar ice provides an ideal environment for operating photo-multiplier-tubes, and its solid surface is advantageous for the installation, operation, and maintenance of a neutrino telescope. The full AMANDA-II detector comprises more than 600 light sensitive optical modules (OMs), each consisting of an 8-inch photomultiplier tube and supporting electronics in a transparent pressure housing. Most of the OMs are deployed at depths greater than 1500 m below the surface (Figure 4.2). Power is supplied from the surface via electrical cables, which, in some OMs, are also used for signal transmission. Other OMs are read out via optical fiber. The low dark noise rate of the OMs (being operated in a cold in sterile environment) permits to use a simple majority trigger that is implemented in the surface electronics. With the specific trigger conditions presently used, AMANDA records atmospheric muons at an average rate around 90 Hz. The track reconstruction accuracy for muons induced by neutrinos of TeV energies is around two degrees after applying standard quality criteria [111]. Presently, atmospheric muon-neutrinos created in the northern hemisphere are detected at an average rate of  $\sim 4$  per day [111]. AMANDA-II in its final configuration has been operational from the beginning of the year 2000 on. The data collected so far permitted to measure the spectrum of atmospheric neutrinos, place limits on the flux of extra-terrestrial neutrinos, and probe physics beyond the Standard Model.

### 4.1 The detection medium: South Polar ice

The particle tracks in a neutrino telescope are reconstructed from the Cherenkov light pattern, mapped with a sparse matrix of optical sensors. Photons in AMANDA typically propagate some tens of meters before hitting an optical module. Track reconstruction, therefore, requires a good understanding of light propagation in the Cherenkov medium. Quantitative modeling of light propagation involves two microscopic processes: Scattering and absorption of photons, which generally depend on the photon wavelength. The AMANDA optical modules are sensitive to visible and ultra-violet light with wavelengths from 300 to 600 nm. In this wavelength interval, deep South Polar ice is extremely transparent, and both scattering and absorption mainly arise from dust impurities. The dust concentration shows a depth dependence, as the Polar glacier has accumulated over millennia as small annual snowfall. Dust impurities at certain depths (and hence the propensity of the ice to scatter and absorb photons) trace the impurities which were present in the Antarctic air and which precipitated in snowflakes at a certain epoch.

The optical properties of the Polar ice have been measured *in situ*, using various artificial light sources that were deployed at depth together with the OMs. These measurements, together with empirical parameterizations of the variations of scattering and absorption with wavelength, allowed to

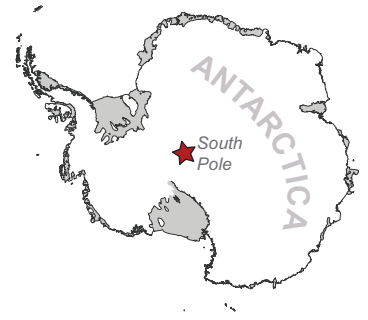


**Figure 4.1** – AMANDA is located on the Antarctic continent, at the geographic South Pole (marked by the red star).

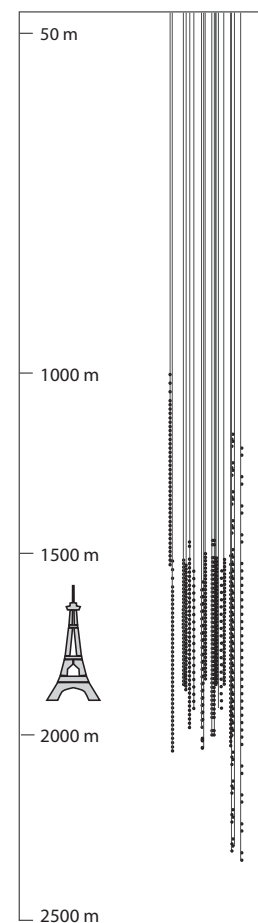


**Figure 4.2** – Arrangement of AMANDA-II OMs (black dots). The sketch of the Eiffel tower (true to scale) is to illustrate the size of the detector.

<sup>7</sup>about  $-20^{\circ}\text{C}$  between depths of 1500-2000 m [110]

model the light propagation in Polar ice at depth between 1100 and 2350 m throughout the wavelength range from 300 nm to 600 nm.

#### 4.1.1 Absorption

The Polar ice is remarkably transparent to light at visible wavelengths and near ultraviolet. With absorption lengths of 100 meters and more, it is much cleaner than any ice grown under laboratory conditions. Figure 4.3 shows the the measured *absorptivity* (defined as the reciprocal absorption length) for several wavelengths between 300 and 600 nm and at depths of 1655, 1675, and 1755 meters. Absorptivity is minimal around 400 nm, reaching values as low as  $10^{-2} \text{ m}^{-1}$ . This is a factor two lower than absorptivities measured in deep sea water [112]. The wavelength dependency is in excellently described by the empirical, *Three-component* model [113] according to which there are three contributions to absorptivity:

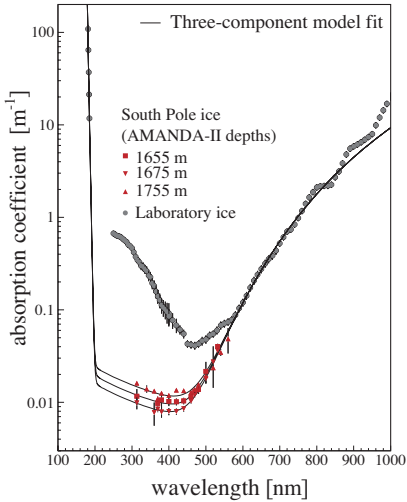


**Figure 4.3** – Wavelength dependence of absorptivity in ice. Measurements in Polar ice (red markers) [114] show excellent agreement with the “*Three-component model*” (black line) [113]. Measurements for ice grown from pristine  $\text{H}_2\text{O}$  under laboratory conditions (gray markers) are shown for comparison. Taken from [114].

1. light absorption due to an electronic band gap in the in the ice crystal, which dominates absorption in the far ultraviolet ( $\lambda < 200 \text{ nm}$ ),
2. absorption due to excitation of  $\text{H}_2\text{O}$  molecules, which is dominate in the infrared ( $\lambda > 500 \text{ nm}$ ), and
3. light absorption due to impurities, such as dust grains inherent in the ice.

In the wavelength interval between 200 and 500 nm, *pure* ice is extremely transparent, and absorptivity depends almost solely on the concentration of impurities. At depths around 1000 m and below 2000 m, the dust concentration are lowest and absorption lengths well in excess of 100 meters are reached.

#### 4.1.2 Scattering

The *geometric scattering length* (the photon mean free path,  $\lambda_s$ ) in South Polar ice is of the order of meters, much shorter than the absorption length. If the scattering were isotropic (*i.e.*, photons were scattered in all directions with equal probability),  $\lambda_s$  would be the length scale over which the initial photon direction is randomized. However, in South Polar ice, scattering is preferentially forward. In this case, the randomization length scale is given by the “*effective scattering length*”<sup>8</sup> (the transport mean free path),

$$\lambda_e = \frac{\lambda_s}{1 - \langle \cos \Theta \rangle}, \quad (28)$$

with  $\langle \cos \Theta \rangle$  being mean scattering angle. The mean scattering angle mainly depends on the size of the scattering center. For scattering on dust grains abundant in South Polar ice, the average  $\langle \cos \Theta \rangle$  is 0.94 [115], and consequently  $\lambda_e$  is significantly greater than  $\lambda_s$ . Apart from dust grains, sub-millimeter-sized air bubbles trapped in the ice can scatter photons. For scattering on air bubbles, the average  $\langle \cos \Theta \rangle$  is 0.75. Air bubbles are responsible for a dramatic decrease of the scattering length above  $\sim 1400 \text{ m}$ . The strong scattering at these shallower depths was the main reason to deploy AMANDA-II in deep ice, below 1500 m. Here, due to the high pressure,

<sup>8</sup>For a collimated light beam in a non-absorbing medium,  $\lambda_e$  has a natural interpretation: It is the distance along the original injection direction after which the *net* flux in that direction is zero.

air bubbles underwent a phase transition from the gas phase to solid air hydrate crystals [116]. The refractive indices of air hydrate and of normal ice are almost identical [117], and consequently, light passes through air hydrate crystals with almost no scattering.

The measured effective scattering length in South Polar ice below 1500 m varies between 15 and 50 meters and depends on wavelength and on depth [114]. The wavelength dependency of scattering can be modeled with a power law as  $1/\lambda_e \propto \lambda^{-\alpha}$  [115], with  $\alpha \approx 0.9$ . The numerical value of the index  $\alpha$  was derived from measurements [114]. For ultra-violet light, the average  $\lambda_e$  is around 20 m. Like absorption, the depth dependence of scattering follows the concentration of dust impurities in the ice.

Figure 4.4 shows the depth dependence of the scattering and absorption lengths in the depth range 1300 to 2200 meters for wavelengths of 300 to 600 nm.

## 4.2 Deployment and detector geometry

AMANDA-II, in its final state, consists of 677 optical modules (OMs). Most of the OMs are contained in a cylindrical volume of 500 m height around the detector center, which is located 1730 m below the surface. The OMs are arranged on 19 vertical strings. During construction, the strings were lowered into water filled holes, drilled with pressurized hot water to a depth of at least 2000 m. Two days after deployment, the OMs were frozen permanently into place. Their relative location after re-freezing could be determined to within less than a meter. Figure 4.5 shows a schematic view of string locations in the horizontal plane.<sup>9</sup> The strings are arranged roughly in three concentric circles of 80, 160 and 200 meter diameter respectively, with one additional string in the center. The strings are numbered according to the chronological order of their deployment. OMs are numbered also chronologically. Within each string, the OM number is incremented with increasing depth.

**Strings 1-4** (OM 1 - OM 86), located in the inner part of the detector, were deployed first (Austral summer 1995/96). Each contain 20 OMs at a vertical spacing of 20 m. These four strings cover the depth range 1500m to 2000 m. The central string (string 4) comprises six additional OMs, which were deployed for test purposes. The OMs are located at the bottom of the string and are not used for physics analyses.

**Strings 5-10** (OM 87 - OM 302) were deployed in 1996/97. Each string carries 36 OMs with a vertical spacing of about 10 m. These strings are a little shorter than strings 1-4 and cover a depth range from 1500 m to 1800 m.

**Strings 11-13** (OM 307<sup>10</sup> - OM 344) were deployed in 1997/98. These strings extend the depth range of the detector by  $\sim 350$  m in both upward and downward direction. In the central region (1500 m - 2000 m), each string contains 26 OMs, spaced by 20 m. Up to 16 additional OMs per string are deployed with larger vertical spacing in the upper and lower extensions. The main purpose of these OMs was to explore the optical properties of the ice over a larger depth range, in anticipation of the future

<sup>9</sup>A detailed OM map showing the vertical OM spacing for each particular string is shown in Figure 6.3 in section 6.2.1.

<sup>10</sup>OM 303, 304, 305, and 306 are missing due to time pressure at deployment

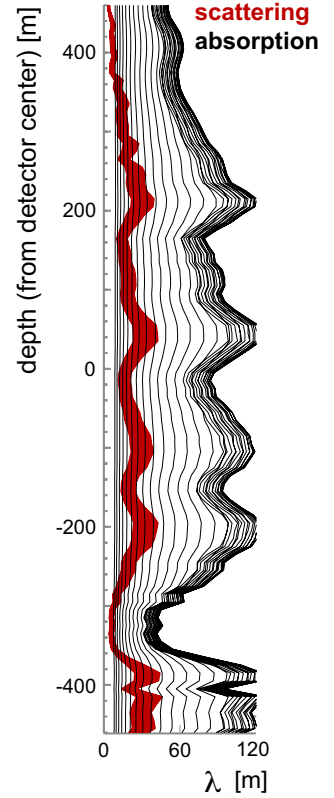


**Figure 4.4** – Absorption length (black) and scattering length (red) at depths between 1300 and 2200 m. The depth range on the abscissa is relative to the center of the AMANDA detector, located at 1730 m. Each graph corresponds to the scattering or absorption length for one particular wavelength between 300 and 600 nm. Taken from [118].

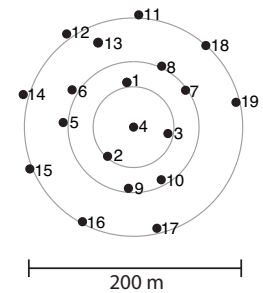


**Figure 4.5** – Arrangement of the 19 AMANDA-II strings in the horizontal plane. The string numbering corresponds to the order in which there were deployed.

IceCube detector. OMs on the upper and lower string extensions are usually not used in physics analyses.

**Strings 14-19** (OM 345 - OM 681) were deployed during Austral summer 1999/2000. Each string comprises 43 OMs at a vertical spacing of 15 m. Five of the strings cover the central range from  $\sim 1500$  m. to  $\sim 2000$  m. String 17, unintentionally, ranges from  $\sim 1000$  to  $\sim 1500$  m. During deployment, this string got stuck in its bore-hole, which was re-freezing faster than expected.

### 4.3 The optical module

Each OM consists of an 8-inch photomultiplier tube (PMT) and its base, enclosed in a pressure resistant glass sphere, to which they are optically and mechanically coupled with transparent, refraction index adapted silicon gel (Figure 4.6). Most OMs are also equipped with a nylon ball, located either inside (strings 11-19) or outside (strings 1 to 10) the pressure sphere, which is connected to the surface via an optical fiber. The nylon ball serves as light diffuser for laser signals that are transmitted from the surface for calibration purposes.

The PMTs are operated at a high gain, typically  $10^9$ , to make it possible to distinguish single photo-electron pulses from dark noise after attenuation over 2 km-long cables.

**Sensitivity:** The OMs are sensitive to light with wavelengths between 300 and 600 nm. The limit at long wavelengths is set by the decline in photo cathode quantum efficiency, which is maximal ( $\sim 22\%$ ) at wavelength around 390 nm and falls below 1% around 600 nm [119]. The short wavelength limit is set by the transmission properties of the glass spheres (Figure 4.7). After using first generation spheres for strings 1-4, with a cut-off transmittance ( $< 5\%$ ) close to 340 nm, second generation spheres with better transmission properties ( $\sim 65\%$  at 340 nm) were used for strings 5-19. The  $\lambda^{-2}$  wavelength spectrum of Cherenkov light, when convoluted with the glass transmission characteristics and the PMT quantum efficiency, results in an OM sensitivity maximum near 400 nm, where, incidentally, Polar ice is most transparent.

**Dark noise rates:** Being operated in cold and sterile environment, the OM dark noise rate is dominated by the radioactivity inherent in the glass. The second generation pressure spheres, used in strings 5-19, have superior transmittance, but a higher contamination of radioactive  $^{40}\text{K}$ , resulting in a noise rate around 1.5 kHz, substantially higher than the 300-500 Hz noise rate in the first generation OMs.

**Afterpulsing:** Afterpulses occur if residual gas atoms in the PMTs are ionized by the electron cascade between the dynodes. Because of their higher mass, positive gas-ions drift towards the cathode more slowly than electrons drift towards the Anode. The pulse caused by positive ions when hitting the cathode is delayed relative to the electron pulse by a PMT-specific drift-time, which mainly depends on the geometry of the tubes. In AMANDA-PMTs, afterpulses happen typically about  $6\ \mu\text{s}$  after the main signal. The probability for afterpulsing to occur is proportional to the number of initial photoelectrons.

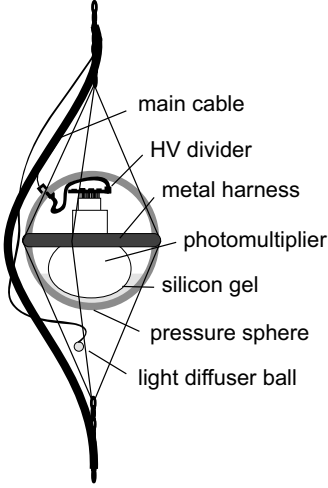


Figure 4.6 – The optical module.

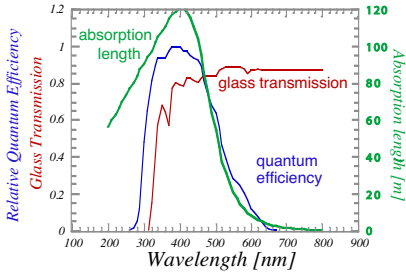


Figure 4.7 – Wavelength dependency of glass transmission (first generation pressure spheres) and PMT quantum efficiency, compared to the absorption length in Polar ice. From [120].

**Signal readout:** The step-wise deployment of AMANDA-II also went along with an improvement of PMT signal transmission techniques. The OMs on strings 1-4 are connected to the surface with coaxial cables, which is highly dispersive and has a strong attenuation. Typical single photo-electron pulses have amplitudes around 1 V and a width of 10 ns. After transmission to the surface through coaxial cable, pulses have amplitudes of only a few milli-Volts and are up to 600 ns wide [119]. Coaxial cables, however, have the advantage of being insensitive of “cross-talk”, *i.e.*, noise pick-up from pulses in adjacent cables by induction.

In strings 5-10, the coaxial cables were replaced by twisted pair cables, whose dispersion and attenuation is lower by roughly a factor of three [121]. Single photo electron pulses from these OMs have widths of 100 - 200 ns and have accordingly higher amplitudes. Cross-talk is an additional source of noise in these strings. The origin of the cross talk is not fully understood. Cross Talk patterns were studied in great detail [122], and we can say that a least a portion of the cross-talk happens between adjacent cables during transmission to the surface.<sup>11</sup>

Optical modules on the outer strings (strings 11-19) are read out via optical fiber. A *Light Emitting Diode* (LED) located inside each module transforms the PMT pulse into a light pulse, which is then transmitted to the surface through an optical fiber. As the fiber is essentially dispersion-free, a nearly identical copy of the original pulse can be produced at the surface with a photo-diode (Figure 4.8), and pulses with separation of as little as 10-15 ns can be resolved. Also, the problem of cross-talk during signal transmission is eliminated. However, the optical fibers have proven somewhat more vulnerable to damage during refreezing after deployment, with a loss rate of nearly 10%. Those OMs whose fibers were broken are read out via twisted pair electrical cable, with however slightly worse transmission properties than the cable used for strings 5-10.<sup>12</sup>

**PMT jitter:** The the transit time of the electron cascade through the tube shows variations, referred to as the PMT jitter. Deviations from the mean transit time are approximately Gaussian, with the width of the Gaussian depending on the geometry of the tube and arrangement of the dynodes [119]. For the 12 dynode PMTs used in AMANDA, the jitter is about 2.5 ns [124].

## 4.4 Surface electronics

After transmission to the surface, the PMT pulses are amplified. Electrically transmitted pulses are amplified with so-called *SWedish AMPlifiers* (SWAMPs), optically transmitted pulses are amplified in *Optical Receiver Boards* (ORBs). Both types of amplifiers have dual output. One output channel is used to build the trigger and measure the timing of the arriving PMT pulses (channel **A**), the other one is used to measure the pulse amplitude with a peak sensing ADC (channel **B**, see Figure 4.9).

In channel **A**, the amplified PMT pulses are fed into a constant-threshold discriminator. The discriminator produces rectangular pulses of predefined height, starting when the input voltage rises above threshold and ending when it falls below it. One copy of the discriminator output is given

<sup>11</sup>There are strong indications that cross-talk also happens within the surface electronics. Surface cross-talk patterns have however never been investigated in detail.

<sup>12</sup>Twisted pair cables used as backup readout in strings 11-19 is thinner than the ones used in strings 5-10 [123].

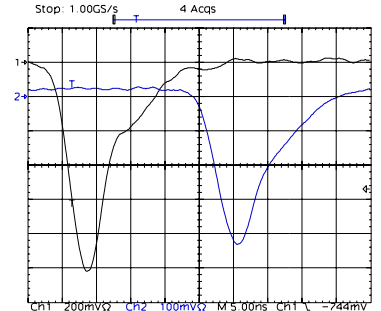
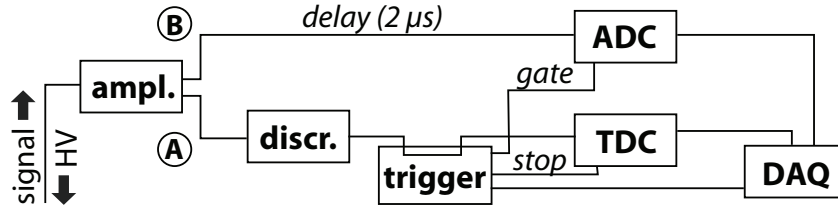


**Figure 4.8** – PMT pulse before (black) and after (blue) transmission over 2 km optical fiber. From [121].

**Figure 4.9** – Scheme of the AMANDA surface electronics. From [125].



to the *Multiplicity ADDer module* (MADD)<sup>13</sup>, which is used to form the multiplicity trigger, another copy is given to a multi-hit *Time to Digital Converter* (TDC) to record the starting and ending times of the pulses.

#### 4.4.1 Multiplicity trigger

Most physics analyses use the data stream defined by a 24-fold majority trigger. An event is triggered if pulses from at least 24 OMs are received at the surface within a coincidence window of  $2.5 \mu\text{s}$ . The MADD module in the trigger logic stretches the incoming pulses to  $2.5 \mu\text{s}$  lengths. When the sum of the stretched signals rises above the multiplicity threshold (which was set to 24 during the year 2000), a trigger is issued. In addition to the multiplicity trigger, other triggers are implemented (logical *OR*): A so-called *string-correlation trigger*, optimized for low energy events, requires several neighboring OMs in one string to fire in coincidence. AMANDA can also be triggered externally from the SPASE air shower array [126], located at the surface.

#### 4.4.2 Timing measurement: Time to Digital Converter (TDC)

The TDCs used to measure the pulse timing have a buffer depth of 16 edges (corresponding to eight pulses each composed of a leading and a trailing edge), and a buffer length of  $32 \mu\text{s}$ . The TDC buffers are read out when they receive a *common stop* signal, which is issued  $10 \mu\text{s}$  after the trigger. The TDCs provide the timing information of PMT pulses from  $22 \mu\text{s}$  before to  $10 \mu\text{s}$  after the trigger. This readout window is much longer than the duration of a typical event. Hits due to the passage of a relativistic particle are spread over a few micro seconds around the trigger time (Figure 4.10). Hits received during the first  $15 \mu\text{s}$  of the interval are related to either PMT noise or to radioactivity in the glass spheres. The hit rate observed in this time window is used to determine (and monitor) the noise rates of individual OMs. In general, each OM in an event will produce a series of pulses, corresponding to several photoelectrons produced at the photocathode. If more than eight pulses arrive within the  $32 \mu\text{s}$  buffer window, the respective OM is flagged as “*overflowed*”. Two different types of TDCs are used in AMANDA, which slightly differ in their overflow behavior. Strings 1-10 are connected to CAMAC TDCs; strings 11-19 are connected to VME TDCs. In both types of TDCs edges are kept for  $32 \mu\text{s}$  and then cleared. If the buffer has filled up and a new edge arrives,

- the CAMAC-TDC will discard the oldest edge in favor of the new edge, whereas
- the VME TDC will keep the first 16 edges and ignore any new edge.

<sup>13</sup>In practice, the discriminator and the MADD are realized within one single electronics unit, the DMADD (*Discriminator Multiplicity ADDer*).

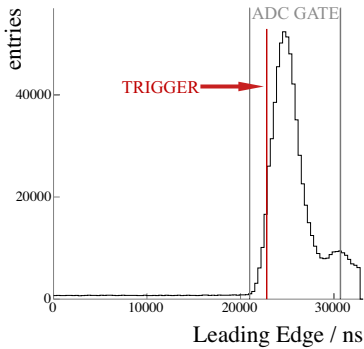


**Figure 4.10** – Distribution of pulse *leading edges* of atmospheric muon events. Most of the hits attributed to the actual event occur in a small time interval, about  $[-2 \mu\text{s}, 5 \mu\text{s}]$  around the trigger time (around 22000 ns). Earlier hits are due to dark noise, later ones are predominantly due to afterpulsing of the PMTs. The ADC gate is open during the time span where most photon hits from crossing relativistic particles are expected.

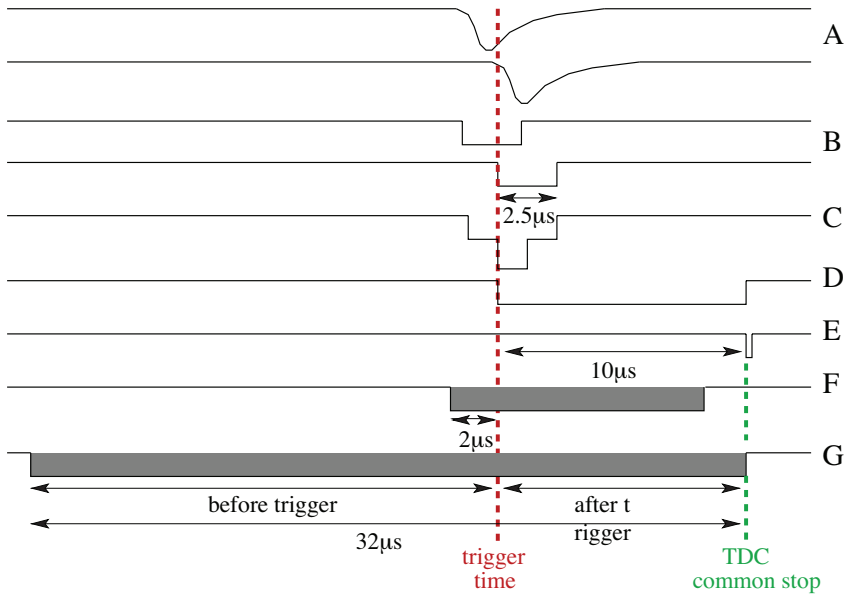


**Figure 4.11** – Time correlations between trigger, ADCs and TDCs. At threshold crossing time of each amplified PMT pulse (A), a rectangular pulse of  $2.5 \mu\text{s}$  length is created (B). If the sum of these pulses (C) crosses a certain threshold (24 in AMANDA-II), a trigger is issued, and the ADC gate (D) is opened for  $10 \mu\text{s}$ . After these  $10 \mu\text{s}$ , the TDCs receive the *common stop* signal (E). The input to the ADCs is delayed by  $2 \mu\text{s}$  compared to the TDC inputs, and the ADCs are sensitive  $2 \mu\text{s}$  before and  $8 \mu\text{s}$  after the trigger time (F). The TDCs in contrast keep record of the pulse leading and trailing edges  $22 \mu\text{s}$  before and  $10 \mu\text{s}$  after the trigger time (G).

While this subtlety is of minor interest in standard neutrino searches, where the average signal event produces no more than a couple of photoelectrons, it is of particular importance for the analysis of very bright events. Especially the OMs in the inner part of the detector (strings 1-10, which are connected to CAMAC-TDCs) have a high probability to produce after-pulses. In bright events, the timing information carried by unscattered photons (which enables an accurate track reconstruction) is overwritten by after pulses or hits from highly scattered photons, which contain no information about the particle direction.

#### 4.4.3 Amplitude measurement: Analog to Digital Converter (ADC)

The amplifier output from channel **B** of the SWAMPS is delayed by  $2 \mu\text{s}$  and then fed into a peak-sensing *Analog to Digital Converter* (ADC) to measure the pulse amplitude. The ADC is operated with a  $10 \mu\text{s}$ -wide gate. The gate is opened by the trigger signal, such that, due to the delay, the ADC is sensitive  $2 \mu\text{s}$  before and  $8 \mu\text{s}$  after the trigger (Figure 4.11). While the TDC buffer depth is much longer than the duration of an actual event, the time interval over which the ADCs are sensitive is chosen such that it brackets the time interval in which hits due to Cherenkov photons from a relativistic particle are expected (*cf.* Figure 4.10).

The ADCs used in AMANDA are *peak-sensing*, that is, in case an OM sees multiple pulses, only the largest amplitude is recorded, and the rest of them will be lost. In this case, there is an ambiguity in assigning the peak amplitude to one particular hit in the OM. Because the probability of two or more highly scattered photons arriving at a module simultaneously is very small, the amplitude is usually assigned to the first pulse in the series, and subsequent pulses are assumed to be single photo electrons. In electrically read out OMs, dispersion can cause several subsequent pulses to merge into one, and, in general, the resulting amplitude is not just the sum of the amplitudes of the contributing pulses (Figure 4.12). Since the pulse shape information is not recorded, the true number of photoelectrons

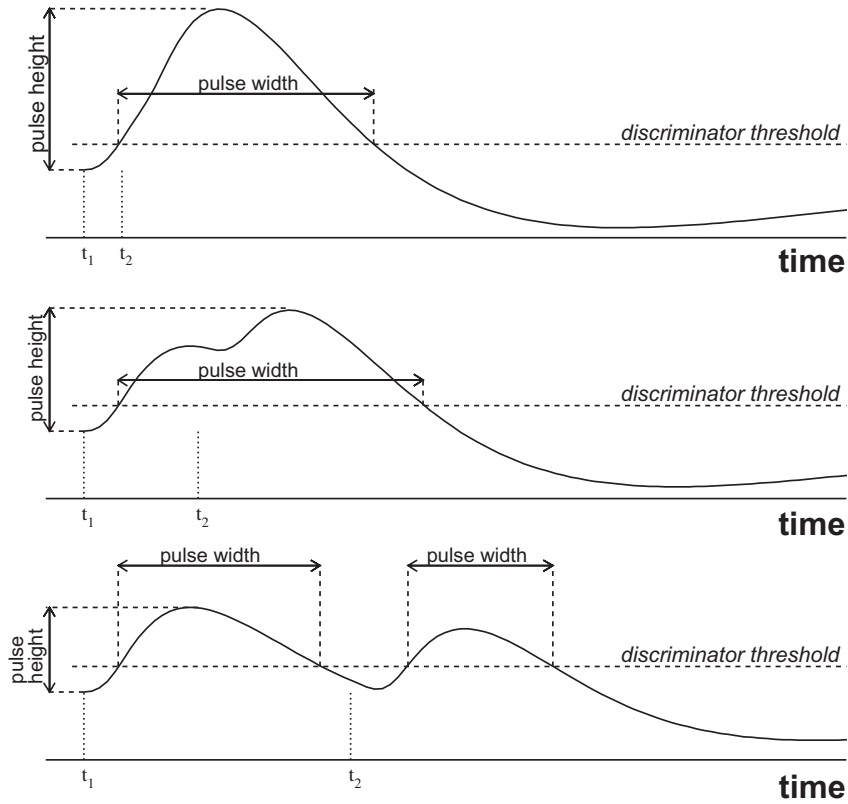


**Figure 4.12** – Multi-photoelectron pulses in AMANDA. Two single-photoelectron pulses arriving at times  $t_1$  and  $t_2$  can easily merge into one pulse, due to dispersion. In case of two separate pulses, only the highest amplitude will be recorded. Therefore, recorded amplitude is not a direct measure the number of initial photo electrons (adapted from [127]).

initially created at depth cannot be retrieved.<sup>14</sup> Nevertheless, the peak amplitude provided by the ADCs will be correlated to the amount of light initially seen by an OM.

#### 4.4.4 The data acquisition system (DAQ)

For each triggered event, pulse data for all fired OMs (or *channels*) is written to disk and magnetic tape, along with the time at which the trigger was issued. The trigger time is taken from a GPS clock.<sup>15</sup> An event, ready for analysis, contains the following information:

- The trigger time, and the particular trigger condition that was fulfilled. In case multiple triggers were issued, the event contains multiple trigger times.
- The starting and ending time of each pulse (*leading and trailing edge*) within the  $32 \mu\text{s}$ -readout window of the TDCs,
- One peak amplitude per channel from the ADCs,

<sup>14</sup>In principle, one could use both, pulse amplitude and width (time span between leading and trailing edge) to reconstruct the number of photo electrons. However, the detector simulation does not reproduce dispersion of pulses from individual OMs accurately: While the extend of smearing in reality will depend on cable length (*i.e.*, depth), the simulation uses template PMT pulse shapes that are independent of depth (see section 5.1.2).

<sup>15</sup>A second data acquisition system (the TWR DAQ) based on *Transient Waveform Recorders* has been operational from 2003 on. PMT pulses are digitized at the surface, and the full “wave form” is recorded. Both data acquisition systems were operated in parallel until 2006/2007, when the conventional system was finally decommissioned.

- One *overflow bit* per fired channel, which is set to *true* in case the TDC has recorded more than 16 edges.

#### 4.4.5 Dead time

While TDCs and ADCs are being read out, they are not able to collect data. During this time the data acquisition is blocked: a *veto* inhibits the acceptance of further triggers. The amount of this *dead-time* during data taking depends on the frequency at which events are triggered and written out. At an average trigger rate of 90 Hz, the detector is “dead” for a fraction of 17% of the data taking time.

### 4.5 Calibration

The passage time of a relativistic particle through AMANDA-II is of the order of micro-seconds. Track reconstruction requires the times at which photo-electrons are produced at depth to be known with nanosecond precision. In order to retrieve the actual hit times, the pulse *leading edges* (as received by the surface DAQ) have to be corrected for cable delay and dispersion. The number of initial photoelectrons is inferred from the ADC voltage.

#### 4.5.1 Time calibration

The time at which photoelectrons were produced at depth ( $t_{OM}$ ) can be retrieved from the *leading edge* times at the surface ( $t_{LE}$ ) with adequate accuracy as:

$$t_{OM} = t_{LE} - \frac{\alpha}{\sqrt{V_{ADC}}} - t_0. \quad (29)$$

The constant  $t_0$  is the pulse transit time through electrical cable or optical fiber. The term  $\alpha/\sqrt{V_{ADC}}$  is the so-called *slewing-correction* (see Figure 4.13). It corrects for the amplitude dependent pulse rise time: If two pulses occur at the same time but have different amplitudes, the pulse with the higher amplitude will cross the constant discriminator threshold earlier.

Both constants,  $t_0$  and  $\alpha$ , are OM-specific and are measured annually during the summer maintenance period: Light pulses of varying intensity from a YAG laser located at the surface are transmitted through an optical fiber and released near the OM (Figure 4.14). A linear fit to the distribution  $t_{LE}$  versus  $1/\sqrt{V_{ADC}}$ , gives a total time offset  $t'_0$  and the slope  $\alpha$ . The actual cable delay  $t_0$  is calculated from  $t'_0$  by subtracting the transit time of the light pulse ( $t_{fiber}$ ) and the photon propagation time from the diffuser ball, from which the light was released, to the OM ( $t_{transport}$ ).

Generally, the hit times retrieved from the surface leading edge times according to equation (29) are accurate to within  $\sim 5$  ns. However, in case an OM has seen a series of hits, the slewing correction is strictly correct only for one of them. During calibration, one therefore applies the slewing correction for the peak ADC value to earlier hits (which are most likely due to un-scattered photons) and corrects later hits for the rise time of a one-photoelectron pulse.

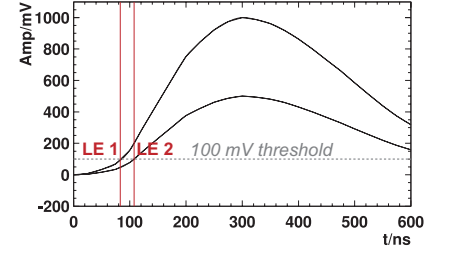


**Figure 4.13** – Slewing correction of leading edges. Due to dispersion, higher amplitude pulses will cross the the fixed discriminator threshold earlier. As the rising of the pulse can be described by a parabola [119], the slewing correction is proportional to  $1/\sqrt{V_{ADC}}$ .

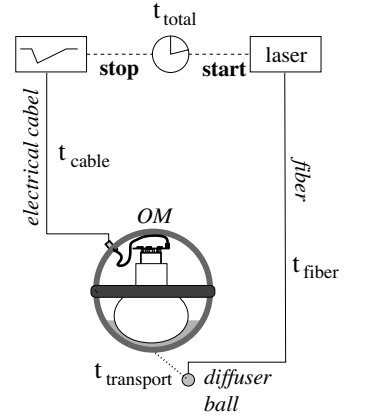


**Figure 4.14** – Time calibration. the cable delay is measured from the time difference between the emission of a laser pulse (start) at the and the leading edge received at the surface (stop). The transmission time of the light pulse ( $t_{fiber}$ ) and the photon propagation time ( $t_{transport}$ ) are calculable from the fiber length and distance from the diffuser ball to the OM. From [128].

## 4.5.2 Amplitude calibration

The number of photoelectrons ( $N_{\text{PE}}$ ) that contributed to a PMT pulse can be inferred from the pulse amplitude measured at the surface ( $V_{\text{ADC}}$ ) as

$$N_{\text{PE}} = (V_{\text{ADC}} - V_{\text{pedestal}}) \cdot \beta, \quad (30)$$

where  $V_{\text{pedestal}}$  is a constant voltage offset. Both  $\beta$  and  $V_{\text{pedestal}}$  are OM specific. Unfortunately, the ADC pedestals are not known. They were only estimated after 2003 from comparisons between data from the conventional DAQ (described above) and a second DAQ based on *Transient Waveform Recorders* that had been installed in the Polar season 2002/2003 [129]. These comparisons indicate that the ADCs have negative pedestals, which lie around -20 mV for stings 1-4, -30 mV for strings 5-10, and -40 mV for strings 11-19.

The constant  $\beta$  is inferred from ADC voltage observed for single photoelectron pulses,  $V_{1\text{PE}}$ . As the vast majority of pulses observed in atmospheric muon events is due to single photoelectrons,  $V_{1\text{PE}}$  is simply determined from the peak position in the ADC voltage distribution in trigger level data (Figure 4.15).

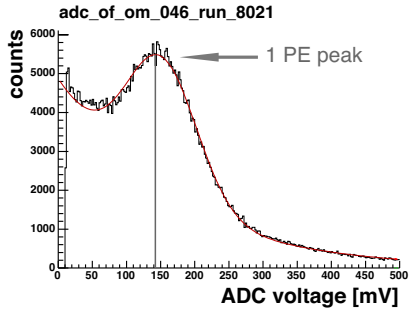


**Figure 4.15** – Distribution of the ADC voltage in trigger level data for one particular OM. The voltage corresponding to a single photoelectron hit is determined from the peak position of this distribution.

## 4.6 Trigger rate

AMANDA-II is taking data continuously from mid February to early November, annually. During the Austral summer the detector undergoes maintenance and calibration. Figure 4.16 shows the trigger rate over four years of data taking (2000 to 2003). The maintenance periods are clearly visible as gaps where no data are available. The annual modulation in the rate, *i.e.*, decrease towards Austral winter and the subsequent rise towards Austral summer is due to seasonal temperature variations in the atmosphere which affect the atmospheric muon rate. This behavior is well understood [130, 131]. The jump in the trigger rate at the end of September 2002 (around day 1000) was caused by sudden warming in the Stratosphere above the Pole (see appendix A). In normal operation, the AMANDA DAQ is continuously collecting data in 24 hour intervals (so-called *runs*), in-between which the DAQ reset and restarted.

Data are written at a rate of some tens of kilobytes per second, depending on the year and season. Each file is approximately 10 minutes livetime equivalent. The AMANDA monitoring system [132] continuously surveys and evaluates the stability of all hardware components on a file-by-file basis.

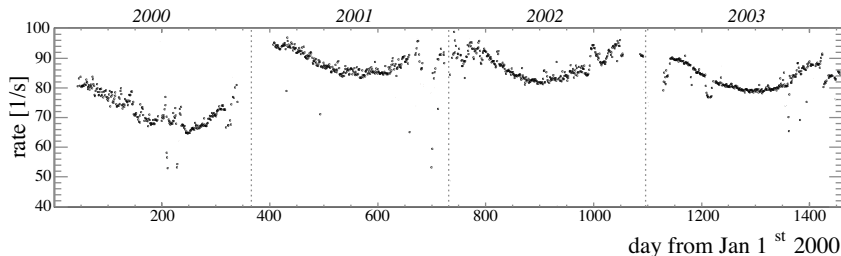


**Figure 4.16** – Deadtime-corrected trigger rate from January 1<sup>st</sup> 2000 to December 31<sup>st</sup> 2003. Several OMs that were malfunctioning in 2000 were recovered during Austral summer 00/01, which lead to a substantial increase in the trigger rate.

## 4.7 Detector monitoring

During regular detector operation, the South Pole is inaccessible (owing to the Antarctic winter), and the data quality is *monitored* remotely from the northern hemisphere [132]. In order to diagnose potential hardware failures at an early stage, the monitoring system surveys (among other things):

- Trigger rates and dead time
- OM specific parameters (monitored for each OM):
  - the dark noise rate (determined from the TDC hit rate over the  $15\ \mu\text{s}$  of the TDC buffer)
  - the total TDC hit rate
  - the total ADC hit rate
  - the position of the single photoelectron peak in the ADC voltage distribution

Hardware failures which require intervention by the winter-over crew<sup>16</sup> are rare. Monitoring information is hence predominantly used offline for selection of data which meet quality standards for various physics analyses.

The distribution shown in Figure 4.17 was generated with the AMANDA monitoring system. It shows the dark noise rates of all OMs in the detector, averaged over one file ( $\approx 10$  minutes of livetime). The dark noise rates are determined from the hit rate recorded over the first 15 ms of the TDC buffer window. Correlated increase of the noise rates for groups of OMs is the prime reason to exclude certain data files (or even entire runs) from the physics analysis.

## 4.8 Removing electronic noise

Events recorded by the DAQ contain a certain fraction of hits due to various types of electronic noise. In extreme cases, the majority of hits, or even the entire event, is due to electronic noise. Although the exact origin of these artifacts is not always understood, these hits or non-physics events can be identified.

### 4.8.1 Hit cleaning

There is a variety of strategies to reject noise hits. The exact *hit-cleaning* procedure varies for different analysis purposes, but the general strategy is as follows.

**Time window cleaning:** Hits due to Cherenkov photons arrive within a short time interval of a few  $\mu\text{s}$  of the TDC buffer around the trigger time. Noise hits are rejected by selecting hits within this time interval. The exact choice of the interval depends on the analysis purpose. Track reconstruction, for instance, requires the event to consist mostly of unscattered Cherenkov photons, and hence, the time interval is usually chosen to be relatively narrow. For assessing the total light yield of an event by counting hits, one uses a broader interval in order to include hits from photons delayed by scattering (or even after-pulses).

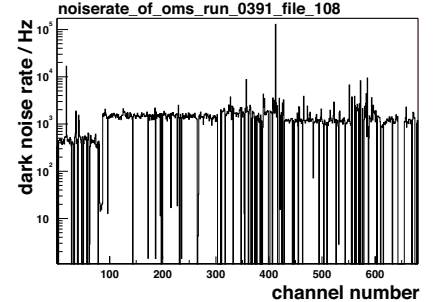


**Figure 4.17** – Dark noise rates of all OMs in the detector. A fraction of the OM show an abnormally high noise rate, others have zero hit rates. Also visible is the difference in the dark noise rate between OM with first generation glass spheres (channel numbers  $\leq 86$ ) and second generation OMs. Noise rates are determined from the hit rate recorded over the first  $15\ \mu\text{s}$  of the TDC buffer [133]. Figure taken from the monitoring system [132].

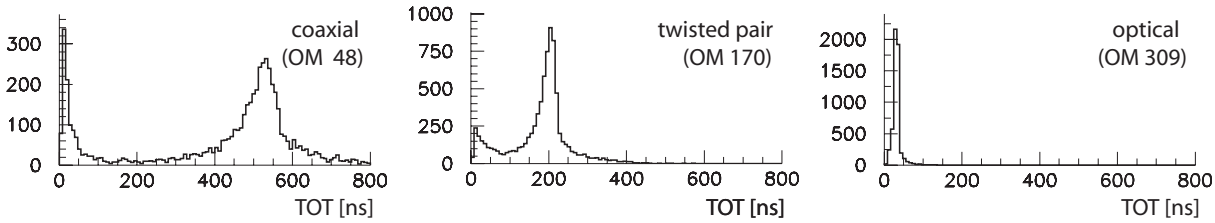


**Figure 4.18** – TOT distribution for an OM which is read out via coaxial electrical cable (left panel), an OM which is read out via twisted pair electrical cable (middle), and an OM which is read out via fiber optics (right). The peak due to single-photoelectron hits lies around 500 ns for the coaxial readout, around 200 ns for the twisted-pair readout, and around 30 ns for the optical readout. Pulses with significantly shorter TOT values are due to electronic noise. From [134].

**TOT cleaning:** Pulses due to electronic noise are typically much shorter than those due to photo-electrons. Requiring a minimum TOT value efficiently removes noise hits. The TOT threshold is set individually for each OM, depending on its TOT characteristics. The TOT characteristics of an OM mainly depends on the signal transmission. Example TOT distributions for OMs which are read out via coaxial or twisted-pair electrical cables and optical fiber, are shown in Figure 4.18. The minimum TOT required for OMs of the same transmission type are very similar. Typical values are 150 ns for OMs read out via coaxial cable, 75 ns for OM read out via twisted pair cable, and 5 ns for those read out via an optical fiber.

**Amplitude cut:** Electronic noise hits typically have amplitudes smaller than single photoelectron hits. Analyses that aim at detecting moderately signals (as for instance neutrinos with TeV energies) keep only hits in channels with a minimum peak amplitude of 0.1 photoelectrons. The threshold can be higher in analyses that search for extremely bright signals.

**Isolation cut (*RT-cleaning*):** Contrary to hits from Cherenkov photons, noise hits occur un-correlated in time and location within the detector. Noise is efficiently reduced by requiring each hit to be coincident with at least one more hit within a certain time and spatial distance. A maximum distance of  $R = 100$  m and a time interval of  $T = \pm 500$  ns are common values to define the coincidence window.

**Cross talk cleaning:** Cross talk is one type of electronic noise which preferably occurs in strings 5-10, where twisted pair cables are used for signal transmission. Capacitative coupling between adjacent cables leads to additional *non-photon* signals in particle induced events. This type of cross talk occurs between OMs located in the same string. By nature, cross talk hits are correlated in both time and space with the actual photon hits, and hence their rejection is more complicated.

Pairs of cross-talking OMs (so-called *talker*- and *receiver*-pairs) are identified using the detector calibration data [135]: During calibration, the high voltage of all OMs but one (the one that is being calibrated) is turned down. The active OM (the *talker*) is fired through a pulse of laser light, and the entire detector is read out. Those OMs for which hits are recorded although their high voltage is turned down are likely to *receive* cross-talk hits from the *talker*-OM also during particle induced events. Figure 4.19 shows a map of talker and receiver OMs in string 6. High level *hit-cleaning* (see

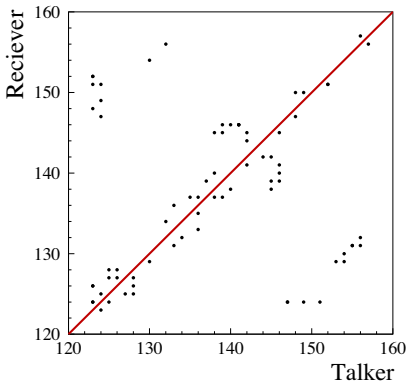


**Figure 4.19** – Cross talk map for string 6 (OM 123 to 158). Each marker indicates where a *talker-receiver*-pair was identified [122].

<sup>16</sup> About 50 people spent the winter at the Amundsen Scott South Pole Station, maintaining a variety of scientific equipment and detection set-ups. Two or three “*winter-overs*” are responsible for the AMANDA and IceCube neutrino telescopes.

section 7.2.1) usually removes hits in receiver OMs if they were recorded in coincidence with a hit in an OM that is known to be a talker to this particular OM.

The second method to identify cross talk relies on the amplitude and TOT characteristics of the hits. Cross talk pulses are induced by other pulses rather than photo-electrons. Therefore they should be the time derivatives of the mother pulse. Hence, cross talk hits are bipolar, and consequently have shorter TOTs. Figure 4.20 shows a the correlation between ADC and TOT values for both photon pulses and cross talk pulses.

Photon- and cross talk hits obviously fall into different region in the ADC-TOT plane. The separation boundary can be parameterized as [122]

$$ADC_{\text{bound}} = e^{A+B \cdot TOT^C} + (TOT/D)^E \quad (31)$$

This function is used to reject cross talk hits during high level hit cleaning. The parameters  $A, B, C, D$ , and  $E$  of equation (31), referred to as *cross-talk constants*, are OM specific and are determined for each individual OM from calibration data.

#### 4.8.2 Events of electronic origin (“Flares”)

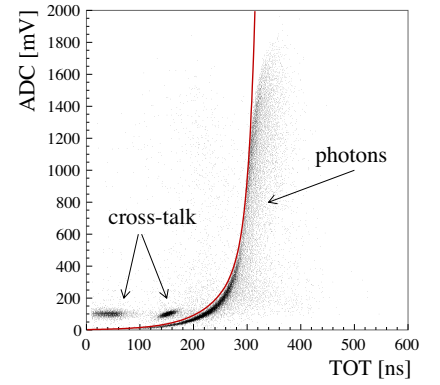
A small fraction of events contain only few photon hits, if any at all. The origin of such events is not fully understood, but they can be identified by an abnormal time pattern of leading edges. For a particle induced event, the hits recorded at the surface originate from PMT pulses that were created at depth and then transmitted over more than a kilometer of either electrical cable or optical fiber. The transit time from the detection point to the DAQ is of the order of micro seconds, of the same order as the duration of the actual event (particle crossing) at depth. The transmission delay is OM specific and depends primarily on the depth at which the OM is located. Therefore, the time pattern of the recorded raw leading edges will to some extent reflect the depth distribution of hit OMs. The OMs are numbered in ascending order from the top to the bottom of each string, and hence the OM number reflects the depth at which a certain OM is located. Hits within one string will therefore always show a *positive* correlation between OM number and leading edge time (higher OM number means later arrival time).

Figure 4.21 shows the correlation between the raw leading edge times and the OM number for a typical atmospheric muon event. Such correlation diagrams are referred to as event *fingerprints*.

If the leading edge times show *no* correlation with OM numbers, the hits recorded during the event were most probably not produced at depth during a particle crossing, but are rather created at or close to the surface. Figure 4.22 shows an example for such an abnormal fingerprint.

The fingerprints themselves cannot be used for tagging *flare* events during data processing. However, the event fingerprints were used to develop a set of observables, nine so-called *flare-indicators* that quantify the probability of an event to be of non-particle origin [134].<sup>17</sup> The flare-indicators are usually used during offline analysis as simple selection criteria requiring sufficiently low indicator values. However, in this analysis events with

<sup>17</sup>The nature of the flare-indicators and their usage in AMANDA analyses is explained in more detail in Appendix B.



**Figure 4.20** – Correlation between ADC and TOT for Cross talk hits compared to photon hits. Cross talk hits can be rejected by requiring the hits to lie left/below the separating border (red line) given by equation (31).

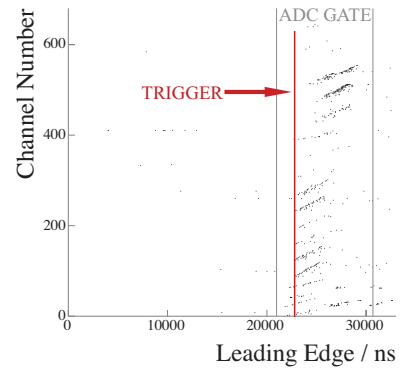


**Figure 4.21** – Fingerprint of an atmospheric muon event.

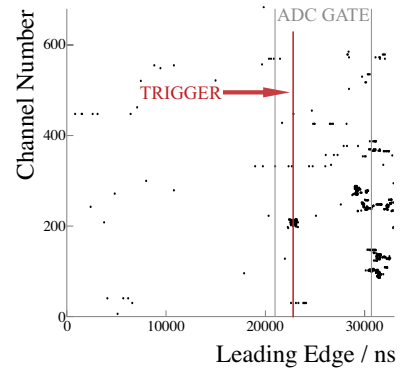


**Figure 4.22** – Fingerprint of a non-particle event (*flare-event*). The absence of a correlation between channel numbers and leading edge times suggests that hits are produced at or close to the surface.

flare characteristics were observed to cluster in time, and hence the flare indicators are also used for defining the initial data set (see section 6.1.1).

## 4.9 Recent results from AMANDA

AMANDA-II is optimized to search for neutrinos with energies in the TeV region. The main detection channel for this purpose is up-going muons (induced by muon neutrinos after traversing the Earth). Selection criteria for up-going muons are well established, and have been applied to multiple years of data. Figure 4.23 shows the reconstructed arrival directions of several thousand neutrinos selected from data taken between 2000 and 2004 [111].

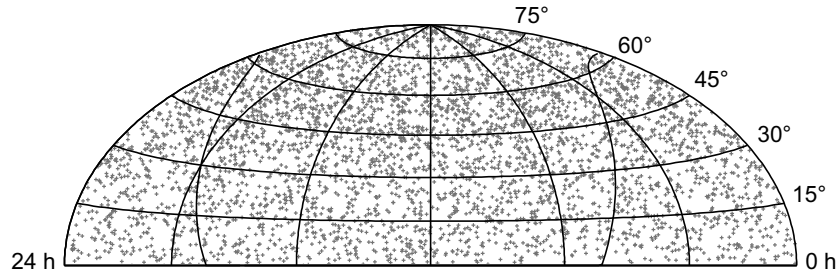


**Figure 4.23** – AMANDA-II skymap of neutrino arrival directions in the northern hemisphere. From [111].

Neither a statistically significant clustering of the neutrino arrival direction was found in the data, nor an excess of neutrino candidates with higher energies than expected from the atmospheric neutrino spectrum [136, 99]. The limits that were placed on the flux of extraterrestrial neutrinos from both point-like and diffuse sources are the most stringent ones to date.

Figure 4.24 shows the signature of a neutrino event observed with AMANDA-II during the year 2000.

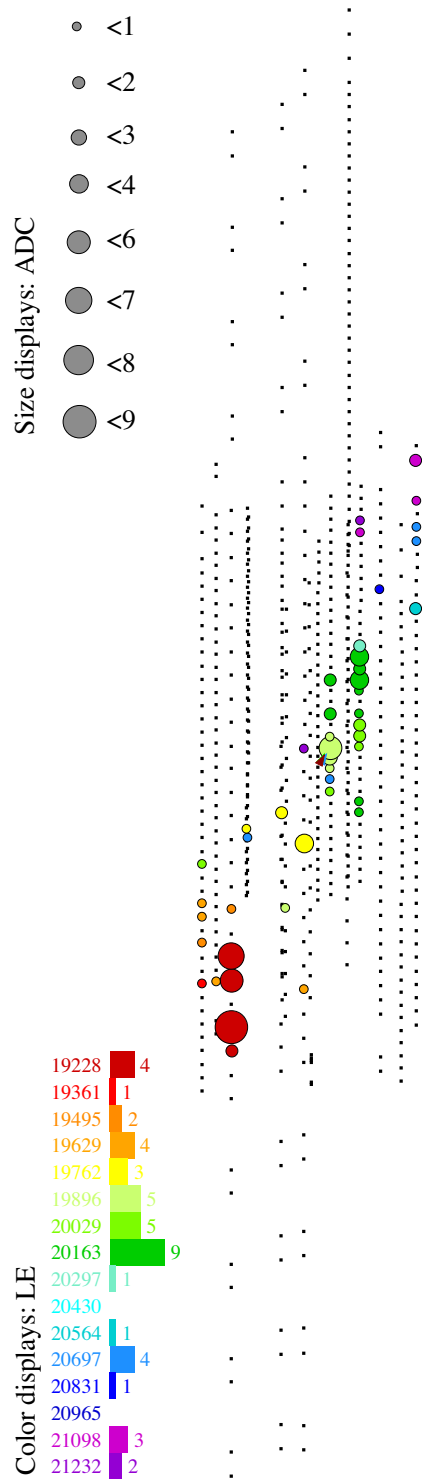
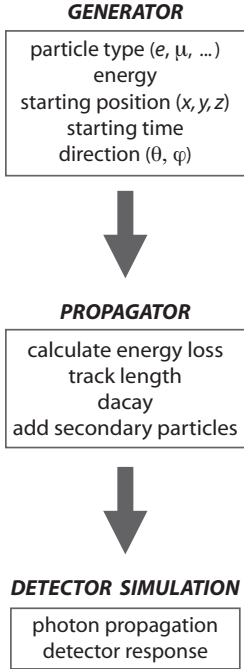


**Figure 4.24** – Signature of a neutrino-induced muon from the 2000 data set. Colored circles indicate an OM that has detected light. Their color represents the reconstructed photon arrival times; their size represents the amplitude (in photo electrons) of the hits.

## 5 Simulation of particles in AMANDA-II

The simulation of events in the AMANDA detector proceeds in three subsequent steps:



1. Generation of primary particles.
2. The propagation of particles, *i.e.*, the simulation of the energy loss and the generation of secondary particles along the initial track.
3. The detector simulation.

A schematic sketch of the data flow is shown in Figure 5.1.

The standard event generators used in AMANDA allow to simulate atmospheric muons and neutrino induced leptons of all three flavors. In case of atmospheric muons, the event generation includes the simulation of the particle cascade which is induced by cosmic ray interactions with air nuclei in the atmosphere. Only muons which are capable of reaching the detector are written out. The simulation of neutrino induced leptons involves the potential interaction and absorption of the primary neutrinos during their passage through the Earth. Neutrinos are usually simulated with an energy spectrum  $\propto E_\nu^{-1}$ . The simulated events can later be re-weighted according to an arbitrary neutrino spectrum (describing either atmospheric neutrinos or neutrinos of astrophysical origin) as desired.

The simulation of magnetic monopoles is not foreseen within the standard simulation set-up and requires modifications to the simulation software.

### 5.1 The detector simulation

The detector response to the Cherenkov light emitted by either primary or secondary particles depends on the following parameters:

- the particle type (*e.g.*, muon, electron, ...),
- the track starting position and a starting time,
- the track direction, given as zenith angle  $\theta$  and azimuth  $\varphi$ ,
- the track length, and
- the energy of the particle.

These quantities are passed to the detector simulation. The simulation of the detector response breaks up into two parts:

1. The simulation of the detector response itself, *i.e.*, the simulation of the OMs and data acquisition system components, and
2. the simulation of the Cherenkov light generation and propagation through the detection medium, *i.e.*, the polar ice.

**Figure 5.1** – The simulation of events proceeds in three general steps (see text): The *generation* and *propagation* of particles, and the *detector simulation*.

### 5.1.1 Photon Tracking

A relativistic muon emits more than  $10^7$  Cherenkov photons during its passage through the detector. The propagation of each individual Cherenkov photon is too CPU intensive to be performed for each simulated event. Therefore, the light propagation is simulated beforehand with a separate program (the *Photon Transport and Detection* program PTD [120]). The relevant probability distributions are stored in large look-up tables which are then accessed by the detector simulation, *amasim* [128] (see below).

PTD pre-calculates the OM response to Cherenkov light from muons and electromagnetic or hadronic cascades. The program simulates scattering and absorption of photons on their way from the point of emission to the PMT photocathode. *I.e.*, PTD not only tracks photons through ice, but also through the glass and gel layers surrounding the PMTs. The simulation results are stored in two five-dimensional tables, which contain the arrival time distribution of Cherenkov photons in an OM at a certain distance and with a certain orientation relative to the particle track, and the probabilities for photoelectrons to be produced. The time  $t$  is taken relative to the *Cherenkov time*. The Cherenkov time is the propagation time of a Cherenkov photon from the point of emission to the photocathode without delay due to scattering. The spatial coordinates which describe the geometry of the particle with respect to the OM are sketched in Figure 5.2.

A photon table represents the cylindrical volume with the length  $z_{\max}$  and the radius  $\rho_{\max}$  centered around the location of an OM. Standard muon tables used for mass production have maximum ranges of 250 to 400 meters in both longitudinal and radial directions. The simulation of extremely bright events, such as the Cherenkov signatures from magnetic monopoles, requires tables of longer range. For each coordinate inside the table range and each possible orientation, the following quantities are stored:

- the mean number of photo-electrons produced per square meter photocathode, assuming a peak PMT quantum efficiency of 100%, and
- the probability distribution of the delay times relative to the Cherenkov time.

During the simulation process, the tabulated values are scaled according to the actual photocathode area and quantum efficiency (which are set individually for each OM).

The following parameters are specific to a certain set of photon tables:

- The mean scattering angle and geometric scattering length in the medium. These values are taken from the *in-situ* measurements described in section 4.1.
- The absorption length and its dependency on the wavelength according to the *Three Component Model* (see section 4.1.1).
- Spectral characteristics and angular distribution of the emitted photons, which is usually the Cherenkov wavelength spectrum and emission geometry for either relativistic muons ( $v \approx c$ ), or for particles of an electromagnetic or hadronic cascade in ice. In addition, PTD allows to simulate various artificial light sources, like those deployed with the AMANDA strings.

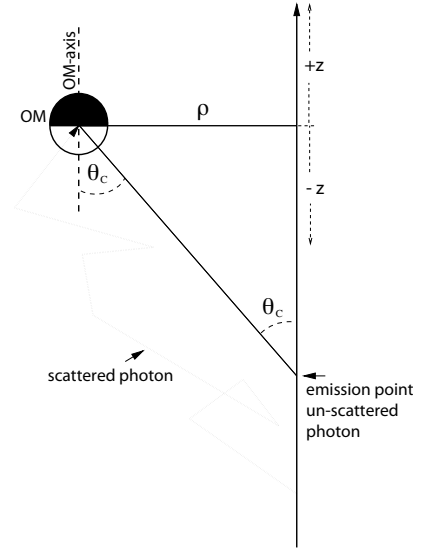


**Figure 5.2** – The photon table coordinate system [128]. The distance between OM and particle track is given by two spatial coordinates  $(z, \rho)$ , where  $z$  is the distance along the particle track measured from the point of minimum distance between particle and OM. The orientation of the OM with respect to the path of an unscattered Cherenkov photon is given by two angles  $(\theta, \phi)$  which are not shown in the figure.

- The wavelength dependent transmissivity of the OM pressure sphere and the silicon gel layer between sphere and PMT. Tables are usually generated for the transmissivity of the more transparent, second generation OM spheres (see section 4.3). The sensitivity of OMs with less transparent spheres is scaled down accordingly during the simulation process.
- A model for the “hole ice”, *i.e.*, the ice around the OMs inside the refrozen bore-hole. This refrozen ice has a higher concentration of air bubbles than the surrounding bulk ice, resulting in a shorter scattering length. The hole ice model model that describes experimental data best assumes a geometric scattering length of 50 cm within cylindrical volume of 60 m cm diameter around the OMs [137, 138].

Within the volume represented by a photon table, the optical properties of the bulk and the hole ice (*i.e.*, scattering and absorption lengths) are constant. To account for the variations with depth, different tables are used for different OMs, depending on their location. The most commonly used simulation set-up defines 16 ice-layers of varying optical properties within AMANDA’s depth range [139]. In this approach, the tabulated photon detection probabilities for a certain OM correspond to the detection probabilities of photons that propagates through optically homogeneous ice with optical properties identical to those prevailing at the OM location.<sup>18</sup> This approach is valid for moderately bright events, in which most of the photons do not propagate through more than one ice layer, and the response of an OM is governed by the optical properties of its immediate surroundings. Relativistic monopoles, however, are visible over hundreds of meters away from the particle track. For simulation such extremely bright events, more accurate results are obtained by using average ice properties throughout the entire depth range. The simulations for this analysis were performed using photon tables with averaged optical parameters of the so-called MAM ice-model [141].<sup>19</sup>

In order to simulate events in AMANDA, one usually needs two sets of photon tables:

1. Muon tables, which contain the OM response to Cherenkov light from muon tracks<sup>20</sup>. Since a muon radiates continuously along an elongated track, photons emitted from many different points in space contribute to the total OM response.

---

<sup>18</sup>In the meantime, the PTD photon tracking package was replaced by a newer package (**Photonics** [140]), which tracks photons through individual ice layers. The **Photonics** was still in an early testing phase when Monte Carlo events for this analysis were being produced, and is hence not used in this work.

<sup>19</sup>The modeling in of the light propagation through Polar ice is still being refined. The optical parameters entering the photon propagation simulation during generation of the photon tables are being varied, and simulation results are compared to experimental data. As of today, the simulation results are still not completely satisfactory. In this simulation effort, we use average optical parameters of an ice model that is referred to MAM model (*Muon Absorption Model*). In the MAM ice model, the photon absorption lengths are slightly enhanced, compared to values obtained from *in-situ* measurements. The absorption lengths that finally entered the model were fit to high quality atmospheric muon data (hence the name). The original MAM ice model is a 16 ice layer model. Here, we use *averaged* parameters of the model.

<sup>20</sup>In practice, we use three sets of muon tables, rather than one: 1) tables for muons which start within the volume over which the table is valid, 2) muons which stop within this volume, and 3) those which both start and stop within the volume. Technically, only one muon table would suffice. The use of three sets of tables is however more efficient with respect to computing time (see [128] for details).

2. so-called *shower* tables, which contain the OM response to Cherenkov light from electromagnetic or hadronic cascades. In contrast to elongated muon tracks, electromagnetic or hadronic cascades are contained within a small volume. Although the Cherenkov emission is peaked at the Cherenkov angle, the Cherenkov cone is less pronounced than for muons. The total number of emitted Cherenkov photons scales linearly with the cascade’s energy. Shower tables are usually produced for a cascade of 1 GeV energy [91], and the response to cascades of arbitrary energy is calculated by scaling the light intensity (*i.e.*, the number of photoelectrons) accordingly. Electromagnetic and hadronic cascades are treated with different scaling factors, in order to account for the reduced light output from hadronic cascades [91]. The emission geometries of hadronic and electromagnetic cascades are not identical [91], but differences are largely washed out over length scales at which AMANDA collects light.

Photon tables for relativistic magnetic monopoles are similar to muon tables because the Cherenkov signature of monopoles is track-like. Monopole tables, however, have to be generated with different light intensity and, if the monopoles move slower than the vacuum speed of light, with a different Cherenkov angle.

### 5.1.2 Simulation of the detector response

The simulation of the detector response for Cherenkov light emitting particles is performed with the detector simulation package `amasim` [128]. The data generated by the program are almost identical to the data taken with the AMANDA detector, which enables us to use the same processing chain for both simulated and experimental data from an early processing stage on.

The detector simulation package `amasim` reads and writes events in `f2000` format [142], an `ascii`-format which was developed in the 1990s together with the `rdmc` I/O-library [143]. An `f2000`-file consists of a file header followed by a stream of subsequent events. During mass simulation, `amasim` reads the required event parameters (particle type and energy, track position, time, direction, and length) from `f2000`-files, which were written by the Monte Carlo generator and particle propagator packages (see below). `amasim` distinguishes two types of particles: (track-like) muons, and cascades. In general, a muon signature contains contributions from the continuous Cherenkov emission of the muon itself, and Cherenkov emissions from secondary particle cascades produced along the muon track (the stochastic energy losses). Secondary cascades are simulated only for processes above an energy deposit larger than 0.5 GeV. Secondary processes below 0.5 GeV are extremely frequent, and are treated as quasi-continuous enhancement of the muon Cherenkov light intensity.

### 5.1.3 Simulation of the OM

For each track and cascade of an event passed to `amasim`, the mean number of photoelectrons  $\langle N_{\text{PE}} \rangle$  at each OM location is retrieved from the PTD tables.  $\langle N_{\text{PE}} \rangle$  is then scaled with the photocathode area, the relative sensitivity and the PMT quantum efficiency of the respective OM. The simulation of the OM response, then, proceeds as follows

1. The number of photoelectrons,  $N_{\text{PE}}$ , is randomized using a Poisson distribution with mean  $\langle N_{\text{PE}} \rangle$ .
2. For each photoelectron, the corresponding ADC voltage is randomized according to the individual distributions of amplitudes for single-photoelectron signals (*c.f.* Figure 4.15).
3. For each photoelectron, a random scattering delay is chosen from the delay probability distribution in photon tables.
4. A Gaussian smearing is added to the hit times to simulate the transit time jitter.

This process results in a series of amplitudes and hit times  $T_i, A_i, i = 1, \dots, N_{\text{PE}}$ . In case of muon tracks, the amplitudes are scaled by an energy dependent factor

$$A = A^{\text{bare muon}} \cdot 1.72 + 0.023 \cdot \ln(E_\mu[\text{GeV}]), \quad (32)$$

in order to account for the quasi-continuous Cherenkov emissions from low energy secondary particles [91].<sup>21</sup>

Dark noise hits are added randomly according to noise rates measured for individual OMs. The amplitudes of noise hits are simulated as single-photoelectron signals, similar to the procedure described above. The noise rates are assumed to be constant.

Afterpulses are added to the hit series with a typical probability and time delay relative to the initial photon pulse. The probabilities for afterpulsing and characteristic delays were determined from the hit time distribution of the already deployed OMs [128]. The values are set individually for each OM; typical values are 6% per single photoelectron for the afterpulse probability and  $6 \mu\text{s}$  for the delay relative to the photon hits. Hits are simulated over a time window of  $64 \mu\text{s}$ , which is significantly larger than the  $32 \mu\text{s}$  of the data acquisition.

#### 5.1.4 Signal transport to the surface

The transit time of the PMT pulses to the surface is several micro seconds. In order to mimic the output of the real detector and to simulate the trigger correctly, the OM specific cable delays (measured during the calibration of the detector) are added to the simulated hit times.

Transmission over kilometer-long electrical cables also means smearing of the pulse shapes. The degree of smearing increases with cable length (*i.e.*, depth). Depth dependent smearing of the pulses is not simulated. Instead, `amasim` uses a set of template pulse shapes for specific types of OMs and signal readouts. The template pulse shapes were obtained by averaging digitized single-photoelectron pulses taken with an oscilloscope from OMs in the ice.

Cross talk, which predominantly occurs in the twisted pair cables, is not simulated. The cross talk cleaning (see section 4.8.1) is still applied to simulated data, in order to reproduce the potential loss of actual photon hits caused by the applied cleaning criteria. Due to the simplified simulation of

---

<sup>21</sup>The parameterization of the light yield from secondary processes was obtained from GEANT [144] simulations.

the PMT pulses using template ADC spectra and pulse shapes, the ADC-TOT characteristics of individual OMs differs between experimental and simulated data. Figure 5.3 shows a comparison of ADC-TOT characteristics in experimental and simulated data for one particular OM (OM # 264). This OM is located at the bottom of string 9. For bottom OMs, the smearing of the pulse associated with the transmission over kilometer-long cable is strongest. *I.e.*, single-photoelectron pulses are wider and have lower amplitudes than the average (template) pulse. For OM264, the separating boundary between photon hits and cross-talk hits in experimental data (grey line in Figure 5.3) is indeed shifted towards larger TOT and smaller ADC values compared to the boundary in simulated data (for the sake of clarity, the boundary for simulated data is *not* shown in the figure). For *simulated* data, a large fraction of the single-photoelectron hits falls into the cross-talk region that was determined for *experimental* data. Those simulated photon hits would be removed by the cross-talk cleaning if exactly the same ADC-TOT cut were applied to simulated as for experimental data.

In order to be able to apply cross talk cleaning also to simulated data, dedicated cross talk constants (see equation 31 in section 4.8) are determined from the ADC-TOT characteristics of the simulated OMs.

### 5.1.5 Simulation of the surface electronics

For each channel, the net surface pulse is retrieved by adding a template pulse shape (shifted by the respective cable delay time) for each of the photoelectrons and for each noise hit and each after pulse. The resulting pulse is used to determine the threshold crossing time and peak amplitude. Thresholds are set individually for each channel, according to the hardware settings of the detector.

The Multiplicity trigger, ADC gate, TDC buffer length *etc.* can now be simulated realistically. Also the overflow behavior of VME and CAMAC TDCs (see section 4.4.2), is reproduced accurately.

### 5.1.6 Calibration

The calibration constants  $t_0$  and  $\alpha$  (see section 4.5) depend on the surface pulse shapes. The template pulses used by `amasim` have different constants than pulses in experimental data. Like for the cross talk constants, dedicated calibration constants have to be determined for simulated data. The calibration constants are obtained with the same fitting procedure as used for the experimental data.

Figure 5.4 shows a comparison of calibrated hit times in experimental data and in simulated atmospheric muon events at trigger level. The hit times, amount of noise, and afterpulsing show good agreement.

## 5.2 Simulation of magnetic monopoles

The simulation of magnetic monopoles is not implemented in the simulation packages. However, existing packages are modified to simulate events induced by magnetic monopoles.

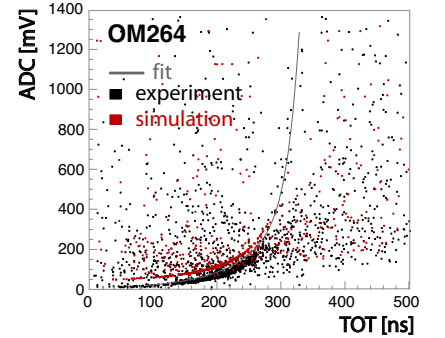


**Figure 5.3** – ADC-TOT characteristics of OM264 for experimental data (black markers) and simulated data (red markers). The separating boundary between photon hits and cross talk hits in *experimental* data (equation (31)) is indicated by as grey line. For this particular OM, the separating boundary in *simulated* data (not shown) is shifted towards smaller TOT and higher ADC values.

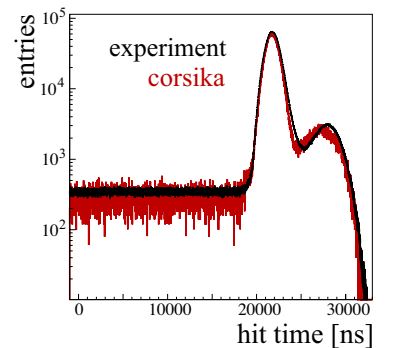


**Figure 5.4** – Calibrated hit times for experimental data (black) and simulated atmospheric muon events (red).

### 5.2.1 Monopole track generation

Like muons, monopoles produce a track like Cherenkov signature. Therefore, it is technically most convenient to pass events containing a single particle track labeled as a muon to `amasim`.

The program `muo0` is a generator for single particle tracks whose types are contained in the `rdmc`-library. The output format is `f2000`. In order to produce initial tracks that will later become monopole signatures, we use `muo0` to generate an isotropic flux of muons. The muon tracks are sampled such that their vertices are homogeneously distributed on a generation plane of radius  $R_0 = 1000$  m at a distance of 1000 m from the detector center (Figure 5.5). The muon direction is pointing perpendicularly towards the detector center. The generation plane may take all possible orientations relative to the detector, resulting in an isotropic muon flux through the detection volume.

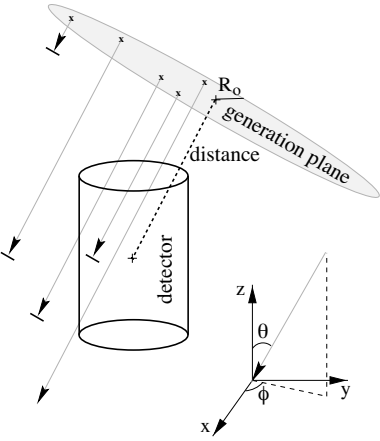


**Figure 5.5** – Generation of muon tracks with `muo0`. The tracks are sampled from generation plane with radius  $R_0 = 1000$  m at a constant distance of 1000 m to the detector center. From [145].

All dependencies on the particle energy are disabled in the following processing steps. The muon energy can hence be set to an arbitrary value.

### 5.2.2 Monopole propagation

The length of a particle track is usually calculated from the energy loss simulated with the propagator program. Energy loss processes other than Cherenkov radiation strongly depends on the monopole mass. In the mass range interesting for AMANDA, the velocity of the monopole can be assumed constant over the detector's sensitive volume [146], and we can neglect the probability of monopoles potentially stopping in the detector.

Cherenkov light from secondary processes is only relevant for monopoles of extremely high Lorentz boosts (see section 2.5.2), Such Lorentz boosts are expected only for extremely light monopoles, which are unlikely to reach AMANDA. Therefore, secondary Cherenkov light is neglected in the simulation, and monopole track lengths are set manually to a fixed value of 10 km.<sup>22</sup>

### 5.2.3 Monopole photon tables

The simulation of monopoles of different speed and charge requires the generation of dedicated photon tables: One set of photon tables is generated for each combination of monopole speed and charge.<sup>23</sup>

For this analysis, we consider only minimally charged monopoles carrying one Dirac charge, and four distinct monopole velocities:  $\beta = 0.76$  (just above the Cherenkov threshold in ice),  $\beta = 0.8$ ,  $\beta = 0.9$ , and  $\beta = 1.0$ .<sup>24</sup> Average ice properties and a range of  $\rho_{\max} = z_{\max} = 1000$  m are used.

<sup>22</sup>The track lengths were set using a *Perl* script within the `f2000` data stream.

<sup>23</sup>Because of the dependence of the Cherenkov angle on the monopole *speed*, the generation of one set of photon tables per speed is a necessity. The monopole *charge* on the other hand only affects the intensity of the Cherenkov light (the intensity scales with the monopole charge as  $d^2N / dx d\lambda \propto g^2$ ). Hence, an approximate simulation of monopoles with various charges can be accomplished by scaling the OM sensitivities in the detector simulation appropriately.

<sup>24</sup>Theoretically of course, the velocity  $\beta = 1.0$  is not allowed for a massive particle. However, the velocity can be arbitrarily close to  $\beta = 1.0$ . For the simulation, we use the numerical value  $\beta = 1.0$ , and hence we will refer to ultra relativistic monopoles as  $\beta = 1.0$  monopoles, although this is strictly speaking incorrect.

### 5.2.4 Modification of the detector simulation

The tracks generated with `muo0` are treated by `amasim` like muons, but when these muon tracks are passed to `amasim` along with monopole photon tables, the simulated Cherenkov geometry and intensity will be that of magnetic monopoles. The simulation of the correct monopole Cherenkov response requires some additional smaller modifications to `amasim`.<sup>25</sup>

- The photon arrival times stored in the tables is relative to the Cherenkov time. The conversion to absolute hit times involves the vertex position and time and the particle velocity. As `amasim` assumes all particles to travel at the speed of light, time calculation had to be modified such that `amasim` can handle variable particle speeds.
- By default, on receiving a muon track, `amasim` adds the Cherenkov light due to quasi continuous emissions from low energy secondaries ( $\delta$ -electrons) by scaling the pulse amplitudes according to equation (32). For monopoles, this scaling would depend on the Lorentz boost [47]. For the Lorentz boosts considered here, the light enhancement due to secondary Cherenkov light is negligible compared to the direct Cherenkov emissions. Hence, the light scaling is disabled in the simulation altogether.

Figure 5.6 shows a simulated signature of an up-going  $\beta = 1.0$  monopole in the event display.

### 5.3 Simulation of atmospheric muons

Bundles of down-going muons from extended air showers are the main background to monopole searches. The air shower simulation package `CORSIKA` (*COsmic Ray Simulation for KAscade*) [148] provides a tool to simulate the development of the full particle cascade initiated by interactions of cosmic ray primaries of energies up to  $10^{11}$  GeV.

Atmospheric muon events are simulated as a collaboration-wide data production effort, using `CORSIKA`. These data are however insufficient for monopole searches for a variety of reasons:

- The dominant background to monopole searches, especially for searches above the horizon, are muon bundles from interactions of cosmic rays at highest energies. Due to the steeply falling energy spectrum, the statistics at relevant energies obtained with standard simulation settings is insufficient for statistically sufficient background studies.
- The theoretical input that is used as default spectrum (in terms of both composition and energy) of primary cosmic rays does not describe high energy atmospheric muon data reasonably well (see below).
- The simulation is based on the standard sets of layered PTD photon tables. The approximation of the layering using PTD tables (see above) yields incorrect results in the energy range of interest.

Consequently, a monopole search requires a dedicated simulation effort for both signal and background events.

<sup>25</sup>The modifications to the detector simulation were done to the `amasim` package after the *Grapefruit-fix3* release [147].

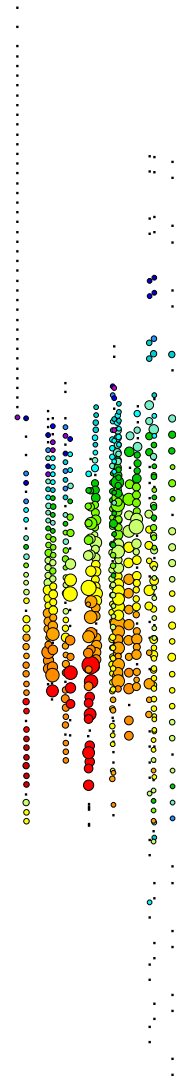


**Figure 5.6** – Cherenkov signature of an up-going relativistic magnetic monopole passing through AMANDA with speed  $\beta = 1.$ . For a better exposure of the time pattern, only the first hit in each OM is displayed.

### 5.3.1 Hadronic interaction models in CORSIKA

CORSIKA provides several options to model the hadronic interaction at high energies. None of the available models yields an accurate reproduction of air-shower data over the full energy range [82, 149]. For this work, we use the model QGSJET01. This model is known to under-produce high energy muons. The shape of the energy spectrum of atmospheric muons is however accurate, and a good agreement between simulated and experimental muon data is achieved by scaling the simulated flux by an overall factor.

### 5.3.2 Cosmic ray composition and energy spectrum

CORSIKA allows to simulate air-showers induced by primary cosmic nuclei from  $Z = 1$  (protons) to  $Z = 26$  (iron). Heavier primaries cannot be simulated.

By default, the AMANDA collaboration uses the *poly-gonato* model (see section 3.1.1) as theoretical input spectrum to their simulations, since it provides a straight forward parameterization of the energy spectra of individual elements [84].

**The poly-gonato model:** According to the *poly-gonato* model, the energy spectrum of an element with nuclear charge  $Z$  is a broken power-law, as

$$\frac{d\Phi_Z}{dE_0}(E_0) = \Phi_Z^0 E_0^{\gamma_Z} \left[ 1 + \left( \frac{E_0}{\hat{E}_Z} \right)^{\epsilon_c} \right]^{-\frac{\Delta\gamma}{\epsilon_c}} \quad (33)$$

The spectral slope  $\gamma_Z$  and the cut-off energy  $\hat{E}_Z$  above which the spectrum steepens (the *knee*) are specific to each element, as well as as the absolute normalization  $\Phi_Z^0$ . Slopes and normalizations are taken from available measurements. The cut-off energies are assumed to scale with  $Z$  as  $\hat{E}_Z = Z \cdot \hat{E}_1$ . The parameter  $\epsilon_c$ , characterizing the smoothness of the change in slope at the knee, and the change of the slope  $\Delta\gamma$  are universal to all elements.

The all particle spectrum is the sum over the contributions of all stable elements of the periodic table up to uranium with  $Z = 92$ :

$$\frac{d\Phi}{dE_0}(E_0) = \sum_{Z=1}^{92} \frac{d\Phi_Z}{dE_0}(E_0). \quad (34)$$

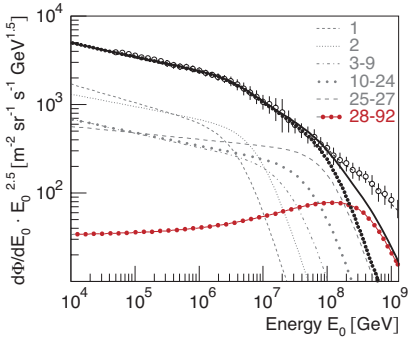


**Figure 5.7** – The poly gonato model. Open markers represent the measured all particle spectrum. The thin dashed, dotted, and dash-dotted lines represent the spectra of individual mass groups as labeled in the plot. The thick dotted line is the sum of all elements up to cobalt ( $Z = 27$ ); the red dash-dotted line is the sum of all elements heavier than cobalt. From [84].

The open parameters of the model, *i.e.*,  $\Delta\gamma$ ,  $\epsilon_c$ , and the proton-knee  $\hat{E}_1$  were fitted to the observed all particle spectrum. Figure 5.7 shows the resulting spectra along with the measured cosmic ray spectrum. Within the *poly-gonato* model, the proton knee is at  $\hat{E}_1 = 4.5$  PeV, the iron knee consequently is at  $\hat{E}_{26} = 26 \times \hat{E}_1 = 117$  PeV. Due to the pre-assumptions, the high energy end of the *poly-gonato* spectrum is dominated by trans-iron elements (see Figure 5.7), and the flux of individual elements drops off steeply after the knee with a slope change  $\Delta\gamma = 2.1$ .

The high energy end of the *poly-gonato* model can obviously not be simulated with CORSIKA, as trans-iron elements are not supported by the package. According to the *poly-gonato* model, those elements start to dominate the cosmic ray spectrum at energies larger than  $\sim 10^8$  GeV. For standard analyses done with AMANDA data, the background posed by muons induced by cosmic ray primaries of multiple-PeV energies is usually totally

negligible. To the searches for monopoles above the horizon, however, such muons prove to be the critical background.

**The two-component model:** Irrespectively of whether or not the *polygono* model is correct, an accurate description of the all particle spectrum at highest energies cannot be achieved with this model, if trans-iron elements are not simulated. An alternative, much simpler input spectrum which does not contain contributions from trans-iron elements (and which can therefore be simulated with CORSIKA) is the *two-component* model [150]. As the name suggests, this model uses only two elements, protons and iron nuclei to represent light in heavy components of the cosmic ray spectrum, respectively.

The *two-component* model assumes a broken power law energy spectrum for each of the two components. The open parameters (the spectral slopes below and above the knee, the position of the knee, and the absolute flux of each element) were fitted to data taken with the KASCADE air-shower array [151].<sup>26</sup>

Figure 5.8 shows the fitted iron on proton spectra along with the measured all particle spectrum. In the *two-component* model, the proton knee is at  $\hat{E}_p = 4.1$  PeV, with a spectral slope change from  $\gamma_p^{(1)} = -2.67$  to  $\gamma_p^{(2)} = -3.39$ . The iron spectrum is featureless in the fitted energy range. The spectral index below  $10^8$  GeV is  $\gamma_{\text{Fe}}^{(1)} = -2.69$ . For our simulations we assume the iron knee to be at  $\hat{E}_{\text{Fe}} = 26 \times \hat{E}_p = 107$  PeV (which lies just above the fit region). We further assume the iron spectrum to continue with the spectral slope  $\gamma^{(2)} = 3.1$  to reproduce the observed all particle spectrum.

### 5.3.3 Importance sampling

The simulation of air-showers with CORSIKA in large numbers is extremely CPU-intensive. With the computing resources at our disposal, the simulation of atmospheric muon events in AMANDA-II proceeds slower than the rate at which they are actually triggered in the experiment. That is, the simulation of one year of livetime equivalent would take more than one year of computing time. If background events are sampled from a realistic probability density (according to one of the theoretical primary spectra energy described above), the vast majority of simulated events will be steeply down-going atmospheric muons at the low energy end of the spectrum. Most of these events will be rejected at a very early stage of the data selection chain. It is therefore desirable to increase the sampling density in the more important regions of the parameter space, *i.e.*, in the region where most of the background is expected at the final analysis level. Such a strategy is referred to as *importance sampling*. In the simulation effort for this analysis, we increase the sampling density with increasing primary energy.<sup>27</sup> During analysis, the events are re-weighted to the physical input spectrum.

<sup>26</sup>The primary spectra were derived from the number of electrons and the number of muons observed in extended air-showers with energies around the knee ( $\sim 10^5 - 10^8$  GeV), making use of the fact that for a given energy, the muon number in an air-shower is increasing with primary mass, while the electron number is decreasing [150].

<sup>27</sup>An alternative approach would be to increase the sampling density with zenith angle. As the direction reconstruction of nearly horizontal muons is usually less accurate, those muons are the most critical background to analyses as TeV neutrino searches.

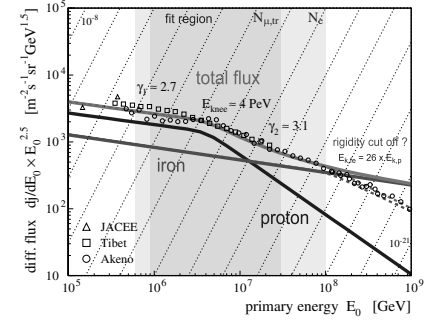


**Figure 5.8** – The Two-Component model. The open markers represent the measured all particle spectrum. The full lines are the fitted proton and iron spectrum, respectively. The iron knee should lie just above the fit region (grey shaded area). From [150].

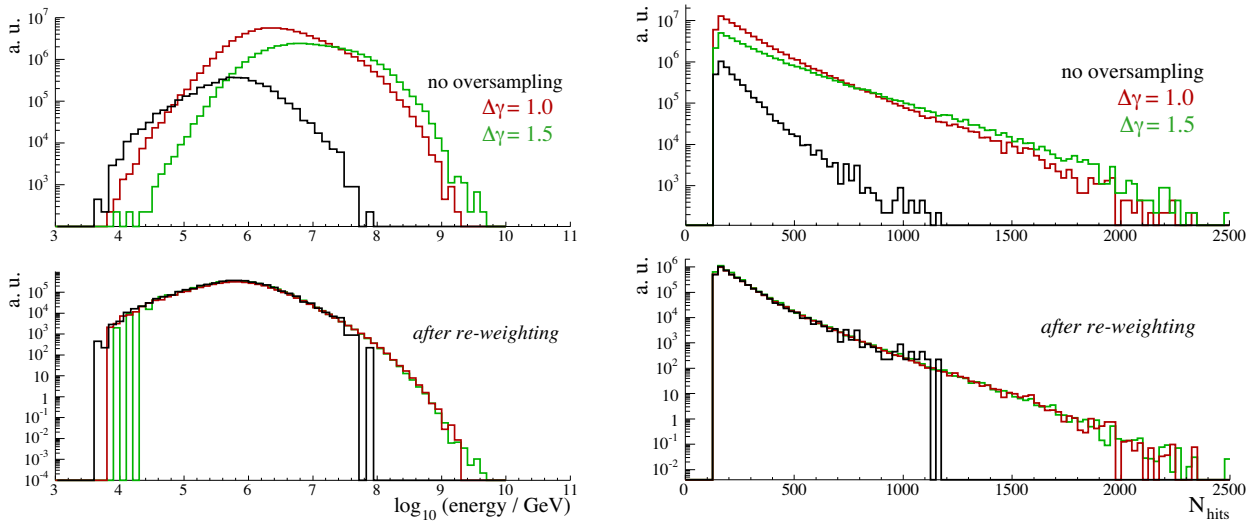


**Figure 5.9** – The effect of importance sampling in CORSIKA (*poly-gonato* model). The left panels show the primary energy spectra for atmospheric muon events in AMANDA-II. The right panels show the hit-multiplicities. Each panel shows the spectra of three event samples, with importance sampling (red and green histograms) and without importance sampling (black histograms). Distributions in the upper panels reflect the probability densities as generated (before re-weighting the events). The distributions shown in the lower panels are obtained after re-weighting the events according to the *poly-gonato* model.

**Importance sampling for the poly gonato model:** For the simulation of the *poly-gonato* spectrum, we sample each individual element with an energy spectrum that is harder by a constant  $\Delta\gamma$ , both before and after the knee. Figure 5.9 shows the effect of this sampling strategy. Shown are the primary energy spectra (left panels of the figure) and the hit multiplicities ( $N_{\text{Hits}}$ ) yielded in the detector (right panels of the figure) for three generated events samples: One without importance sampling, one with an over-sampling factor  $\Delta\gamma = 1$ , and one with an over-sampling factor  $\Delta\gamma = 1.5$ . The computing time used to generate each of the event sample is approximately equal. Sufficient statistics of high energy atmospheric muon events is achieved only with importance sampling.

For the development of selection criteria, we use two of the generated *poly-gonato* samples: the one without importance sampling for developing the first filtering level (at which the data sample is dominated by low energy atmospheric muons), and the sample with an over-sampling factor  $\Delta\gamma = 1$  for the higher analysis levels. The sample with  $\Delta\gamma = 1.5$  is not used, because it has too little statistics in the energy region between 10 TeV and 100 TeV.

**Importance sampling for the two-component model:** For the *two-component* model, proton and iron primaries are generated each with an energy spectrum  $\propto E_{\text{primary}}^{-2}$ . During analysis, both components are added and re-weighted according to the model.

### 5.3.4 Atmospheric density effects

The development of air-showers in the atmosphere, and consequently the flux of atmospheric muons, depends on the density of air-molecules (see appendix A), which in turn depends on the atmospheric temperature. Seasonal temperature variations result in variations of the AMANDA-II trigger rate, which are of the order of 10%.

CORSIKA allows to simulate different atmospheric density profiles, representing various geographic locations and seasons. For the South Polar atmosphere, four density profiles are implemented: a profile typical for the month March (Antarctic autumn), one for July (winter), one for October (spring), and one for December (summer). Background simulations for AMANDA-II are usually done using the October profile, since it yields an event rate closest to the annual average. For this analysis, we use three different profiles: March, July, and October, in order to account for seasonal variations in the event rate. (The December profile is not used because no data for analysis purposes are taken during the summer.)

### 5.3.5 Muon Propagation

From the simulated air-shower, muons with an energy  $E_\mu > 273 \text{ GeV}$  are written to an `f2000` file. Muons of lower energies will not reach the detector and are dropped from the data stream. The muon energy loss due to ionization, bremsstrahlung, photo-nuclear interactions, and pair-production during passage through air, snow (the top 200 m layer of the Polar ice), and ice are simulated with the *Muon Monte Carlo* `muc` [152]. Apart from the secondary energy losses, the program calculates the distance after which the muons stop or decay in flight, *i.e.*, the track lengths. Radiative processes which result in an energy loss greater than 0.5 GeV are treated individually. Type, energy, vertex, time, and direction of the corresponding secondary particles are added to the `f2000` stream. Passed to `amasim`, the Cherenkov light from these secondaries is treated individually, while the emissions from low energy, quasi-continuous processes are accounted for through scaling of the initial amplitudes as described in section 5.1.3 above.

### 5.3.6 Photon tables for muons

Radiative energy losses of high energy atmospheric muons can deposit a large amount of light in AMANDA-II. Also, atmospheric muons can occur in extended bundles of multiple nearly parallel tracks. Since the light intensity from a single muon track is much less intense than that of magnetic monopoles, and since `amasim` treats each muon and secondary particle cascade individually, the background simulation does not suffer from a shorter photon table range, as would the the simulation of magnetic monopoles. For this analysis we use muon tables that were generated for searches for high energy muon neutrinos. The tables have a range of  $\rho_{\max} = z_{\max} = 400 \text{ m}$ . Like the monopole tables, they are generated with average ice properties throughout the whole detection volume.

Figure 5.10 shows the signature of a simulated atmospheric muon bundle induced by a primary iron nucleus with an energy  $\sim 40 \text{ PeV}$ .

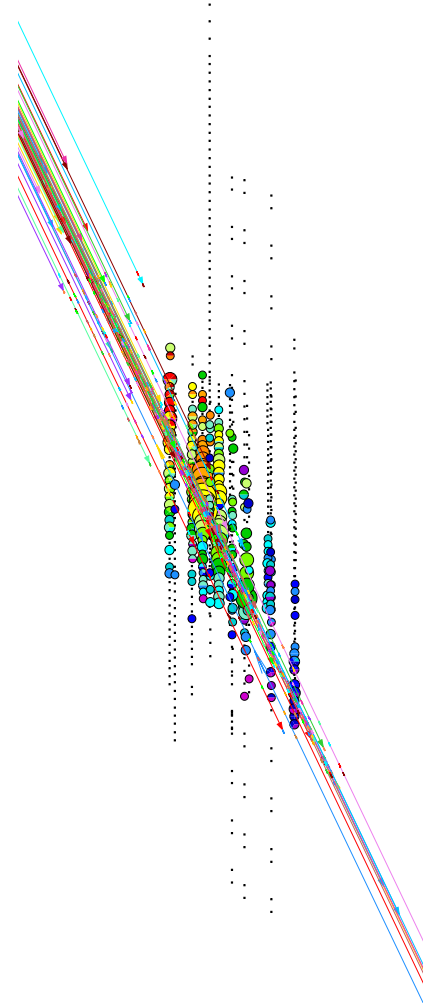


**Figure 5.10** – Simulated atmospheric muon bundle in AMANDA-II induced by a 40 PeV iron nucleus.

## 6 Data Pre-processing and first level data selection

The data processing effort for this analysis starts from the raw data. The total data volume amounts to roughly 1.5 terabytes. The full statistics of raw data is available only on magnetic tape archives. A small portion ( $\mathcal{O}(1\%)$ ) of the raw data is translated into an analysis data format and made available on disk.

The preparation of analysis-ready data sets is achieved by three processing steps (Figure 6.1):

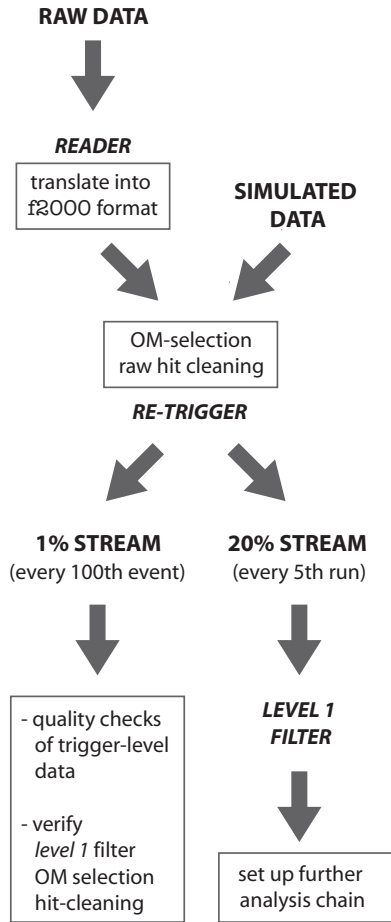


**Figure 6.1** – Processing scheme for the two data streams that are used for the development of data selection criteria. A third data stream, 80% of the data set, is used to derive the final analysis result. This data is processed only *after* the full analysis chain has been established.

1. The translation of experimental data in DAQ binary format to the f2000 analysis format on which the analysis software operates. Simulated data is produced already in in f2000 format.
2. *Retriggering* of the data after applying a first OM selection and hit cleaning based on monitoring data (see section 4.7.)
3. A *level 1* filter, which reduces the initial data volume by roughly a factor 100.

Both the retriggering and the *level 1* filter, as well the higher level processing steps described in the following chapters, are realized with the AMANDA software package *Sieglinde* [153]. The analysis package *Sieglinde* can operate on both f2000 data and data using the package’s own binary data format, which is based on the ROOT framework [154]. The latter format is used for this analysis from retrigger level on.

Two data streams are produced that are used for the development of higher level data selection:

1. A so-called *minimum-bias* data stream of roughly 1% of the available data, which is used for quality checks of trigger level data and verification of the *level 1* filter. This data stream comprises every 100th event that passes the retriggering.
2. A data stream of roughly 20% of all available data which is used to optimize the data selection chain up to the final analysis level. This data stream is written out after applying the *level 1* filter and comprises every fifth run.

The data set complementary to the 20 percent of the data which are used to develop the analysis is set aside and kept blinded until the analysis is finalized. Only then, it is processed and filtered using the the developed selection criteria. At the final selection level, the data set is unblinded and eventually used to derive the final analysis result.

### 6.1 Experimental and simulated data sets

The experimental and simulated data streams are further sub-divided into three separate streams. This is necessary, because three different detector configurations, in terms of properly functioning OMs, were defined for the year 2000 (see section 6.2.1). Each OM selection applies for a certain time period of the year [133] (Table 2). Each of the three periods roughly falls

<i>PERIOD I:</i>	Feb. 15 <sup>15</sup> – May 6 <sup>th</sup>
<i>PERIOD II:</i>	May 7 <sup>th</sup> – Sep. 2 <sup>nd</sup>
<i>PERIOD III:</i>	Sep. 3 <sup>rd</sup> – Nov. 4 <sup>th</sup>

**Table 2** – Starting and ending dates of the three OM selection periods for the year 2000 [133].

into one Antarctic season, *i.e.*, *PERIOD I* roughly covers the Antarctic autumn, *PERIOD II* covers the winter, and *PERIOD III* covers the spring. For the simulation, we use the appropriate atmospheric profiles (March, July, and October) to reproduce the respective event rates.

### 6.1.1 The 2000 data set

In 2000, the regular data taking period started on February 13<sup>th</sup> (day 44, starting with run 193), and ended on November 4<sup>th</sup> (day 309, ending with run 281). The total data taking time amounts to 248.3 days. The dead time varies slightly with time (periods with higher trigger rates also have a higher dead time fraction). For this analysis the total the livetime was calculated on a run-by-run basis.<sup>28</sup> On average, 17% of the exposure time is lost due to dead time of the DAQ system. From the resulting 202 days of effective livetime, about 7 days livetime equivalent is rejected because of insufficient data quality.

Within the standard data selection strategy [133, 156], individual files are rejected if more than 50 OMs show an abnormally high noise rate.<sup>29</sup> In addition, extremely short runs are excluded. A run usually lasts 24 hours. An early termination indicates hardware or DAQ problems. Therefore, we exclude runs which comprise less than 5 files ( $\sim 50$  minutes livetime equivalent) from the analysis.

In addition, we perform a file cleaning based on nine *flare-indicators* (described in section 4.8.2 and appendix B). Each flare indicator is a positive number, which is a measure the probability of an event to be due to electronic noise. Specifically, in a sample of  $N$  events, one expects less than one event with an indicator value

$$I \gtrsim \log N + 1 \quad (35)$$

in any of the nine indicators. As this analysis concerns  $\mathcal{O}(10^9)$  events, we consider each event with any indicator value greater than 10 as a *flare event*. Flare events preferentially occur over distinct time periods. Figure 6.2 shows an example of one run in which the flare rate is enhanced over a time span of three hours. Such time periods were excluded from this analysis on a file-by-file basis (see also appendix B.2). A list of rejected files is given in Table 3. Altogether, about 40 hours of effective livetime were excluded because of enhanced flare rates.

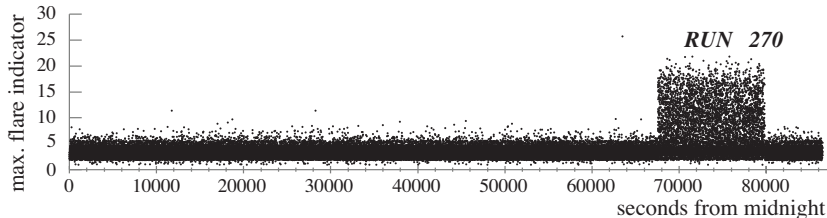


**Figure 6.2** – Time dependence of the maximum value of the nine flare indicators assigned to events in run 270. The run has an enhanced flare rate over  $\sim 3$  hours. Time is measured in seconds from midnight.

After rejection of periods of insufficient data quality and correction for dead time, a total of 194 days of effective livetime remains for analysis.

<sup>28</sup>The *Live and Dead-time Analysis* web interface [155], allows to calculate live and dead time for arbitrary data taking periods between 1999 and today.

<sup>29</sup>Total outage of individual OMs is less critical. Dead OMs can be excluded from data analysis during offline filtering in both Monte Carlo and experimental data streams. After identification and exclusion of such OMs, the multiplicity trigger condition is re-applied as offline software trigger (see section 6.2.3).

run	day	files	seconds	duration [s]	dead time fraction [%]	livetime [s]
270	115	110-129	67329-79805	12476	16.806	1037.9
271	116	all	entirely rejected	86313.9	17.155	71506.8
272	117	all	entirely rejected	86313.9	17.242	71431.6
305	127	48-51	50618-52755	2137	17.63	1760.2
<b>total</b>						145736.5

**Table 3** – List of files that were rejected because of a high fraction of flare events.

### 6.1.2 Blindness

The AMANDA detector has been built to discover phenomena that have been postulated but not observed so far. In order to prevent physicists from biasing their analyses, *i.e.*, adjusting analyses to an anticipated outcome, the AMANDA collaboration has agreed on a *blind* analysis procedure [157], in which any experimental data that enter the final physics result must either be altered or kept blind until the entire analysis chain is finalized. While a standard point source search uses the former approach (data are altered, in that the reconstructed particle directions are randomized), a diffuse search will keep the majority of the data fully blind and will, therefore, heavily rely on Monte Carlo simulations. In an ideal blind analysis, the entire analysis chain is developed without any reference to experimental data at all. The complete analysis is optimized on Monte Carlo simulations and then applied to experimental data without change. However, simulations often do not fully reproduce reality, and experimental data have to be used to some extent, in order to identify unsimulated backgrounds or determine normalization factors.<sup>30</sup>

For this analysis we use a “data prescaling” approach, in which the analysis is developed on the prescaled fraction of the data and then applied to the remainder. The pre-scaled data set in our case comprises roughly 20% of the data.

### 6.1.3 Simulated data sets

Using the techniques described in chapter 5, events are simulated with sufficiently high statistics. The statistical error of the final analysis is negligible compared to the systematic error.

#### Magnetic monopole events

For each of the four considered monopole speeds ( $\beta = 0.76$ ,  $\beta = 0.8$ ,  $\beta = 0.8$ , and  $\beta = 1.0$ ), a sample of  $2.5 \cdot 10^7$  tracks was generated as described in section 5.2.1. The detector simulation yields triggers for 12% to 7% of the generated tracks, dependent on velocity (see Table 4).

#### Atmospheric muon events

In order to establish sufficient background statistics, several data samples were generated for each of the three OM selection periods (defined in Table 2), using different importance sampling strategies:

<sup>30</sup>For this analysis for instance, the atmospheric muon background simulated with CORSIKA describe experimental data reasonably well up to a scaling factor, which is assessed by comparing event rates in simulated and experimental data. Analyses for which atmospheric neutrinos pose the dominant background, also determine the absolute normalization of the simulated background from experimental data, because the absolute flux of atmospheric neutrinos is theoretically uncertain.

$\beta$	#tracks	trigger efficiency
0.76	$2.5 \cdot 10^7$	$\sim 7\%$
0.8	$2.5 \cdot 10^7$	$\sim 9\%$
0.9	$2.5 \cdot 10^7$	$\sim 11\%$
1.0	$2.5 \cdot 10^7$	$\sim 12\%$

**Table 4** – Statistics of generated monopole events with various speeds  $\beta = v/c$ .

composition	sampling in energy	energy range [GeV]	atmosphere	#primaries	trigger efficiency
<i>poly-gonato</i>	<i>poly-gonato</i>	$800 - 10^{11}$	<i>March</i>	$3.88 \cdot 10^{10}$	$\sim 6 \cdot 10^{-5}$
<i>poly-gonato</i>	<i>poly-gonato</i>	$800 - 10^{11}$	<i>July</i>	$5.66 \cdot 10^{10}$	$\sim 5 \cdot 10^{-5}$
<i>poly-gonato</i>	<i>poly-gonato</i>	$800 - 10^{11}$	<i>October</i>	$3.07 \cdot 10^{10}$	$\sim 6 \cdot 10^{-5}$
<i>poly-gonato</i>	<i>poly-gonato</i> , $\Delta\gamma = 1$	$10^3 - 10^{11}$	<i>March</i>	$1.02 \cdot 10^9$	$\sim 0.3\%$
<i>poly-gonato</i>	<i>poly-gonato</i> , $\Delta\gamma = 1$	$10^3 - 10^{11}$	<i>July</i>	$1.48 \cdot 10^9$	$\sim 0.3\%$
<i>poly-gonato</i>	<i>poly-gonato</i> , $\Delta\gamma = 1$	$10^3 - 10^{11}$	<i>October</i>	$8.04 \cdot 10^8$	$\sim 0.3\%$
proton	$E^{-2}$	$10^4 - 10^{11}$	<i>October</i>	$7 \cdot 10^8$	$\sim 0.3\%$
iron	$E^{-2}$	$10^4 - 10^{11}$	<i>October</i>	$7 \cdot 10^8$	$\sim 0.3\%$

**Table 5** – Background samples generated with CORSIKA.

- For background studies up to *level 1* selection, we use a background sample generated without importance sampling, assuming a cosmic ray composition and energy spectrum according to the the *poly-gonato* model. This sample yields the best statistics of low energy atmospheric muons.
- For higher filtering levels, we use a background sample with a cosmic ray composition according to the *poly-gonato* model and oversampling in energy by  $\Delta\gamma = 1$  for the spectral slope of each element. This background sample describes the background of misreconstructed atmospheric muons, *i.e.*, those muons which were reconstructed as up-going, reasonably well up to the final analysis level. So, this sample is sufficient for the search for monopoles below the horizon.
- For the search for monopoles above the horizon, we use a background sample composed of iron and proton primaries sampled from an  $E^{-2}$  energy spectrum. This event sample is used only for the final analysis levels, when the lack of trans-iron primaries in the CORSIKA simulation of the *poly-gonato* spectrum becomes apparent.

The event statistics for all generated background samples is listed in Table 5, along with the fraction of generated events that yield a trigger in the detector simulation.

## 6.2 Retriggering

The purpose of the retriggering is to eliminate features from the experimental data set which are not reproducible with simulations. One such feature is transient OM behavior. The detector simulation assumes all OMs to be functioning steadily (except those that are known to be permanently damaged). In particular, the noise rates are assumed to be constant (section 5.1.3). In simulated events, individual OMs produce hits and contribute to the multiplicity trigger with constant probabilities. In reality however, the OM noise rates show a transient behavior. After sorting out abnormally noisy or *dead* OMs (*OM-cleaning*), and rejection of *hits* which are believed to originate from electronic noise (*hit-cleaning*), the multiplicity trigger condition is re-imposed.

### 6.2.1 Standard OM selection

Many OMs operate stably when data taking starts, and become unstable later in the year. In order to use as many OMs as possible, *i.e.*, maximize the detector that is effectively being used, the full data taking time is divided into three periods, and a list of unstably operating OMs is compiled for each of the periods.

At this early level of analysis, we use a standard OM selection criteria, which were established within an earlier data filtering effort [133]. The OM selection is based on the dark noise rates which are available from the monitoring data. OMs with noise rates higher than  $\sim 8$  kHz and lower than  $\sim 80$  Hz are excluded. Table 6 lists the number of OMs that were excluded over a certain period, along with identification numbers of the runs for which the specific selection was applied. A complete list of the identification numbers of excluded OMs can be found in [133].

	<i>PERIOD I</i>	<i>PERIOD II</i>	<i>PERIOD III</i>
run	193-281	282-474	475-584
day	44-125	126-244	245-309
# excl. OMs	136	147	169

**Table 6** – Number of OMs excluded during specific selection periods [133].

Apart from those OMs that were identified as unreliable, those OMs which are located outside the main detector volume are not used in the physics analysis. For many of them, calibration constants are not available, or they are located at shallow depths (as, for instance, OMs of string 17), where residual air bubbles cause too strong photon scattering. These excluded OMs are listed in Table 7.

OM Id	location
OM 81-86	bottom OMs of string 4
OM 307-310 and OM 337-344	bottom and top OMs of string 11
OM 345-352 and OM 379-386	bottom and top OMs of string 12
OM 387-394 and OM 421-428	bottom and top OMs of string 13
OM 555-596	string 17

**Table 7** – OMs that are permanently excluded from physics analysis.

The OM map in Figure 6.3 shows the location of the OMs excluded by the standard OM selection within the AMANDA-II array.

cable type	TOT-cut
Coaxial	> 150 ns
Twisted-Pair	> 75 ns
Fiber	> 5 ns

**Table 8** – Typical TOT cuts.

### 6.2.2 Hit cleaning for the retrigger

The hit-cleaning at this level consists only of TOT cleaning which rejects extremely narrow pulses (see section 4.8.1). A more sophisticated hit cleaning is applied at later analysis levels. The TOT cuts are set individually for each OM, but they do not vary much within a certain class of OMs. Typical cut values are listed in Table 8. Apart from extremely narrow pulses, pulses with unreasonably large TOTs are rejected. The upper bound on the TOT is 2000 ns for all OM types.

### 6.2.3 Re-imposing the multiplicity trigger

After applying the OM- and hit-cleaning as described above, a multiplicity trigger condition is re-imposed by requiring at least 24 OMs to be hit within

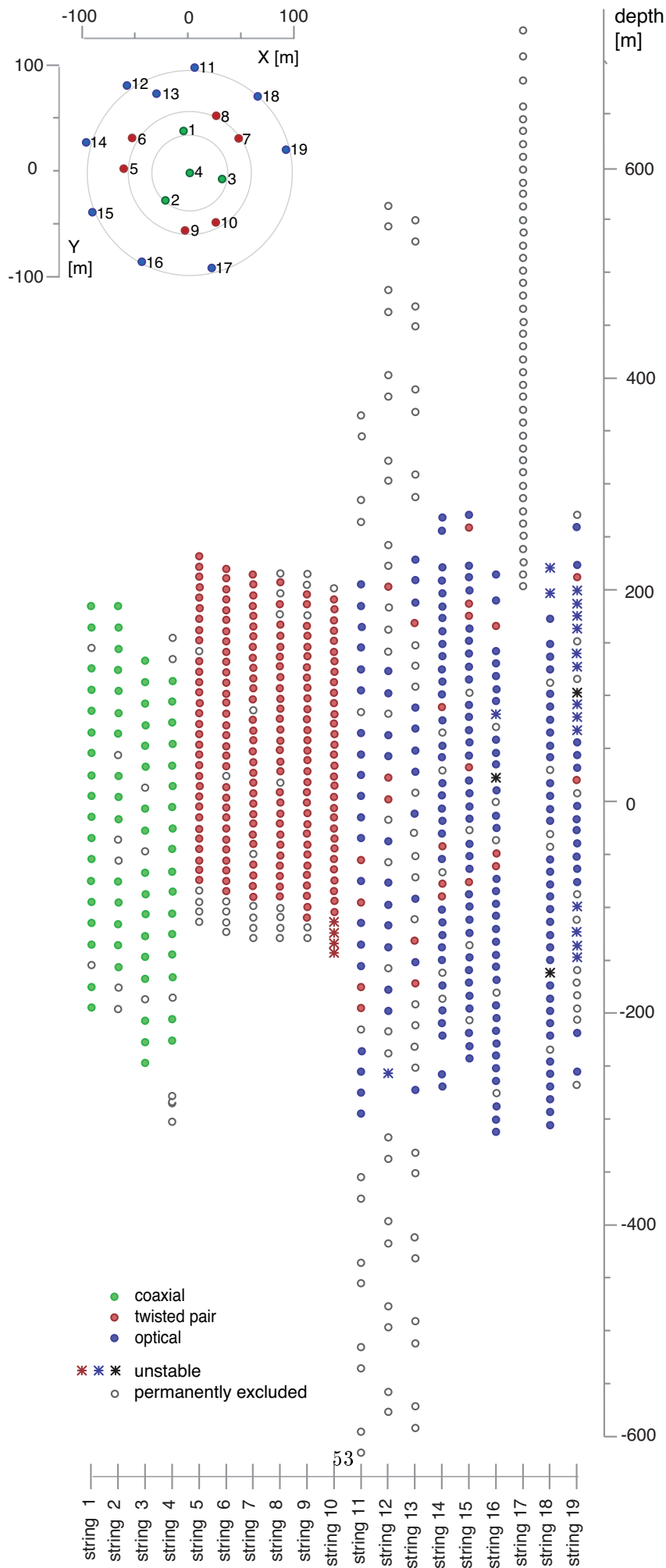


**Figure 6.3** – Map of the OM positions within the AMANDA-II detector. (The depth is relative to the detector center (1730 m below the surface). Locations of OMs that are permanently excluded from physics analyses (either due to irrecoverable damage or because they are located outside the main detection volume) are marked with open circles. OMs that are rejected only for a limited time period during the year 2000 are marked as asterisks.

Locations of first generation OMs, read out via coaxial cables, are marked in green. Those OMs were deployed with strings 1-4 in innermost part of the detector. These strings each contain 20 OMs at a vertical spacing of 20 m. The central string (string 4) has six additional test modules at the bottom, which are not used in data analysis.

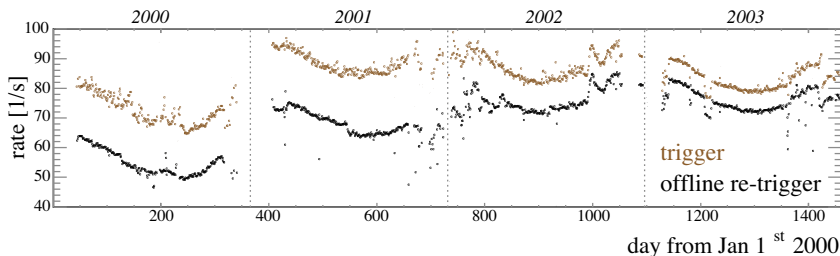
Locations of second generation OMs, read out via twisted pair cables, are marked in red. Most of these OMs are located at strings 5-10, which contain 36 OMs at 10 m intervals.

Locations of OMs with optical fiber transmission are marked in blue. These OMs were deployed with strings 11-19, which define the surface area of the detector. In case the optical fiber was damaged during deployment, the OMs are read out electrically via twisted pair cables (red). Due to hardware differences, these OMs behave differently from the twisted-pair OMs deployed in strings 5-10. The pulses at the surface are generally wider, with a TOT similar to those transmitted over coaxial cable.

Strings 11-13 contain 26 OMs spaced by 20 m in the central region of the detector (between -250 and 250 m). Additional OMs on these strings at deeper and shallower depths were deployed for exploring the ice properties outside the main detection volume and are not used in data analysis.

Strings 14-19 have 42 OMs spaced by 15 m. String 17 got stuck at shallower depth during deployment and is not used for the analysis.

**Figure 6.4** – Deadtime-corrected event rate from January 1<sup>st</sup> 2000 to December 31<sup>st</sup> 2003 before (brown) and after (black) retriggering.



a time window of  $2.5 \mu\text{s}$ . Figure 6.4 shows the effect of the offline retrigger. On average 77% of the experimental events pass the retrigger selection.

For simulated atmospheric muon events, the retrigger passing rate is a little higher, 83% on average. This is expected, because the hit-selection filters out unsimulated electronic noise hits. Monopole events are marginally affected by the retriggering, because the hit multiplicity is generally higher. About 98% of the monopole events pass the retriggering, independently of the monopole speed.

<i>PERIOD I</i>	1.31
<i>PERIOD II</i>	1.30
<i>PERIOD III</i>	1.27
average	1.30

**Table 9** – The ratio of experimental to simulated events at retrigger level.

A first sanity check of simulated and experimental data is a comparison of the observed event rates after imposing the retrigger. Table 9 lists the ratio between number of retriggered events in experimental data and simulated data. On average, this ratio is 1.3. The deficit in simulated atmospheric muon events is expected from the used hadronic interaction model (QGSJET01). The ratio remains approximately constant over the three pre-defined OM-selection periods, for which different atmospheric profiles were used for the air-shower simulation.

### 6.3 Analysis Level 1

The purpose of the *level 1* filter is the reduction of the data volume to a manageable size. A reduction to about 1% of the initial volume is achieved by placing two cuts on observables that are sensitive to the amount of light deposited during the event:

- **NHits**: the total number of pulses (hits) recorded. Each channel can record up to eight pulses and this number can substantially exceed the number of OMs in the detector.
- **FRAC 1**: the fraction of all hit OMs for which only a single hit was recorded (as opposed to those OMs for which multiple hits were recorded).

These two observables are key observables to this analysis. They are used repeatedly throughout the selection chain, with modifications of the hit- and OM selections applied before their calculation.<sup>31</sup> At this analysis level, we use hit cleaning criteria that were established for standard neutrino searches and have been used in a variety of analyses (see *e.g.* [93]). The OM selection applied is the same as used for the retriggering.

<sup>31</sup>Both hit and OM selection had to be refined at higher analysis levels, in order to ensure agreement between experimental and simulated data. At the final analysis levels in particular, satisfactory agreement was achieved only by using only those hits that were recorded for OMs with optical fiber readout.

observable	OM selection	Hit cleaning
<b>NHits</b> <b>FRAC 1</b>	standard	<i>TOT cleaning:</i> standard, see Table 8
		<i>RT-cleaning:</i> coincidence within $R \leq 100$ m $t \leq 500$ ns
		<i>Amplitude cut:</i> $ADC > 0.1$ photoelectrons
		<i>Time window:</i> $t > 14000$ ns

**Table 10** – OM selection and Hit cleaning used for the *level 1* cut parameters.

### 6.3.1 Hit cleaning for the *level 1* filter

The standard hit-selection criteria were introduced earlier in section 4.8.1. Apart from the TOT-cleaning that was already used for retriggering, we apply an amplitude cut, an isolation cut (*RT-cleaning*), and a cut on hit times which rejects early noise hits but includes hits from late photons and potential after pulses. Cross talk cleaning was not applied at this level, because cross talk constants (necessary for the cleaning based on the OM ADC-TOT characteristics, see section 5.1.4) for simulated data were not available at the time when the data were filtered.<sup>32</sup> The applied hit cleaning criteria are specified in Table 10. Figure 6.5 illustrates the effect of the various criteria on the hit set.

### 6.3.2 Cuts

The cut parameters **NHits** and **FRAC 1** are calculated using the cleaned hit sets. Figure 6.6 shows the distribution of both cut parameters for simulated signal and background, and for 1% of experimental events that passed the retriggering (*minimum-bias* data). The distributions are shown separately for each of the three OM selection periods. For each of the periods, simulated atmospheric muon events describe experimental data reasonably well. The histograms for simulated atmospheric muons are scaled to match the total number of events observed in experimental data (scaling factors are given in Table 9). Magnetic monopole events are arbitrarily normalized to a flux large enough for the distribution to be well visible against the muon background. The flux strengths for each of the monopole samples ( $\beta = 0.76$  to  $\beta = 1.0$ ) are assumed to be equal, meaning that the differences between the samples with respect to the integral of each histogram reflect differences in the trigger efficiencies.

Events with less than 140 hits or events in which more than 72% of all hit OMs have only a single hit are removed from the data stream.

Roughly 1% of experimental events pass these criteria. The passing rate for simulated atmospheric muons is slightly higher than for experimental events. After applying the cuts, the ratio of experimental events to simulated events is 1.22 on average, slightly lower than at retrigger level. The ratio remains approximately constant for the three OM selection periods (see Table 11). Between 75% and 81% of the monopole events pass *level 1* cuts, dependent on the monopole speed. The exact passing efficiency are given in Table 12 at the end of this chapter.

<sup>32</sup>Earlier filtering efforts of AMANDA-II had by mistake used identical cross talk constants for both experimental and simulated data. The error remained long undetected, because analyses using the filtered data were predominantly relying on directional information from track reconstruction algorithms. For these analyses, the influence of cross talk cleaning is weaker than for observables involving hit counting.

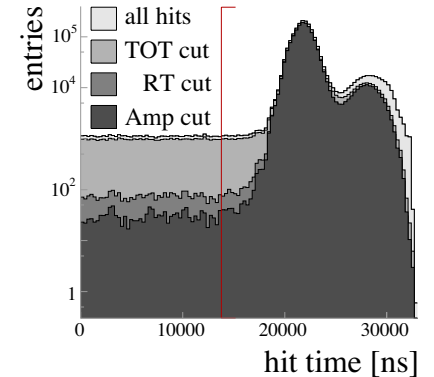


**Figure 6.5** – Timing distribution of hits passing the various hit cleaning criteria as defined in Table 10. The five superimposed histograms correspond to the distribution without hit cleaning (lightest gray), and to progressively tighter cleaning: TOT-, *RT*-, and Amplitude cleaning (darker grays). The effectiveness of individual criteria against random noise hits can be inferred from the amount of hits remaining in the first 14000 ns of the readout window. The time window cut is indicated by the red line.

cut # 1 and # 2

<b>NHits</b>	$\geq 140$
<b>FRAC 1</b>	$\leq 0.72$

<i>PERIOD I</i>	1.23
<i>PERIOD II</i>	1.23
<i>PERIOD III</i>	1.19
average	1.22

**Table 11** – Ratio between the number of experimental events and simulated atmospheric muon events after applying *level 1* cuts.

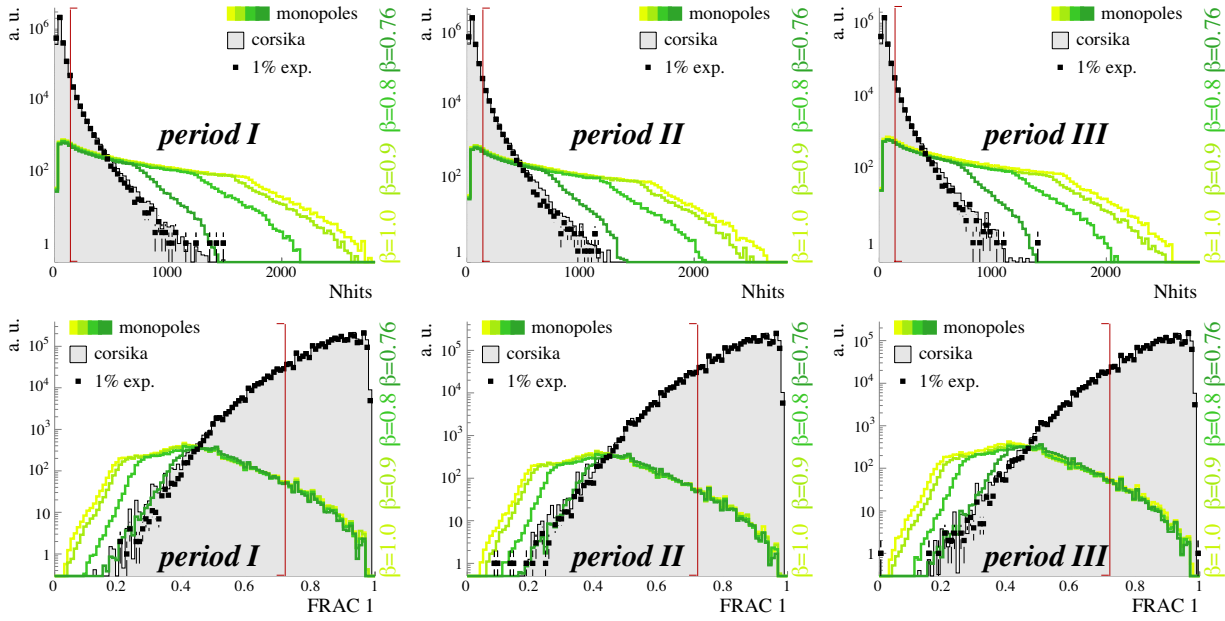


**Figure 6.6** – *Level 1* cut parameters  $N_{\text{Hits}}$  (top row) and  $\text{FRAC } 1$  (bottom row). Black markers indicate experimental data (*minimum-bias* stream), grey histograms are the simulated atmospheric muon background (CORSIKA), and green open histograms are simulated magnetic monopoles with speeds from  $\beta = 0.76$  (darkest green) to  $\beta = 1.0$  (lightest green). The agreement between experimental data and simulated atmospheric muons is equally good for all three periods. The two cuts (indicated by red lines) reduce the data set to  $\sim 1\%$  of the originally triggered events.

## 6.4 Conclusions

For the first two analysis levels (retrigger level and *level 1* filter), experimental data are well reproduced by simulated atmospheric muons. Both the overall event rate and distributions of key observables, such as  $N_{\text{Hits}}$ , show a good agreement. Specifically, seasonal variations of the event rate can be reproduced by using appropriate atmospheric profiles available in CORSIKA. Figure 6.7 shows the event rates in simulated and experimental data observed after applying *level 1* cuts. The  $\sim 20\%$  deficit in the absolute rate of simulated events is caused by the used hadronic interaction model QGSJET01 (see section (5.3.1)) and is expected.

The further data selection is described in detail in the following chapters and proceeds iteratively. For optimizing the higher level cuts, CORSIKA events are normalized to match the number of observed in the 20% experimental data set. The passing rates of the experimental and the simulated events are generally not exactly equal, and the normalization will be adjusted at each analysis level. Constancy of the normalization after applying progressively tighter cuts is an important check of the consistency of the analysis. Passing rates and normalization constants for the first two analysis levels are summarized in Table 12.

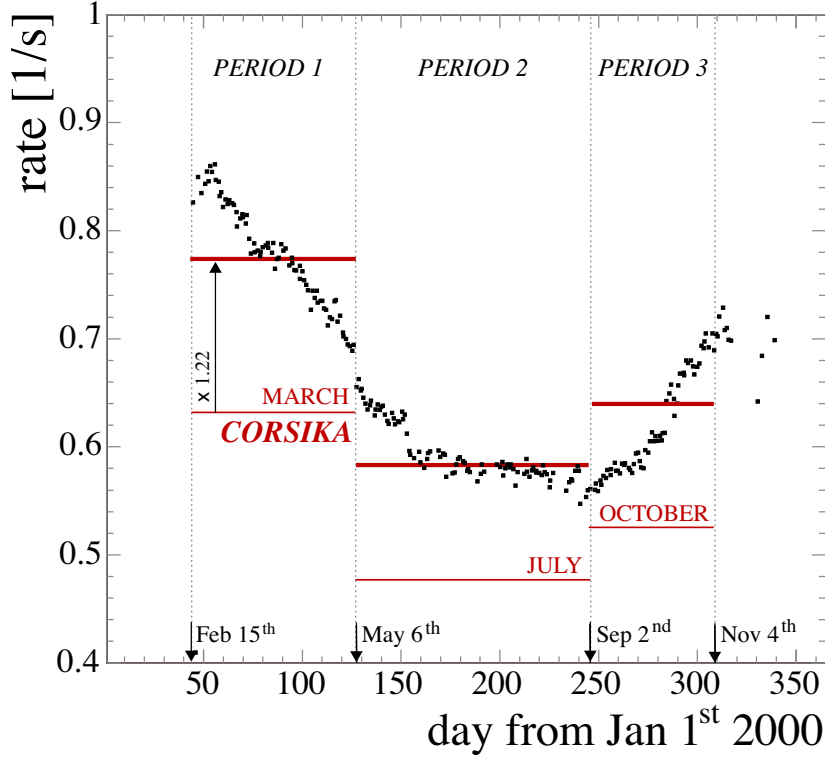


**Figure 6.7** – Daily rate of experimental events passing the *level 1* filter as defined in section 6.3 (black markers) compared to the rate of simulated atmospheric muon rate using various atmospheric models, resembling the South Pole atmosphere during March, July, and October, respectively (thin red lines). The overall seasonal variation in the event rate are reproduced well. The simulated background rate has to be scaled by a factor 1.22 (heavy red lines) in order to match the muon rate observed in experimental data. This scaling is expected for air-shower simulations using the QGSJET01 interaction model (see section 5.3.1).

level	fraction of passing events					normalization	
	monopoles				CORSIKA	experimental	
	$\beta = 1.0$	$\beta = 0.9$	$\beta = 0.8$	$\beta = 0.76$			
retrigger	98%	98%	98%	98%	83%	77%	1.3
<i>level 1</i>	81%	81%	80%	75%	1.4%	1.3%	1.2

**Table 12** – Fraction of events passing the retriggering and the *level 1* filter, and the scaling factor necessary to normalize the simulated event rate to the rate observed in experimental data.

## 7 Higher level data selection

Ultimately, this analysis aims at searching for both up- and down-going monopoles, and the final selection criteria will be optimized separately for particles entering from either above or below the horizon. After the selection criteria applied in the the next two analysis levels (*level 2* and *level 3*, described in this chapter) the data set will be split into two separate data streams, containing up- and down-going tracks respectively (*c.f.* Figure 7.1).

Because the Cherenkov emissions from relativistic magnetic monopoles are by several orders of magnitude more intense than that from relativistic muons, most of the observables used as cut parameters are a measure of the light yield. These observables are by nature mutually correlated. A Linear Discriminant Analysis is an efficient and robust tool to separate signal from background in the presence of such mutual correlation.

In addition to the light yield, we use the particle directions, which are obtained from track reconstructions, to suppress the background of down-going atmospheric muons. Track reconstructions are relatively CPU intensive and are, therefore, applied only after further data reduction. In the next processing level, the data are further reduced based on fast-to-compute measures of the light yield and the results of a fast *first guess* algorithm, the *linefit* (see section 7.1.3 below). A *likelihood reconstruction* (see section 7.1.2 below) is then applied to the reduced data set. While the *linefit* is an analytic method and hence completely deterministic, the likelihood reconstruction uses a numerical procedure to find the minimum of a rather complicated multi-dimensional likelihood function, which involves random processes. There is no guarantee that the obtained solution is in fact the “correct” one, *i.e.*, the *global* minimum of the function. Hence, it is desirable to apply the likelihood reconstruction repeatedly with altering (but predefined) seeds, and adopt the best solution as the ultimate reconstruction result. Iterating the reconstruction process several times obviously increases the required CPU time. So, an iterative likelihood reconstruction can only be applied on a relatively small data set.

This analysis is the first monopole search performed with a blindness condition. Many (usually small) discrepancies between the real detector and the idealized detector simulation become apparent for high energy events and at higher analysis levels. Presumably, most of the discrepancies are caused by hardware components suffering from additional electronic noise contributions during registration of extremely large Cherenkov signals. The higher analysis levels, therefore, not only involve the selection of events, but also the selection of detector components which still work reliably for large light depositions in the detector.

### 7.1 Processing and data selection strategy

Figure 7.1 shows a schematic sketch of the processing described in this chapter. Filter *level 2* involves the application of the *linefit*, and after further data reduction a likelihood reconstruction using a single iteration. Cuts that remove potential *flare* events (*c.f.* section 4.8.2) are applied at the the end of this level.

In filter *level 3*, an iterative reconstruction is applied. The obtained track direction serves to divide the events into up- and down-going particles,

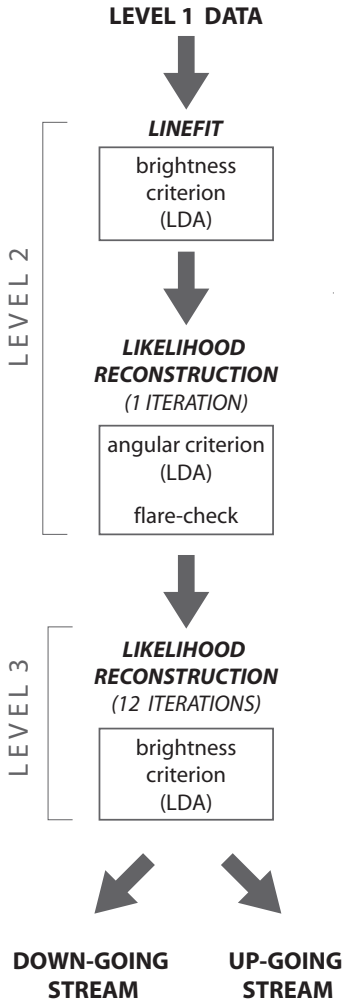


Figure 7.1 – Processing steps after level 1.

which are treated separately from there on (as described in the following chapters). Discrepancies between experimental and simulated data with respect to the reconstructed track direction and observables sensitive to the light yield require drastic tightening of the OM selection at this level. One further cut is imposed using on the light deposition in the detector, assessing the light yield using only those OMs whose response is reproduced most accurately by the simulation.

All cut parameters except the *flare indicators* are optimized using a linear discriminant analysis. The discriminant analysis, the likelihood reconstruction, and the *linefit* are described in the following sections.

### 7.1.1 Linear Discriminant Analysis

Linear Discriminant Analysis (LDA) is an analytical technique to classify objects into mutually exclusive and exhaustive groups based on a set of measurable features. In our case, the recorded events are to be classified as either signal (magnetic monopoles) or background (atmospheric muons). The linear discriminant analysis is a so-called *linear classifier*, providing a decision rule for classifying events based on a *linear discriminant function*

$$d(\vec{X}) = \vec{V} \cdot \vec{X}, \quad (36)$$

where  $\vec{X} = [x_1, x_2, \dots, x_n]$  is a vector containing  $n$  event features, and  $\vec{V} = [v_1, v_2, \dots, v_n]$  is a vector of optimized coefficients. That is, the discriminant function is simply a weighted sum of the  $n$  observables. Geometrically, the  $n$ -dimensional vector  $\vec{X}$  is projected onto the vector  $\vec{V}$ . One possible optimization of the coefficients  $\vec{V}$  is to maximize the *Fisher criterion* [158],

$$f = \frac{(\langle d_1 \rangle - \langle d_2 \rangle)^2}{\sigma_1^2 + \sigma_2^2}, \quad (37)$$

where  $\langle d_i \rangle$  and  $\sigma_i$  are the mean values and expected variances of the discriminant function for either signal or background (see Figure 7.2). The Fisher criterion measures the difference of the two means normalized by the averaged variance. The extremum of  $f$  can be found analytically [159], yielding the coefficient vector

$$\vec{V} = \left[ \frac{1}{2}\Sigma_1 + \frac{1}{2}\Sigma_2 \right]^{-1} \cdot (\vec{M}_1 - \vec{M}_2), \quad (38)$$

where  $\Sigma_i$  are the covariance matrices and  $\vec{M}_i$  are the class means in  $n$ -dimensional feature space. These quantities are assessed numerically using subsets (so-called *learning data*) of simulated signal and background events. The resulting discriminant function  $d(\vec{X})$  is called the Fisher discriminant. Figure 7.3 shows example distributions of the learning data used at *level 2* of this analysis in the two-dimensional space, spanned by the observables **NHits** and **NCH**.

The actual classification of the events is done by choosing a threshold value  $d_0$  above or below which the events are assigned to either of the two classes. A common choice of  $d_0$  is the one that minimizes the expected number of misclassified events, that is the sum of the number of signal events that are expected to be classified as background and the number

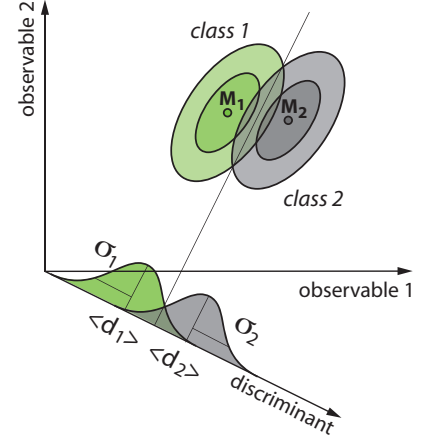


Figure 7.2 – The Fisher discriminant.

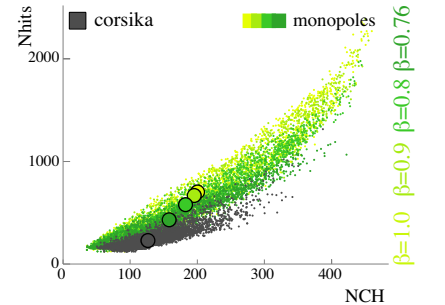


Figure 7.3 – Correlations of the observables **NHits** and **NCH**. Simulated atmospheric muon events (background) are represented by grey markers, simulated signal events are represented by green markers (darkest green for the slowest simulated monopole speed,  $\beta = 0.76$ , lightest green for the fastest simulated speed,  $\beta = 1.0$ ). The five large round markers indicate the respective class means ( $\vec{M}_i$ ) in feature space.

of background events that are expected to be classified as signal. This number is minimal where the signal and background distributions of  $d(\vec{X})$  intersect [159]. The expected number of misclassified events, then, is just the overlap of the two distributions (*c.f.* Figure 7.2). The overlap, however, depends on normalization of the two distributions. *I.e.*, strictly speaking, we need to know the *a priori* probability for an event to be signal or background in order to minimize the probability of misclassification. In this analysis, the abundance of magnetic monopoles would determine the *a priori* probability of an event to be signal. Since the monopole flux is unknown (barring the fact that it must be extremely small), the choice of  $d_0$  is somewhat arbitrary. Throughout this analysis, the motivation to choose one particular  $d_0$  varies with the analysis level. At lower levels,  $d_0$  is typically chosen such that the maximum possible amount of signal is retained.

Theoretically, the Fisher discriminant yields optimum separation between two classes with normally distributed observables and equal covariance matrices [159]. This is not strictly the case for this analysis (*c.f.* Figure 7.3), meaning that a better separation might be achieved with more sophisticated pattern recognition techniques.<sup>33</sup> However, for an analysis in which data are rather poorly understood, the simplicity, transparency and robustness of a linear classifier compensate for potential losses in performance.

### 7.1.2 The Likelihood Reconstruction

Besides the light yield, the direction of particles entering the detector's sensitive volume is an important observable. The particle is reconstructed from the arrival times of the Cherenkov photons at the OMs using a likelihood method [160]. If we consider a certain detector response  $R = \{r_i\}$  of an event, where  $r_i$  consists of the timing and position information of the  $i$ th hit of the event, we can calculate the individual likelihoods  $\hat{p}_i(r_i|H)$  of each hit to occur with respect to a certain track hypothesis  $H$ . If we assume that the particle travels in a straight line, and neither starts nor stops inside the detection volume, the initial track hypothesis is an infinitely long straight line, which in three dimensional space has five degrees of freedom. They can be chosen as three spatial coordinates  $(x, y, z)$ , defining the position of the muon at some arbitrary time, and two angles  $(\Theta, \Phi)$  defining its direction. In order to reconstruct the track, the five track parameters are varied until the best-fit track hypothesis  $H(x, y, z, \Theta, \Phi)$  is found. The best-fit hypothesis is that which maximizes the likelihood  $L(R|H)$ , or equivalently, its logarithm

$$\log[\mathcal{L}(R|H)] = \log \left( \prod_{i=1}^{N_{\text{hits}}} \hat{p}_i \right) = \sum_{i=1}^{N_{\text{hits}}} \log(\hat{p}_i) \stackrel{!}{=} \text{max} . \quad (39)$$

The individual hit probabilities  $\hat{p}_i$  are approximated with an analytic function, the *Pandel* function [161]. The Pandel function gives the probability for a Cherenkov photon to arrive with a certain time delay  $t$  relative to the *Cherenkov time* at an OM located at a certain perpendicular distance  $\rho$  from the track. Particles are assumed to travel at the speed of light, pho-

<sup>33</sup>The separating boundary defined by a linear classifier is a hyper-plane in  $n$ -dimensional feature space. More complex (*i.e.*, bent) hyper-surfaces obtained from higher order classifiers can yield a better separation, if the events are distributed in a more complex way (*i.e.*, if the distributions deviate significantly from normal distributions).

tons are assumed to be emitted at the respective Cherenkov angle. Figure 7.4 shows the time delay probabilities calculated with the Pandel function at a fixed distance of  $\rho = 20$  m. At such short distances, the Pandel function has a sharp maximum at  $t = 0$ , corresponding to unscattered photons arriving at the OM. In a real detector however, the hit times are smeared with the PMT transit-time jitter. When calculating the hit probabilities, the jitter is accounted for by a convolution of the Pandel function with a Gaussian of width 7 ns [162].

With increasing distance  $\rho$ , the Pandel function becomes increasingly flat, and the maximum position shifts towards larger time delays, as it becomes increasingly unlikely that photons arrive at the OM without being delayed by scattering. Figure 7.5 displays the hit probabilities as a function of both time delay and distance from the track. Two slices with constant distance  $\rho$  are highlighted as white lines in order to illustrate the change in shape.

The maximum of the likelihood is found by *minimizing* the *negative* log-likelihood function (equation (39)). This enables us to use standard “minimizer” packages that implement numerical minimizing algorithms. By default, the AMANDA software uses the Simplex algorithm (see for instance [163]) available from the TMinuit-package [164]. Numerical minimization algorithms have the best chance to find the global minimum of the overall negative likelihood if most of the contributing individual hit likelihood functions  $\hat{p}_i$  have sharp extrema. That means, the track reconstruction will be most accurate for events containing mostly hits from unscattered photons. The least scattered photons are those which arrive at an OM first. Therefore, only the first hits recorded in each channel are passed to the likelihood reconstruction. The reconstruction of extremely bright events is usually less accurate, because most of the hit OMs are located at large distances from the track. Even first photons are multiply scattered, and the maxima of the corresponding time delay distributions are less pronounced (*c.f.* Figure 7.5).

Another factor that influences the reconstruction accuracy is the the initial hypothesis from which the minimizer starts to scan the likelihood space for its global minimum. If the initial hypothesis is not in the vicinity of the global minimum, the minimization algorithm might converge only to a local minimum. The initial hypothesis passed to the likelihood reconstruction is determined with so called *first guess* algorithms which calculate the approximate track parameters with an analytic method (see below). Since these algorithms do not account for light propagation in the ice, the obtained track parameters might be very inaccurate. This is especially true for very bright events in which photons propagate over large distances before actually being detected. In case of a weak *first-guess*, the accuracy of the likelihood reconstruction can be improved by repeating the minimization process several times using alternative start hypotheses. These hypotheses can either be results of various first guess algorithms, or even random track parameters. The latter approach is used in this analysis. In order to have fully reproducible results, subsequent minimizations are seeded with *pseudo-random* track parameters, which are obtained from the preceding reconstruction result using a Sobol sequence (see for instance [163]). The initial start hypothesis is obtained from the so-called *linefit*.

### 7.1.3 The Linefit

A very fast and relatively simple *first-guess* algorithm is the *linefit* [166]. It uses a very simple description of the track, completely independent of

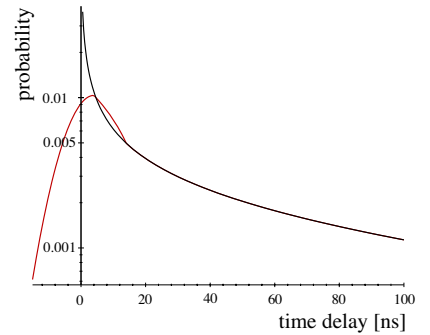


**Figure 7.4** – Time delay distribution for Cherenkov photons arriving at an OM located at 20 m distance from the particle track according to the Pandel function (black line). The Pandel function is convoluted with a Gaussian to account for the jitter in the PMT transit time (red line). From [128].

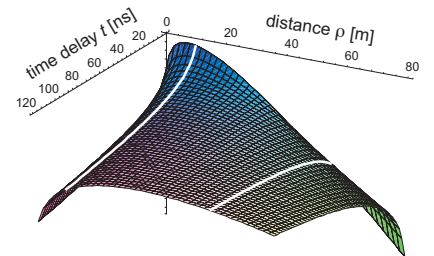


**Figure 7.5** – Pandel function dependent on time delay  $t$  and distance  $\rho$ . Two slices at constant  $\rho$  are highlighted in white, in order visualize the change of the shape of the time delay distribution with distance. From [165].

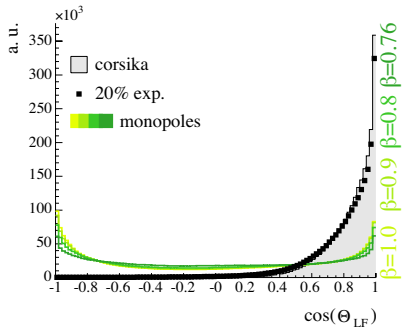


**Figure 7.6** – Cosine of the zenith angle obtained from the weighted *linefit*. The AMANDA coordinate system is defined such that a zenith angle of  $0^\circ$  corresponds to a vertically down-going track.

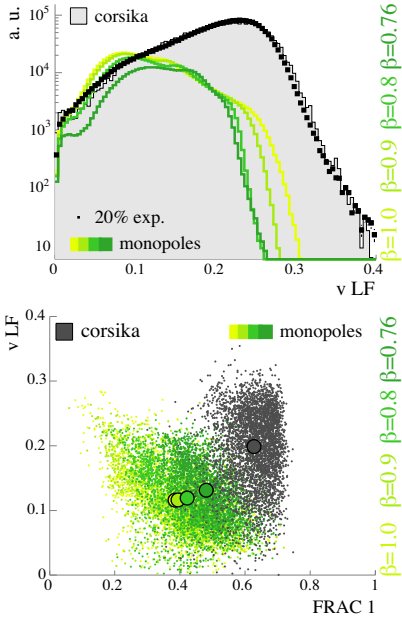


**Figure 7.7** – The velocity of the weighted *linefit*  $v_{LF}$  (upper panel) and its correlation to **FRAC 1** (the fraction of hit OMs with a single pulse), which is a measure of the light intensity radiated from a track (lower panel).

light propagation and optical module response. It assumes light to travel along a straight line with an arbitrary but constant velocity  $\vec{v}$ . The spatial positions  $\vec{r}_i$  and  $t_i$  at which photons are detected can then be described by a linear relation as

$$\vec{r}_i = \vec{r}_0 + \vec{v}(t_i - t_0), \quad (40)$$

Minimizing  $\chi^2 = \sum_i (\vec{r}_i - \vec{r}_0 - \vec{v} \cdot t_i)^2$  gives the solution

$$\vec{v} = \frac{\langle \vec{r}_i t_i \rangle - \langle \vec{r}_i \rangle \langle t_i \rangle}{\langle t_i^2 \rangle - \langle t_i \rangle^2}, \quad \vec{r}_0 = \langle \vec{r}_i \rangle - \vec{v} \langle t_i \rangle, \quad (41)$$

where angle brackets indicate averaging over  $i$  hits. This solution gives an approximate direction as well as a vertex location and a “velocity”  $\vec{v}$ .<sup>34</sup> As for the likelihood reconstruction, it is important to use the times  $t_i$  of the first hits in each OM.

The pointing accuracy of the *linefit* can be improved by weighting the individual hits with the amount of light at the particular OM. The actual number of photoelectrons ( $N_{PE}$ ) registered by an OM cannot be reconstructed from the data (*c.f.* section 4.4, Figure 4.12). The most reasonable estimate for  $N_{PE}$  is to assume that the measured peak amplitude (ADC) is produced by the first hit, and that all subsequent hits are due to single photoelectrons:

$$N_{PE} \approx \text{ADC} + n_{\text{hits}}^{OM} - 1, \quad (42)$$

where  $n_{\text{hits}}^{OM}$  is the total number of hits seen by the OM. A weighting with the square of the estimated number of photoelectrons,  $N_{PE}^2$ , results in an angular resolution (defined as the median of space angle between the the directions of the true and the reconstructed particle direction) of  $\sim 8^\circ$  for atmospheric muons, and  $20^\circ$  to  $35^\circ$  for relativistic monopoles, dependent on velocity. This is substantially better than the angular resolution achieved without weighting ( $\sim 15^\circ$  for atmospheric muons, and  $35^\circ$  to  $60^\circ$  for monopoles [167]) and than the angular resolution achieved with other first guess methods.<sup>35</sup>

Figure 7.6 shows the cosine of the zenith angle ( $\cos \theta_{LF}$ ) obtained from the weighted *linefit* for 20% of the experimental data set and simulated atmospheric muon and monopole events after applying *level 1* selection criteria. A zenith angle of  $0^\circ$  ( $\cos \theta_{LF} = 1$ ) corresponds to a vertically down-going direction. Most of the atmospheric muon events are reconstructed as down-going tracks ( $\cos \theta_{LF} > 0$ ). Experimental and simulated data show reasonable agreement.

Apart from the particle direction, we use the magnitude of the “velocity” parameter ( $\vec{v}$  in equation (40)) as a cut parameter, because it relates to the light intensity radiated from a particle: bright events have more hits at large distances from the track, which, projected on straight line, result in slower velocity. Figure 7.7 shows the velocity of the *linefit* (weighted with  $N_{PE}^2$ , see equation (42)) and its correlation to **FRAC 1** (the fraction of OMs with only a single hit).

<sup>34</sup>The velocity of the *linefit* cannot be considered as a reconstructed particle velocity, since it does not account for photon propagation in the ice.

<sup>35</sup>The weighted *linefit* was superior to other first guess algorithms (the *Dipolefit*, *Direct Walk*, and *JAMS*) [160] that are available in the *Sieglinde* package.

## 7.2 Analysis Level 2

The next filtering level consists of two additional cuts. The first cut is based on the amount of light deposited in the detector. The cut parameter is the Fisher discriminant composed of five fast-to-compute observables:

- **NHits**, as used in *level 1*,
- **FRAC 1**, as used in *level 1*,
- **FRAC 1<sub>optical</sub>**: The fraction of hit *optically read-out* OMs with only a single hit,
- **NCH**: the number of channels (OMs) which have recorded at least one pulse, and
- **vLF**: the velocity of the weighted *linefit*.

After imposing the cut on the Fisher discriminant, the remaining events are reconstructed with a likelihood reconstruction. A second cut is imposed, which exploits the reconstructed track directions. The cut parameter is a Fisher discriminant composed of

- **FRAC 1** (as above), and
- $\cos\Theta$ : The reconstructed zenith angle of the single iteration likelihood reconstruction.

The OM selection in this level is identical to the one used in *level 1*, except for **FRAC 1<sub>optical</sub>**, which uses only the sub-set of optically read-out channels.

### 7.2.1 Hit cleaning

Track reconstructions require an enforced hit-cleaning in order to select only the least scattered photons. In order to reject noise hits more efficiently, the *level 1* hit cleaning is refined (Table 13 summarizes the hit cleaning criteria applied at this level):

**Time window cleaning:** The time window is narrowed to use only hits which are recorded after 17000 ns. As demonstrated in Figure 7.8, even monopoles as slow as  $\beta = 0.76$  (the slowest and least bright monopoles considered) produce hits only in this time interval.<sup>36</sup>

For the likelihood reconstruction and the *linefit*, we use only hits around the trigger time between 17000 and 25000 nanoseconds. For the other observables, we include also late hits up to the end of the TDC recording window.

<sup>36</sup>The looser time selection used in *level 1* ( $t_{\text{hit}} > 14000$  ns) was chosen in order to sustain the possibility to use the same pre-filtered data-set also to search for monopoles with speeds below the Cherenkov threshold. Because of their lower speed, and due to the fact that these monopoles would be only moderately bright, the Cherenkov signature of these monopoles would probably contain early hits which occur substantially before the multiplicity trigger is fulfilled.

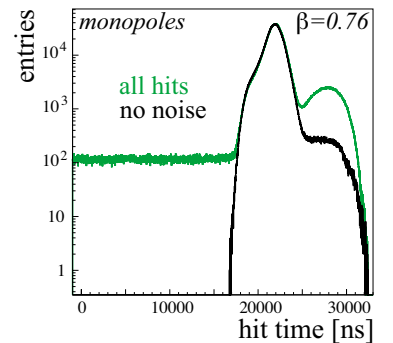


**Figure 7.8** – Time distribution of hits from simulated  $\beta = 0.76$  monopoles including noise and after-pulsing (green histogram) and hits from Cherenkov photons only (black histogram).

observable	OM selection	Hit cleaning
NHits FRAC 1 NCH	standard, as <i>level 1</i>	<i>TOT cleaning:</i> as <i>level 1</i> <i>RT-cleaning:</i> as <i>level 1</i> <i>Amplitude cut:</i> as <i>level 1</i> <i>Time window:</i> >17000 ns <i>cross talk cleaning:</i> map, ADC-TOT
FRAC 1 <sub>optical</sub>	only optically read out OMs	
vLF cos $\Theta$	standard, as <i>level 1</i>	<i>TOT, RT, Amplitude:</i> as <i>level 1</i> <i>cross-talk cleaning:</i> <i>Time window:</i> [17000:25000] ns <i>reject hits in overflowed OMs</i> <i>reject hits with missing leading edges</i> <i>use only first hit in each OM</i>

**Table 13** – OM selection and Hit cleaning used for the *level 2* cut parameters.

**Cross-talk cleaning:** For the OMs on strings 5-10, two criteria are applied in order to reject potential cross talk hits:

1. Hit cleaning based on the “cross-talk map”: A hit occurring in an OM identified as cross-talk *receiver* is removed, if the leading edge of the hit was recorded at the surface in coincidence with a leading edge of a pulse from a corresponding *talker* OM and if the amplitude of the pulse in the *talker* OM exceeded a certain threshold. The coincidence time windows and amplitude thresholds are specific to individual *talker-receiver* pairs. Appropriate values are determined from calibration data [135, 122].
2. ADC-TOT cleaning: The cut in the ADC-TOT plane (*c.f.* section 4.8.1) is placed conservatively, such that separating boundary defining the actual cut is shifted by -25 ns and 25 mV relative to the boundary obtained from the actual fit (see Figure 7.9). The standard ADC-TOT cleaning procedure used for most AMANDA-II analyses removes *all* hits that lie outside the photon region of the ADC-TOT plane (see section 4.8.1). This usually results in a removal of subsequent hits in case an OM has recorded a series of multiple hits: Late hits are likely to be due to single photoelectrons, and have smaller TOTs and smaller amplitudes than the first pulse. With their smaller TOTs, these hits fall outside the photon region of the ADC-TOT plane, because the cleaning algorithm assigns the *peak*-ADC to all hits in an OM. In order to preserve subsequent hits, we use a modified cross talk cleaning for this analysis, which removes only first hits in each OM. Subsequent hits are generally kept.

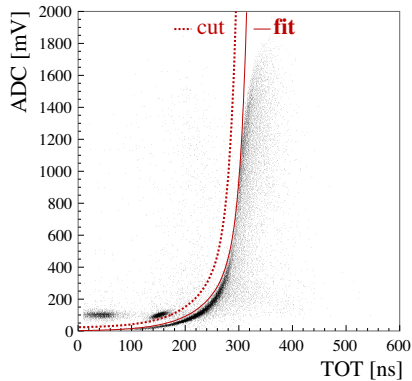


**Figure 7.9** – The cross talk cleaning cut in the ADC plane.

**Rejection of hits in overflowed OMs:** For the likelihood reconstruction, it is essential that the used hit times correspond to the arrival time of the first photon at an OM. Therefore, we reject hits overflowed channels (*i.e.*, channels which received more than the maximum 16 edges) if the respective channel is connected to a CAMAC TDC (see section 4.4.2).<sup>37</sup>

<sup>37</sup>For the channels which are connected to a VME TDC, the rejection of hits in overflowed channels is unnecessary, since early hits are not discarded in favor of later ones.

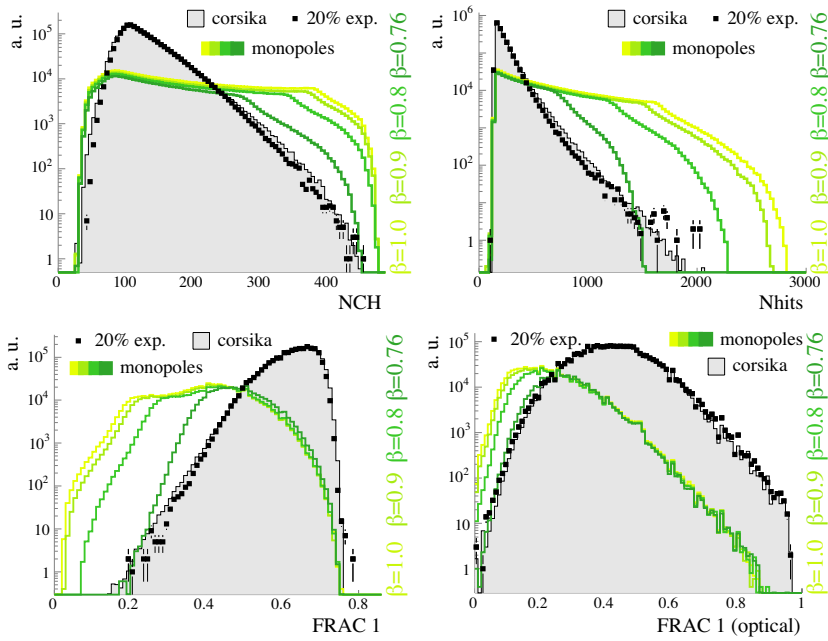


**Figure 7.10** – Four of the five observables that serve as an input for the *level2* discriminant analysis. Green open histograms are the distributions for simulated monopoles, grey histograms for simulated muon background, and black markers represent the 20% experimental data set. The fifth input observable, the velocity of the *linefit* ( $v_{LF}$ ), is shown in Figure 7.7.

For the calculation of observables which are sensitive to the light yield, hits in overflowed channels are included, because the overflow indicates the registration of many photons.

**Rejection of hits without leading edges:** Unpaired edges sometimes occur in a recorded edge series due to digitization errors. Both cases, missing leading and missing trailing edges are observed. In case of a missing leading edge, the *Sieglinde* calibration module inserts the trailing edge time of the preceding hit for the missing leading edge, in case of a missing trailing edge it inserts a trailing edge at the time of the following leading edge.<sup>38</sup>

Hits whose leading edges were “assigned” by the calibration module are excluded from the likelihood reconstruction. For the calculation of observables sensitive to the light yield, those hits are included.

## 7.2.2 Brightness criterion

The observables **NCH**, **NHits**, **FRAC 1**, and **FRAC 1<sub>optical</sub>** are shown in Figure 7.10 for simulated signal and background and 20% experimental data. The fifth observable entering the Fisher discriminant, **vLF**, is shown in Figure 7.7. All observables show a good agreement between experimental data and simulated data. Using the observables as a one-dimensional cut parameters would result in a great loss of signal events.

In order to calculate the Fisher discriminant, covariance matrices of signal and background samples  $\Sigma_1$  and  $\Sigma_2$  as well as the sample means  $\vec{M}_1$  and  $\vec{M}_2$  are determined numerically, using subsets of 1000 events from the *CORSIKA* simulation and 1000 events from the  $\beta = 0.76$  monopole sample. We use the slowest and least bright monopoles ( $\beta = 0.76$ ) for optimization, since these are most difficult to separate from background, and at this early analysis level, we want to preserve as much signal as possible.

<sup>38</sup>If the edge series starts with a trailing edge (*i.e.*, no preceding trailing edge is available) 0 ns is inserted for the missing leading edge, if the series ends with leading edge, a trailing edge is inserted at the end of the TDC buffer.

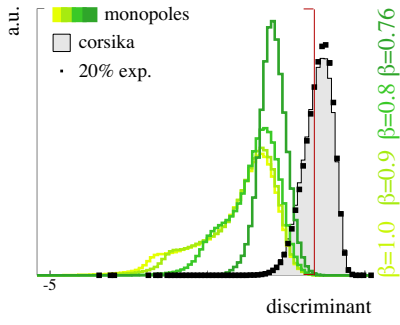


**Figure 7.11** – Fisher discriminant calculated from five input observables (*c.f.* equation (43)). All histograms are normalized to contain the same number of events. The red line indicates where the cut is placed.

The vector of coefficients for each of the input variables,  $\vec{V}$ , is calculated according to equation (38). The resulting Fisher discriminant (*c.f.* equation (36)) is

$$d = \begin{pmatrix} 5.697 \\ 4.008 \\ -0.727 \\ 0.008 \\ -0.004 \end{pmatrix} \cdot \begin{pmatrix} \mathbf{vLF} \\ \mathbf{FRAC\ 1} \\ \mathbf{FRAC\ 1_{optical}} \\ \mathbf{NCH} \\ \mathbf{NHits} \end{pmatrix} \quad (43)$$

Figure 7.11 shows the distributions of the discriminant for simulated signal and background, and for 20% experimental data. The Fisher discriminant yields a much better separation of signal and background than any potential one-dimensional cut-parameter. The cut is placed at  $d_0 = 3.4$  such that essentially all of the simulated signal (> 99%) is kept. About 60% of the background is rejected.

The reason for placing the cut so loosely is that at this level, up- and down-going particles are treated equally. After this cut, the events will be reconstructed with the likelihood reconstruction, which allows to identify atmospheric muon events more efficiently: The bulk of the atmospheric muon background events will be reconstructed (correctly) as down-going, and can be rejected with an angular criterion. Of those background events that are misreconstructed as up-going, many will have low hit multiplicities. These events can be rejected with a much looser cut on the light yield than that required for the down-going tracks.

*cut #3*

---


$$\begin{pmatrix} 5.697 \\ 4.008 \\ -0.727 \\ 0.008 \\ -0.004 \end{pmatrix} \cdot \begin{pmatrix} \mathbf{vLF} \\ \mathbf{FRAC\ 1} \\ \mathbf{FRAC\ 1_{optical}} \\ \mathbf{NCH} \\ \mathbf{NHits} \end{pmatrix} < 3.4$$


---

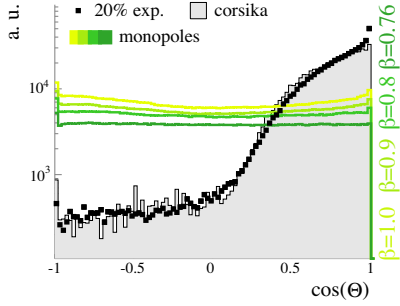


**Figure 7.12** – Cosine of reconstructed zenith angle.

### 7.2.3 Angular criterion

The events passing *cut #3* are reconstructed with the likelihood reconstruction, using only one single iteration. The direction obtained from the weighted *linefit* serves as initial track hypothesis.

Figure 7.12 shows the cosine of the track zenith angle ( $\cos \Theta$ ) obtained from the reconstruction. A zenith angle of  $0^\circ$  ( $\cos \Theta = 1$ ) corresponds to a vertically down-going direction. Most of the atmospheric muon events (>96%) are reconstructed as down-going ( $\cos \Theta > 0$ ). The fraction of events that are misreconstructed as up-going is reproduced by the simulation. A large fraction of these events will be identified as down-going by an iterative likelihood reconstruction, that will be applied after further data reduction.

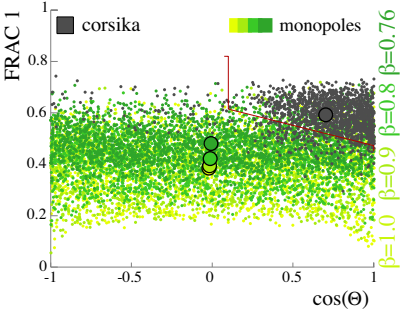


**Figure 7.13** – Correlation of the reconstructed zenith angle and **FRAC 1**. The red line indicates the two-dimensional cut.

We reject the bulk of low-energy atmospheric muons using a cut on **FRAC 1** which depends on the reconstructed zenith angle. Atmospheric muons lose a large fraction of their energy when traversing the ice overburden above the detector. The amount of Cherenkov light that atmospheric muons can deposit in the detector is correlated with the amount of matter traversed upon reaching the detector, and hence with the zenith angle of the incoming muons (more inclined muons have a longer path through the ice, and will have lost more of their initial energy when they reach the detector). Figure 7.13 shows the correlation between **FRAC 1** (sensitive to the light yield) and the cosine of the zenith angle obtained from the single-iteration reconstruction. Nearly vertical muons are capable of depositing more light (yielding a lower value of **FRAC 1**) than muons with directions close to the horizon. The two-dimensional cut that was placed using both observables is indicated as a red line in Figure 7.13.

The cut was found with a discriminant analysis of the two input observables ( $\cos\Theta$  and **FRAC1**). It is optimized using sub sets of the simulated atmospheric muon background and the simulated magnetic monopoles with  $\beta = 0.76$ . The learning data samples each comprised 1000 events which were reconstructed with zenith angles smaller than  $\sim 84^\circ$  ( $\cos\Theta > 0.1$ ). The optimization yields the discriminant function:

$$d = \begin{pmatrix} 1.07 \\ 6.03 \end{pmatrix} \cdot \begin{pmatrix} \cos\Theta \\ \mathbf{FRAC1} \end{pmatrix}. \quad (44)$$

Figure 7.14 shows the distributions of the Fisher discriminant for simulated signal and background and experimental events in the angular region  $\cos\Theta > 0.1$ . The event samples are normalized such that they contain equal numbers of events. The cut is placed at  $d_0 = 4.3$ , where the background and signal distributions intersect. If the number of expected signal and background events were in fact equal, this cut position would correspond to the minimum expected number of misclassified events. Since the number of expected monopole events is certainly smaller than the number of atmospheric muon events, this choice of the cut position is somewhat arbitrary.

*Cut # 4* is applied only in the angular region ( $\cos\Theta > 0.1$ ). In this region, 12.1% of the simulated atmospheric muon events pass. The passing rate in experimental data is only slightly higher (12.5%). The fraction of passing monopole events is between 81% and 91%, depending on the monopole speed.

The average ratio of the three OM selection periods is 1.34. Although *cut # 4* rejects a slightly higher fraction of experimental events in the angular region above  $\cos\Theta > 0.1$ , the total fraction of events passing *level 2* cuts is higher for experimental data than for simulated atmospheric muons. This is due to the fact that the fraction for which the likelihood reconstruction yielded a zenith angle below  $\cos\Theta = 0.1$  is slightly higher in experimental data than in simulated data. The ratio between the number of experimental events and the number of atmospheric muon events predicted by the simulation (when considered the full angular region) is listed in Table 14.

#### 7.2.4 Flare check

A small fraction of the events recorded by AMANDA is known to be due to electronic noise. The so-called *flare-indicators* are a set of observables that provide a tool to detect such events [134]. Cuts on the flare indicators are used to clean the data set from obvious electronic artifacts before further selection criteria are developed. Because the applicability of the flare indicators to events with extremely large light yield had not been investigated before, the *flare-check* has not been applied at an earlier stage of the analysis.

In total, there are nine flare indicators and not all them are practical for this analysis (see appendix B). We use four indicators which proved to be robust also for events with high light yield. The indicators are based on certain event features that preferentially occur in events of electronic origin:

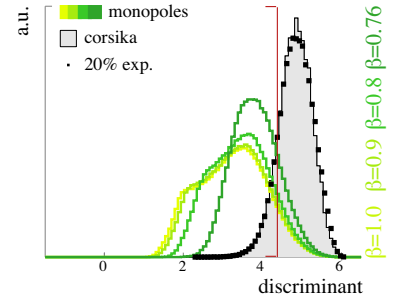


**Figure 7.14** – Fisher discriminant (equation (44)) in the down-going region  $\cos\Theta > 0.1$ .

$$\frac{\text{cut \# 4}}{\left( \begin{pmatrix} 1.07 \\ 6.03 \end{pmatrix} \cdot \begin{pmatrix} \cos\Theta \\ \mathbf{FRAC1} \end{pmatrix} \right) < 4.3}$$

<i>PERIOD I</i>	1.38
<i>PERIOD II</i>	1.37
<i>PERIOD III</i>	1.25
average	1.34

**Table 14** – Ratio between the number of experimental events and the number of simulated atmospheric muon events after applying *level 2* cuts.

- An abnormally high fraction of amplitudes recorded by the ADCs, while no edges recorded by the respective TDCs. The flare indicator which provides a measure for the probability of this abnormality to occur is called **flare\_only\_adc**.
- An abnormally high fraction of unpaired edges. The corresponding flare indicator is called **flare\_missing\_ch**.
- An abnormally high fraction of hits with extremely short TOTs in a certain subset of channels that are read out electrically. The corresponding flare indicator is called **flare\_short\_H**.
- An abnormally high number of hits occurring in strings 5-10, compared to the number of hits occurring in strings 11-19. The corresponding flare indicator is called **flare\_induc\_1119**.

The distributions of the used flare indicators and the imposed cuts (cuts #5 (a-d)) are shown in Figure 7.15

*cuts #5 (a-d)*

<b>flare_only_adc</b>	<	7
<b>flare_missing_ch</b>	<	10
<b>flare_short_H</b>	<	7
<b>flare_induc_1119</b>	<	7

After applying *level 2* cuts, only one experimental event in the 20% data set is removed by the flare cleaning cuts. The simulated events pass without exception. That is, the cuts imposed so far have removed most of the flare events already. Still, cuts 5 (a-d) are applied, in order to remove flare events that are potentially present in the 80% blinded data set.

### 7.3 Analysis Level 3

At this level, an iterative likelihood reconstruction is applied, based on which the events are separated into up- or down-going particles. Starting from the track of the previous single-iteration reconstruction, the minimization process is repeated twelve times. The subsequent starting tracks are found using a Sobol sequence.

Before searching up- and down-going samples separately for monopole signatures, a final brightness criterion is applied which mainly aims at the rejection of low-multiplicity misreconstructed events which are not reproduced by the simulation (see below). The cut parameter is a Fisher Discriminant from two observables:

- $\text{NCH}_{\text{optical}}^{z < 100}$ : The number of hit optically read out OM which are located at depth greater than  $z = 100$  m above the detector center (corresponding to depths greater than 1630 m below the surface).
- $\text{NHits}_{\text{optical}}^{z < 100}$ : The number of hits in optically read out OM below  $z = 100$  m.

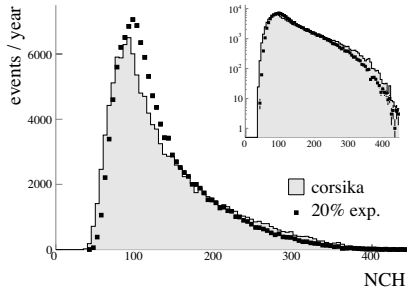


**Figure 7.16** – Number of hit channels in 20% experimental data (black markers) compared to atmospheric muons (grey histograms) after applying *level 2* cuts in linear (large panel) and logarithmic (small panel) representation. The hit cleaning and OM selection corresponds to the one applied at *level 2*, see Table 13 in section 7.2.1).

#### 7.3.1 OM selection

The observables that provide a measure for the amount of light deposited in the detector are related to the multiplicity of hits recorded during an event. At this level of the analysis, observables like **NCH** or **NHits** show a slight disagreement between experimental and simulated data. Figure 7.16, for instance, shows the **NCH** distribution after applying *level 2* cuts. Similar disagreements are also observed in the **NHits** distribution.

Good agreement between experimental and simulated data with respect to key observables like **NCH** and **NHits** can be reestablished by using a

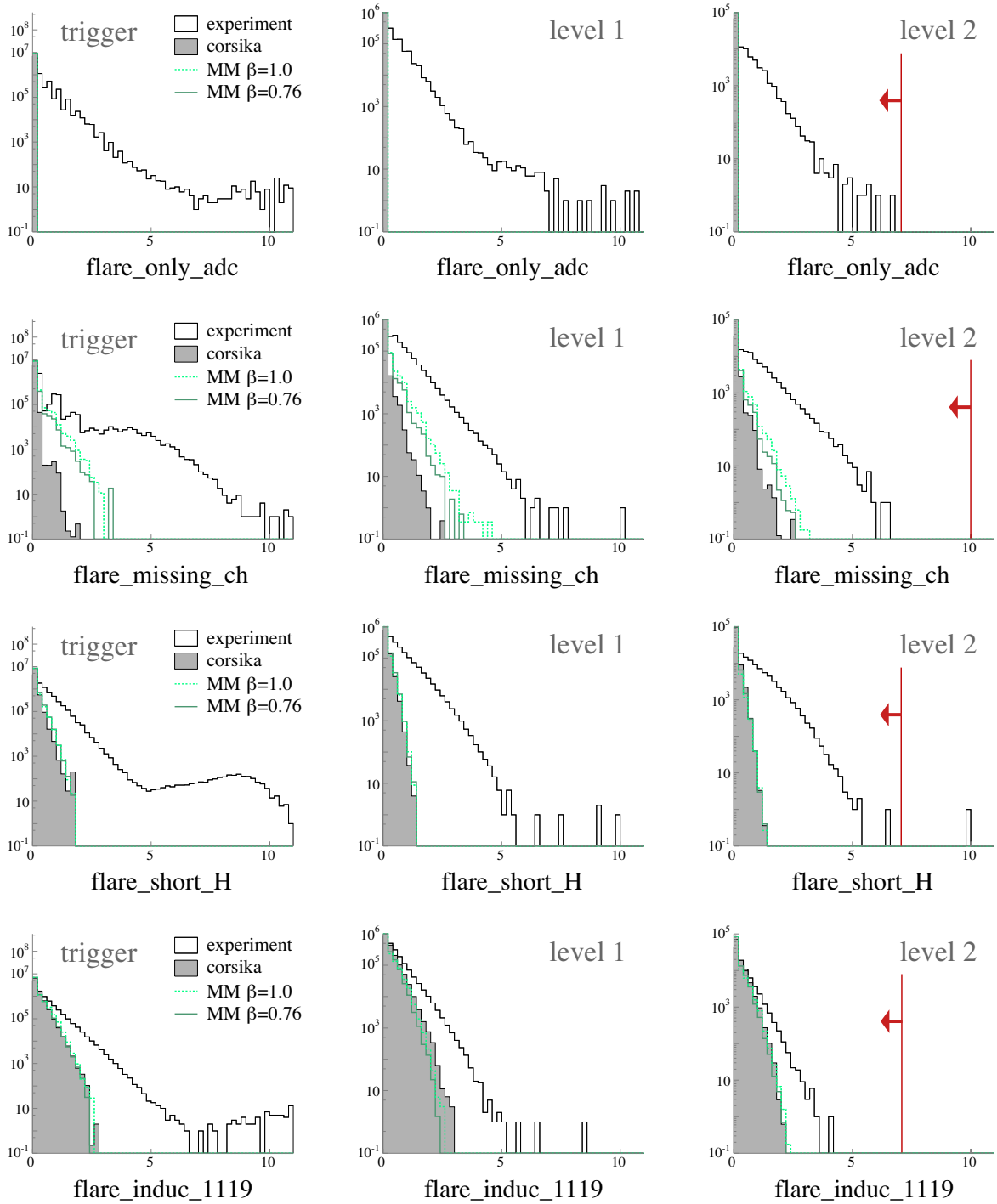


**Figure 7.15** – Flare indicators that are used as cut-parameters in this analysis at re-trigger level (left column), *level 1* (middle) and *level 2* (right column). Open histograms black represent experimental data (1% for trigger level, 20% at higher levels), grey histograms are the simulated atmospheric muon background, open green histograms represent simulated monopole signal for monopole speeds  $\beta = 1.0$  (dashed, light green) and  $\beta = 0.76$  (dark green). Each flare indicator is a measure of the probability of an events to be due of pure electronic origin. Higher indicator values indicate a high probability of the event to be a flare (see section B). In this analysis they are applied after *level 2* cuts (see text). The cuts are marked by red lines.

observable	OM selection	Hit cleaning
$N\text{Hits}_{\text{optical}}^{z < 100}$	extended (see appendix C), $z < 100$ m	<i>TOT, RT - cleaning:</i> standard (see level 2)
$N\text{CH}_{\text{optical}}^{z < 100}$		<i>cross-talk, time-window:</i> see level 2 <i>amplitude cut:</i> $> 0.6$ PE
$\cos \Theta$	extended (see appendix C)	<i>TOT, RT, Amplitude:</i> as above <i>cross-talk cleaning:</i> as above <i>time-window:</i> [17000:25000] ns <i>reject hits in overflowed channels</i> <i>reject hits with missing leading edges</i> <i>use only first hit in each OM</i>

**Table 15** – OM selection and Hit cleaning used for the *level 3* cut parameters.

rigorous OM selection, which includes only the best understood OMs, and which are well described by the detector simulation. The development of this extended OM selection is described in detail in appendix C. The most radical cleaning steps of the extended OM selection are

- the rejection of all OM with electrical readout, and
- the rejection of all OMs located above a depth of  $z = 100$  m above the detector center (Figure 7.17).

Further cleaning steps involve:

- the rejection of all OMs in string 13,
- the rejection of OMs which have recorded only *incomplete* hit information for more than 10% of all recorded hits. A hit is incomplete, if it either consists of only TDC edges or it consists of only an ADC value.

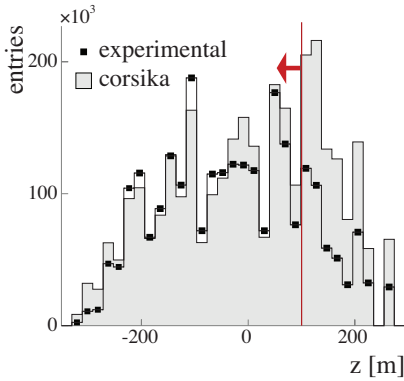


**Figure 7.17** – The depth distribution of hits in optically read-out OMs for simulated atmospheric muons (grey histogram) and experimental data (black markers). Experimental data have substantially less hits in the upper part of the detector than predicted by the simulation. OMs in the depth range  $z > 100$  m are excluded.

A set of 125 OMs pass the OM selection criteria listed above. The behavior of this subset of OMs is fully reproduced by the detector simulation. Only these 125 OMs are used for the calculation of cut parameters sensitive to the light yield of an event.

For the iterative likelihood reconstruction, the first two cleaning steps (rejection of electrically read-out OMs and OMs located at depths shallower than 100 m above the detector center) are unnecessary, since for these OMs the timing distribution of the first hits recorded in each OM is simulated accurately (see appendix C.5). The OM selection applied for the cut parameters used at filter *level 3* are summarized in Table 15.

### 7.3.2 Hit cleaning

The hit cleaning criteria applied for the *level 3* cut parameters are identical to the ones used at *level 2* (see Table 13), with one exception: The amplitude cut was raised to a threshold amplitude of 0.6 photoelectrons.

### 7.3.3 Light yield criterion

The last cut that is applied before the data set is separated into up- and down-going particles is a Fisher discriminant composed of the number of hit

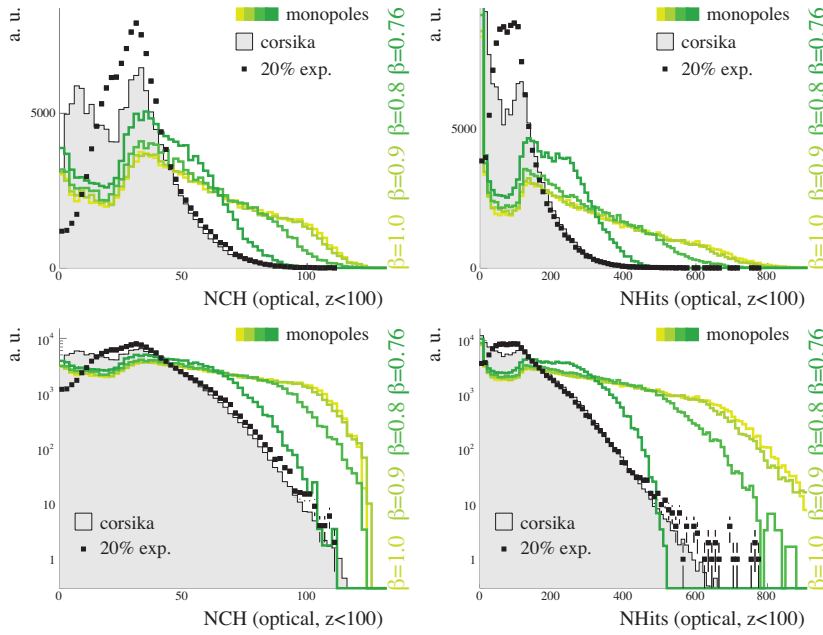


**Figure 7.18** – Input observables to the *level 3* Fisher discriminant  $\text{NCH}_{\text{optical}}^{z < 100}$  (left) and  $\text{NHits}_{\text{optical}}^{z < 100}$  (right) in linear (top panels) and logarithmic (bottom panels) representation.

optical modules and total hit multiplicity after applying the extended OM selection and hit cleaning criteria summarized in Table 15. The two input observables ( $\text{NCH}_{\text{optical}}^{z < 100}$  and  $\text{NHits}_{\text{optical}}^{z < 100}$ ) are shown in Figure 7.18.

The extended OM selection strongly affects the multiplicity distributions for events with low hit multiplicities. The disagreement between experimental and simulated data in the low multiplicity range is an effect related to the removal of OMs in the upper part of the detector: For simulated events, OMs in the upper part of the detector had contributed most of the hits to the overall multiplicity (*c.f.* Figure 7.17). *I.e.*, the exclusion of the OMs located at the shallowest depths removes a large fraction of hits in simulated data. Hence the hit multiplicity distributions for simulated data now peaks at small values. For experimental data in contrast, OMs at in the upper part of the detector contributed fewer hits to the overall multiplicity, and hence the removal of these OMs has a smaller effect on the hit multiplicity distribution.

The disagreement between experimental and simulated data in the low multiplicity range is ignored. As this analysis aims at detecting events with extremely high light yield, good agreement in the high multiplicity tails is of prime importance. As demonstrated in Figure 7.18, good agreement at high multiplicities is established. We ignore the disagreement in the low multiplicity region and remove low multiplicity events with a the cut on the Fisher discriminant composed of  $\text{NHits}_{\text{optical}}^{z < 100}$  and  $\text{NCH}_{\text{optical}}^{z < 100}$ .

Like the discriminant analyses at previous analysis levels, the Fisher criterion is minimized for learning data comprising 1000 events of the simulated  $\beta = 0.76$  monopoles and simulated atmospheric muons respectively. This optimization yields the following discriminant function:

$$d = \begin{pmatrix} 0.073 \\ -0.030 \end{pmatrix} \cdot \begin{pmatrix} \text{NCH}_{\text{optical}}^{z < 100} \\ \text{NHits}_{\text{optical}}^{z < 100} \end{pmatrix} \quad (45)$$

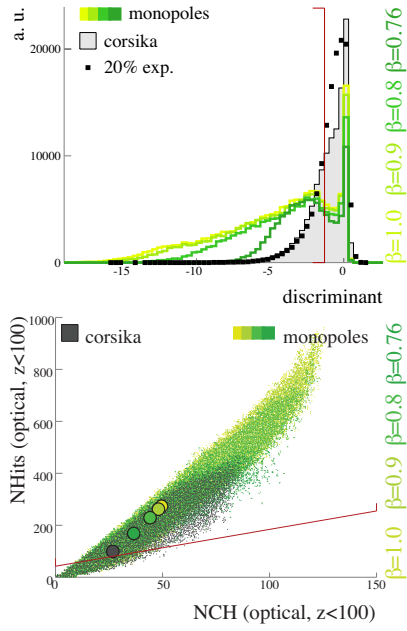


**Figure 7.19** – Top: Discriminant function (equation (45)). Bottom: *Cut # 6* in the  $\text{NHits}_{\text{optical}}^{z < 100}$ - $\text{NCH}_{\text{optical}}^{z < 100}$ -plane.

*cut # 6*

$$\begin{pmatrix} 0.073 \\ -0.030 \end{pmatrix} \cdot \begin{pmatrix} \text{NCH}_{\text{optical}}^{z < 100} \\ \text{NHits}_{\text{optical}}^{z < 100} \end{pmatrix} < -1.3$$

<i>PERIOD I</i>	1.09
<i>PERIOD II</i>	1.10
<i>PERIOD III</i>	0.97
average	1.08

**Table 16** – Ratio between the number of experimental events and simulated atmospheric muon events after applying *level 3* cuts.

**Figure 7.20** – Reconstructed zenith angle for simulated atmospheric muon events (grey histograms) and experimental data (black markers) before applying *cut # 6* (left panel) and after applying *cut # 6* (right panel).

The distributions of the discriminant function for simulated signal and background samples and for the experimental data is shown in the top panel of Figure 7.19. A cut is placed on the value of the discriminant function ( $d < 1.3$ ) such that events in the region where simulated and experimental data disagree (corresponding to low multiplicity events) are removed. The bottom panel of Figure 7.19 shows a representation of the imposed cut as a separating boundary (red line) in the  $\text{NHits}_{\text{optical}}^{z < 100}$ - $\text{NCH}_{\text{optical}}^{z < 100}$ -plane.

The cut removes about 74% of the remaining experimental data and about 67% of the remaining simulated atmospheric muon events. The fraction of removed signal events lies between 23% and 30%, depending on the monopole velocity.

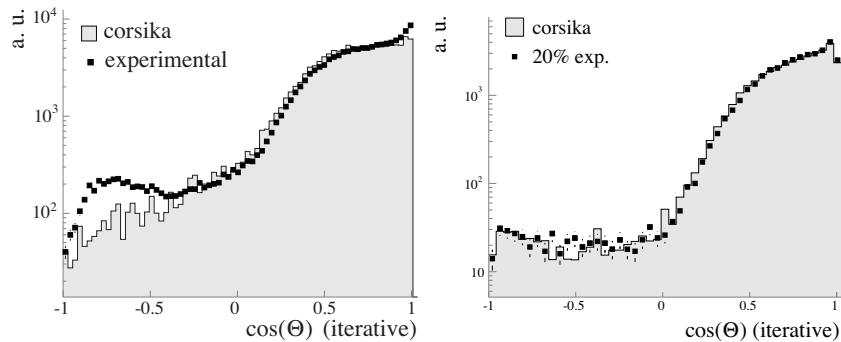
Apart from removing a sizable fraction of the remaining atmospheric muon background, *cut # 6* has another important effect: It eliminates the excess of misreconstructed atmospheric muon in experimental data.

Good agreement between experimental and simulated with respect to the reconstructed zenith angle data is achieved over the full angular region. Figure 7.20 compares the reconstructed zenith angle for simulated atmospheric muon events and experimental events before and after applying *cut # 6*.

*Cut # 6* removes a higher fraction of experimental events than of simulated events and the ratio between the number of experimental to simulated atmospheric muon events is 1.08, slightly lower than at earlier selection levels. The event ratios for each of the three OM selection periods are listed in Table 16.

## 7.4 Conclusions

With data selection described so far, we achieve a reduction of the experimental data set by a factor  $\mathcal{O}(10^{-4})$ . The signal passing efficiency lies between 48% ( $\beta = 0.76$  monopoles) and 60% ( $\beta = 1.0$  monopoles) compared to trigger level. The difference between the number of experimental events and the number of simulated atmospheric muon events passing each cut is at the order of a percent. The largest difference in the passing rate occurs with *cut # 6* ( $\sim 7\%$ ). The difference is less than a percent for all other applied cuts. This is a substantial improvement over previous analyses where the passing rates of experimental and simulated data differed by up to 50% (see *e.g.* [168, 169]). The passing efficiencies for each filter level of this chapter are listed in Table 17.



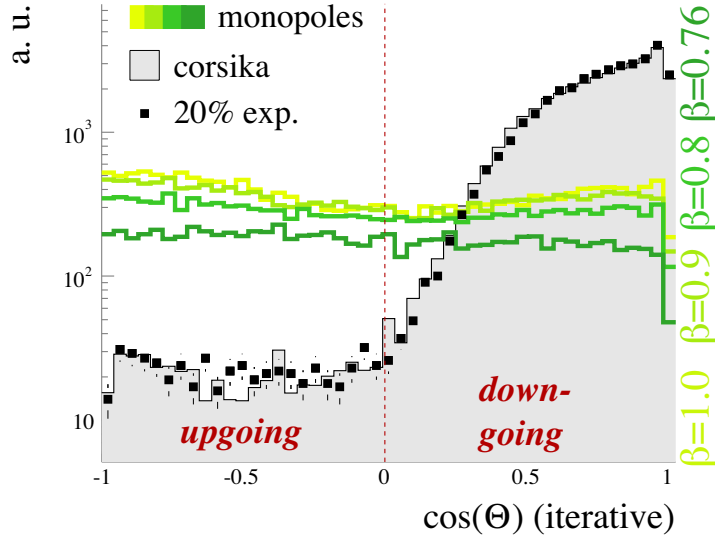


**Figure 7.21** – Based on the reconstructed zenith angle obtained from the 12-fold iterative likelihood reconstruction, the data-set is divided into two angular regions: Up-going particles ( $\cos \Theta < 0$ ) and down-going particles ( $\cos \Theta \geq 0$ ).

Of particular importance is the accurate description of misreconstructed atmospheric muons by the simulation. Based on the results of the 12-fold iterative likelihood reconstruction, the data-sets are divided into up-going ( $\theta > 90^\circ$ ) and down-going ( $\theta \leq 90^\circ$ ) particles (see Figure 7.21). The distribution of the reconstructed zenith angles agrees well over the full angular region. Accordingly, the ratio between experimental events and simulated atmospheric muon background is approximately equal in both up- and down going samples: The ratio for events which are reconstructed as up-going is 1.12, only marginally higher than 1.08, the ratio for events which are reconstructed as down-going.

level	fraction of passing events				normalization		
	monopoles				CORSIKA	experimental	
	$\beta = 1.0$	$\beta = 0.9$	$\beta = 0.8$	$\beta = 0.76$			
level 2	96%	96%	95%	91%	4%	5%	1.3
level 3	77%	77%	76%	70%	33%	26%	1.1

**Table 17** – Fraction of events passing the *level 2* and *level 3* filter, and the necessary scaling factor to normalize simulated and experimental event rates. The percentage of passing events is taken relative to the previous selection level.

## 8 Up-going monopoles

The search for monopoles entering from the northern hemisphere is in principle background-free, since up-going leptons can be induced by atmospheric neutrinos only. Leptons induced by atmospheric neutrinos would however only result in a Cherenkov light yield comparable to that expected from magnetic monopoles if the initial neutrino had an energy in the PeV range. Atmospheric neutrinos with such high energies can in principle be produced in prompt decays of charmed mesons in the atmosphere [170, 171], but the expected event rate in a detector like AMANDA-II would be negligible [172, 173]. Besides, at such high energies, the neutrinos would largely be absorbed in the Earth and would only contribute to the background for the search for down-going monopoles.

<i>PERIOD I</i>	1.06
<i>PERIOD II</i>	1.30
<i>PERIOD III</i>	0.91
average	1.12

**Table 18** – Ratio between the number of experimental events and the number of simulated atmospheric muon events which are reconstructed as up-going.

After rejecting events which are reconstructed with a zenith angle smaller than  $90^\circ$ , the 20% experimental up-going data sample contains 516 events. The background simulation predicts 461.2 misreconstructed atmospheric muon events. The ratio between experimental and simulated events (Table 18) is consistent the ratio observed at earlier analysis levels, and is also consistent with the ratio observed for the down-going data sample. Hence we can assume the remaining background indeed consists of misreconstructed atmospheric muon events.

In order to eliminate the remaining background in the up-going data sets, we apply two cuts using

- $|\Theta_{\text{allOMs}} - \Theta_{\text{optical}}|$ , the difference in the zenith angle obtained from the iterative likelihood reconstruction and the zenith angle obtained from an additional likelihood reconstruction using only a sub-set of the detector (the optically read out OMs, see below), and
- $\Sigma \text{ADC}_{\text{optical}}^{z < 100}$ , the sum of the measured pulse amplitudes in optically read-out OMs located below a depth of  $z = 100$  m relative to the detector center.

The final cut is optimized such that the expected limit on the flux of magnetic monopoles is most stringent.

### 8.1 Rejection of misreconstructed atmospheric muon bundles

There is a variety of cut parameters which provide a measure of the reconstruction accuracy, and which are commonly used in AMANDA analyses to identify misreconstructed atmospheric muons. Searches for up-going neutrinos in the TeV range, for instance, use cuts based on the overall track likelihood ( $L(R|H)$ ), see equation (39) in section 7.1.2), observables related to the number of unscattered Cherenkov photons<sup>39</sup>, or to the *smoothness*<sup>40</sup> of the hit pattern. For this analysis, none of these observables yielded sufficient suppression of the misreconstructed muon background at reasonable

<sup>39</sup>If a large fraction of the recorded photon arrival times are consistent with the arrival times of un-scattered Cherenkov photons (so-called *direct hits*), the track is probably reconstructed accurately.

<sup>40</sup>The *smoothness* of an event is calculated with a Kolmogorov-Smirnov test, in which a certain one-dimensional distribution of the observed hit pattern (*e.g.*, hit times of the projections of the hits on the reconstructed track) is compared to the perfectly even (“smooth”) distribution resulting from a constant light emission in hypothetical non-granular detector (see [174] and references therein).

loss in signal. Hence, we use a different method to further reject misreconstructed atmospheric muons.

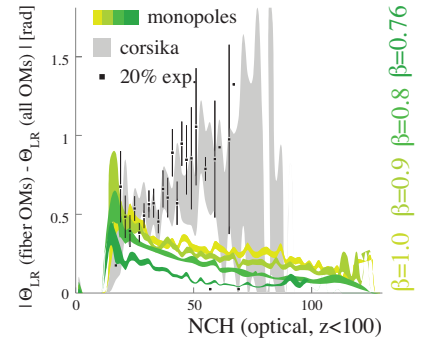
As pointed out in section 7.1.2, the reconstruction of events with high hit multiplicities can sometimes fail, because many of the detected photons are delayed by scattering in the ice. In case of atmospheric muon events, there is another reason for the reconstruction to be less accurate in for high hit multiplicities: Those events which yield the most Cherenkov light either consist of extended bundles of many muons, or, in case the muon multiplicity in the bundle is small, most of the light deposition results from a few catastrophic energy losses of individual muons. In both cases, the light pattern in the event deviates from the single track hypothesis that enters the likelihood reconstruction. This would imply that the likelihood landscape does not possess a pronounced maximum at the direction of the incoming muon bundle.

One possibility to “measure” the goodness of the maximum to which the reconstruction converged is to compare the likelihood of the reconstructed track (*i.e.*, the best-fit track) to the likelihood of the second-best track found during the iteration process. A small difference in the likelihoods means that the likelihood landscape possesses at least two close-to-degenerate maxima. If this is observed, one would have to conclude that the hit pattern is ambiguous with respect to the single-muon hypothesis (and hence strictly speaking not reconstructible), or that the number of iterations used in the reconstruction was insufficient to find the global maximum. In either case the reconstruction result is not reliable. Such ambiguous events should be rejected because of their high probability of being misreconstructed.

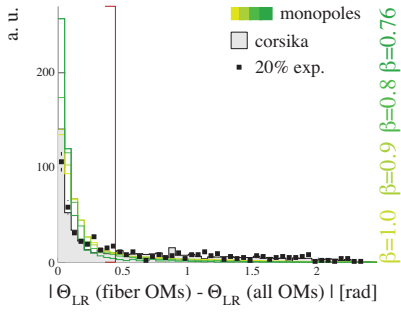
The option to store multiple results obtained during an iterative likelihood reconstruction was made available in the `Sieglinde` reconstruction software only during the course of this analysis. For the 12-fold iterative reconstruction used here, only one (the best-fit track) was stored. Hence, we use a different method to test the quality of the reconstruction result: We add another single-iteration reconstruction which uses only reduced hit information, namely only hits in the optically read-out OMs.<sup>41</sup> The result of the 12-fold reconstruction is used as a seed. If this seed provides a good track hypothesis for the observed hit pattern, the additional single iteration should yield a similar result. Otherwise the numerical algorithm seeking the global extremum in the likelihood space will probably be “driven away” from the initial track hypothesis.

Figure 8.1 shows the mean difference in the zenith angles of the seed track (*i.e.*, the 12-fold likelihood reconstruction) and the track obtained with the additional iteration as a function of the event’s light yield. The light yield is measured via the number of hit OMs,  $\text{NCH}_{\text{optical}}^{z < 100}$ . (as for the previous analysis level, we use optically-read out OM below a depth of  $z = 100$  m for measuring the light deposition.) For the simulated muon background and for experimental data, the zenith angle difference increases with light yield, whereas for monopoles the difference decreases. This is probably due to the fact the single-muon hypothesis does not provide a good description for large muon bundles or muon events with large secondary cascades. For magnetic monopole events in contrast, the direct Cherenkov emission from the single monopole track dominates, yielding a better fit with the single-muon hypothesis. Although for monopoles with speeds different from  $\beta =$

<sup>41</sup>Otherwise the OM selection and hit cleaning used for this reconstruction remain the same as fro the 12-fold iterative reconstruction.



**Figure 8.1** – Mean difference between the zenith angles obtained from the 12-fold iterative likelihood reconstruction and the subsequent single-iteration reconstruction using only optically read-out OMs as a function of the light yield. The black markers with error bars are the mean zenith angle differences for experimental data and its error for 20% experimental data. The colored graphs represent the mean zenith angle difference in simulated data. The widths of the graphs represent the error of the mean.



**Figure 8.2** – Cut on the zenith angle difference (in rad) between the 12-fold likelihood reconstruction and the single-iteration likelihood reconstruction using only optically read-out OMs.

*cut # u.1*

$$|\Theta_{\text{allOMs}} - \Theta_{\text{optical}}| < 25^\circ$$

1.0 the muon hypothesis deviates from the simulated particles in speed and Cherenkov geometry, the reconstruction appears to converges to a more stable result for slower monopoles than for muon bundles with the same light yield: The zenith angle difference at a fixed light yield decreases with monopole speed. This is due to the fact that the higher Cherenkov light intensity allows faster monopoles to pass farther outside the instrumented volume and still deposit the same amount of Cherenkov light as slower monopoles.

In order to eliminate the high multiplicity misreconstructed muon events, we reject events for which the zenith angle difference is greater than  $25^\circ$  (about 4.4 rad). Figure 8.2 shows the distributions of the zenith angle difference for simulated signal and and background events and for 20% of the experimental data set. The cut is marked with a red line.

*Cut # u.1* removes 40% of the remaining experimental events and 41% of the simulated atmospheric muon background. Most importantly, it removes preferentially background events with the highest hit multiplicities. The fraction of passing monopole events lies between 82% ( $\beta = 1.0$ ) and 95% ( $\beta = 0.76$ ).

## 8.2 Final light yield criterion

Figure 8.3 shows the distributions of four observables that are a measure of the light yield: the number of hit OMs (top left panel), the number of hits (top right), the sum of the calibrated pulse amplitudes (ADC values) in photoelectrons (bottom left), and the average calibrated ADC (bottom right). All observables were calculated using the same OM and hit selection as used for the observables used for *cut # 6* in section 7.3.3.

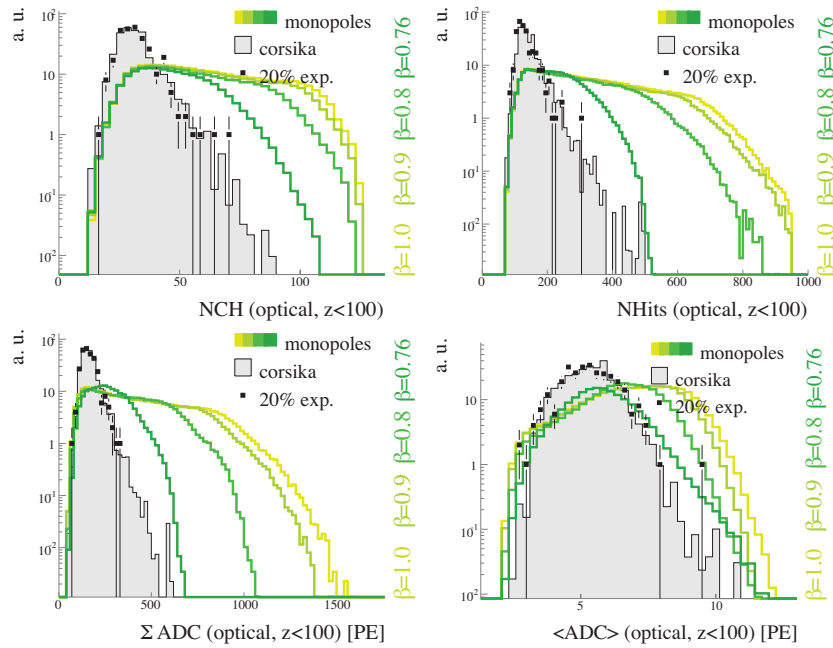


**Figure 8.3** – Observables sensitive to the light yield after applying *cut # u.1*. Number of hit OMs ( $NCH_{\text{optical}}^{z<100}$ , top left), number of hits ( $NHits_{\text{optical}}^{z<100}$ , top right), amplitude sum ( $\Sigma ADC_{\text{optical}}^{z<100}$ , bottom left) and mean amplitude ( $\langle ADC \rangle_{\text{optical}}^{z<100}$ , bottom right). All observables are calculated using only optically read-out OMs below a depth of  $z = 100$  m relative to the detector center.

optimization speed	cut $\Sigma \text{ADC}_{\text{optical}}^{z < 100}$	background events	sensitivity ( $\Phi_{90}$ ) [ $\text{cm}^{-2} \text{s}^{-1} \text{sr}^{-1}$ ]			
			$\beta = 1.0$	$\beta = 0.9$	$\beta = 0.8$	$\beta = 0.76$
$\beta = 1.0$	476 PE	0.23	$4.16 \times 10^{-17}$	$4.80 \times 10^{-17}$	$7.54 \times 10^{-17}$	$9.75 \times 10^{-16}$
$\beta = 0.9$	476 PE	0.23	$4.16 \times 10^{-17}$	$4.80 \times 10^{-17}$	$7.54 \times 10^{-17}$	$9.75 \times 10^{-16}$
$\beta = 0.8$	424 PE	0.73	$4.24 \times 10^{-17}$	$4.82 \times 10^{-17}$	$6.92 \times 10^{-17}$	$5.02 \times 10^{-16}$
$\beta = 0.76$	300 PE	10.14	$7.13 \times 10^{-17}$	$7.88 \times 10^{-17}$	$1.00 \times 10^{-16}$	$2.32 \times 10^{-16}$

**Table 19** –  $\Sigma \text{ADC}_{\text{optical}}^{z < 100}$  cuts, expected number of background events in 80% experimental data, and flux average upper limits at 90% confidence level (in units of  $\text{cm}^{-2} \text{s}^{-1} \text{sr}^{-1}$ ) resulting from optimizing the experimental sensitivity to each of the four simulated monopole speeds.

Only the amplitude sum  $\Sigma \text{ADC}_{\text{optical}}^{z < 100}$  (shown in the bottom left panel of Figure 8.3) is used as final cut parameter, the other observables are displayed in order to demonstrate the general good agreement between experimental and simulated data.<sup>42</sup>

The final cut on  $\Sigma \text{ADC}_{\text{optical}}^{z < 100}$  is optimized such that we expect to place the most stringent limit on the flux of magnetic monopoles after unblinding the data (The optimization process and its underlying statistical arguments are explained in detail in appendix D). At each potential cut value, we calculate the expected number of remaining background events from the simulated atmospheric muon background and the number of remaining signal events for each of the simulated monopoles speeds. Figure 8.4 shows the number of remaining events as a function of the  $\Sigma \text{ADC}_{\text{optical}}^{z < 100}$  cut.

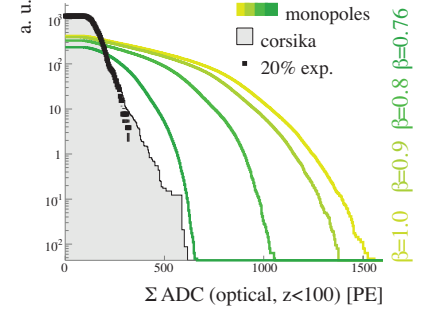
The number of expected background events corresponds to certain *experimental sensitivity* [175], defined as average event upper limit (*i.e.*, the average number of signal events that can, at a certain confidence level, be excluded to be present in the data set after application of the cut) obtained in an ensemble of (hypothetical) repeated identical experiments in absence of signal (see appendix D.3).<sup>43</sup> The flux upper limit ( $\Phi_{90}$ ) that is expected to be placed is that flux for which the number of expected signal events meets the event upper limit (see appendix D.4). We place the cut where  $\Phi_{90}$  reaches its minimum.

Figure 8.5 shows the dependency of the average 90% C.L. flux upper limits ( $\Phi_{90}$ ) on the  $\Sigma \text{ADC}_{\text{optical}}^{z < 100}$  cut for each of the simulated monopole samples. For different monopole speeds, the limit reaches its minimum at different cut positions. Table 19 summarizes the the optimum cut for each of the four simulated monopole speeds, the number of expected background events expected to remain in the 80% data set after application of the optimized cut, and the resulting sensitivities (average flux upper limits  $\Phi_{90}$ ) for each monopole speed.

Applying four different cuts, each one optimized for monopoles with one of simulated speeds, would in principle be possible. This would mean to perform four separate unblinding procedures, each with a different final cut.

<sup>42</sup>Each of the observables as well as linear combinations of them which maximize the Fisher criterion (equation (37) in section 7.1.1) were tested as potential cut parameters with respect to the expected upper limit: the number of hit OMs ( $\text{NCH}_{\text{optical}}^{z < 100}$ ), the number of hits ( $\text{NHits}_{\text{optical}}^{z < 100}$ ), and the amplitude sum ( $\Sigma \text{ADC}_{\text{optical}}^{z < 100}$ ) yielded approximately equal limit setting potentials when used as one dimensional cut parameters, the mean amplitude ( $\langle \text{ADC} \rangle_{\text{optical}}^{z < 100}$ ) was inferior. Using multiple observables as a Fisher discriminant did not improve the expected upper limit. For the sake of simplicity, we chose to apply a one-dimensional cut.

<sup>43</sup>For our optimization we use the the average upper limits at 90% confidence level.



**Figure 8.4** – Number of remaining events dependent on the cut on  $\Sigma \text{ADC}_{\text{optical}}^{z < 100}$  for simulated atmospheric muons (grey histogram), 20% experimental data (black markers) and simulated magnetic monopoles (green histograms).

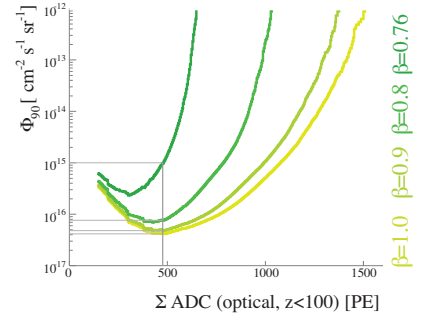


**Figure 8.5** – Flux average upper limit (90% C.L.) for the four simulated monopole speeds dependent on the  $\Sigma \text{ADC}_{\text{optical}}^{z < 100}$  cut.

*final cut (up-going)*

$$\Sigma \text{ADC}_{\text{optical}}^{z < 100} > 476 \text{ PE}$$

For the sake of simplicity however, we use the optimized cut for  $\beta = 1.0$  monopoles. This cut yields optimum sensitivity also for  $\beta = 0.9$  monopoles (see table 19); for  $\beta = 0.8$  monopoles this cut yields a sensitivity only slightly worse ( $\sim 10\%$ ) than the optimum. Only for  $\beta = 0.76$  monopoles the choice of the cut results in a significant loss in sensitivity (roughly a factor of 4) compared to the optimum.

The optimum sensitivity for  $\beta = 1.0$  and  $\beta = 0.9$  monopoles is achieved with requiring  $\Sigma \text{ADC}_{\text{optical}}^{z < 100}$  to be greater than 476 photoelectrons (PE). The expected remaining background of misreconstructed atmospheric muons in the 80% blinded experimental data is 0.23 events. No event from the 20% data set passes this cut. The average event upper limit at this background expectation is  $\bar{\mu} = 2.63$ . The flux level of relativistic magnetic monopoles that would on average result in 2.63 events in after application of the final cut lies between  $4.16 \cdot 10^{-17} \text{ cm}^{-2} \text{ s}^{-1} \text{ sr}^{-1}$  ( $\beta = 1.0$ ) and  $9.75 \cdot 10^{-16} \text{ cm}^{-2} \text{ s}^{-1} \text{ sr}^{-1}$  ( $\beta = 0.76$ ), depending on the monopole speed (see Table 19).

The background expectation of  $\langle n_b \rangle = 0.23$  events corresponds to the sum of weights ( $\sum \omega_i$ ) from  $N = 8$  simulated atmospheric muon events that survived all cuts. The statistical error on  $\langle n_b \rangle$  is

$$\sigma(\langle n_b \rangle) = \sqrt{\frac{\sum \omega_i^2}{N} - \left(\frac{\sum \omega_i}{N}\right)^2} = 0.027. \quad (46)$$

The number of signal events passing all cuts is  $\mathcal{O}(10^5)$  for all generated monopole velocities. The relative statistical error on the signal expectation ( $\sqrt{N}/N = \mathcal{O}(10^{-3})$ ) is hence marginal. The impact of both statistical and systematic errors on the final analysis is discussed in chapter 10.

### 8.3 Unblinding result

The so-far blinded 80% of the experimental data set is processed in the same manner as the 20% test sample and identical cuts are imposed. Figure 8.6. shows the distribution of the final cut parameter ( $\Sigma \text{ADC}_{\text{optical}}^{z < 100}$ ) for the 80% unblinded data set (the 20% sample is discarded) before the application of the final cut (marked by the red line).

No experimental event passes the final cut. The event upper limit (constructed according to [175]) for an observation of zero events with an expectation of 0.23 events is 2.21. This is lower than the the average event upper limit ( $\bar{\mu} = 2.63$ ), because the number of events observed after unblinding is lower than the number of events expected. (The corresponding 90% C.L. flux limits are accordingly lower than the sensitivities quoted in Table 19.) However, for a legitimate analysis result, we must account for systematic and statistical errors. The incorporation of errors into the confidence belt construction results in slightly higher flux limits than the construction ignoring systematic uncertainties (see chapter 10).

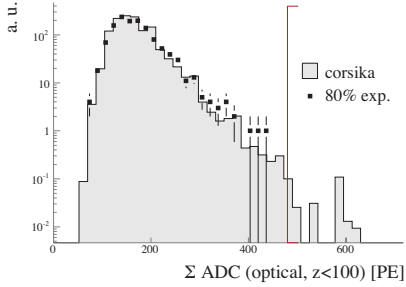


**Figure 8.6** – Distribution of the final cut-parameter for the 80% unblinded data set.

## 9 Down-going monopoles

Roughly 99% of the experimental data set after applying *level 3* cuts are reconstructed as particles entering from above the horizon. The 20% experimental data set for the down-going monopole search comprises roughly  $35 \times 10^3$  events. The average ratio of the number experimental events to the number of events predicted by the atmospheric muon simulation is  $\sim 1.1$  (see Table 20 for the ratio in each of the three OM selection periods) and is consistent with the assumption that the data set is dominated by atmospheric muon events. Most of these events are bundles containing a large number of muons.

The much larger background from down-going atmospheric muons requires several additional cuts. Consequently, the sensitivity to down-going monopoles will be inferior compared to the search for up-going monopoles. Despite being less sensitive, the search for down-going monopoles is motivated by the larger monopole mass range for which the result will be valid: As the ability of magnetic monopoles to penetrate matter increases with the monopole mass, the search for down going monopoles will have a much lower mass threshold.

Most of the cut parameters used to distinguish monopoles from muon bundles are measures for the light yield:

- $\text{NHits}_{\text{optical}}^{z < 100}$ , the number of hits
- $\Sigma \text{ADC}_{\text{optical}}^{z < 100}$ , the amplitude sum
- $\langle \text{ADC} \rangle_{\text{optical}}^{z < 100}$ , the mean amplitude, and
- $\text{THW}$ , the half width of the time interval around the median of all hit times which contains half the number of all hits. This observable provides a measure of the "duration" of the event.

All light yield criteria are calculated using only optically read-out OMs below a depth of  $z = 100$  m relative to the detector center. The hit cleaning criteria are those used for the cut at analysis *level 3* (see Table 15).

The light yield criteria are combined with the reconstructed track direction (cosine of the zenith angle from the 12-fold iterative likelihood reconstruction,  $\cos \Theta$ ) using a linear discriminant analysis. Like the angular criterion applied at analysis *level 2* (emphcut #4, section 7.2.3) the multi-dimensional cuts require a larger light deposition for more vertically downward track directions.

### 9.1 Further background rejection

The first cut parameter to reduce the atmospheric muon background is a Fisher discriminant composed of  $\text{NHits}_{\text{optical}}^{z < 100}$ ,  $\text{THW}$ , and the cosine of the reconstructed zenith angle.

Before determining the discriminant function, we remove the dimmest events with one-dimensional cuts on each of the input variables. This ensures that the resulting discriminant function results in an optimum separation of signal and background events at the highest light yields. We require a minimum of 210 hits, and a minimum "time-half-width" ( $\text{THW}$ )

<i>PERIOD I</i>	1.09
<i>PERIOD II</i>	1.10
<i>PERIOD III</i>	0.97
average	1.08

**Table 20** – Ratio between the number of experimental events in the down-going data set.

<i>cuts # d.1 (a-b)</i>		
<b>NHits</b>	>	210
<b>THW</b>	>	300 ns

**Figure 9.1** – One-dimensional cuts (marked by red lines) on  $\text{NHits}_{\text{Optical}}^{z < 100}$  (left) and  $\text{THW}$  (right) applied before the two observables are combined with the cosine of the reconstructed track direction (shown in Figure 7.21, section 7.4) to a multi-dimensional cut (Fisher discriminant).

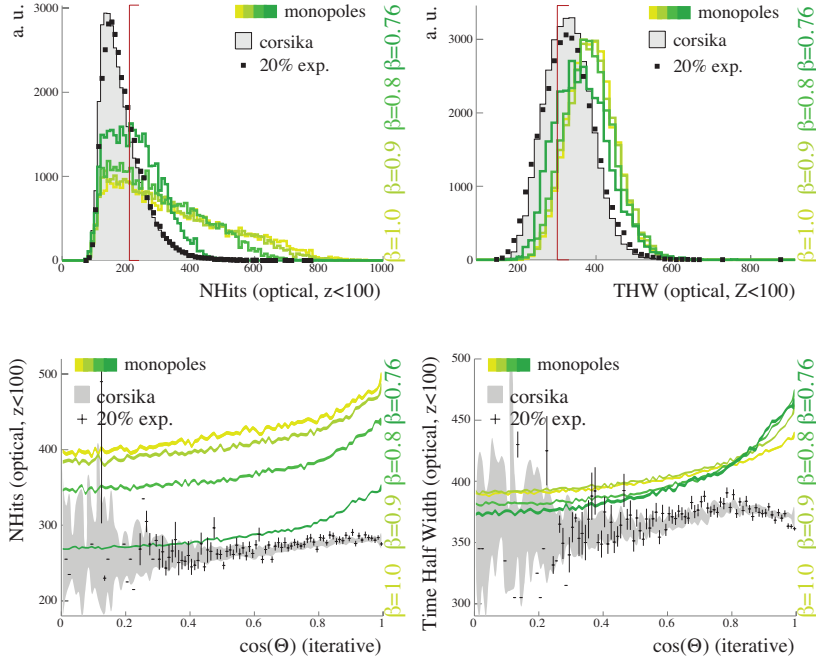


**Figure 9.2** – Mean values of  $\text{NHits}_{\text{Optical}}^{z < 100}$  (left) and  $\text{THW}$  (right) as a function of the reconstructed zenith angle. Simulated data are shown as colored bands, whose widths are a measure for the error of the mean values. The 20% experimental data are shown as black markers.

of 300 ns. The distributions of the two input observables and the applied cuts are shown in Figure 9.1.

Figure 9.2 shows the dependency of the mean values of  $\text{NHits}_{\text{Optical}}^{z < 100}$  and  $\text{THW}$  with with the reconstructed zenith angle for simulated signal and background events, and for experimental data. Both light yield criteria have a positive correlation with the zenith angle. The correlation observed in the 20% experimental data is well reproduced by the background simulation.

Minimizing the Fisher criterion using 1000 events of both simulated atmospheric muon background and simulated  $\beta = 0.76$  monopoles yields the discriminant function

$$d = \begin{pmatrix} 7.351 \\ -0.013 \\ -0.020 \end{pmatrix} \cdot \begin{pmatrix} \cos \Theta \\ \text{NHits} \\ \text{THW} \end{pmatrix}. \quad (47)$$

The distributions of the discriminant function for simulated atmospheric muon background, simulated magnetic monopoles, and 20% of the experimental data set are shown in Figure 9.3. As indicated by the red line in the figure, we reject all event for which the discriminant function takes values greater than -7 (*cut # d.2*). This cut removes 85.5% of the remaining experimental background, while 67% ( $\beta = 0.76$ ) to 86% ( $\beta = 1.0$ ) of the monopole signal is preserved. The fraction of removed simulated atmospheric muon events amounts to 88% and is slightly higher than observed in experimental data.

For one event in the experimental data set the discriminant function takes the remarkably low value of -26, indicating a light yield even higher than that expected from a singly charged relativistic magnetic monopole. Further investigations of the signature support the hypothesis of an immense light deposition in the detector during this particular event (see appendix

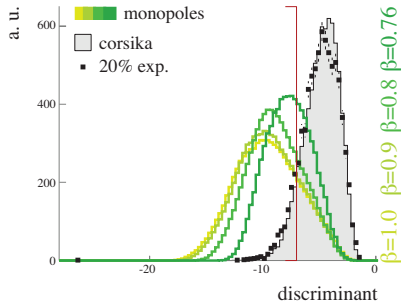


**Figure 9.3** – Cut on Fisher discriminant composed of  $\text{NHits}_{\text{Optical}}^{z < 100}$ ,  $\text{THW}$ , and  $\cos \Theta$  (equation (47)).

$$\text{cut \# d.2} \\ \frac{\begin{pmatrix} 7.351 \\ -0.013 \\ -0.020 \end{pmatrix} \cdot \begin{pmatrix} \cos \Theta \\ \text{NHits} \\ \text{THW} \end{pmatrix} < -7}$$

E). Only after completion of this analysis, the event could be identified as an instrumental background.<sup>44</sup>

Up to this selection level, the atmospheric muon background is well described by the simulated air-showers based on the *poly-gonato* model (see section 5.3.2). With further tightening of the cuts however, most of the atmospheric muon background comes from interactions of cosmic ray primaries with energies above 10 PeV. In this energy range, the lack of trans-iron primaries in the CORSIKA-simulation becomes apparent. Therefore, we use the *two-component* model (see section 5.3.2) for optimizing further selection criteria. Figure 9.4 shows a comparison of the two simulated atmospheric muon samples, *poly-gonato*-model (grey histogram) and *two-component* (light purple histogram). Shown is the high-energy end of the Fisher discriminant used as cut parameter in the previous cut (*cut # d.2*) in semi-logarithmic representation. The difference of the two input spectra is most obvious in those background events with the highest light yield (smallest values of the Fisher discriminant), corresponding to muon bundles induced by the most energetic cosmic ray primaries. The *two-component* model yields better agreement between experimental and simulated data with respect to both the shape of the distribution and the predicted event rates. After imposing *cut # d.2*, the 20% experimental data set comprises 889 events while the *poly-gonato* model predicts 623.8, corresponding to a ratio of 1.4 between observed and simulated events, while the *two-component* model predicts 746.9 events, corresponding to a ratio of 1.2. The latter is in better agreement with the ratio observed at previous analysis levels. Additional comparisons between the *poly-gonato* and the *two-component* model are presented in appendix F.

## 9.2 Final light yield criterion

Like the search for monopoles entering from below the horizon, the search above the horizon uses amplitude information ( $\Sigma \text{ADC}_{\text{optical}}^{z < 100}$ ) as final selection criterion. Since for down-going atmospheric muon background the light yield depends on the zenith angle of the incoming bundles, we combine  $\Sigma \text{ADC}_{\text{optical}}^{z < 100}$  with the cosine of the reconstructed zenith angle ( $\cos \Theta$ ).

As for the previous cut, we remove the events with the least light yield using one-dimensional cuts. After that, the final cut parameter is determined via discriminant analysis. We require an amplitude sum ( $\Sigma \text{ADC}_{\text{optical}}^{z < 100}$ ) of at least 400 photoelectrons and an average amplitude ( $\langle \text{ADC} \rangle_{\text{optical}}^{z < 100}$ ) of at least 6 photoelectrons. The distributions of the two cut parameters and the cut positions are displayed in Figure 9.5.

From the distributions in Figure 9.5 it becomes obvious that the search for down-going monopoles is not sensitive over the full range of simulated monopole speeds. Monopoles with speeds just above the Cherenkov threshold ( $\beta = 0.76$ ) do not deposit enough light in the detector to be distinguishable from the atmospheric muon background.

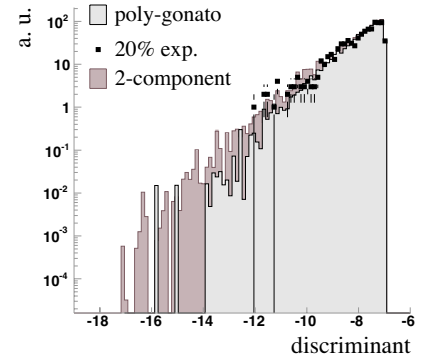


**Figure 9.4** – Discriminant function used in *cut # d.2* for two different sets of simulated atmospheric muon background: The *poly-gonato* model discarding primary nuclei heavier than iron (grey histogram) and the *two-component* model (light purple histogram). 20% of the experimental data set (black markers) are shown for comparison.

*cuts # d.3 (a-b)*

$\Sigma \text{ADC}_{\text{optical}}^{z < 100}$	>	400 PE
$\langle \text{ADC} \rangle_{\text{optical}}^{z < 100}$	>	6 PE

<sup>44</sup>The event was identified as an instance of a certain, until then unknown, class of background. Unlike other detector artifacts (*e.g.*, cross-talk or *flares*) the hits in this class of background are presumably due to photons released by a detector component deployed at depth. The 2000 data set contained only a single instance of this type of background. Since the hit pattern of the event is consistent with light released at depth, there was no reason to suspect the event of being of electronic origin. The analysis of data taken in later years however, revealed ten events with signatures that were virtually identical to the event recorded during the year 2000. See appendix E for further details.

**Figure 9.5** – Cuts on the amplitude sum (left) and the mean amplitude (right) applied before optimization of the final cut.

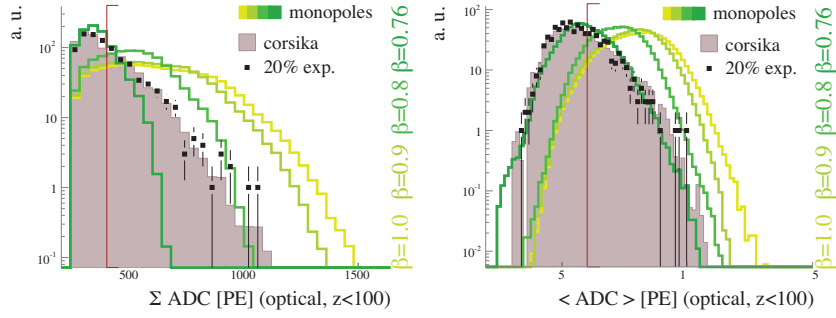


Figure 9.6 shows the correlation between  $\Sigma \text{ADC}_{\text{optical}}^{z < 100}$  and  $\cos \Theta$ , the two input observables to the final cut parameter. The discriminant analysis is performed with 1000 events of each the simulated atmospheric muon background and the simulated magnetic monopoles with speed  $\beta = 1.0$ .

Minimizing the Fisher criterion yields the discriminant function

$$d = \begin{pmatrix} 7.866 \\ -0.010 \end{pmatrix} \cdot \begin{pmatrix} \cos \Theta \\ \Sigma \text{ADC} \end{pmatrix}. \quad (48)$$

The distributions of the discriminant for simulated signal and background and for 20% experimental data is shown in Figure 9.7. The experimental event with the highest light yield (smallest value of the discriminant function) is the same event as the one observed as the extreme outlier the distribution of the discriminant used in *cut # d.2* (see appendix E).

Following the same optimization procedure as used in the search for up-going monopoles, (see previous section and appendix D), we place the final cut such that we expect the most stringent flux limit. The left panel of Figure 9.8 shows the number of events remaining in the simulated and experimental data sets for each potential cut on the discriminant function (equation (48)). The histograms are scaled to the livetime of the 80% (blinded) data set. Hence the cumulative distribution of the 20% experimental data set seems to contain four events that stand out above the simulated background, when in fact there is only a single outlier in 20% experimental data (*c.f.* Figure 9.7).

The right panel in Figure 9.8 shows the expected 90% C.L. flux limits expected for magnetic monopoles with each of the simulated speeds as a function of the cut position. The optimum cuts (*i.e.*, those cuts that

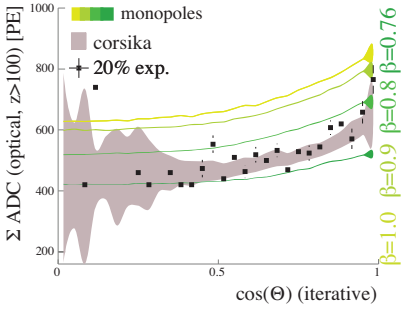


**Figure 9.6** – Correlation between the mean amplitude sum ( $\Sigma \text{ADC}_{\text{optical}}^{z < 100}$ ) and the cosine of the reconstructed zenith angle for simulated atmospheric muons (light purple), simulated magnetic monopoles (green), and 20% experimental data (black markers).

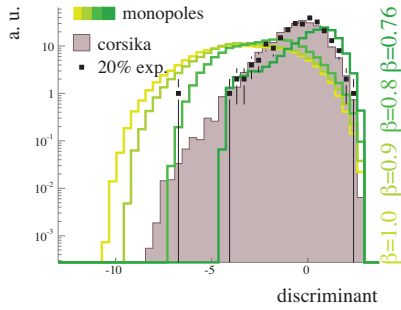
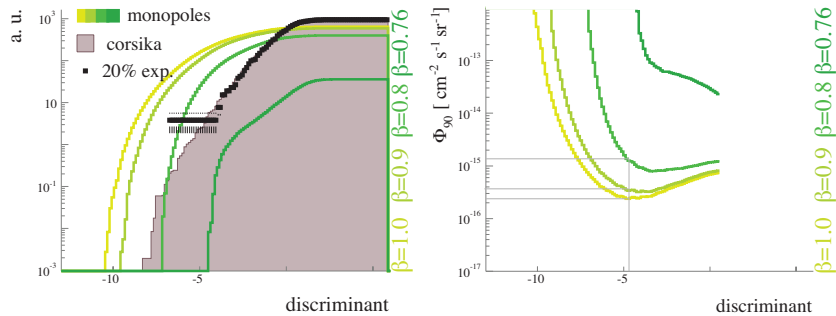


**Figure 9.7** – Distribution of the Fisher discriminant used as the final cut parameter.

**Figure 9.8** – Number of remaining events depending on the cut on the Fisher discriminant (equation(48), left) and the resulting average upper flux limits for each of the simulated monopoles speeds (right).



optimization speed	cut discriminant	background events	sensitivity ( $\Phi_{90}$ ) [ $\text{cm}^{-2}\text{s}^{-1}\text{sr}^{-1}$ ]		
			$\beta = 1.0$	$\beta = 0.9$	$\beta = 0.8$
$\beta = 1.0$	-4.7	2.59	$2.38 \times 10^{-16}$	$3.47 \times 10^{-16}$	$1.37 \times 10^{-15}$
$\beta = 0.9$	-4.1	6.75	$2.42 \times 10^{-16}$	$3.21 \times 10^{-16}$	$9.69 \times 10^{-16}$
$\beta = 0.8$	-3.4	17.41	$2.64 \times 10^{-16}$	$3.23 \times 10^{-16}$	$7.90 \times 10^{-16}$

**Table 21** – Cut values for the Fisher discriminant (equation (48)) optimized for individual monopole speeds, number of background events expected to remain in the unblinded 80% data set, and the average upper flux limits at 90% C.L (in units of  $\text{cm}^{-2}\text{s}^{-1}\text{sr}^{-1}$ ). The search for monopoles above the horizon has no sensitivity for monopoles with speeds as low as  $\beta = 0.76$ .

minimize the average flux upper limit ( $\Phi_{90}$ ) for each simulated monopole speed are listed in Table 21. As mentioned earlier, the analysis is not sensitive to  $\beta = 0.76$  monopoles: The graph representing the expected flux limit for  $\beta = 0.76$  monopoles in Figure 9.8 does not have a minimum.

As for the up-going monopoles, we choose to place only one cut, the one which yields optimum sensitivity for  $\beta = 1.0$  monopoles. The expected flux limit for  $\beta = 1.0$  monopoles reaches its minimum for a cut at  $d_0 = -4.7$ .

The *two-component* model predicts  $\langle n_b \rangle = 2.6$  background events to remain after the final cut. This prediction is obtained from summing the weights of  $N = 126$  simulated atmospheric muon events in the final background sample. According to equation (46) (section 8.2), the statistical error of the background prediction is

$$\sigma(\langle n_b \rangle) = 0.04. \quad (49)$$

The number of passing signal events is  $\mathcal{O}(10^4)$  for each of the monopole samples with  $\beta > 0.8$ , leading to a relative statistical error of  $\mathcal{O}(1\%)$  in the signal prediction.

With a background expectation of  $\langle n_b \rangle = 2.6$ , we yield an average event upper limit (see appendix D) of  $\bar{\mu} = 4.2$  events. For  $\beta = 1.0$  monopoles, this corresponds to a limit expectation of  $\Phi_{90} = 2.38 \times 10^{-16} \text{ cm}^{-2}\text{s}^{-1}\text{sr}^{-1}$ , roughly a factor of six higher than the sensitivity for up-going monopoles of the same speed. The sensitivity to down-going monopoles rapidly diminishes towards slower monopole speeds. For monopoles with  $\beta = 0.8$ , the expected flux limit lies above the *Parker Bound* (see section 2.4).

### 9.3 Unblinding results

After applying the processing steps and selection criteria developed with the 20% sample of experimental data, the 80% data set is unblinded. Figure 9.9 shows the distribution of the final cut parameter (Fisher discriminant equation (48)) before imposing the final cut.

Three experimental events pass the cut. Table 9.3 lists the run number and the days of the year on which the events were recorded, the event identification numbers, and the values of the two observables that entered the Fisher discriminant. The position of the three events in the two-dimensional cut parameter space ( $\cos \Theta - \Sigma \text{ADC}_{\text{optical}}^{z < 100}$  - plane) is shown in Figure 9.10. All three events lie close to the region of the parameter space where the remaining atmospheric muon background is expected. A visual inspection

*final cut (down-going)*

$$\begin{pmatrix} 7.866 \\ -0.010 \end{pmatrix} \cdot \begin{pmatrix} \cos \Theta \\ \Sigma \text{ADC} \end{pmatrix} < -4.7$$

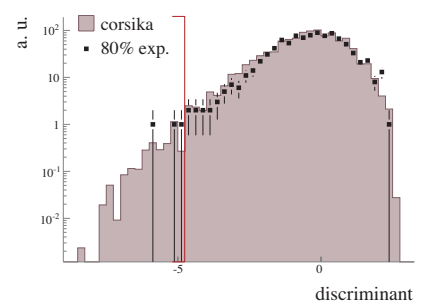
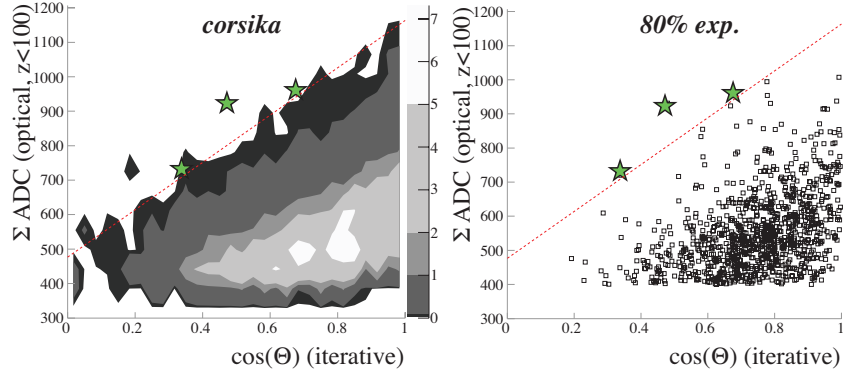


**Figure 9.9** – Distribution of the final cut parameter (Fisher discriminant equation (48)) for the 80% unblinded data set (black markers) and simulated atmospheric muon background (*two-component*-model, light purple histogram). The red line marks the cut.

**Figure 9.10** – The three remaining experimental events (green stars) in the  $\cos\Theta$ - $\Sigma\text{ADC}_{\text{optical}}^{z<100}$  - plane compared to the the distributions of the simulated atmospheric muon background (left panel) and to the 80% experimental data before applying the final cut (red line).



of the event signatures does not reveal any unexpected characteristics, supporting the assumption that the three remaining events are in fact atmospheric muon events. Figure 9.3 shows snapshots of the event signatures in the event display.

A confidence belt construction following Feldman and Cousins [175] yields an event upper limit 4.83, slightly higher than the limit expectation  $\bar{\mu} = 4.2$ . Consequently, the flux upper bounds will be slightly higher than the limit expectations listed in Table 21. In addition, the incorporation of systematic uncertainties in the predicted events rates will alter the final flux limit (see section 10).

run #	day	event #	zenith [°]	$\Sigma\text{ADC}_{\text{optical}}^{z<100}$ [PE]
206	55	484694	61.7	920.7
206	55	624780	46.9	966.3
281	125	2189202	69.8	739.2

**Table 22** – Run number, day of the year (counted from January 1<sup>st</sup> 2000), event identification number, reconstructed zenith angle (12-fold iterative likelihood reconstruction), and amplitude sum (in photoelectrons) recorded in optically read-out channels below a depth of  $z = 100$  m relative to the detector center for the three events in the 80% experimental data set which passed the final cut.

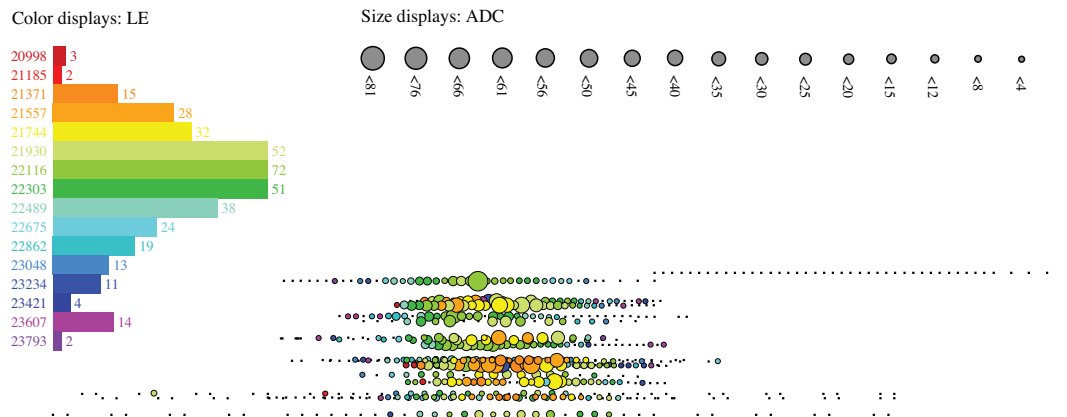
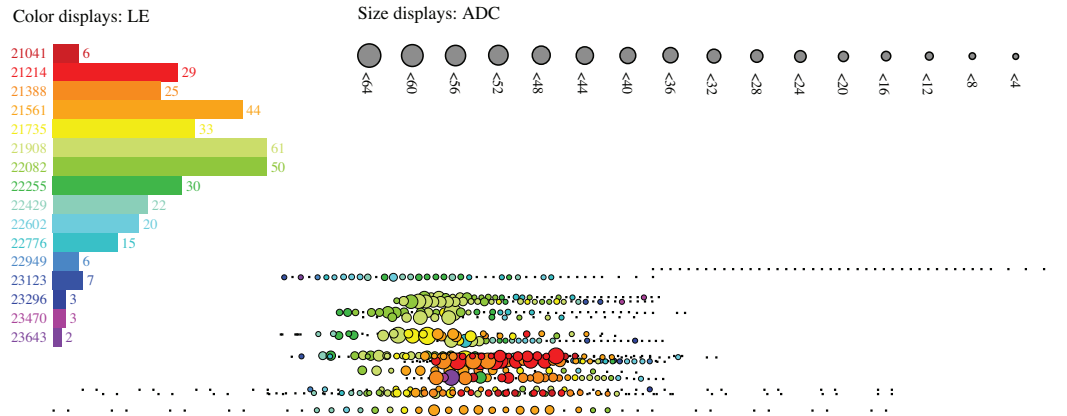
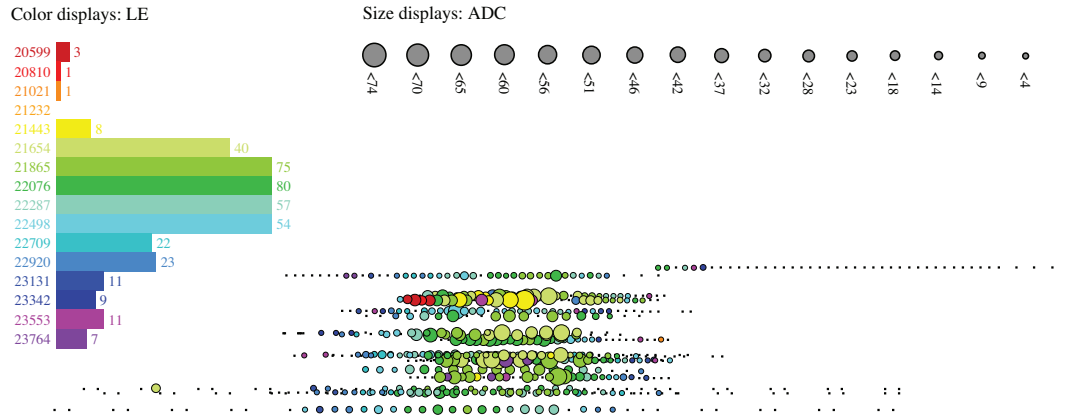


Figure 9.11 – Event displays of the experimental passing the final cut: event #484694 (left), event # 624780 (middle), and event #2189202 (right).

## 10 Limit on the flux of relativistic magnetic monopoles

A limit on a physical quantity can be derived by comparing the number of events expected from all sources of background to the number of events detected in an experiment and determining how much room there is for a contribution from a new process, *i.e.*, for signal. How well the numbers of expected and detected events compare in practice depends on the uncertainties of the predictions for background and detection efficiency.

For this analysis, statistical and systematic uncertainties are incorporated into the limit calculation using a method proposed by Conrad *et al.* [176]. The algorithm is explained in detail in appendix D.5.

### 10.1 Systematic uncertainties

The predicted number of signal and background events are determined from Monte Carlo simulations, which contain various kinds of uncertainties. The most obvious uncertainty is the statistical error associated with the finite number of simulated events in the Monte Carlo samples. The statistical error for this analysis is relatively small, due to the use of importance sampling. While the statistical error is exactly known, the other types of errors, so-called systematic errors, are more speculative. These errors arise from imperfections of the detector simulation and from theoretical uncertainties of the parameters entering the generation of Monte Carlo events.

The estimation of the total systematic uncertainty proceeds differently for signal and background prediction. For the atmospheric muon background we have used experimental data to adjust the event rates observed in simulated data, *i.e.*, we could to some extent “calibrate” the simulation, thereby eliminating some of the uncertainty. For the signal simulation on the other hand, no such calibration beam is available, and the effect of each parameter bearing uncertainty has to be assessed individually.

#### 10.1.1 Systematic uncertainty in the signal detection efficiency

The two parameters that are believed to be most crucial to the detector efficiency are the sensitivity of the OMs and the optical properties of the Polar ice. The effect of uncertainties in these parameters can ideally be determined by generating Monte Carlo samples with various simulation setups, in which the uncertain parameters are modified. For analyses involving very large signals like those from relativistic magnetic monopoles or UHE neutrinos, this would require an impractical amount of computing time.

Hence, we estimate the systematic errors related to the OM sensitivities and ice properties based on systematic studies available in the low energy region.

**Uncertainties in the optical module sensitivity:** Before deployment, the OM sensitivities were measured in the laboratory. The response of the deployed OMs can however deviate from that observed under laboratory conditions. Potential reasons for deviations are a decrease in the transparency of the silicon gel between the PMT and the glass sphere due to

aging, shadowing of the OM sensitive area by the string cable, or air bubbles that accumulate in the vicinity of the OMs during re-freezing of the water in the bore-hole. The OMs are inaccessible after deployment, and their sensitivity can only be evaluated indirectly. The most recent study [165] of OM sensitivities based on atmospheric muon data indicates deviations of the sensitivity up to 15% relative to the values used in the standard simulation setup. The largest deviations ( $\sim -15\%$ ) are observed for OMs located on the four innermost strings (strings 1-4, which were not used for the final selection criteria of this analysis). For a TeV neutrino point source search, such variations in the OM sensitivity change in the signal detection efficiency by  $+2/-10\%$  [93] and the rate of (low energy) background atmospheric neutrinos about twice that. These findings are consistent with an earlier systematic study for the AMANDA-B10 sub-array [177], which showed that variations of the OM sensitivities mostly affect low energy events. The latter study also found a linear dependency between changes in the OM sensitivities and changes of the atmospheric neutrino event: A relative shift of the OM sensitivities by a constant percentage resulted in a shift of the trigger rate by the same percentage.

Given the results presented in [165], we assume the OM sensitivities deviate from the nominal values by less than 15%. If we assume further that the weakening of the dependency of the event rates on OM sensitivities with energy holds up to the highest energies, we would expect the systematic error on the final event rates to be less than 15%. Recent UHE neutrino analyses [178, 179] assumed 15% systematic error due to uncertainties in the OM sensitivity. Because of the absence of a conclusive systematic study, we adopt this (probably overly conservative) value as systematic error.

**Uncertainties in the description of the Polar ice:** The depth dependent optical parameters of the South Polar ice were determined to an accuracy of a few percent [114]. While the numerical values of the measured scattering lengths and absorption coefficients are largely considered trustworthy, there is presently less confidence in the implementation of photon propagation in the simulation software. The distrust refers however solely to the correct treatment of photon propagation through multiple ice layers.

The systematic error related to the photon propagation implementation was studied within the AMANDA-II neutrino point source analysis. The difference in the predicted event numbers from simulations with two alternative sets of photon tables, one generated with the photon tracking package PTD and one generated with Photonics (see section 5.1.1), was as small as 2% for neutrinos with an  $E^{-2}$  power-law energy spectrum and 5% for atmospheric neutrinos. Again, the systematic uncertainty in the event rates seems to decrease with energy. These findings support the idea that for very bright events, which illuminate a wide range of the detector, the layering of the ice becomes negligible. Thus, we can expect that the systematic error introduced by neglecting the layering altogether (as we did for this analysis), will be small at highest energies. A simulation using average optical ice parameters (*BULK-ice*) will however be more sensitive to variations in the parameters themselves. The effect of varied optical parameters in simulations utilizing *BULK-ice* was investigated within the UHE neutrino search with AMANDA-B10 [180]. The optical parameters were varied over a large range, between  $+12\%/-30\%$  (absorption length) and  $+8\%/-21\%$  (effective scattering length) around the standard values. These variations caused a change in the event rates of 34% around the average. The op-

tical parameters of the Polar ice are known to within a few percent, and we can reasonably assume that the systematic error is in effect smaller. For this analysis, we conservatively assume 15% systematic error due to uncertainties in the modeling of the Polar ice.

**Theoretical uncertainty:** Theoretical uncertainties that affect the detection efficiency are related to the monopole propagation in the ice. Our signal simulation neglects Cherenkov light from relativistic secondary particles that are produced in radiative energy loss processes. This additional Cherenkov light would result in an improved detection efficiency, and hence a higher signal expectation. The improvement would however only be significant for extremely relativistic monopoles. Hence, we do not incorporate this theoretical uncertainty in our limit calculation.

The statistical errors in the number of expected signal events (0.1% and 1.5% for up- and down-going signal, respectively) are negligible compared to the assumed systematic uncertainties due to uncertainties in the detector simulation. The two systematic errors considered (15% due to OM sensitivities and 15% due to modeling of the Polar ice) are assumed to be independent resulting in a total error of 21%.

### 10.1.2 Systematic error in the background prediction

Most of the uncertainty in the simulation of cosmic ray induced events is of theoretical nature. The rate of atmospheric muon events in AMANDA-II primarily depends on the absolute flux, the energy spectrum, and, to some extent, on the composition of cosmic rays interacting in the atmosphere above the detector. These quantities have been measured by a variety of experiments which are subject to systematic uncertainties themselves. Estimates of the uncertainty in the absolute normalization of the flux (which has the largest impact in the AMANDA event rate) for instance, range from 20% [84] to a factor of two [46]. Another major source of uncertainty is the modeling of hadronic interactions in high energy air showers. As mentioned in section 5.3.1, the particular interaction model used for this analysis predicts too low a rate of high energy atmospheric muons, while the muon energy spectrum is in good agreement with what is observed experimentally.

The theoretical uncertainty of the absolute flux is compensated through normalizing the number simulated events to the number of events observed in the 20% experimental data. The number of background events predicted by the simulation does however also scale with variations of the parameters in the detector simulation, and normalizing simulated events to experimental data compensates for uncertainties in these parameters as well. Thus, the various error contributions cannot be disentangled.

For this analysis, we have re-adjusted the normalization at each analysis level, up to the penultimate cut level. In order to estimate the *total* uncertainty inherent in the simulation, we consider the variations in the normalization (ratio of number of events in the 20% experimental data set and number of events in the simulated data set) throughout the analysis: Figure 10.1 shows the variations of the normalization with the analysis level. Throughout the analysis, the normalization fluctuates in both directions around its mean value, which amounts to 1.24.<sup>45</sup> The ratio after applying

<sup>45</sup>It is important to note that there is no systematic increase or decrease of the normalization with increasing cut strength (*i.e.*, with increasing energy threshold). Such

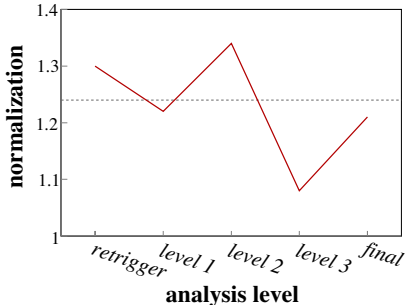


**Figure 10.1** – Normalization factor (ratio between number of events in the 20% experimental data set and number of events in the simulated data set) at each cut level (red line) compared to the average of 1.24 (dotted line). The normalization determined after imposing the penultimate cut is kept and used for predicting the number of events remaining after application of the final cut.

	up-going		down-going	
	signal	background	signal	background
OM sensitivity	15%		15%	
ice properties	15%		15%	
cosmic ray flux + detector response		13%		13%
statistical	0.1%	12%	~1%	1.5%
<b>total</b>	<b>21%</b>	<b>18%</b>	<b>21%</b>	<b>13%</b>

**Table 23** – Relative systematic and statistical errors used for the limit calculation.

the penultimate cut, is 1.21. This normalization factor is kept and used to predict the number of background events that remain after the final cut. We assume that the uncertainty in this prediction is at the same scale as the variation in the normalization over the course of the analysis. We take the maximum deviation from the mean value ( $\sim 13\%$  at selection *level 3*) as estimate for the systematic uncertainty in the background prediction.

This assessment of the uncertainty in the number of expected background events yields a substantially smaller systematic error than assumed in recent UHE neutrino analyses. These analyses considered potential systematic error sources (ice properties, OM sensitivities, cosmic ray flux normalization) independently, resulting in a total systematic error of up to  $\sim 100\%$  [168]. The two approaches may be debatable, but it should be noticed that for an analysis with low background, the dependency of the final limit on systematic uncertainties in the background expectation is weak [176]. Using a systematic uncertainty of 100% in the expected background for this analysis would alter the flux limits by no more than 2% (up-going monopoles) and 13% (down-going monopoles) compared to flux limits obtained assuming the smaller (13%) systematic error.

The statistical error amounts to 12% for the up-going background sample and 1.5% for the down-going sample. Systematic and statistical errors are added in quadrature, resulting in a total error of 18% and 13% for up- and down-going samples, respectively.

## 10.2 Flux limits including systematic and statistical errors

The total errors in the numbers of signal and background events are listed in Table 23. They are incorporated into the calculation of the flux upper limits following the method described in appendix D.5. The incorporation of uncertainties generally leads to a widening of the confidence belt, and consequently, a in a less stringent upper limit. In our case, systematic uncertainties cause a loosening of the flux limits by roughly 7% for both up- and down-going monopoles. The final flux limits obtained for up- and down-going monopoles at the simulated speeds are listed in Table 24.

a trend would suggest a potentially incorrect simulation of the energy response of the detector.

$\beta$	limit [ $\text{cm}^{-2}\text{s}^{-1}\text{sr}^{-1}$ ]
	up-going
0.76	$8.75 \times 10^{-16}$
0.8	$6.70 \times 10^{-17}$
0.9	$4.29 \times 10^{-17}$
1.0	$3.75 \times 10^{-17}$
	down-going
0.8	$1.67 \times 10^{-15}$
0.9	$4.22 \times 10^{-16}$
1.0	$2.89 \times 10^{-16}$

**Table 24** – Limits (in units of  $\text{cm}^{-2}\text{s}^{-1}\text{sr}^{-1}$ ) on the flux of up- and down-going magnetic monopoles including systematic uncertainties.

### 10.3 Discussion

The limits obtained from the monopole search below the horizon (up-going monopoles) are the most stringent constraints on the cosmic flux of magnetic monopoles today. The limits obtained from the search above the horizon are less stringent, but are valid over a larger range of potential monopole masses.

#### 10.3.1 Monopole mass range

The flux limits for up- and down-going monopoles listed in Table 24 apply for those monopoles that can pass through the Earth or the ice overburden above the detector and reach the detector with a speed above the Cherenkov threshold.

The Cherenkov threshold in ice ( $\beta \approx 0.75$ ) corresponds to a Lorentz boost of  $\Gamma = 1.51$ . In order to reach the detector with this at least this boost, the monopole is required to have mass of at least

$$M > \frac{\Delta E}{\Gamma_{\text{initial}} - 1.51}, \quad (50)$$

where  $\Delta E$  is the energy lost during propagation to the detector, and  $\Gamma_{\text{initial}}$  is the Lorentz boost before entering the Earth. That is, relativistic monopoles require a mass at least of the order of the energy loss in order to be detectable.

The minimum masses for which the flux limits on up- and down-going monopoles are valid without further conditions on the initial Lorentz boost are given by the energy losses suffered by monopoles passing the full diameter of the Earth and passing through  $\approx 180$  km ice (the path to reach the detector from just above the horizon), respectively. The modified Bethe-Bloch formula (equation (24), section 3.4.2) predicts a total energy loss of  $\Delta E = \mathcal{O}(10^{11})$  GeV for vertically up-going monopoles, and  $\Delta E = \mathcal{O}(10^8)$  GeV for down-going monopoles entering the detector from just above the horizon. That is, monopole searches below and above the horizon reach full acceptance to moderately relativistic monopoles with masses above  $10^{11}$  GeV and  $10^8$  GeV respectively.

For ultra-relativistic monopoles, full acceptance may be reached for much lower monopole masses. Monopoles with a mass in the PeV region, for instance, are predicted to be capable of penetrating the Earth if they have an initial Lorentz boost around  $\Gamma_{\text{initial}} = 10^5$  or higher (see Figure 3.11 in section 3.4.2).

#### 10.3.2 Comparison to other experimental limits

Figure 10.2 shows the limits in comparison to the best presently available experimental bounds. In the velocity range  $\beta > 0.8$ , the most stringent limits are the ones set by the BAIKAL neutrino telescope. These limits lie between  $5 \times 10^{-17} \text{ cm}^{-2} \text{ s}^{-1} \text{ sr}^{-1}$  ( $\beta = 1.0$ ) and  $1.9 \cdot 10^{-16} \text{ cm}^{-2} \text{ s}^{-1} \text{ sr}^{-1}$  ( $\beta = 0.8$ ), and are valid for monopoles that are capable of penetrating through the Earth [102].

The MACRO experiment constrains the flux of magnetic monopoles below a level of  $1.4 \times 10^{-16} \text{ cm}^{-2} \text{ s}^{-1} \text{ sr}^{-1}$  [58]. This limit is valid for full acceptance over  $4\pi$  sr, *i.e.*, for the mass range in which monopoles can penetrate through the Earth and reach the detector from all directions. For  $2\pi$  sr ac-

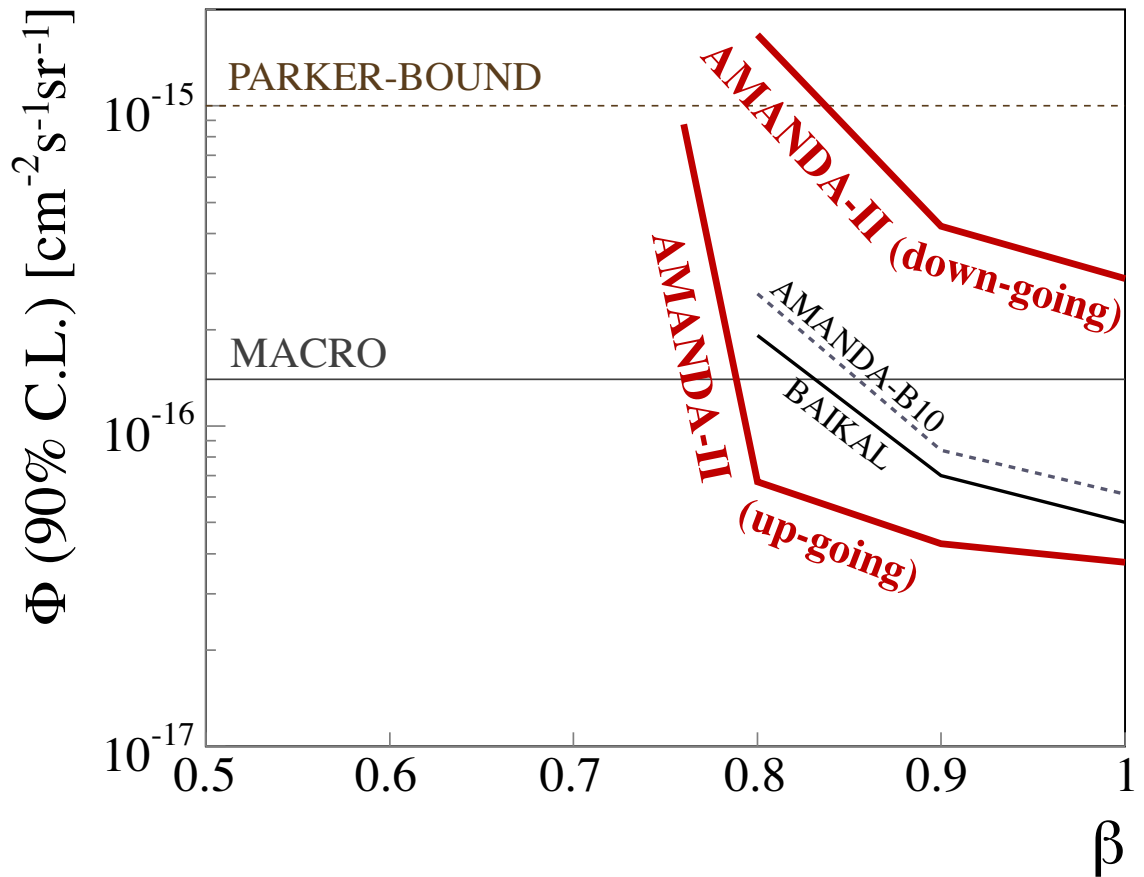


**Figure 10.2** – Limits on the flux of relativistic magnetic monopoles. The AMANDA-II limits (this work) are shown in red. (For the sake of clarity, the limits obtained for the discrete monopole speeds are connected with straight lines.) The limit on up-going monopoles falls below the presently most stringent limit set by the BAIKAL neutrino telescope (black solid line). The former limit obtained from the analysis of data taken with the AMANDA-B10 sub-detector [103] is shown for comparison (gray dashed line).

ceptance, *i.e.*, for the mass range in which monopoles cannot pass through the Earth but reach the detector from above the horizon, the limit has to be multiplied by two [58]. For this case, the MACRO limit is at about the same level as the AMANDA-II limit for down-going monopoles.

## 11 Summary and outlook

Relativistic magnetic monopoles which cross a transparent medium at a speed above the Cherenkov threshold are predicted to emit Cherenkov radiation that is more intense than that emitted by relativistic muons by several orders of magnitude. Data taken with the AMANDA-II neutrino telescope during the year 2000 were searched for the Cherenkov signature of relativistic magnetic monopoles crossing the detector's sensitive volume. Data selection criteria were developed based on simulated atmospheric muon events (the dominant background to this search) and simulated monopole events, in which the monopoles were assumed to carry one Dirac charge and to travel at fractions of the speed of light between  $\beta = v/c = 0.76$  and  $\beta \approx 1$ . In order to ensure that the detector simulation provides an accurate description of the detector response, 20% of the experimental data was used for comparisons between experimental and simulated data throughout the analysis. This subset was then discarded, and only the complementary 80% of the data (totaling approximately 155 days of dead-time corrected data taking time), which were kept blind during the development of the analysis, were used to derive upper limits on the monopole flux.

Two separate flux limits were derived for monopoles entering from below and from above the horizon, respectively. The analysis considering monopoles entering from below the horizon yielded flux limits between  $3.8 \times 10^{-17} \text{ cm}^{-2} \text{ s}^{-1} \text{ sr}^{-1}$  ( $\beta \approx 1$ ) and  $8.8 \times 10^{-16} \text{ cm}^{-2} \text{ s}^{-1} \text{ sr}^{-1}$  ( $\beta = 0.76$ ) at the 90% confidence level. In the velocity range  $\beta > 0.8$ , these limits are the most stringent experimental limits at the time of this writing.

Because of the much larger background from down-going atmospheric muons, the analysis considering monopoles entering from above the horizon yielded limits less stringent by roughly an order of magnitude. These much looser limits are however valid for monopoles of lighter mass and lower speeds. Monopoles reaching the Earth at a speed around  $\beta = 0.9$  for instance, would have to be at least as heavy as  $10^{11}$  GeV to reach the detector from below, while a mass of  $10^8$  would suffice to reach the detector from above the horizon. For monopoles that are incapable of crossing the Earth but are capable of penetrating the matter overburden above the detector, the limit derived in this work is approximately at the same level as the presently most stringent limit placed by the MACRO experiment. The search for monopoles above the horizon presented in this work is the first analysis of this kind performed with AMANDA-data. It proves that neutrino telescopes can search relativistic magnetic monopoles above the horizon, and that these searches, despite the large atmospheric muon background, have sensitivities well below the Parker bound.

This work concerns AMANDA-II-data of the year 2000 only. The remaining data collected AMANDA-II could be searched for monopole signals as well, but the analysis of already existing data taken with the much larger IceCube detector [67], a cubic-kilometer scale neutrino telescope presently under construction at the South Pole, would yield a much better sensitivity than that achieved with the analysis multiple years of AMANDA-II data.

The construction of the IceCube detector started in the Polar season 2004/2005 and is expected to be completed by the beginning of 2011. In its final state, the IceCube detector will consist of  $\sim 5000$  optical modules deployed on 80 vertical strings. The instrumented volume will span a depth range between 1400 and 2400 meters below the ice surface and will cover a square-kilometer-sized hexagonal area in the horizontal plane. The large volume

and sparse instrumentation of the detector are ideal for the detection of rare signals with high Cherenkov light deposition. Figure 11.1 shows the Cherenkov signature of a simulated 6 PeV muon in the IceCube detector. Similarly large signals would be expected for relativistic magnetic monopoles passing through the detector. The grey shaded area indicates the location and the cross-sectional area of the AMANDA-II detector within the IceCube instrumented volume.

While conclusive studies of the sensitivity of the full IceCube detector to relativistic magnetic monopoles have not yet been undertaken, first simulations of the intermediate deployment stages of the detector indicate that upcoming monopole searches will reach sensitivities roughly an order of magnitude below the limits presented in this work [181].

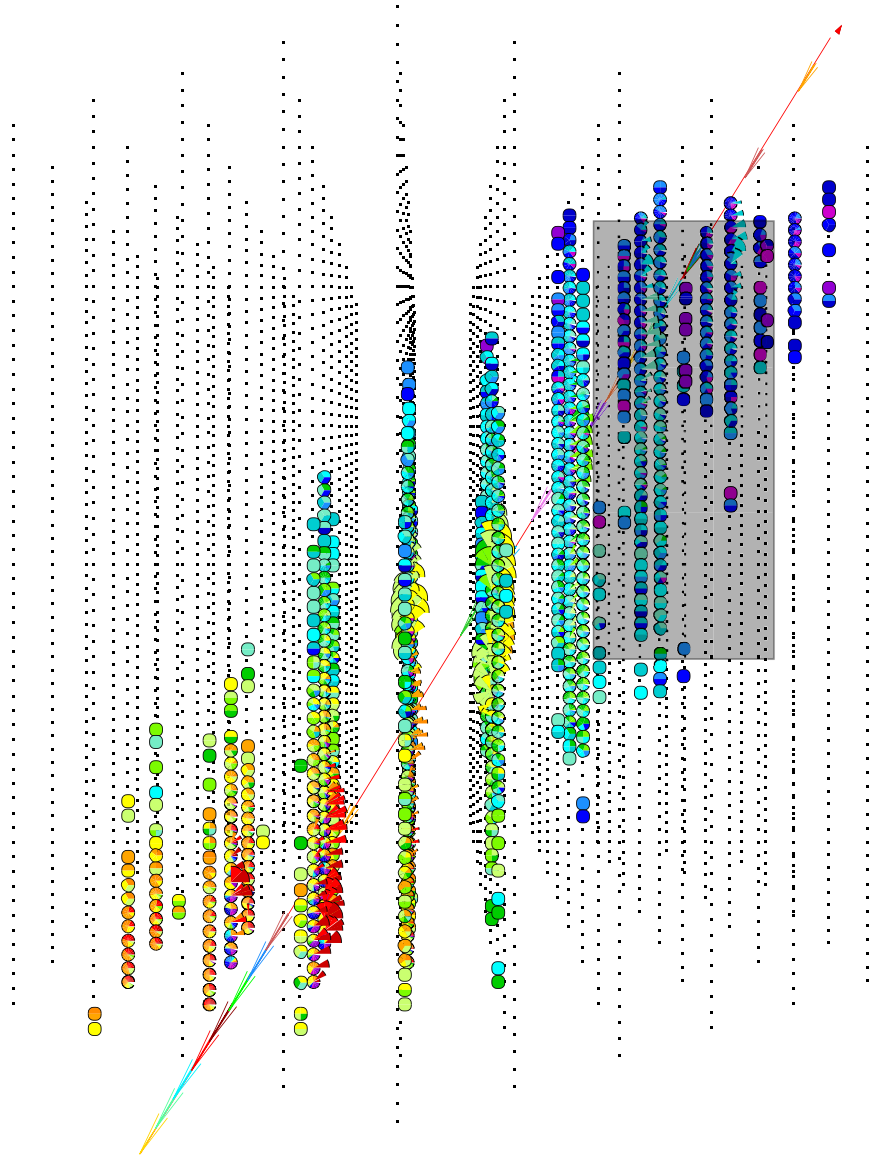


**Figure 11.1** – Simulated 6 PeV muon crossing the IceCube detector [182]. The grey shaded area indicates the location and the cross-sectional area of the AMANDA-II detector.

## A Seasonal variations of the event rate

When cosmic rays interact with air molecules in the atmosphere, mesons are produced which either re-interact to produce particles of lower energy or which decay into muons. While the decay length of the mesons depends solely on energy, the mean interaction length of the mesons depends on the density of the atmosphere. The largest variations of the atmospheric density are caused by seasonal variations of the air temperature over the year. One therefore expects seasonal variations of the atmospheric muon rate in a detector like AMANDA.

### A.1 The AMANDA-II trigger rate and the *effective* atmospheric temperature

If atmospheric muons arrive at the ice surface with an energy of 500 GeV or greater, they will be capable of reaching the AMANDA-II detector with sufficient energy to cause a trigger. In this energy range, the main reason for variations in the muon flux are temperature variations in the upper atmosphere: During summer, the increase of temperature results in an expansion of the atmosphere. In low density air, the mean free path of the mesons produced in cosmic ray interactions is longer than in dense air, and a larger fraction of the mesons decay into muons before they interact. As a consequence the flux of highly energetic atmospheric muons is larger during the summer than during the winter.

A full quantitative treatment of the development of the particle cascades would involve full particularities of the density profile and chemical composition of the atmosphere. In the altitude range of interest however, the atmosphere can be treated as ideal gas with constant molar mass ( $M = 28.96$  g/mol), and the local air density can be obtained from temperature and pressure measurements (which are delivered by weather balloons) via the ideal gas law:

$$\rho = \frac{p \cdot M}{R \cdot T}, \quad (51)$$

where  $p$  is the air pressure,  $T$  is the temperature and  $R$  is the universal gas constant (8.31451 J/(K · mol)). The vertical temperature and pressure profiles have a rather complicated structure. Examples of the vertical temperature structure of the Polar atmosphere are shown in Figure A.1. To a good approximation however, variations of the muon rate in an underground (or under water/ice) detector depend only on the so-called *effective* temperature [130]. The effective temperature is defined as the temperature of an hypothetical *isothermal* atmosphere that would result in the same meson intensity as that produced in a real atmosphere having a temperature distribution  $T(X)$ , where  $X$  is the atmospheric depth. The effective temperature  $T_{\text{eff}}$  is a weighted average over the temperature profile from ground to the top of the atmosphere. It is calculated as [131]

$$T_{\text{eff}} = \frac{\int \frac{dX}{X} T(X) [\exp(-X/\Lambda_\pi) - \exp(-X/\Lambda_N)]}{\int \frac{dX}{X} [\exp(-X/\Lambda_\pi) - \exp(-X/\Lambda_N)]}, \quad (52)$$

where  $\Lambda_\pi = 160$  gm/cm<sup>2</sup> is the atmospheric attenuation length for pions, and  $\Lambda_N = 120$  gm/cm<sup>2</sup> is the atmospheric attenuation length for nucleons.

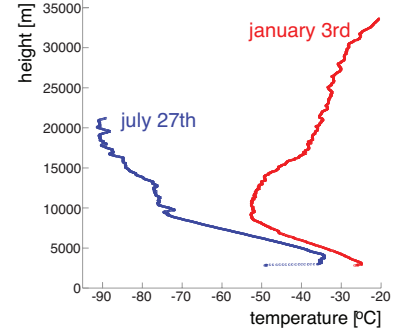


**Figure A.1** – Examples for temperature profiles of the atmosphere above the South Pole. The temperature profiles were delivered by weather balloons which were launched from the South Pole Station in 2003 on an Antarctic summer day (January 3<sup>rd</sup>, red graph) and an Antarctic winter day (July 27<sup>th</sup>, blue graph), respectively. The increase of the temperature in the stratosphere (above  $\gtrsim 10000$  m) is due to absorption of UV light.

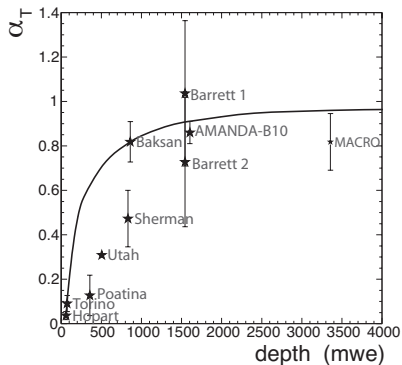


**Figure A.2** – Depth dependence of  $\alpha_T$  as measured by several underground muon detectors. The depth is given in meter water equivalent. The black curve indicates the theoretical expectation [130]. Taken from [183].

Fluctuations of the effective  $\Delta T_{\text{eff}}$ , then, relate to fluctuations of the muon rate in an underground detector  $\Delta R_\mu$  as

$$\frac{\Delta R_\mu}{\langle R_\mu \rangle} = \alpha_T \frac{\Delta T_{\text{eff}}}{\langle T_{\text{eff}} \rangle}, \quad (53)$$

where  $\langle R_\mu \rangle$  and  $\langle T_{\text{eff}} \rangle$  are the average muon rate and effective temperature, respectively. That is, the deviation of the measured muon rate from its mean will be directly proportional to the deviation of the effective temperature from its mean. The proportionality constant  $\alpha_T$  depends on the depth at which the muon intensity is measured. Figure A.2 shows  $\alpha_T$  measured by several underground muon detectors. Data taken with the AMANDA-B10 detector during the year 1997 were used to determine the value of  $\alpha_T$  for the AMANDA depth [183]. The measurement is in good agreement with the theoretical prediction [130].

It would be worthwhile to re-assess  $\alpha_T$  using several years of data taken with the full AMANDA-II array. This has however not been done yet. Nevertheless, the effective temperature of the South Polar atmosphere was determined for this analysis for the following reason: A blind analysis requires an excellent understanding of the experimental data, and stable trigger rate is a key-requirement in data quality assurance. For AMANDA monopole searches, initially four years of experimental data were filtered from raw data on (although only one year was finally fully analyzed). The trigger and re-trigger rates between January 1<sup>st</sup> 2000 and December 31<sup>st</sup> 2003 are shown in figure A.3. After correction for detector dead time, the average trigger rate over a year lies between 75 and 90 Hz. The average rate is lowest in 2000 ( $\sim 75$  Hz) and increases after the maintenance period 2000/2001. This increase is due to the recovery of several damaged or un-reliable optical modules during the Polar season 2000/2001. Throughout each year, the trigger rate varies smoothly around its mean as the seasons change. Apart from these seasonal variation, the trigger-rate shows several sudden jumps. Most of the rate instabilities occur at the beginning and at the end of each year, indicating that the DAQ was recording data although detector maintenance had already started. The maintenance periods, as well as the periods during Austral winter during which the trigger-rate shows sharp jumps or drops (for instance during days 196 to 198, or 209 to 211 in 2000) are rejected by the standard file selection (see section 6.1.1).

One discontinuity in the trigger rate however remains even after the application of quality criteria: At the end of the year 2002, the trigger rate shows a sudden jump around day # 1000. All data taken during this time period pass the file selection. An investigation of the atmospheric temperature reveals, that this sudden increase of the trigger rate coincides with a sudden increase of the temperature in the upper atmosphere above the South Pole.

## A.2 Sudden stratospheric warming in 2002

At least one weather balloon is launched every day from the South Pole station, measuring temperature, pressure and altitude during its ascension. The balloon data are available from the Antarctic Meteorological Research Center web site [184].

In order to understand the discontinuities in the AMANDA-II trigger rate, data from daily weather balloon launches during the time period between

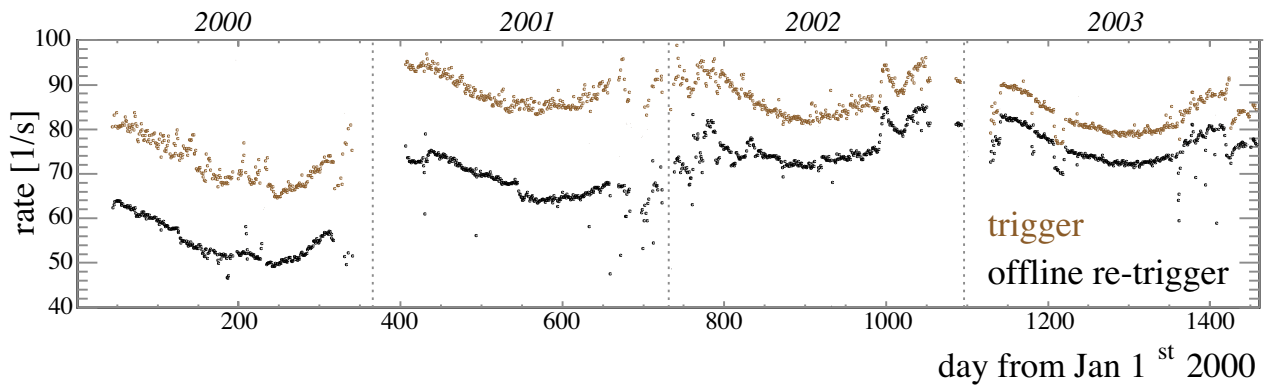


**Figure A.3** – Trigger rate from January 1<sup>st</sup> 2000 to December 31<sup>st</sup> 2003 before selection of stable data taking periods. The brown markers indicate the raw trigger rate of the detector, while the black markers indicate the event rate after a first data cleaning (the so-called *re-triggering*, see section 6.2.3 that is supposed to remove most of the electronic noise. The rising trend the event rate over the years is due to changes in the hardware of the detector. Individual malfunctioning modules in the array were recovered during the summer season (mostly during the Polar season 2000/2001), increasing the detector efficiency.

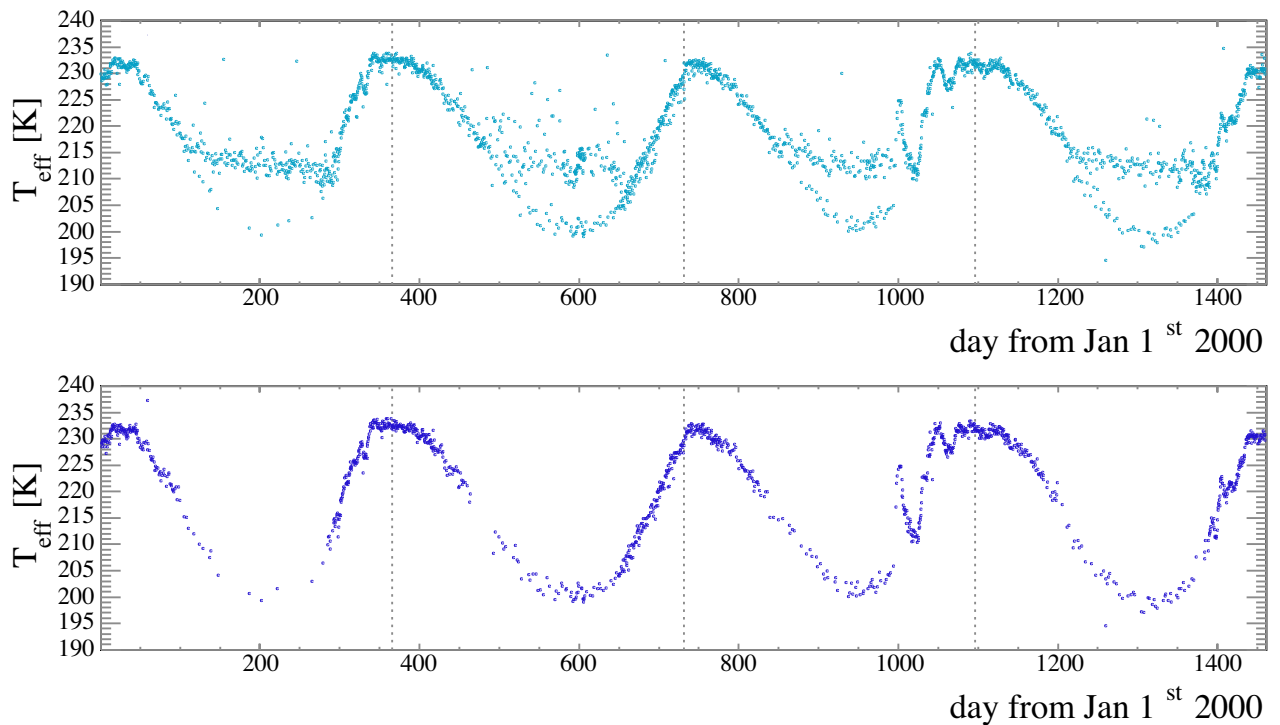


**Figure A.4** – Effective temperature calculated from data taken with weather balloons launched from the South Pole station. The upper panel shows the effective temperature from data of *all* balloon flights between 1<sup>st</sup> 2000 to December 31<sup>st</sup> 2003. The lower panel shows the effective temperature for only those flights where the balloon reached an altitude of at least 20000 meters.

January 2000 and December 2003 were analyzed. As the weather balloons take measurements roughly every 10 to 20 meters altitude during their ascension, the data from one balloon flight contain the local atmospheric temperature taken at only discrete atmospheric depths  $X_i$ . In order to calculate the effective temperature, the integral in equation (52) has to be approximated with a sum over discrete data points:

$$T_{\text{eff}} \approx \frac{\sum_i T(X_i)(\Delta X)_i/X_i [\exp(-X_i/\Lambda_\pi) - \exp(-X_i/\Lambda_N)]}{\sum_i (\Delta X)_i/X_i [\exp(-X_i/\Lambda_\pi) - \exp(-X_i/\Lambda_N)]}. \quad (54)$$

The daily effective temperature between January 1<sup>st</sup> 2000 and December 31<sup>st</sup> is shown in the upper panel of Figure A.4. The temperature curve clearly follows the Antarctic seasons, as expected. However, during the winter months, the effective temperatures seems to be ambiguous. The temperature curve is split into two sub-curves. An investigation of the balloon data revealed that the upper branch of temperature curve corresponds to those flights in which the weather balloon did not reach the top of the atmosphere. The lower panel of Figure A.4 shows the effective temperature calculated for only those flights in which the balloon reached an altitude of at least 20000 meters. This simple selection smoothes the temperature curve.

Around day #1000, the effective temperature shows a sudden increase, similar to that observed in the AMANDA-II trigger rate. Figure A.5 shows a zoomed view of the effective temperature and the trigger rate for the time period from September to December 2002.<sup>46</sup> The “oscillation-like” structures in both curves coincide.

With this sudden increase in the muon rate, AMANDA has observed an unusual sudden warming of the stratosphere above the South Pole [185]. This incident, which occurred around September 25<sup>th</sup> 2002, is well known among atmospheric scientists [186], mainly because the sudden stratospheric warming caused a split of the Ozone Hole [187].<sup>47</sup>

Temperature and ozone concentration in the atmosphere are highly correlated for the following reason: Ozone depletion in the upper atmosphere progresses most efficiently in the presence of (1) Stratospheric Polar Clouds, and (2) UV radiation. During the Polar winter night, a circumpolar wind develops in the middle to lower stratosphere, the so-called Polar Vortex. The cyclone confines a cylindrical volume of extremely cold air above the Polar region, in which Stratospheric Polar Clouds can form. With the beginning of spring, sun light reaches the Polar region, but low temperatures and stratospheric clouds persist, as the cold air is trapped within the Vortex. Ozone is efficiently depleted. Around September 25<sup>th</sup> 2002, however, the Polar Vortex split into two separate cyclones, and with it, the Ozone Hole split into two smaller holes. Cold air was no longer trapped above the South Pole. The temperature in the stratosphere jumped by  $\sim 40$  K within days.

Figure A.6 shows snapshots of the ozone concentration in the atmosphere of the southern hemisphere and the temperature measured at two different pressure levels in the upper atmosphere (100 mbar and 30 mbar) between September 15<sup>th</sup> and October 4<sup>th</sup>.

<sup>46</sup> Unfortunately, AMANDA was not taking data from mid-November on, because of maintenance work. Hence, the trigger rate curve is cut off around day # 1050.

<sup>47</sup> A non-technical report on the incident can be found on the NASA web site <http://www.gsfc.nasa.gov/topstory/20020926ozonehole.html>.

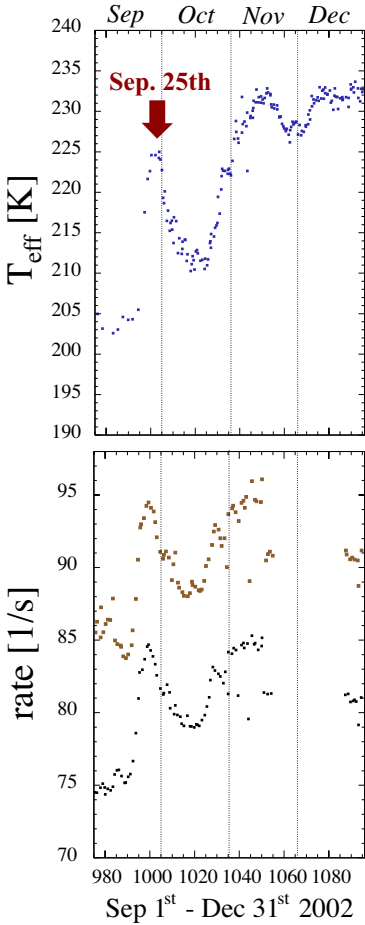


**Figure A.5** – Effective temperature (top) and trigger rate between September 1<sup>st</sup> and December 31<sup>st</sup> 2002.

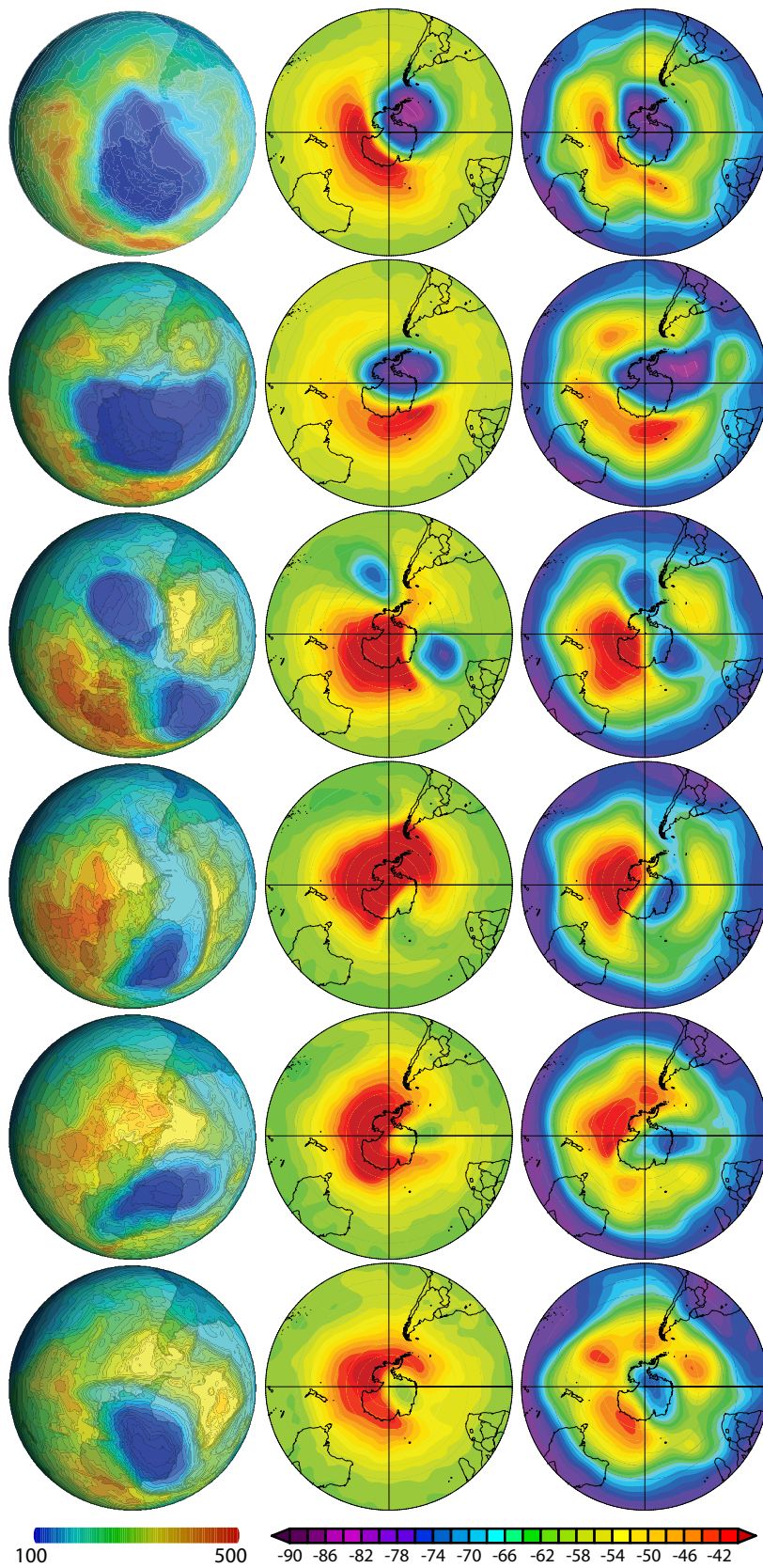


**Figure A.6** – Ozone concentration (left column) and atmospheric temperatures in the 30 mbar (middle column) and 100 mbar (right column) layers on the southern hemisphere. Each row shows snapshots of ozone and temperature for one particular day during the dramatic stratospheric warming in 2002: September 15<sup>th</sup> (top row), September 20<sup>th</sup>, September 25<sup>th</sup>, September 30<sup>th</sup>, October 4<sup>th</sup>, and October 9<sup>th</sup> (bottom row). Ozone contours correspond to Dobson Units (Dobson Units give the thickness (in units of  $10 \mu\text{m}$ ) of the ozone layer if all ozone contained in an air column overhead were compressed to 1 atm standard pressure and  $0^\circ\text{C}$  [188]); temperatures are in  $^\circ\text{C}$ . Ozone plots are provided by NASA [189], temperature plots were generated with the web-interface to the climate research data base of the *National Oceanic & Atmospheric Administration* (NOAA) [190].

## B Tagging events caused by electronic noise

An indication that AMANDA data have admixtures of hits and/or entire events that are not caused by light in the detector was first observed in the overall data-rate (bytes per second) which showed occasional jumps, while the trigger rate remained approximately constant. These states of high data rates were investigated in great detail [134]. It was found that data taken during these periods contained many events with high hit multiplicities. The correlation between hit-times and the depths of the OMs in which these hits supposedly occurred indicated that these events were of pure electronic origin. Figure B.1 shows examples of the correlation of leading edge times and OM number<sup>48</sup> (the so-called *fingerprints*) in a typical atmospheric muon event (upper panel) and in events caused by electronic noise, referred to as *flare events* hereafter.

The so-called *flare checker* module (developed in [134]) is a tool to identify and reject potential flare events based on nine variables, the nine *flare-indicators*.

### B.1 The flare indicators

For developing the flare checker, flare events were selected and inspected. A set of nine features was identified which commonly occur in flare events and are untypical for particle induced events:

- (1) a high fraction of channels for which a peak ADC value was recorded, but neither leading nor trailing edges,
- (2) a high fraction of channels which have unpaired edges, *i.e.*, channels where the recorded edge series contain at least two consecutive leading or two consecutive trailing edges,
- (3) many hits in otherwise dead channels,
- (4) many hits with extremely short TOT in channels with signal transmission via twisted pair cables,
- (5) many hits with extremely short TOT in channels with signal transmission either via coaxial cable or via twisted pair cable if the corresponding OM is a so-called *hybrid* OM,<sup>49</sup>
- (6) many hits with extremely long TOT, occurring significantly before the trigger time,
- (7) many TDC edge series which start or end with an unpaired edge which is nevertheless well contained in the TDC buffer (if an edge series either starts with a trailing edge or ends with a leading edge *and* there is large time gap between unpaired edge and the boundary of the TDC buffer, the first or last pulse would have had an overlong TOT.),

<sup>48</sup>OMs in each string are numbered such that the OM with the lowest number is closest to the surface, and the OM number increases with depth. Hence the OM number is a measure for the depth at which the OM is located.

<sup>49</sup>Hybrid OMs are OMs which are read out via twisted pair cables but contain an LED for pulse conversion from electrical to optical. For test purposes, a few such hybrid OMs were deployed with strings 5-10. The fiber readout is however not used during normal data taking. Anyway, due to the hardware differences, the TOT characteristics of hybrid channels differs from the one of conventional twisted pair channels. As pulses from hybrid channels typically have larger TOTs (similar to coaxial channels), they fall, in the context of flare indicators, into the same class as coaxial channels.

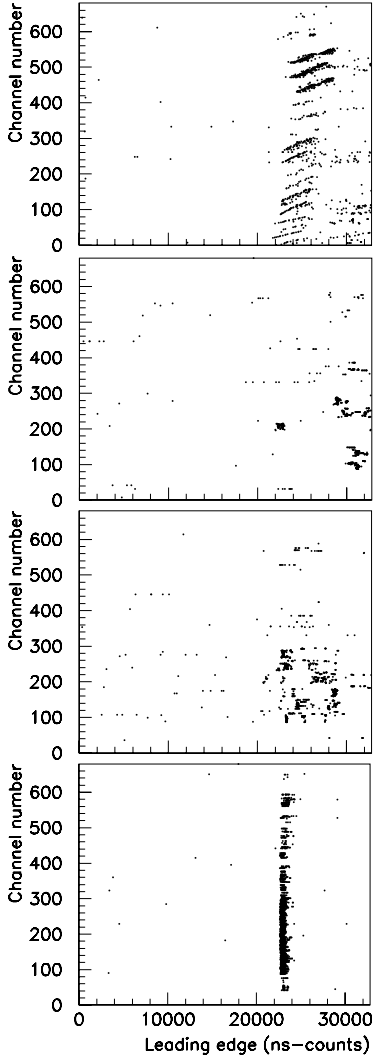


**Figure B.1** – Fingerprints of an atmospheric muon event (uppermost panel) and of three flare events. In flare events, leading edge time and the depth in which the hit supposedly occurred are totally uncorrelated. This suggests that the pulses are created close to the surface. Taken from [134].

- (8) an extremely high number hits occurring in strings 5-10 (whose channels are particularly prone to noise pick-up) compared to the number of hits occurring in strings 1-4, and
- (9) an extremely high number hits occurring in strings 5-10 compared to the number of hits occurring in strings 11-19.

The probability for particle induced events to expose one of the above flare features was obtained from atmospheric muon data at trigger level. For each feature a so-called *flare-indicator* was defined such that it represented the negative logarithm of the probability for a muon event to expose as much of the flare feature as actually observed. In particular, in a sample of  $N$  particle events the expected number of events with an indicator  $I$  above a certain value  $I_{\text{cut}}$ ,  $N(I > I_{\text{cut}})$ , falls like [134].

$$N(I > I_{\text{cut}}) \sim N \cdot 10^{-I_{\text{cut}}}. \quad (55)$$

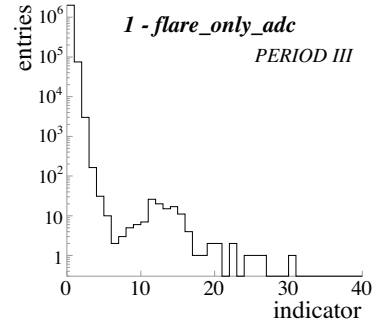
That is, one expects less than one event with  $I_{\text{cut}} > \log_{10} N$  in an event sample with  $N$  events.

Figure B.2 shows an example of the flare indicator based on feature (1) from the above list. The shape of the distribution is typical: The extent to which flare features are found in muon data falls exponentially, visible as the exponential fall-off at low indicator values. Those events with higher indicator values ( $> \sim 7$  in this example) are probably due to electronic noise, or have at least a significant contribution from noise hits.

Flare checking is *extremely* important to monopole search. In many flare events, a large number of hits is observed, which is also expected for the signal of relativistic monopoles. On the other hand, monopole Cherenkov signatures may yield so much light that many TDCs overflow (*i.e.*, register more than 16 edges) during an event. This could wash out the space-time pattern of hits that is typical for the Cherenkov emission, and the event fingerprint might appear less structured than for low energy atmospheric muon events. Events with extremely high hit multiplicities might, to some extent, expose flare features. To what extent the flare indicators are enhanced in signal events can, unfortunately, not be determined from Monte Carlo simulations, because the origin of electronic noise causing flare events or are not understood and hence not included in the detector simulation. Therefore, the suitability of the flare indicators for potential signal events has to be assessed from experimental data alone.

### B.1.1 Flare indicators in this analysis

The first flare indicator (referred to as **flare\_only\_adc** hereafter) is based on the number of channels which recorded a valid ADC but no edges (see item (1) in the above list) This mis-behavior cannot be reproduced in the Monte Carlo. *I.e.*, the indicator is zero for simulated events. Figure B.3 shows this flare indicator for experimental data at trigger level and *level 1* of this analysis, simulated atmospheric muon events, and simulated magnetic monopoles with  $\beta = 1.0$  and  $\beta = 0.76$  (both at *level 1*). The distributions are shown separately for each of three periods for which different OM selections were defined (see section 6.2.1). Experimental data are shown at both trigger level (1% of the data set, open histograms) and at *level 1* as defined in section 6.3 (20% of the data set, black markers). Apparently, *level 1* cuts remove many events which expose the flare feature **flare\_only\_adc**. (This is also the case for most of the



**Figure B.2** – Distribution of the flare indicator (1) **flare\_only\_adc** at trigger level (*minimum-bias* data). The indicator is defined such that for muon events the indicator value falls exponentially towards higher values. The exponential part of the distribution ends roughly at 7, consistent with  $\sim 3 \cdot 10^6$  entries in the histogram (see equation (55)). Events with indicator values above this value are likely to be due to electronic noise, or have significant admixtures of noise hits.

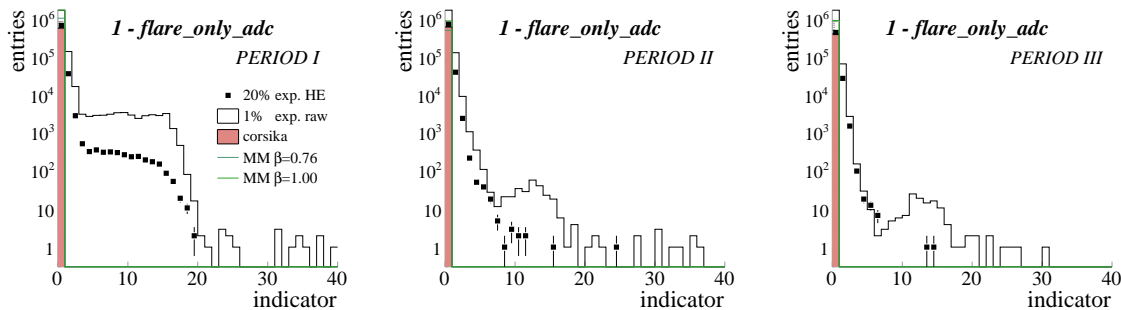


**Figure B.3** – Flare indicator `flare_only_adc` for each of the three OM selection periods. The open histograms correspond to  $\sim 1\%$  of the experimental data set at trigger level. The black markers are 20% of the experimental data at *level 1* of this analysis. For simulated events (colored histograms), the `flare_only_adc` indicator is always zero.

other indicators, see below.) We also observe that during *PERIOD I* the `flare_only_adc` distribution looks different from the subsequent periods, indicating a change in the detector stability. For this particular indicator, a set of channels which are malfunctioning (*e.g.*, due to increased noise of the ADCs) over a certain time period might be responsible for high indicator values. Inspections of the time variability of this indicator (see below) showed that in fact most of the events with indicator values greater than 7 are clustered in a small time interval at the end of *PERIOD I* (see top panel of Figure B.6).

Figures B.4 and B.5 show the distributions for the eight remaining flare indicators (plotted in the same manner as `flare_only_adc` in Figure B.3). For experimental data, the typical shape of an exponential at small indicator values (due to muon events) and an additional bump at higher indicator values (due to flare events) is clearly visible. For some indicators, The distributions differ for the three time periods, suggesting instabilities in the detector behavior.

### B.1.2 Time dependent behavior of the indicators

One reason for specific flare indicators to show transient behavior is that they can be dominated by certain groups of OMs that are malfunctioning over certain time periods. Another reason for periods of enhanced flare rates can be temporarily increased electronic noise in the entire detector, which might, for instance, be caused by bad weather conditions. Figure B.6 shows the behavior of the nine flare indicators with time. Events with extremely high flare indicator values cluster in certain time intervals. For the indicator `flare_only_adc`, the cluster at the end of *PERIOD I* (around day 117) is clearly visible. Other clusters on day 146 and 157 are visible in a variety of indicators. These periods were inspected and certain time periods were excluded from the analysis.

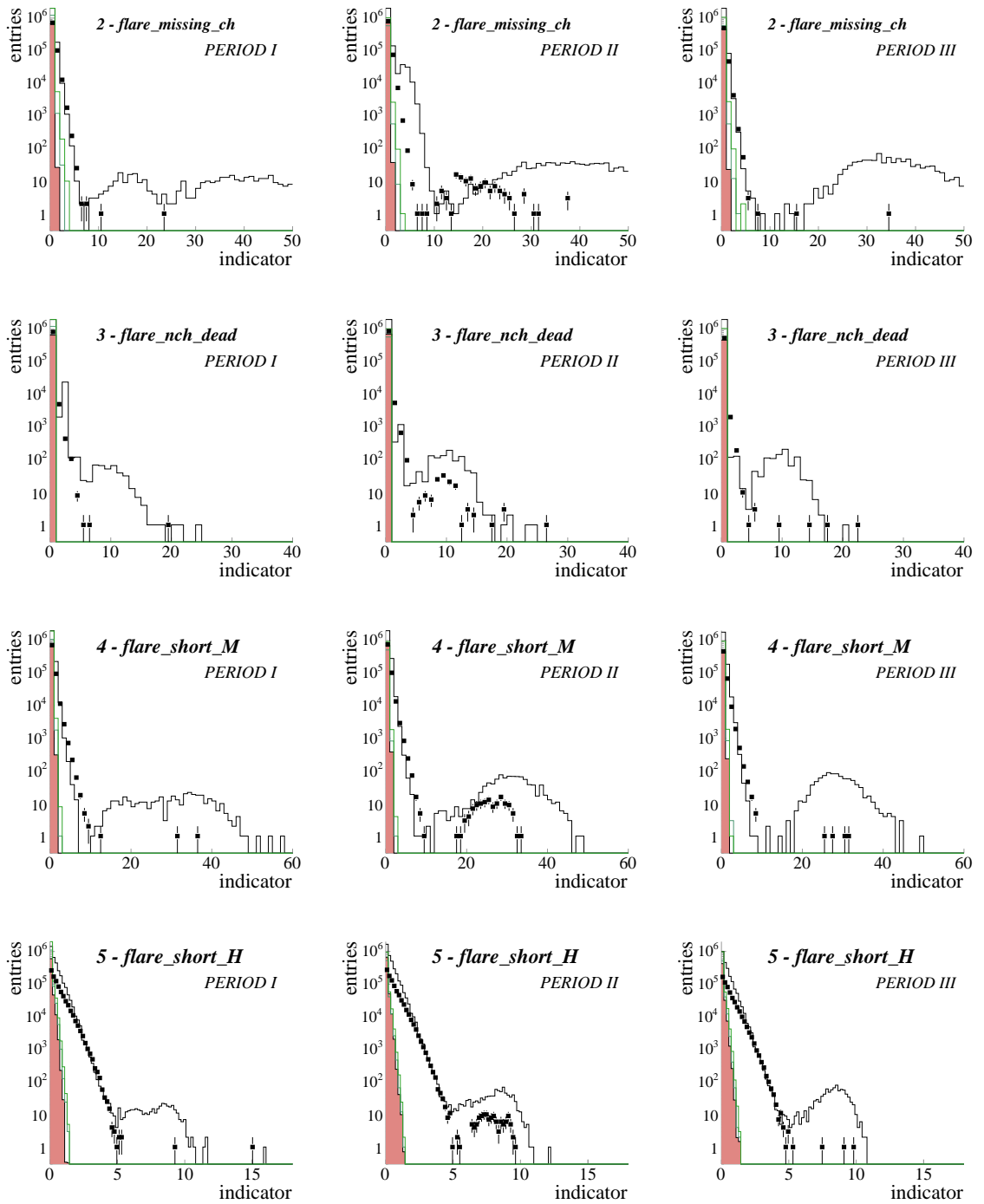


Figure B.4 – Flare indicators (2) to (5).

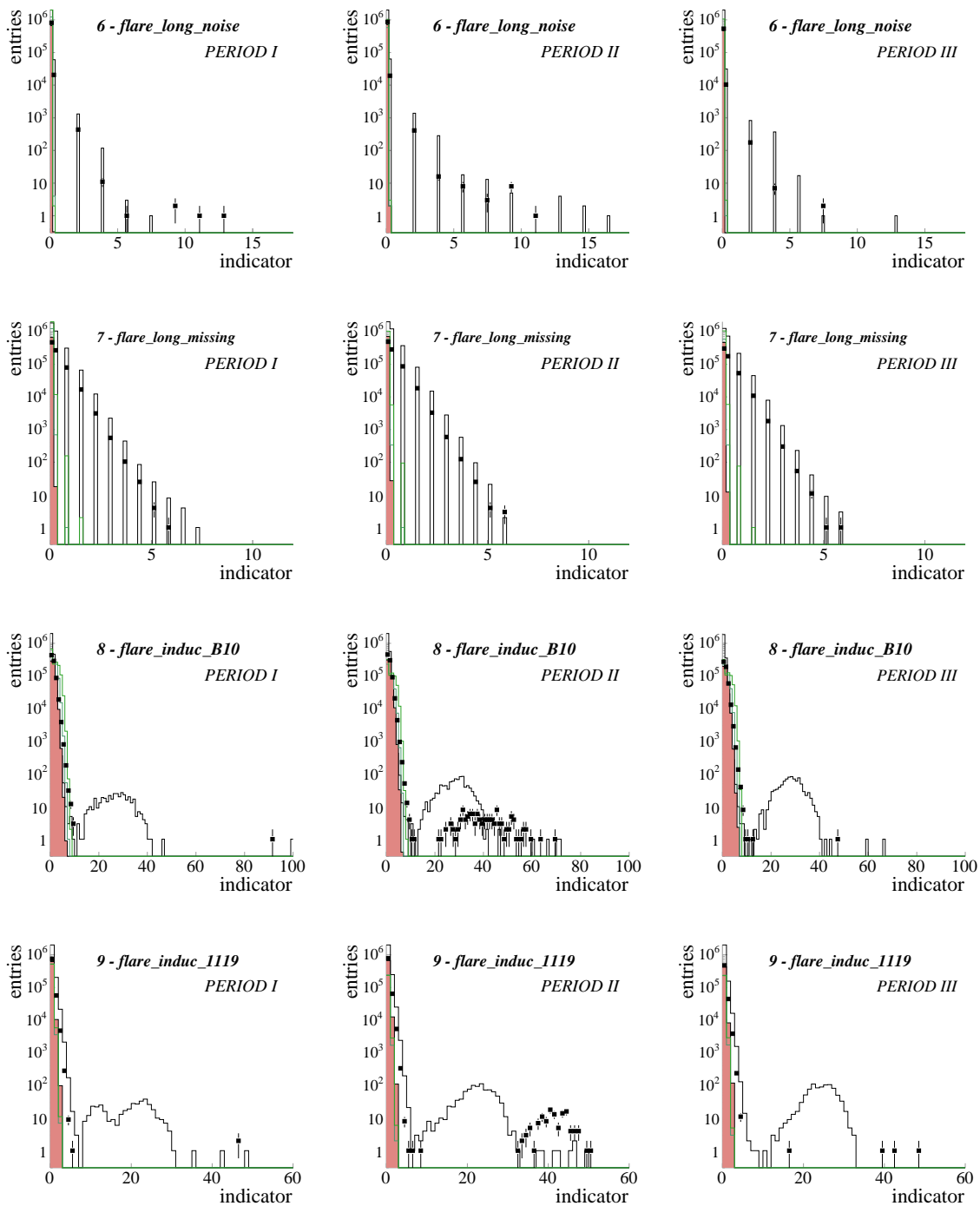
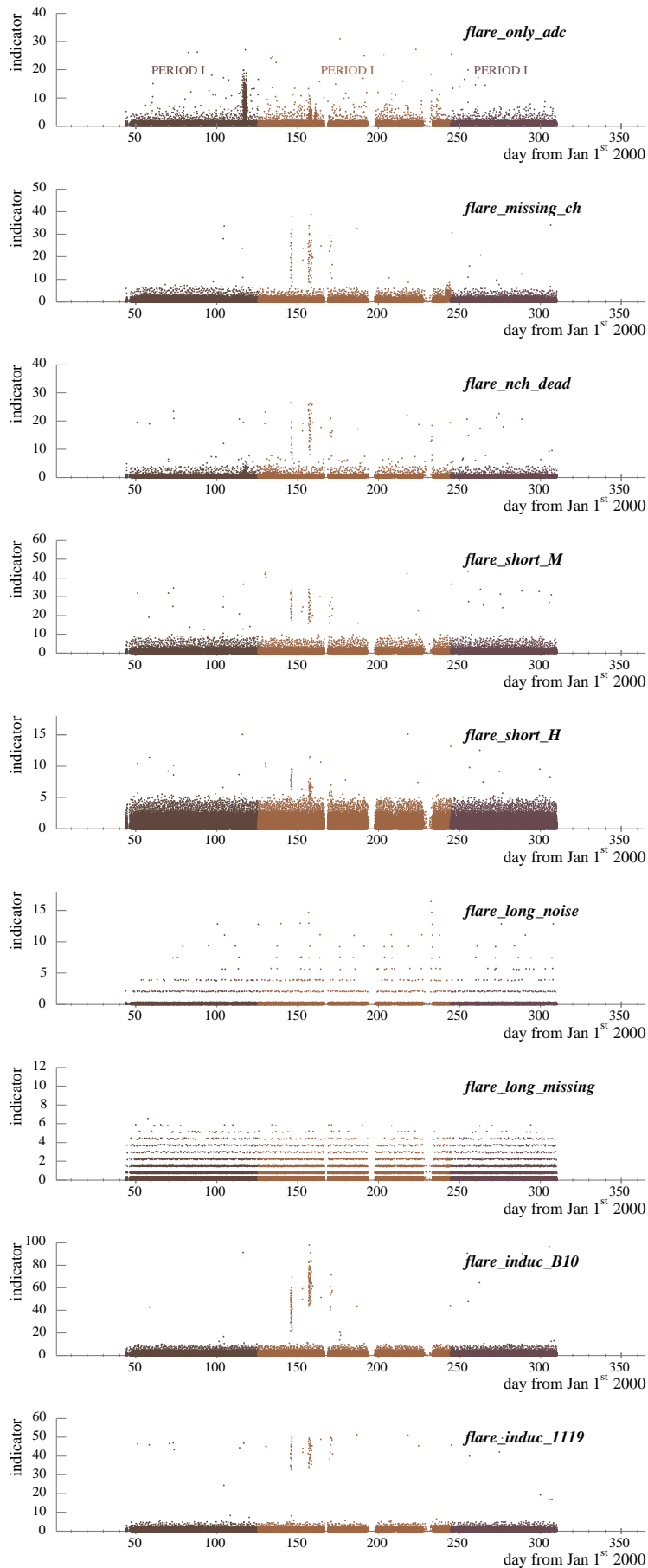


Figure B.5 – Flare indicators (6) to (9).



**Figure B.6** – Flare indicators versus day, counted from January 1<sup>st</sup> 2000. Events in each OM selection period are plotted in different colors. Most of the events with extremely high flare indicators cluster in short time intervals.

## B.2 File selection using flare indicators

Instead of using individual flare indicators, time periods of enhanced flare rates were identified using the maximum indicator value among all the nine flare indicators. According to equation (55), the number of events out of  $N$  above a certain  $I_{\text{cut}}$  in *any* of the nine indicators is [134]

$$9 \cdot N \cdot 10^{-I_{\text{cut}}} \approx N \cdot 10^{I_{\text{cut}}+1}. \quad (56)$$

As this analysis concerns  $\mathcal{O}(10^9)$  events, an event was considered a flare event if any of the nine indicators had a value greater than 10.

All those runs which either contained 10 flare candidates or more after imposing *level 1* cuts or those in which more than 0.1% of all events at *level 1* were flare candidates were inspected for clustering of flare events in time. Figure B.7 shows those runs in which clustering occurred.

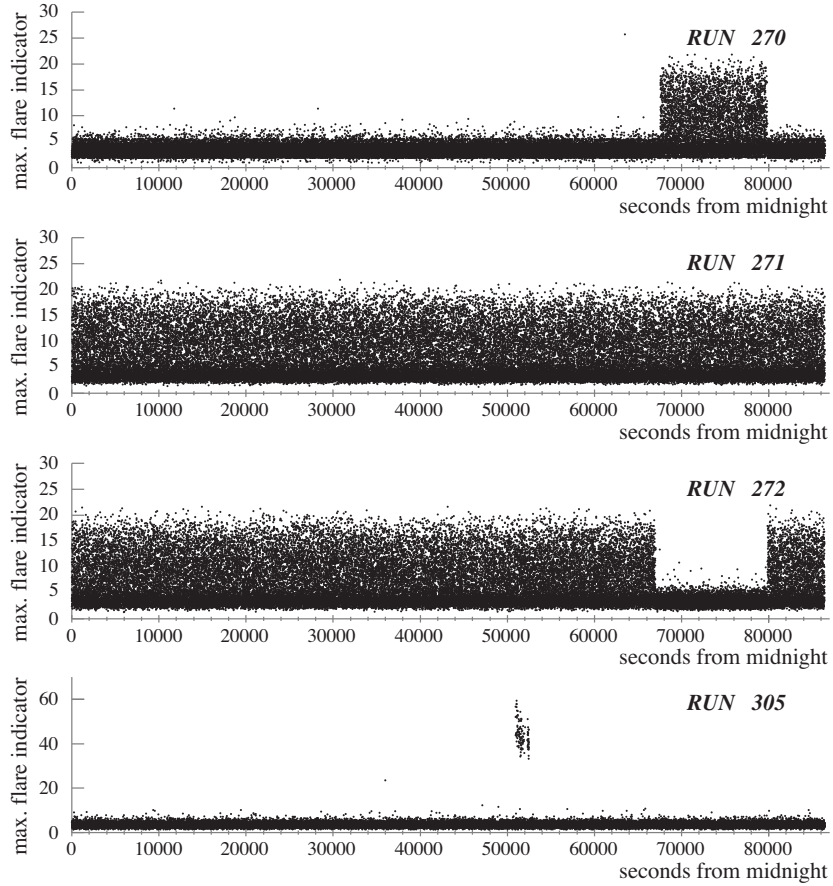


**Figure B.7** – Maximum value of flare indicators versus time for events in individual runs in which the flare rate is temporarily enhanced. Time is measured in seconds from midnight.

For this analysis, run 271 and run 272 were rejected entirely, as well as shorter time intervals during run 270 and run 305. The time period with run 270 and run 272 is visible in Figure B.6 (uppermost panel). Run 305 was taken on day # 146. This cluster is also visible in Figure B.6. The rejected time intervals are listed in Table 25.

In some runs with a high flare rate, flare events do not cluster in short time intervals. Figure B.8 shows the time dependence of the maximum flare indicator for run 322 (taken on day 157). This run has a very high percentage of events with flare indicators greater than 10 ( $\sim 1.2\%$ ). The

run	day	period	flare events	flare percentage	seconds rejected
270	115	I	12476	4%	67329-79805
271	116	I	14562	27%	all
272	117	I	12195	23%	all
305	127	II	127	0.2%	50618-52755

**Table 25** – Time periods which were excluded from further analysis because of their enhanced flare rates.

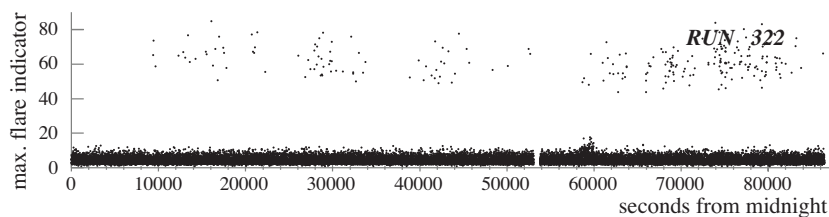


**Figure B.8** – Run 322 is an example for a run with a high fraction of flare candidates. The events with a high flare indicator do however not cluster in time.

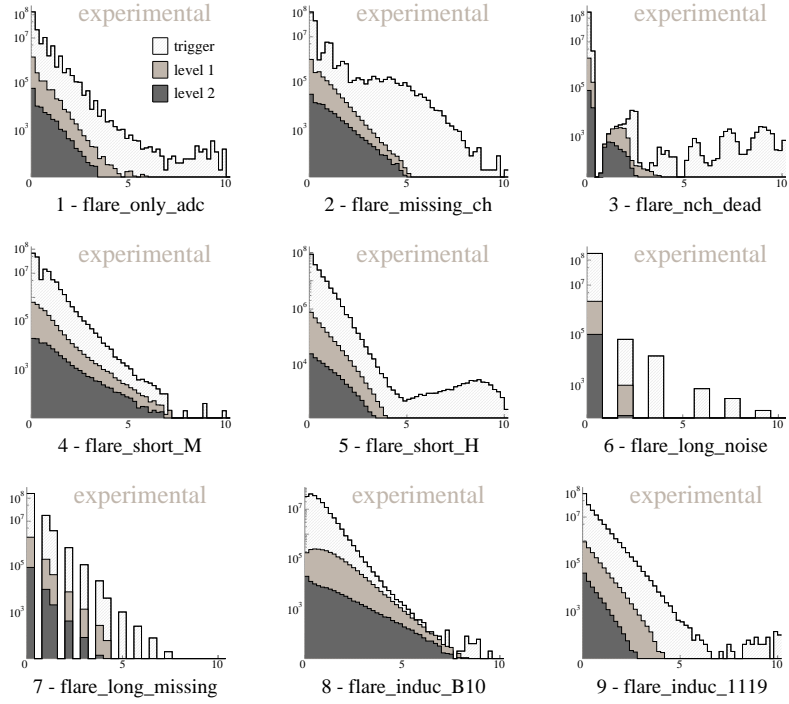
events are however spread over the entire data taking time, meaning that an additional flare checking on an event-by-event basis is required. Flare events usually have abnormally high values in more than one indicator. Therefore, it is not necessary to impose cuts on all nine flare indicators in order to remove flare events. Most neutrino searches used a subset of four flare indicators as cut parameters: (4) (`flare_short_M`, based on short TOT hits in strings 5-10), (8) (`flare_induc_B10`, based on the ratio of hits in strings 5-10 to hits in strings 1-4), and (9) (`flare_induc_1119`, based on the ratio of hits in strings 5-10 to hits in strings 11-19) [93]. For this analysis, these indicators are however not appropriate.

### B.3 Indicator stability for high multiplicity events

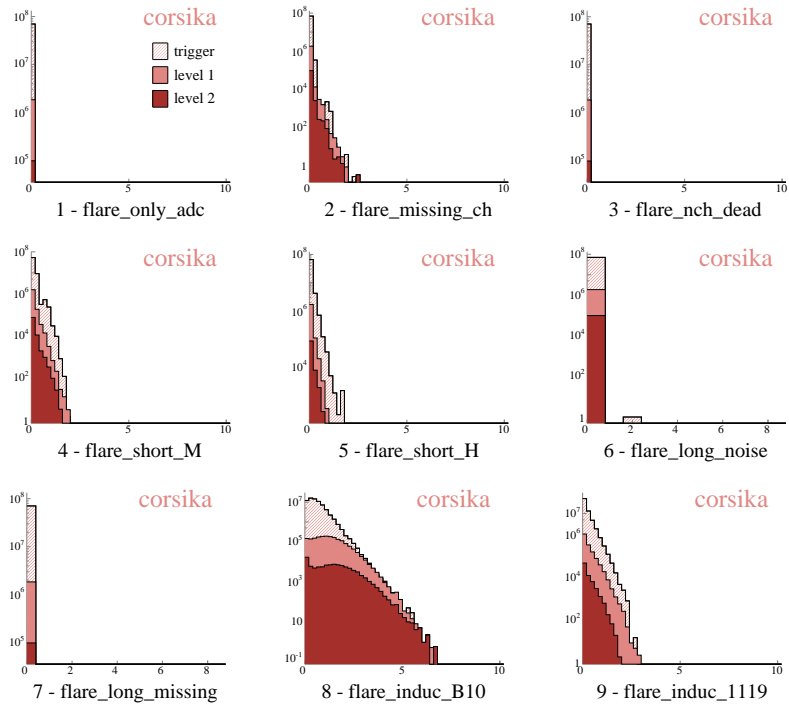
During their development, flare indicators were normalized and calibrated using trigger level muon data. *I.e.*, predominantly events of low energy and with low hit multiplicity were used to assess the probability with which flare features occur in particle induced events. However, there are some indications that the amount of noise in the detector rises with amount of light seen by the detector, as for instance the poor agreement in the hit multiplicities observed in electrically read-out OMs (see appendix C). This is probably caused by some sort of cross talk. The cross talk does not necessarily have to occur during pulse transmission to the surface via electrical cables. It might also occur within the data acquisition electronics at the surface. If the amount of cross talk (or other electronic noise) rises with the number of pulses registered at the surface, then high multiplicity events would by nature have flare features. Before using the flare indicators in a monopole search (or any other analysis which selects high multiplicity events), we have to ensure that the indicators are reliable for high multiplicity events.

Figure B.9 shows the nine flare indicators observed in experimental data at trigger level, *level 1*, and *level 2*. According to equation (55), we expect the exponential slope of an indicator to be independent of the number  $N$  contained in the event sample. However, for some of then indicators the slope does change, most obviously for indicator (2) (`flare_missing_ch`, which is based on the number of un-paired edges), indicator (4) (`flare_short_M`), and indicator (8) (`flare_induc_B10`).

The change in slope could either mean that the *level 1* and *level 2* cuts accumulate flare events, or that the respective indicators are unstable in



**Figure B.9** – Behavior of the nine flare indicators of experimental events with progressively tighter cuts. Each panel shows one of the indicators at trigger level (open histograms), *level1* (light grey histograms), and *level2* (dark grey histograms) of this analysis.



**Figure B.10** – Behavior of the nine flare indicators of simulated atmospheric muon events (CORSIKA) with progressively tighter cuts. Each panel shows one of the indicator at trigger level (open histograms), *level1* (pink histograms), and *level2* (red histograms).

events with high light yield. If the latter is true, the indicators should not be used in analyses that aim at detecting high energy events.

Simple and robust measures for the light yield are the number of hit optical modules (**NCH**) and the number of recorded hits (**NHits**). In order to confirm that the change of the slope is in fact due to high light yield, the indicator distributions were investigated for separate multiplicity bands with respect to **NCH** and **NHits**. Figure B.11 shows the flare indicators **flare\_missing\_ch**, **flare\_short\_M**, and **flare\_induc\_B10** of experimental data for three hit-multiplicity bands:  $\text{NHits} < 500$ ,  $500 \leq \text{NHits} < 1000$ ,  $1000 \leq \text{NHits} < 1500$ , and  $\text{NHits} > 1500$ .<sup>50</sup>

**Indicator (2) flare\_missing\_ch:** For this indicator, the change of the slope is not correlated with the hit multiplicity. In particular, higher multiplicity events tend to have lower indicator values. The same is true for channel multiplicity bands (**NCH**, not shown). Hence, **flare\_missing\_ch** is a suitable observable to reject flare candidates.

**Indicator (4), flare\_short\_M:** Higher multiplicity events tend to have higher indicator values. The same behavior is observed when channel multiplicity bands are considered [191]. The behavior is however not reproduced by the simulation. The **flare\_short\_M** indicator is measure of the fraction of hits with extremely short TOTs occurring in strings 5-10 (read out via twisted-pair cables). We must conclude that in extremely high multiplicity events, hits in OMs of these strings have substantial *admixtures* of non-photon hits. Consequently, **flare\_short\_M** is not a suitable observable to reject flares. The unreliability of the OMs in strings 5-10 in extremely bright events was also noticed at higher analysis levels (see appendix C). Consequently, hits in strings 5-10 do not enter the final selection criteria.

**Indicator (8), flare\_induc\_B10:** For this indicator, the change of the slope is reproduced in both simulated atmospheric muon events (see Figure B.10) and simulated signal events [191]. Hence, it cannot originate from un-simulated electronic effects. The multiplicity-dependent behavior of **flare\_induc\_B10** is not understood [192]. Obviously, this indicator is not a suitable observable for this analysis.

The flare indicators that were finally used in this analysis were the indicators (1), (2), (5), and (9). The applied cuts are listed in table 26.

indicator#	cut
(1)	<b>flare_only_adc</b> < 7
(2)	<b>flare_missing_ch</b> < 10
(5)	<b>flare_short_H</b> < 7
(9)	<b>flare_induc_1119</b> < 7

**Table 26** – Cuts imposed on the flare indicators.

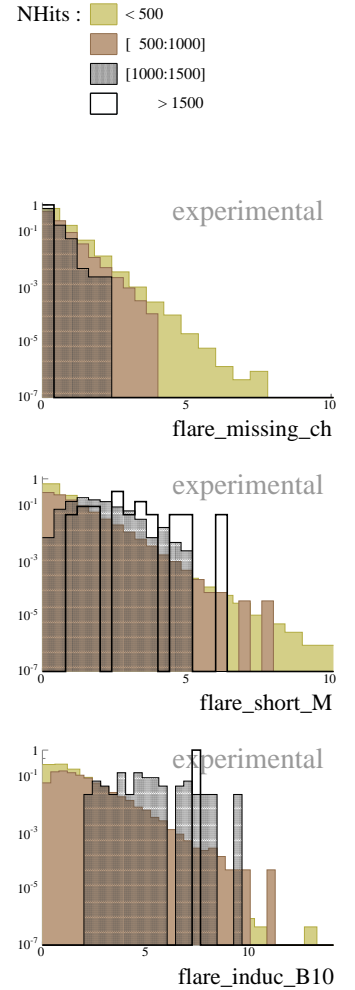


**Figure B.11** – Flare indicators (2) **flare\_missing\_ch** (top), (4) **flare\_short\_M** (middle), and (8) **flare\_induc\_B10** (bottom) for various hit-multiplicity intervals. The histograms in each plot are normalized such that they contain the same number of events.

<sup>50</sup>The corresponding multiplicity bands in **NCH** rather than **NHits**, and the indicator behavior for simulated signal and background events can found in [191].

## C The extended OM selection

After applying *level 2* cuts, we observe a disagreement in the hit multiplicity distributions (*c.f.* Figure 7.16 in section 7.3.1).

An investigation of the multiplicity distributions of OMs with different readout types reveals that the disagreement of the over-all distribution is due to the electrically read-out channels. Figure C.1 shows the **NCH** distributions for OMs that are read out via coaxial or twisted-pair electrical cable and via optical fiber. The agreement between experimental and simulated data is reasonable only for the optically read out channels. For electrically read-out channels, the shift in the peak positions of the **NCH** distributions of experimental data towards higher values indicates an increased noise contribution in these channels. The premature cut-off of the distribution at highest multiplicities that is observed for strings 1-4 could be either due to dead OMs that have not been identified by the OM selection, or due to removal of a larger fraction of hits in experimental than in simulated data by the hit cleaning.

In the following sections we investigate

- whether the applied hit cleaning removes certain classes of hits in experimental data which are not removed in simulated data (section C.1),
- whether particular parts of the detector show an increased contribution of electronic noise (*e.g.*, cross-talk hits) during actually particle induced events (section C.2.1), and
- whether both ADC and TDC of each OM behave consistently (section C.3).

Based on these investigations, we define an extended OM selection, which is used from analysis *level 3* on. In addition to those OMs which are already excluded by the standard OM selection, we reject OMs whose behavior during particle induced events is not reproduced by the simulation. Although some sources of the disagreement between experimental data and simulation could at least be isolated, they could not entirely be eliminated. This is especially true for the hit multiplicities of the electrically read-out channels.

In addition to the disagreement in the electrically read out channels, we observe a disagreement between experimental and simulated data with respect to the depth distribution of hits: The simulation predicts a higher hit rate in the upper part of the detector than observed in experimental data (see section C.4).

In order to maintain reasonable agreement between simulated and experimental data, we will use only OMs which are read out via optical fiber and which are located below a certain depth to compute observables related to the amount of light deposited in the detector. For the likelihood reconstruction in contrast, we will use both electrically and optically read out OMs over the full depth range of the detector. This is possible since the reconstruction relies only on the arrival times of the first photons at each OM, which are reproduced reasonably well by the simulation (see section C.5).

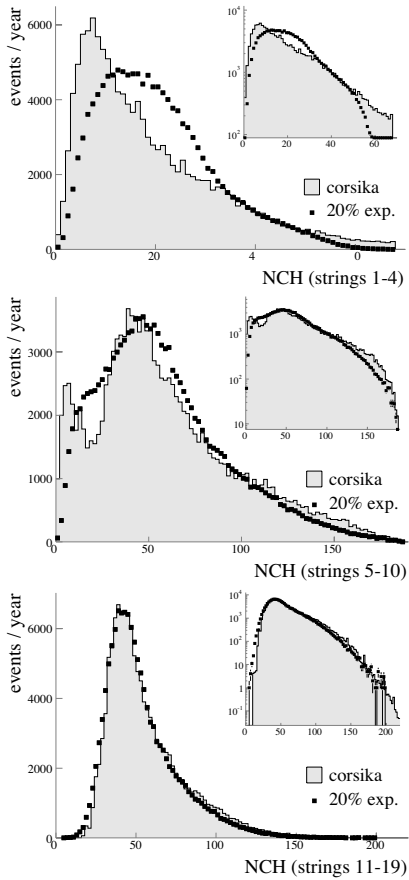


**Figure C.1** – NCH distributions after applying *level 2* cuts for OMs which are read out via coaxial cable (uppermost panel), twisted-pair cable (middle), and optical fiber (bottom).

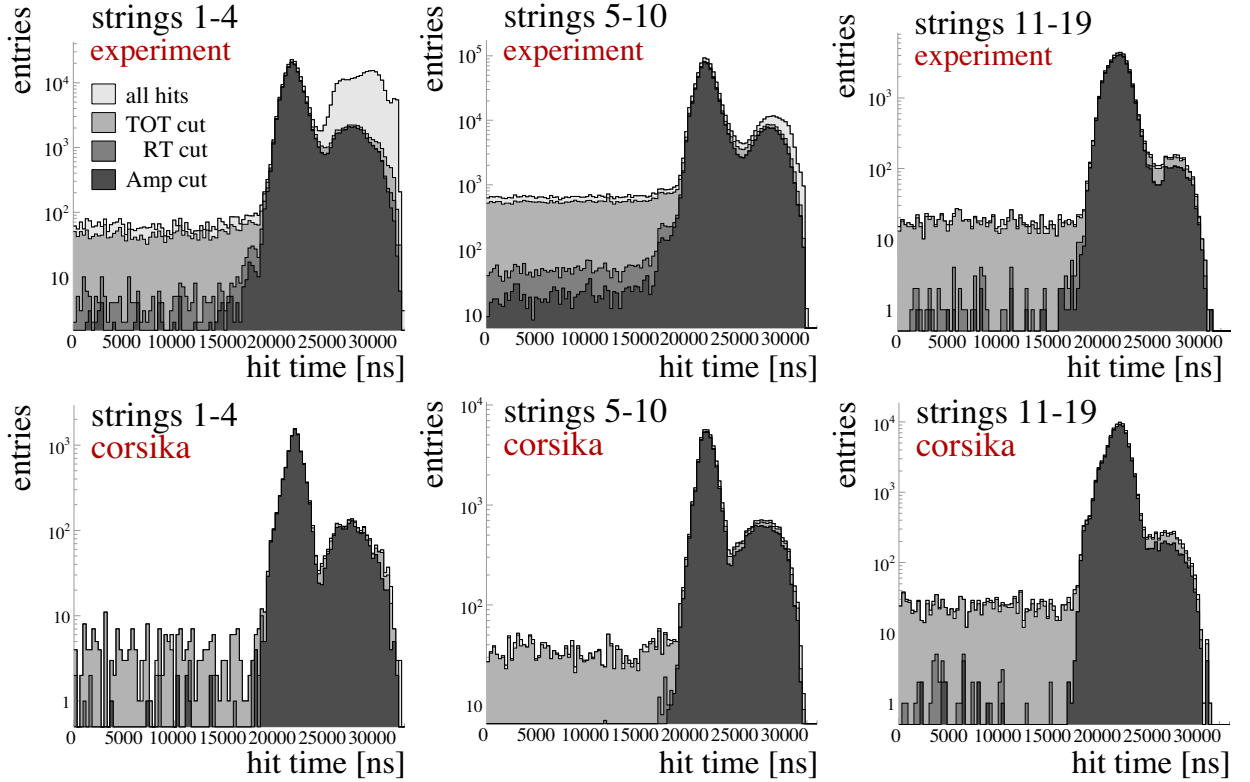


**Figure C.2** – Time distribution of hits in experimental data (top row) and CORSIKA events (bottom row) for OM read out via coaxial cable (left column), twisted pair cable (middle column), and optical fiber (right column).

### C.1 The impact of the hit cleaning

One possible explanation for the disagreement in the **NCH** and **NHits** distributions is that the hit cleaning procedure removes different portions of hits in experimental and simulated data. Figure C.2 shows the effect of the various hit cleaning steps on experimental and simulated data for OMs with different readout types. Shown are the calibrated times of the remaining hits after each cleaning step.

The only striking discrepancy occurs in the after-pulse region (hit times later than 25000 ns) for OMs in strings 1-4 (which are read out via coaxial cable). Experimental events have more hits in this time region, which are, however, removed by the TOT cleaning. TOT cleaning removes not only hits with extremely short TOT (as typical for electronic noise) but also hits with unreasonably long TOT ( $>2000$  ns). Many hits in the after-pulse region occurring in strings 1-4 are, in fact, sorted out by the latter criterion (unreasonably long TOT).

Figure C.3 shows the TOT for hits in string 1-4 versus time. Most hits later than 25000 ns have TOT greater than allowed by the TOT cleaning. A small fraction of hits around the trigger peak (between 20000 and 25000 ns) appear to have TOTs of 10000 ns or larger. These are hits whose trailing edge was missing. In case of missing trailing edges, the Sieglinde calibration module assumes that the buffer ending time as trailing edge. Hits with missing edges, however, account for only a small fraction of the hits with extremely large TOT.

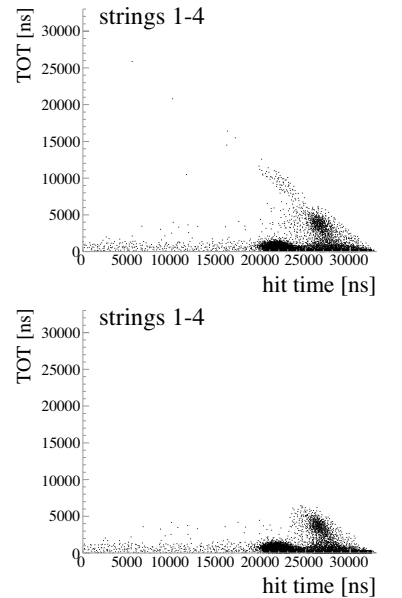


**Figure C.3** – TOT versus hit time for OMs in strings 1-4 for all hits (top) and only hits with “paired” edges (bottom).

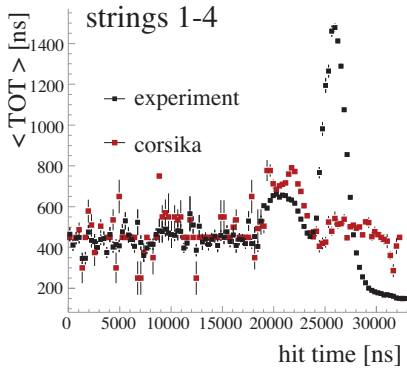


**Figure C.4** – Profile plot of TOT for hits in strings 1-4 dependent on the hit time for experimental data (black) and simulated atmospheric muons (red).

Late hits with extremely large TOT have also been observed at the final analysis levels in ultra-high energy neutrino searches [193]. It was observed that many channels in which these hits occurred have a “normal” pulse with moderate amplitude (from one to a few photoelectrons) around the trigger time, which are then preceded by an extremely wide pulse and by additional extremely small pulses [194]. In many cases, the small ripples following the large pulse cause the channel to overflow, so that no hits pass the TOT cleaning for that OM. It is unreasonable to assume that the late hits were due to after-pulsing, since a large amount of after-pulses would only be expected for large initial pulses (which were not observed). Therefore, most of the late hits in strings 1-4 must be of other instrumental nature, which is, in contrast to after-pulsing, not included in the simulation.

The same instrumental effect is observed in this analysis. Figure C.4 compares the mean TOT of hits in strings 1-4 versus time in experimental and simulated data after applying *level 2* cuts. In experimental data, the average TOT for late hits between about 24500 and 28000 ns is abnormally high, while it is abnormally low for even later hits.

In case of overflowed channels, the initial photon pulses are replaced by late pulses with abnormal TOT (which do not pass the hit cleaning). Figure C.5 demonstrates that the fraction of overflowed channels in experimental data is indeed higher than predicted by the simulation. If no hit-cleaning is applied except the time-window cleaning, the upper end of the NCH distributions of simulated and experimental data for strings 1-4 agree fairly well (Figure C.6). The disagreement in the lower end of the distribution however remains, indicating that there are additional contributions of noise hits in experimental data.

## C.2 Noise contributions

Apart from the disagreement in the hit multiplicities, the experimental data set at *level 2* of this analysis contains more events that are reconstructed as up-going particles than predicted by the simulation (*c.f.* Figure C.22 in section 7.3.1). In an early AMANDA-B10 analysis [195], the amount of misreconstructed experimental events could substantially be reduced by excluding additional OMs, which were particularly prone to cross talk. These cross talk hits (which were not removed by the standard cross talk cleaning) often drew the likelihood reconstruction into an upward direction. In order to identify parts of the detector that are abnormally noisy and could potentially be the source of the disagreements in the zenith angle distribution and/or the hit multiplicities, sub-sets OMs are investigated in terms of agreement with the simulated data and stability of hit frequency.

### C.2.1 String-wise hit frequency

In the aforementioned analysis of AMANDA-B10 data, the OMs that often caused the likelihood reconstruction to fail were located on string 9 and 10. While the OMs in question showed normal dark noise rates (and were hence not identified by the standard OM selection), they were particularly susceptible to noise pick-up during actual particle induced events, presumably due to cross talk in the twisted-pair cables.

In order to detect increased noise-pickup in particular strings, we investigate what fraction of the total number of recorded hits occurs in each

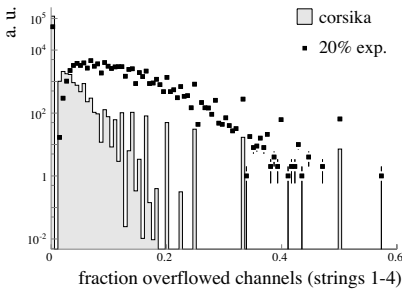


**Figure C.5** – Fraction of OMs in strings 1-4 which are overflowed (*i.e.*, recorded more than 16 edges in an event).

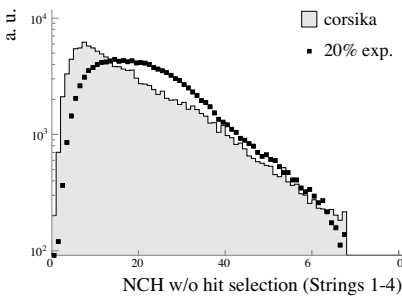


**Figure C.6** – NCH distribution for strings 1-4 if no hit cleaning is applied except for the time window cleaning. Only hits after 17000 ns are considered.

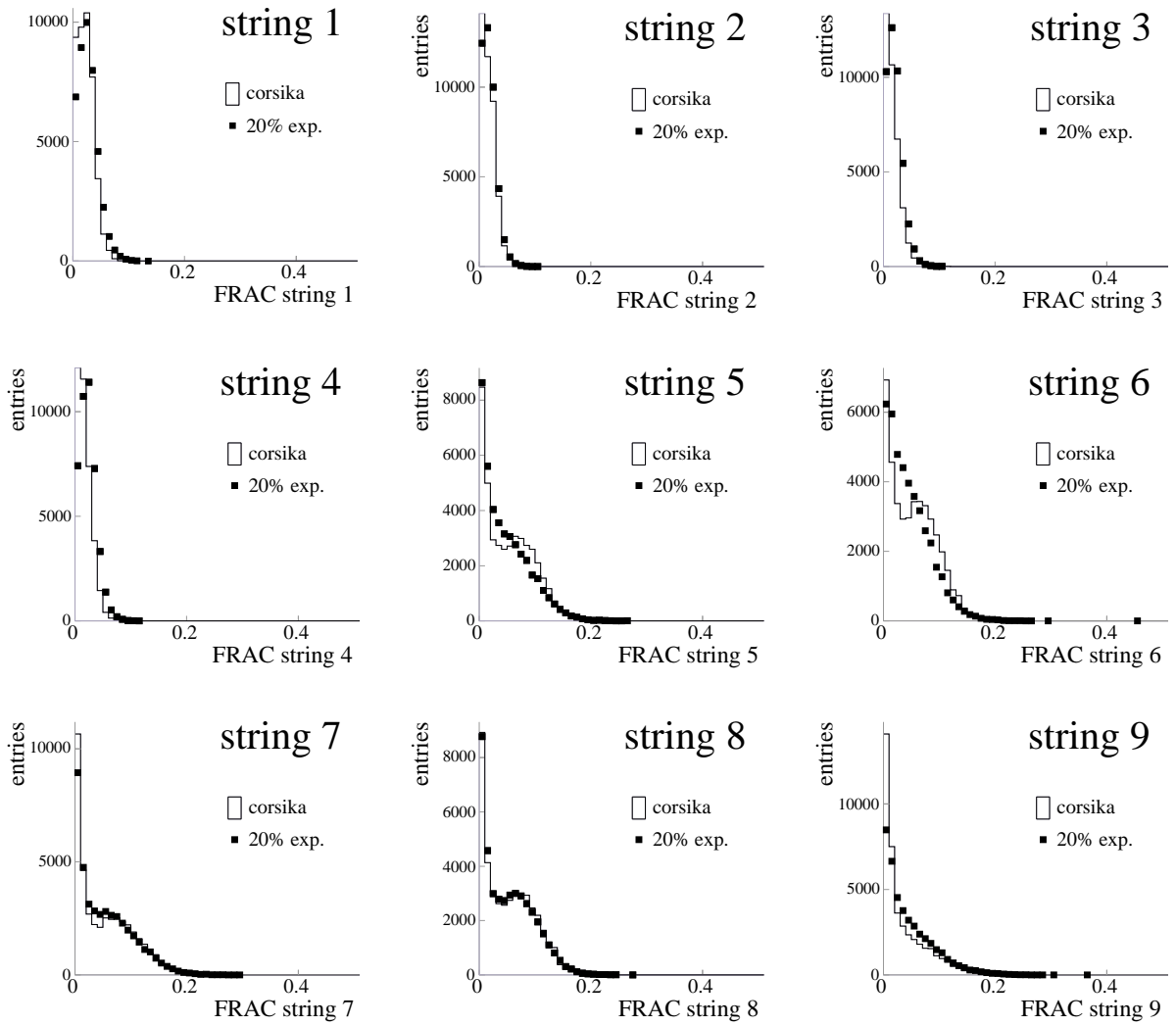


**Figure C.7** – Fraction of hits recorded in one particular string (strings 1 to 9), relative to the total number of hits recorded for experimental data (black markers) and simulated atmospheric muons (open histograms). Only hits that pass the *level2* hit selection for observables related to the light yield (*c.f.* Table 13 in section 7.2.1).

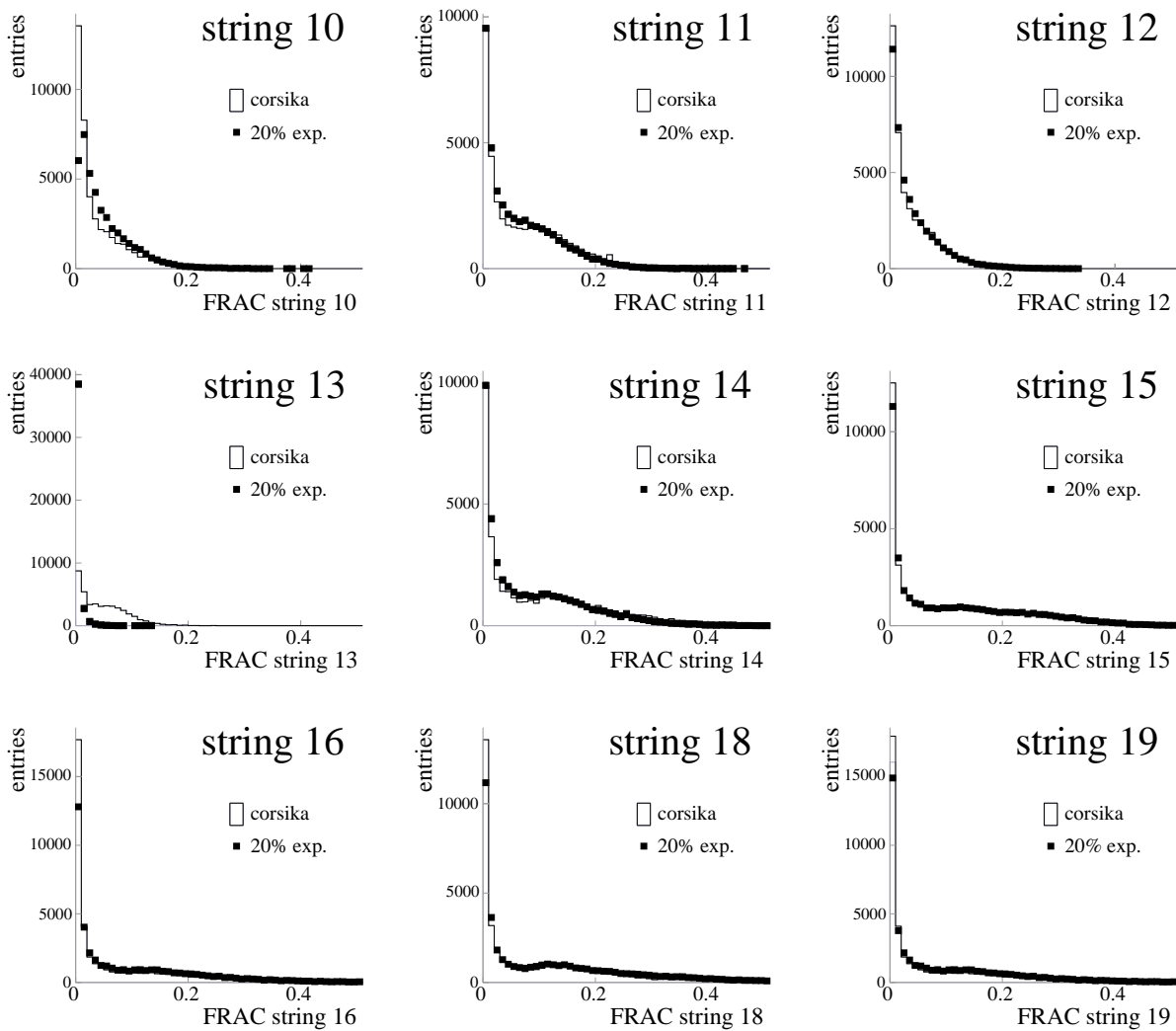


**Figure C.8** – Fraction of hits recorded in one particular string (strings 10 to 19), relative to the total number of hits recorded for experimental data (black markers) and simulated atmospheric muons (open histograms). The *level 2* hit selection for observables sensitive to light yield has been applied (*c.f.* Table 13).

particular string. An increased fraction of hits in one string compared to what is predicted by the simulation would indicate a contribution of un-simulated noise hits. Figures C.7 and C.8 show the fraction of hits per event that are recorded in strings 1 to 9 and in strings 10 to 19, respectively (string 17 is not shown since it is excluded from analysis). Only those hits which pass the *level 2* hit cleaning and OM selection (*c.f.* Table 13 in section 7.2.1) are taken into account.

We observe the following:

- For strings 1 to 4, the agreement is relatively good. In the lowest bin of the distribution, experimental data have generally less entries than simulated data, reflecting the shift of the peak position of **NCH** distribution towards higher multiplicities in experimental relative to simulated data. This peak shift is present for all of the four inner strings, and is apparently *not* caused by a sub-set of individual OMs.
- For strings 5 to 10, experimental data are less accurately reproduced by the simulation. For strings 5 to 8, the distribution of simulated events has a double peak structure. This structure is also observed for the overall channel multiplicity in strings 5 to 10 of simulated data (*c.f.* Figure C.1). The double peak is due to the fact that strings 5 to 10 are shorter compared to the other strings in the array. Figure C.9 shows the channel multiplicity in strings 5 to 10 versus the average depth of hit OMs (in the entire detector) for simulated atmospheric muon events. For those events with in which the channel multiplicity in strings 5 to 10 is smaller than 20 (the position of the first peak in the **NCH** distribution, *c.f.* Figure C.1), the mean depth of hit OMs is located below a depth of  $z \sim 100$  m, roughly at the depth where strings 5 to 10 end. That is, the events with a low number of hit OMs in strings 5 to 10 are those in which most of the light is deposited in the bottom part of the detector (or even below the instrumented volume). Only photons relatively far away from the initial particle track can cause hits in strings 5 to 10. This explains the double peak structure of the **NCH** distribution for these strings, which is, however, washed out for experimental data.

The double peak structure of the **NCH** distribution is especially poorly reproduced for strings 6 and 7, which suggests that these strings have a high fraction of cross-talk hits which are not efficiently removed by the hit cleaning.

For string 9 and string 10, neither simulated nor experimental data have a double peak structure. This is probably because those strings have fewer neighboring strings which span a larger depth range (There is a larger gap in the outer ring on which the optically read-out strings are located, between string 16 and 19, *c.f.* Figure C.10)

- For the optically read-out strings (11–19) the agreement is very good, except for string 13, which has virtually no hits in experimental data (see below).

Generally, we can conclude that the disagreements in the hit multiplicities observed in the electrically read-out strings is not caused by individual OMs, since all observed disagreements are equally present in each string.

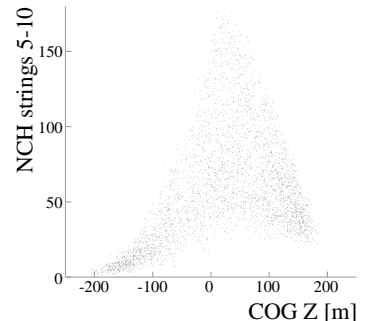


**Figure C.9** – Channel multiplicity (**NCH**) in strings 5 to 10 versus average depth (relative to the detector center) of hit OMs ( $z$ -coordinate of the “Center Of Gravity”, *COG Z*) for simulated atmospheric muons.

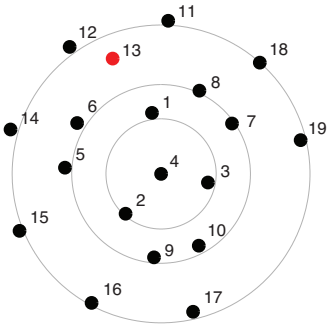


**Figure C.10** – Location of string 13 (red) within the detector array

### C.2.2 String 13

In experimental data, string 13 records fewer hits than predicted by the simulation (*c.f.* Figure C.8). The other optically read-out strings in contrast, are well described by the simulation. Figure C.10 shows the location of string 13 within the AMANDA-II-array.

One potential explanation is that string 13 was entirely dead over a long time period during the year 2000 (which could for instance be due to a temporary outage of the high voltage). This is however not the case. Figure C.11 shows the hit fraction of hits recorded in strings 13 (bottom panel) as a function of the day of the year. The black markers are the hit fraction found in experimental data, the horizontal line represent the average hit-fraction predicted by the background simulation. The hit fractions in the neighboring strings (strings 11 and 12) are shown for comparison (top and middle panel). While the hit rates in strings 11 and 12 are stable and in good agreement with the simulation, the hit rate in string 13 is practically zero throughout the entire year.

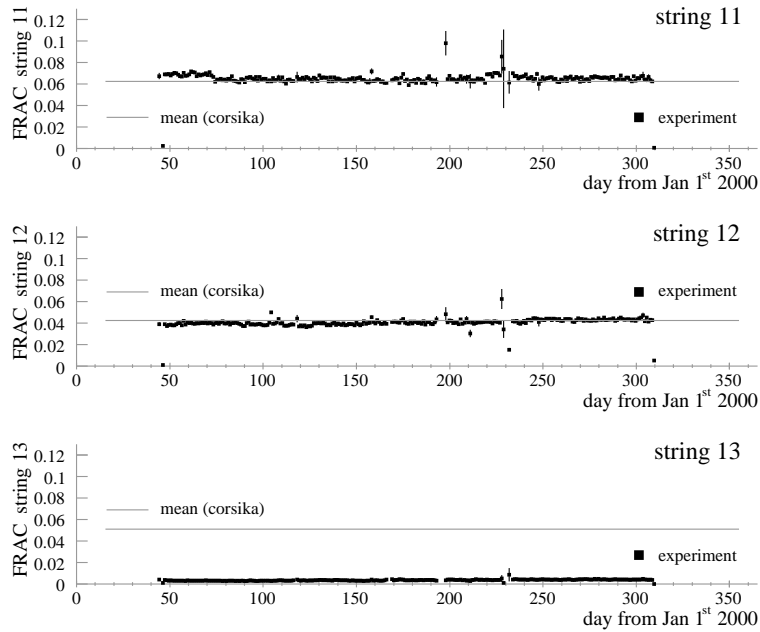


**Figure C.11** – Fraction of hits recorded in string 11 (top), string 12 (middle), and string 13 as a function of time. Black markers indicate the hit fraction observed in experimental data, grey lines indicate the average fraction predicted by the simulation.

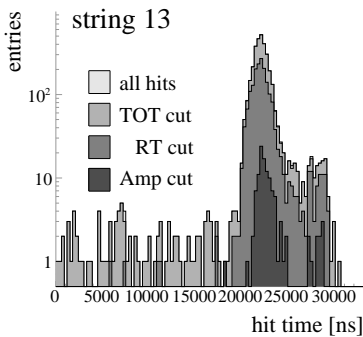


**Figure C.12** – Hit times for string 13 after each hit cleaning step.

A complete outage of the entire string over the full data taking period is unlikely, as it would presumably have been detected by the monitoring system. Hence, the hits in string 13 must be lost during the hit cleaning. Figure C.12 shows the hit times in string 13 after each hit cleaning step (*c.f.* Table 13 in section 7.2.1). Essentially all hits are removed by the amplitude cut. The amplitude cleaning removes hits in OMs with extremely small peak amplitudes ( $<0.1$  photoelectrons), or hits in OMs for which the peak amplitude is *undefined*. Undefined amplitudes should occur only if all hits recorded by an OM lie outside the time interval in which the ADC gate is open, *i.e.*, if the pulses arrive at the surface either more than  $2 \mu\text{s}$  before or more than  $10 \mu\text{s}$  after the trigger time. Then, no ADC is recorded for the OM, and the amplitude remains undefined for all hits.

Figure C.13 shows the uncalibrated leading edge times (*i.e.*, the times at which pulses arrive at the surface) for those hits in string 13 with undefined

amplitudes. Only hits which pass the TOT cleaning are considered. The two vertical lines mark the time interval over which the ADC gate is open. Most of the hits in string13 fall into the time interval in which the ADC is supposedly sensitive. This is very surprising, since the monitoring data indicated normal ADC rates for most of the channels.

The strange behavior of string 13 was understood only several months after these investigations were complete [196]. The issue could be traced back to an error in the detector configuration file that was used during the year 2000. The detector configuration file contains information about which OM is connected to which ADC and TDC channel at the surface. In the detector configuration used during 2000, the ADC units are mismatched for string 13: The ADC values recorded for OMs in the bottom half of string 13 were assigned to the OMs in the top half of the string, and vice versa. Since the assignment of TDC channels are correct, all hits in string 13 are composed of TDC edges of one OM and the ADC value of another, which can only incidentally result in a hit passing the hit-cleaning.

A correction for this error is only possible by processing the data from scratch using a corrected mapping scheme when translating from raw binary data into the analysis data format [197]. We therefore exclude hits in string 13 from analysis *level 3* on.

### C.3 ADC-TDC inconsistencies in strings other than string 13

The standard OM selection evaluates the reliability of individual OMs mainly by their dark noise rates. The dark noise however does not give any information about the propensity of an OM or its surface hardware (ADC and TDC) to pick up noise during particle induced events.

The AMANDA surface electronics are set up such that pulses caused by a particle crossing at depth are registered by both TDCs and ADCs. The surface hardware of an OM is clearly unreliable if the recorded hits frequently contain information from from either of the two units only.

#### C.3.1 Missing ADC information

Ideally, undefined ADC values occur only if an OM had no hits during the time interval during which the ADC gate is open. Figure C.14 show the leading edge times of pulses for which no ADC value is recorded in simulated data. In the idealized detector simulation, no hits with missing ADC information are registered in the time interval during which the ADC gate is open (marked by vertical lines).

In practice however, undefined ADC values occur occasionally even if TDC edges are recorded during the time interval when the ADC is supposedly sensitive. Figure C.15 shows the leading edge times of hits which pass the TOT cleaning and which have undefined ADC values for strings 1-4, strings 5-10, and strings 11-19 (string 13 is already excluded). The vertical lines mark the time interval over which the ADC gate is open. Contrary to expectations, in experimental data, most of the hits with undefined amplitudes lie *within* the time interval during which the ADC should be sensitive. The detector simulation does not reproduce such behavior.

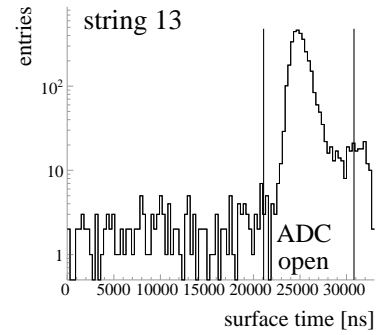


**Figure C.13** – Leading edge times of hits with undefined amplitudes in string 13.

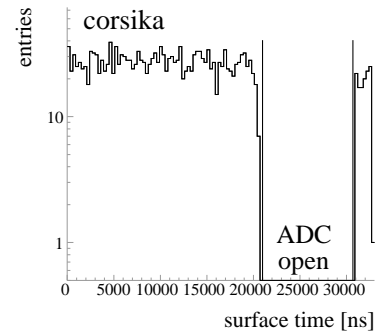


**Figure C.14** – Leading edge times of hits with undefined ADC values for *simulated* atmospheric muon events. For simulated events, hits with missing ADC information occur only at the beginning and at the end of the TDC buffer window, when the ADC is insensitive.

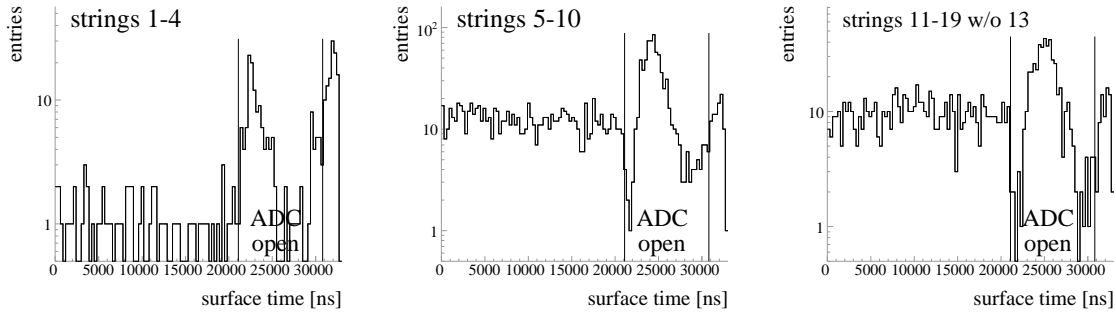


**Figure C.15** – Leading edge times of hits with undefined ADC values in *experimental* data for strings 1-4 (left), strings 5-10 (middle), strings 11-19 (right). The time interval over which the ADC gate is open is marked by vertical lines.

The hit cleaning removes hits with undefined amplitudes. This is desirable only if these hits are in fact an artifact of the TDCs (*i.e.*, they are not due to photons). If, on the other hand, the amplitudes were missing due to a malfunctioning of the ADCs, the hit cleaning would remove actual photon hits, which is obviously undesirable as it would introduce discrepancies between experimental and simulated data. Since we do not know whether the ADCs or the TDCs are responsible for the observed inconsistency (and hence we do not know whether or not the hits with missing ADC information are due to photons) we exclude those OMs which particularly often have undefined ADC values although TDC edges were recorded during the time interval over which the ADC gate is open.

The fraction of hits with missing ADC information is determined for each individual OM in the detector. Figures C.16 to C.18 show the fraction of hits in each OM that have an undefined ADC despite the fact that they were recorded in the time interval during which the ADC gate is open, relative to the total number of hits occurring during this time window. Some OMs have particularly high fractions of undefined ADC values.

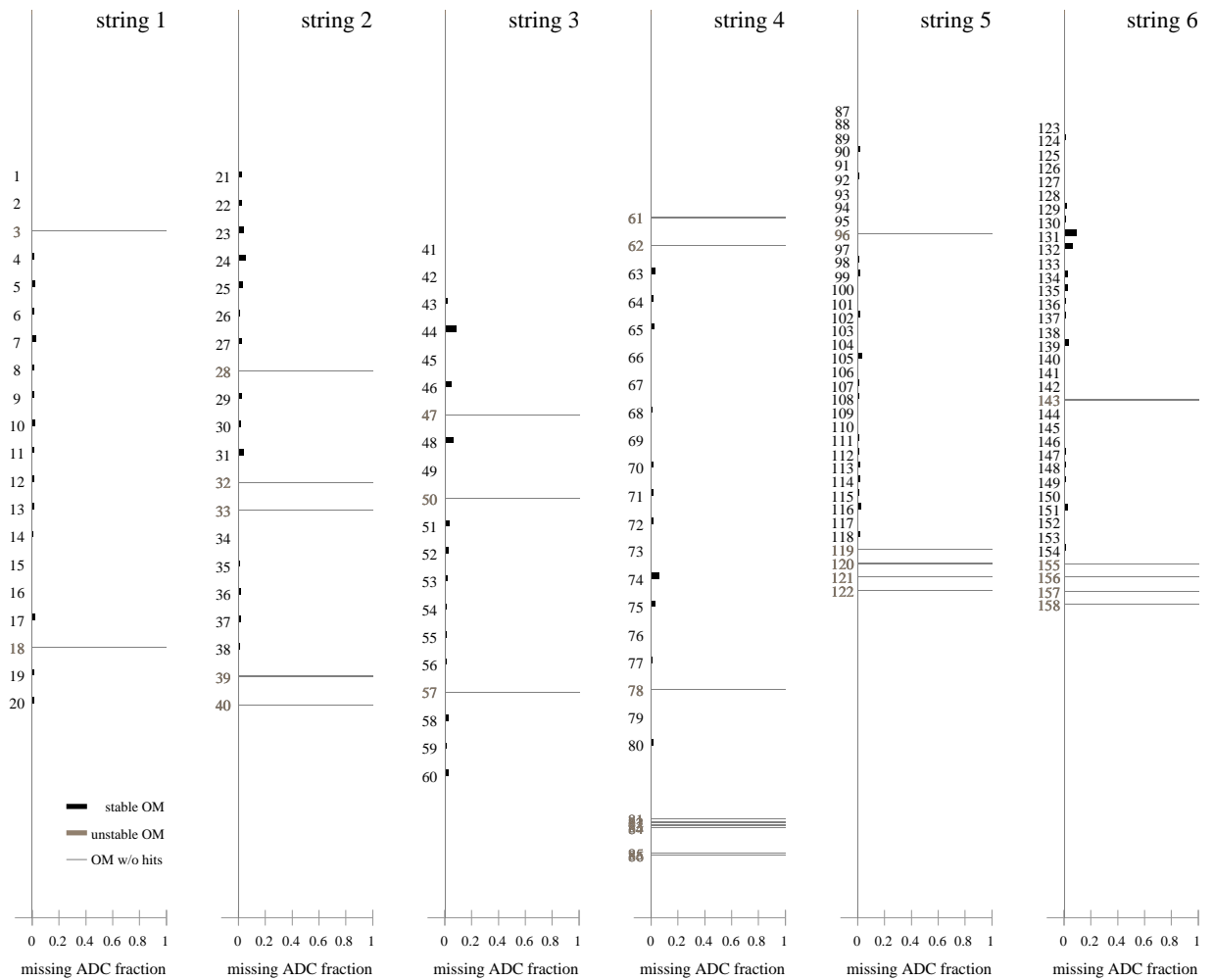


**Figure C.16** – Fraction of hits with undefined amplitudes despite they were recorded in the time interval during which the ADC gate is open. Each panel shows the OMs in one particular string from string 1 (leftmost) to string 6 (rightmost). The numbers at the y-axis are the OM identification numbers. Numbers printed in black are those OMs that are considered stable, *i.e.*, those OMs that passed the standard OM selection. Numbers printed in grey are those OMs that are unstable during the year 2000, *i.e.*, those OMs that are rejected for at least one of the OM selection periods (*c.f.* section 6.2.1). The horizontal black and grey bars represent the fraction (ranging from 0 to 1) of hits for which no amplitude was recorded although the ADC is supposedly sensitive. The thin, grey horizontal lines indicate that the respective OM never registered a hit during the time window when the ADC is open.

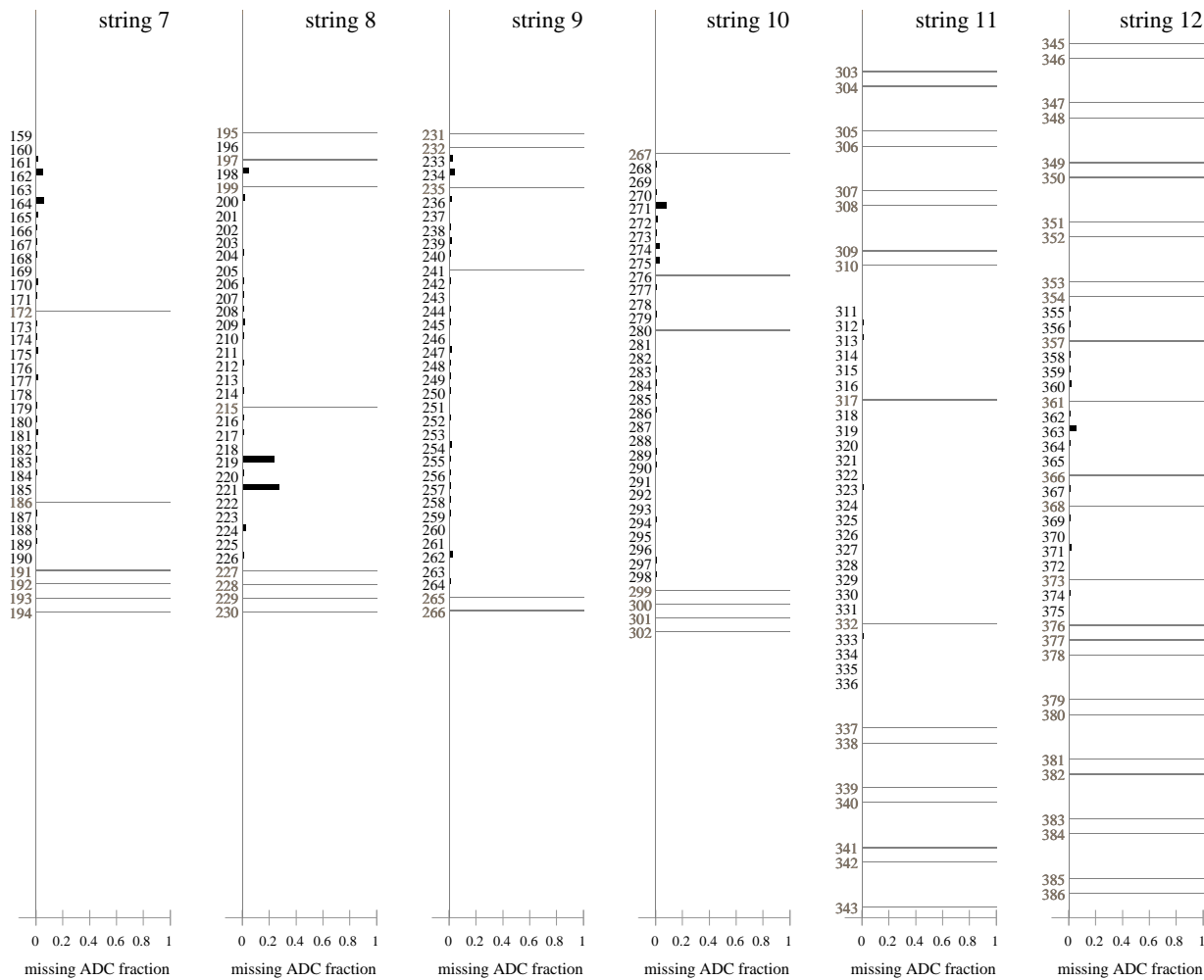


**Figure C.17** – Fraction of hits with undefined amplitudes despite they were recorded in the time interval during which the ADC gate is open. Each panel shows the OMs in one particular string from string 7 (leftmost) to string 12 (rightmost). The numbers at the y-axis are the OM identification numbers. Numbers printed in black are those OMs that are considered stable, *i.e.*, those OMs that passed the standard OM selection. Numbers printed in grey are those OMs that are unstable during the year 2000, *i.e.*, those OMs that are rejected for at least one of the OM selection periods (*c.f.* section 6.2.1). The horizontal black and grey bars represent the fraction (ranging from 0 to 1) of hits for which no amplitude was recorded although the ADC is supposedly sensitive. The thin, grey horizontal lines indicate that the respective OM never registered a hit during the time window when the ADC is open.

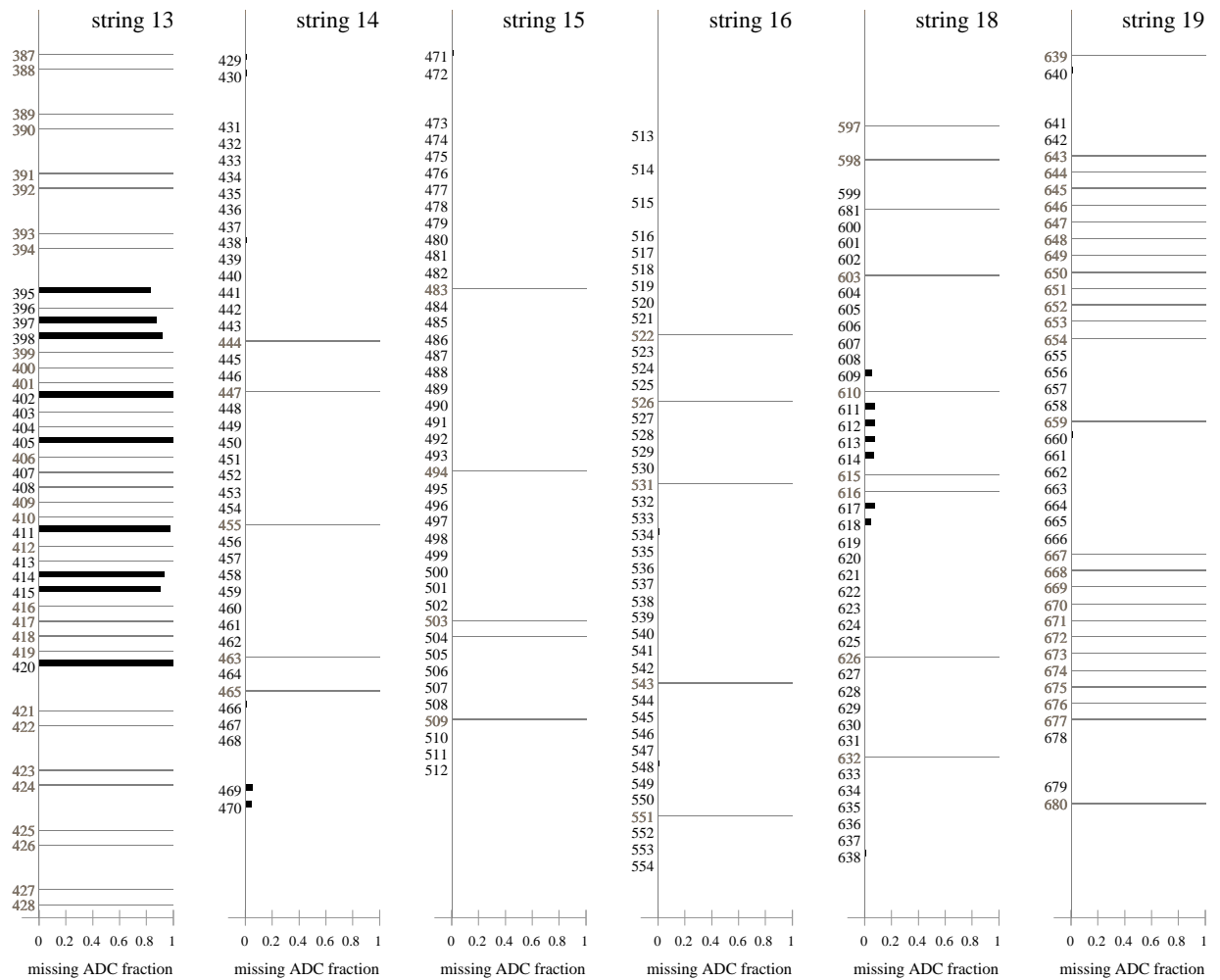


**Figure C.18** – Fraction of hits with undefined amplitudes despite they were recorded in the time interval during which the ADC gate is open. Each panel shows the OMs in one particular string from string 13 (leftmost) to string 19 (rightmost). The numbers at the y-axis are the OM identification numbers. Numbers printed in black are those OMs that are considered stable, *i.e.*, those OMs that passed the standard OM selection. Numbers printed in grey are those OMs that are unstable during the year 2000, *i.e.*, those OMs that are rejected for at least one of the OM selection periods (*c.f.* section 6.2.1). The horizontal black and grey bars represent the fraction (ranging from 0 to 1) of hits for which no amplitude was recorded although the ADC is supposedly sensitive. The thin, grey horizontal lines indicate that the respective OM never registered a hit during the time window when the ADC is open.

For this analysis, we exclude those OMs for which the fraction of undefined ADC values is larger than 10%. These are the OMs with the identification numbers 219, 221, 600, 609, 611-614, 617, 618, 634, 635, and 642. For two of these 13 OMs (OMs 219 and 221), the reason for the high fraction of missing ADC values is again a mismatching in the detector configuration file: The TDC channels to which these two OMs are connected were interchanged.

### C.3.2 Permanently damaged OMs

Figures C.16 to C.18 show some OMs which never record a hit during the ADC sensitive time window. The OMs have the identification numbers 241, 276, and 280. These OMs are not excluded by the standard OM selection. The OMs were however tagged as permanently damaged in an older OM-database. This valuable information was apparently lost during the transition to the new analysis software *Sieglinde* (which uses a different OM database than the previous software), and rediscovered in the course of this analysis. For this analysis, these OMs are excluded from analysis *level 3* on.

### C.3.3 Missing TDC edges

While some OMs tend to have undefined ADC values although TDC edges were recorded within the time window when the ADC is sensitive, the opposite is true for some other OMs: These OMs frequently record a valid ADC (above the standard hit selection threshold of 0.1 photoelectrons) while the TDC does not record any edges. Such behavior again indicates malfunctioning of either ADC or TDC of the respective channels.

Figures C.19 to C.21 show the the fraction of hits in each OM for which only an ADC value but no TDC edges was recorded, relative to the total number of hits recorded by the OM.

For this analysis, we reject those OMs for which more than 10% of the recorded hits consist only of of an ADC value. This is the case for OMs 94, 488, 491, 493, 499, 501, 502, 506, 521, 600, 634, 635, and 642.

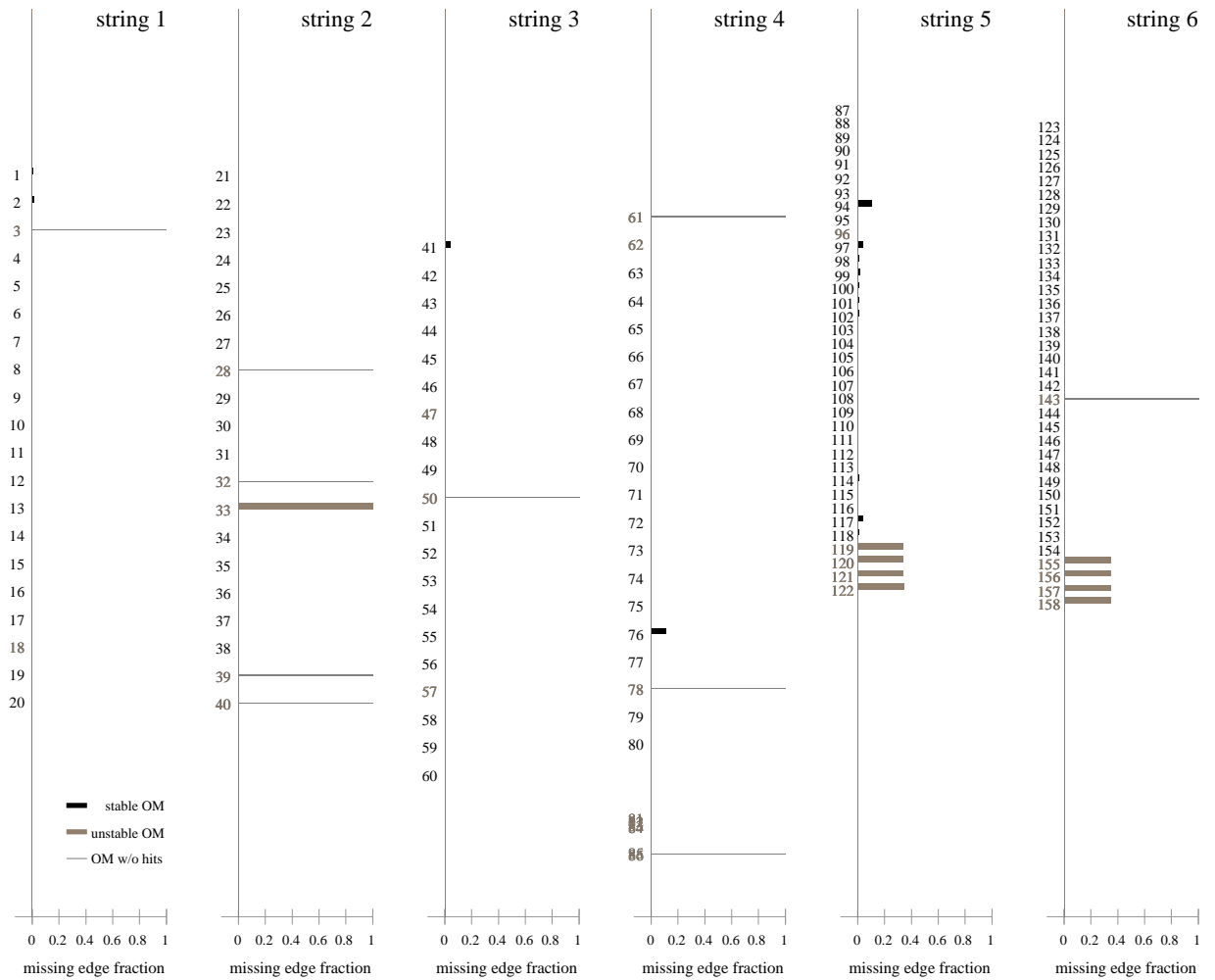


**Figure C.19** – Fraction of hits only registered by the ADC in strings 1 to 6. The black horizontal bars represent this fraction for stable OMs, and the grey bars represent OMs that were rejected by the standard OM selection for at least one of the OM selection periods. The thin grey horizontal lines indicate that an OM was never hit.

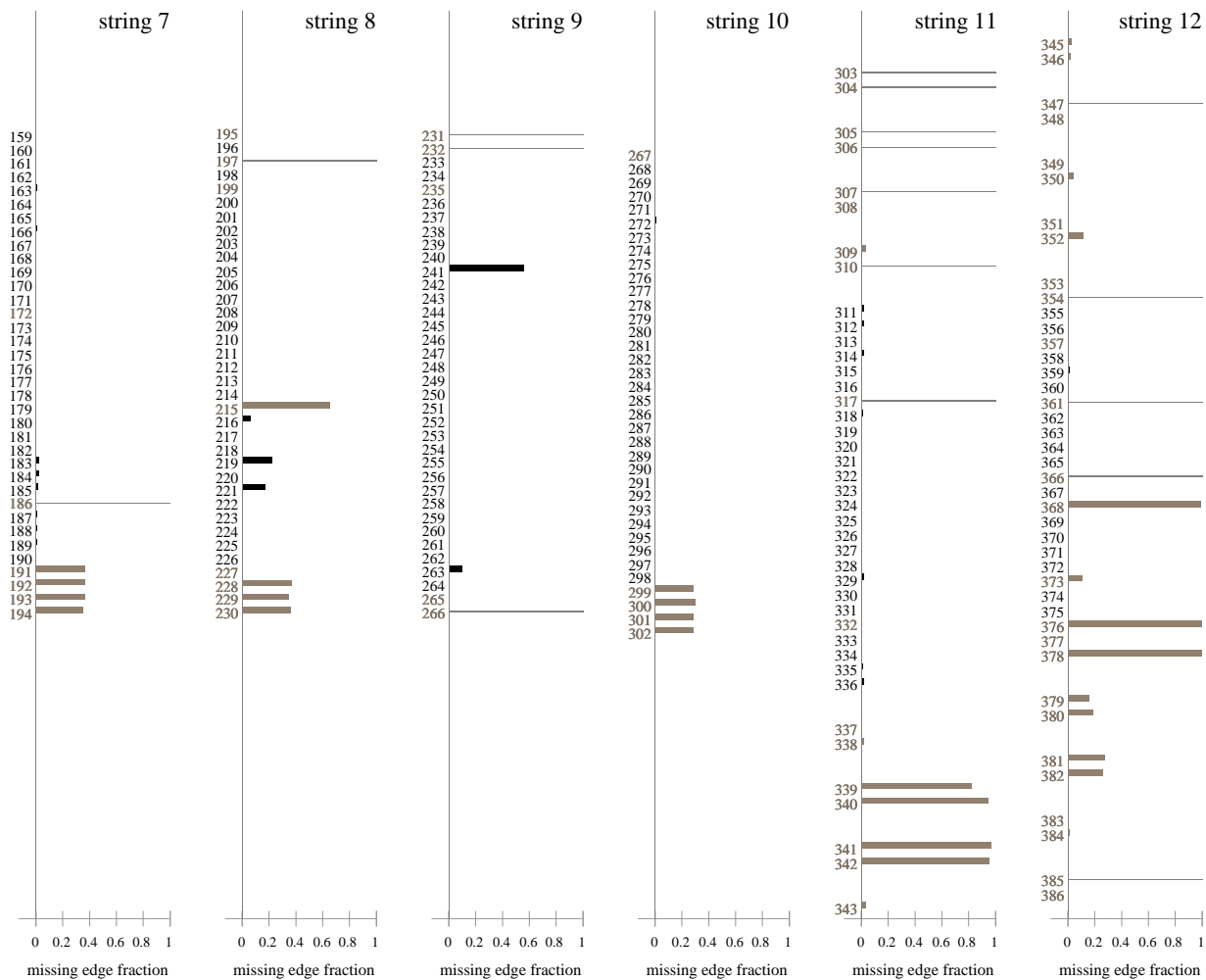


**Figure C.20** – Fraction of hits only registered by the ADC in strings 7 to 12. The black horizontal bars represent this fraction for stable OMs, and the grey bars represent OMs that were rejected by the standard OM selection for at least one of the OM selection periods. The thin grey horizontal lines indicate that an OM was never hit.

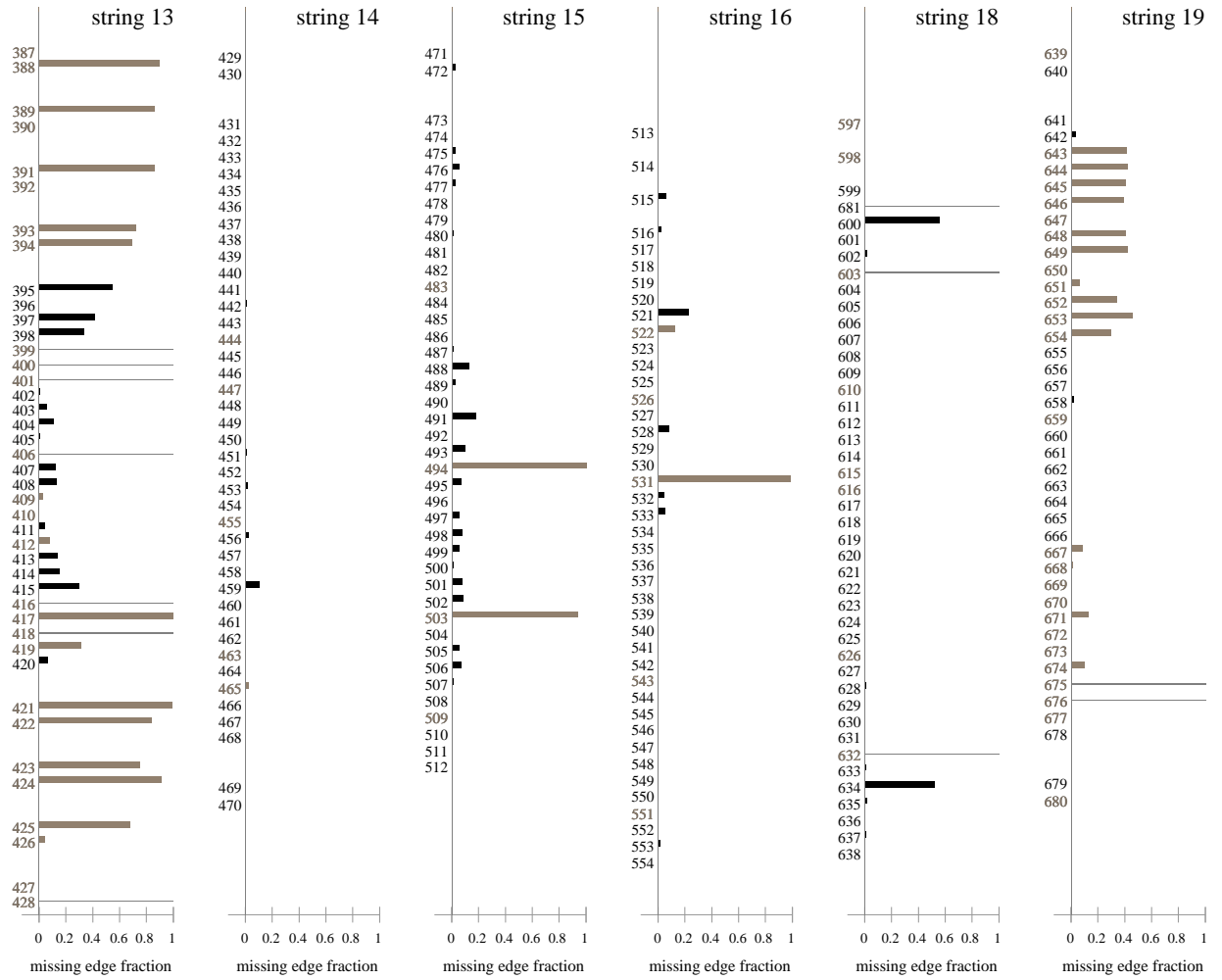


**Figure C.21** – Fraction of hits only registered by the ADC in strings 13 to 19. The black horizontal bars represent this fraction for stable OMs, and the grey bars represent OMs that were rejected by the standard OM selection for at least one of the OM selection periods. The thin grey horizontal lines indicate that an OM was never hit.

OMid	string	reason to reject	comment
94	5	12% lost TDC edges	
219	8	21% lost ADC, 22% lost edges	mismapped TDC in detector config
221	8	23% lost ADC, 16% lost edges	mismapped TDC in detector config
241	9	67% lost TDC edges, no good hits	flagged in OMDB
276	10	no good hits	flagged in OMDB
280	10	no good hits	flagged in OMDB
459	14	11% lost TDC edges	
488	15	19% lost TDC edges	
491	15	20% lost TDC edges	
493	15	24% lost TDC edges	
499	15	14% lost TDC edges	
501	15	15% lost TDC edges	
502	15	17% lost TDC edges	
505	15	16% lost TDC edges	
506	15	20% lost TDC edges	
521	16	27% lost TDC edges	
600	18	57% lost TDC edges	
609	18	13% lost ADC	
611	18	24% lost ADC	
612	18	23% lost ADC	
613	18	17% lost ADC	
614	18	16% lost ADC	
617	18	15% lost ADC	
618	18	11% lost ADC	
634	18	53% lost TDC edges	
635	18	11% lost TDC edges	
642	19	10% lost TDC edges	

**Table 27** – List of those OMs which are excluded from this analysis from analysis *level3* on, due to either inconsistent behavior of their ADC or TDC, or because of permanent damage. Those OMs which are located in string 13 or which are already excluded by the standard OM selection are not listed.

### C.3.4 List of excluded OMs

All OMs which are excluded either due to inconsistencies in their ADC and TDC behaviors or due to permanent damage, and which are not already excluded by the standard OM selection (or located on string 13) are listed in Table 27.

The investigation of ADC-TDC inconsistencies was intended to resolve disagreements in the hit multiplicity distribution of the electrically read-out channels. Alas, most of the OMs whose ADC and TDC values are frequently inconsistent are located on strings which are read out via optical fiber, so the removal of OMs listed in Table 27 will not substantially improve the agreement between experimental and simulated data with respect to the hit multiplicities.

## C.4 Depth distribution of hits

Apart from the disagreeing multiplicities, first tests of the performance of the iterative likelihood reconstruction on subsets of the data indicated that the fraction of misreconstructed atmospheric muons is greater in experimental data than in simulated data. This phenomenon was observed

previously in AMANDA analyses and as of this writing remains poorly understood.<sup>51</sup> Figure C.22 shows the cosine of the reconstructed zenith angle in CORSIKA events and experimental data.

Contrary to the disagreement in the hit multiplicities, the increased fraction of misreconstructed events is not caused by additional noise hits. Rather, it is related to a lack of hits in the upper part of the detector. Figure C.23 shows the number of hit OMs with optical readout ( $NCH_{\text{optical}}$ ) for events that are reconstructed as up-going ( $\cos \Theta < 0$ ). Only optically read-out OMs are considered here, because the electrically read-out ones are less understood. For experimental data, the  $NCH_{\text{optical}}$  distribution falls off more steeply. An investigation of the depth distribution of the hits revealed that experimental data have fewer hits in the upper part of the detector than predicted by the simulation. Low multiplicity events without any hits in the upper part of the detector tend to be misreconstructed as up-going particles. Such events occur more frequently in experimental than in simulated data, hence the increased rate of misreconstructed events.

The lack of hits is present for events that are reconstructed as both up- and down-going particles. Figure C.24 compares the depth distribution for simulated and experimental events independent of the reconstructed track direction. Again, only optically read-out channels are considered. For simulated data, OMs in the top half of the detector ( $z > 0$ ) are hit more frequently than those in bottom half. Such behavior would be expected for atmospheric muon events, since the muons enter the detector from above and a large portion range out within the detection volume. In experimental data, however, OMs in top and bottom half are hit about equally frequently.

The reason for the lack of hits in the upper part of the detector is not fully understood. It is however certain that it is not a result of the data selection: The disagreement between experimental and simulated data with respect to the depth distribution of hits is qualitatively the same at each data selection level from trigger level on. The disagreement is also present for the inner strings of the detector which are read out via electrical cables.

Disagreements in the depth distribution of hits have been observed previously and were considered a result of the simplified photon propagation through the Polar ice in the simulation [139]. Remarkably however, some disagreement is still present in the latest simulation set-ups, in which photons are tracked through multiple ice layers [198]. In a recent simulation effort (performed for a search for ultra high energy neutrinos in the 2003 data set [178]), agreement between experimental and simulated data could only be established by down-scaling the sensitivities of most of OMs in the upper part of the detector in the simulation (see [199] and [200] for details). For this analysis, we discard OMs located more than 100 m above the detector center, above which the observed hit probabilities deviate most from the predicted ones (*c.f.* Figure C.24).

From data selection *level 3* on, the light deposition in the detector is estimated only via optically read-out OMs located at a depth below  $z = 100$  m relative to the detector center. The removal of (according to this brightness assessment) "dim" events eliminates the excess of misreconstructed events

<sup>51</sup>To most analyses, the unsimulated background is relatively unproblematic. Searches for neutrino point sources do not rely on simulation, as the background is estimated ("off-source") from experimental data. In searches TeV neutrino fluxes in general, a large fraction of the unsimulated misreconstructed background muons is rejected with quality cuts, which however only efficient in exactly this energy range.

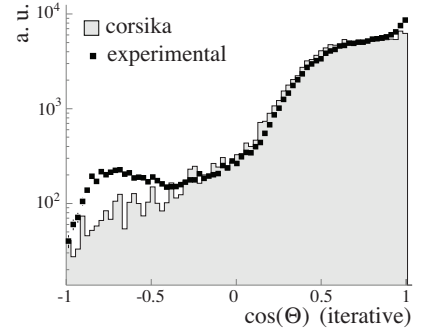


**Figure C.22** – Cosine of the reconstructed zenith angle obtained from an iterative likelihood reconstruction after applying *level 2* cuts.

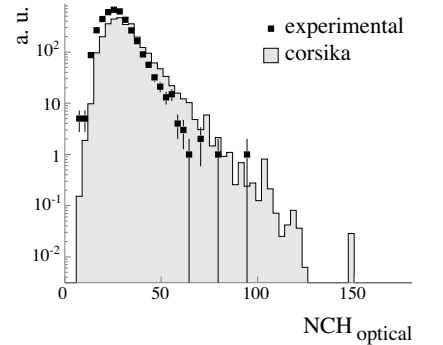


**Figure C.23** – Number of hit OMs with optical read-out.

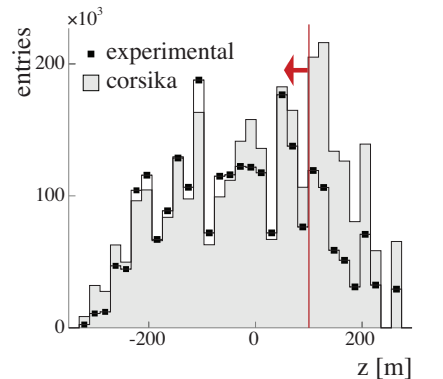
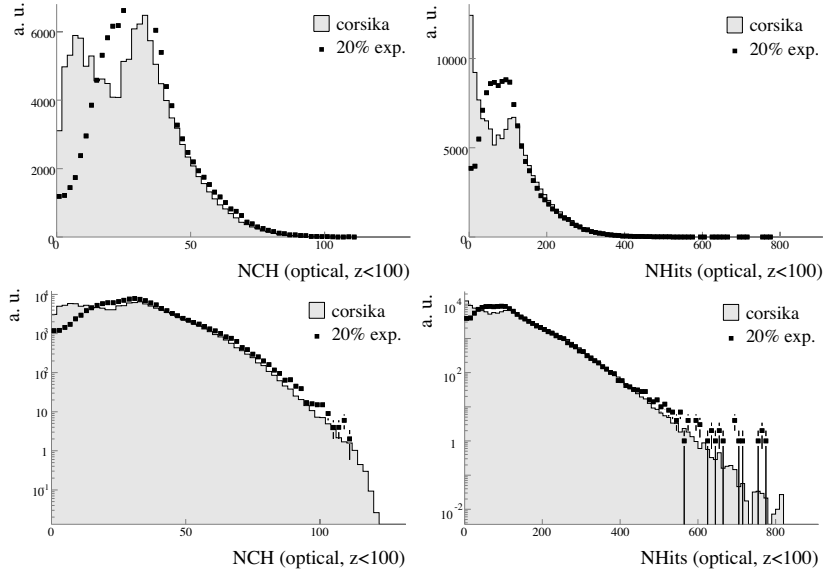


**Figure C.24** – The depth distribution of hits in optically read-out OMs.

**Figure C.25** – Channel and hit multiplicities ( $\text{NCH}_{\text{optical}}^{z < 100}$ , left and  $\text{NHits}_{\text{optical}}^{z < 100}$ , right) for OM with optical read-out, located below a depth of  $z = 100$  m relative to the detector center in linear (upper panels) and logarithmic (lower panels) representation.



in experimental data. A Fisher discriminant composed of  $\text{NCH}_{\text{optical}}^{z < 100}$  and  $\text{NHits}_{\text{optical}}^{z < 100}$  (channels and hit multiplicity taken from optically read-out channels below a depth of  $z = 100$  m) serves as cut parameter to remove these events (*c.f. cut # 6*, section 7.3.3). The distributions of the two input observables for simulated atmospheric muons and experimental data are shown in Figure C.25, both in linear and logarithmic representation. The removal of OMs in the upper part of the detector dramatically affects the agreement between experimental and simulated data for low multiplicity events: For simulated data, the multiplicity distributions peak at the lowest multiplicities. This is expected, since most of the hits occurred in the upper part of the detector, which is now excluded. For experimental data, there is no peak at the low-multiplicity end. This is also reasonable, since experimental data have fewer hits in the upper part of the detector, and hence the exclusion of the upper OMs does not reduce the overall hit multiplicity as much as in simulated data.

The disagreement for low multiplicities in the distributions poses however a less severe problem for this analysis, since low multiplicity events are not considered. Good agreement for extremely bright, high multiplicity events on the other hand is essential. The logarithmic representation of the multiplicities shown in the bottom panels of Figure C.25 demonstrate that good agreement is achieved for high multiplicities.<sup>52</sup>

Removing low multiplicity events with a cut based on hit multiplicities only in the optically read-out OMs below  $z = 100$  m (*cut # 6*) eliminates the excess of misreconstructed atmospheric muons in experimental data. Figure C.26 shows the cosine of the reconstructed zenith angle obtained from the iterative likelihood reconstruction after applying *cut # 6*.

### C.5 OM selection for the likelihood reconstruction

As stated above, good agreement between experimental and simulated data can be preserved at higher analysis levels, only if we use only optically read-

<sup>52</sup>The slight excess of experimental events at the highest multiplicities is (at least to some extent) attributed to the composition of primary cosmic rays that entered the simulation of the atmospheric muon sample (see appendix F).

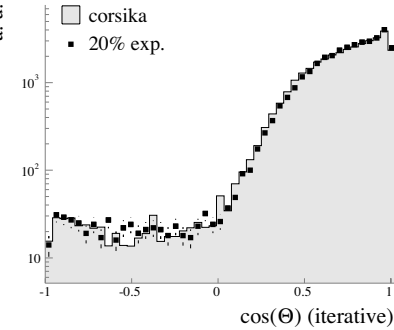


**Figure C.26** – Reconstructed zenith angle for simulated atmospheric muons (grey histogram) and experimental data (black markers) after removing low multiplicity events using a cut on the Fisher discriminant composed of  $\text{NCH}_{\text{optical}}^{z < 100}$  and  $\text{NHits}_{\text{optical}}^{z < 100}$  (*cut # 6* in section 7.3.3).

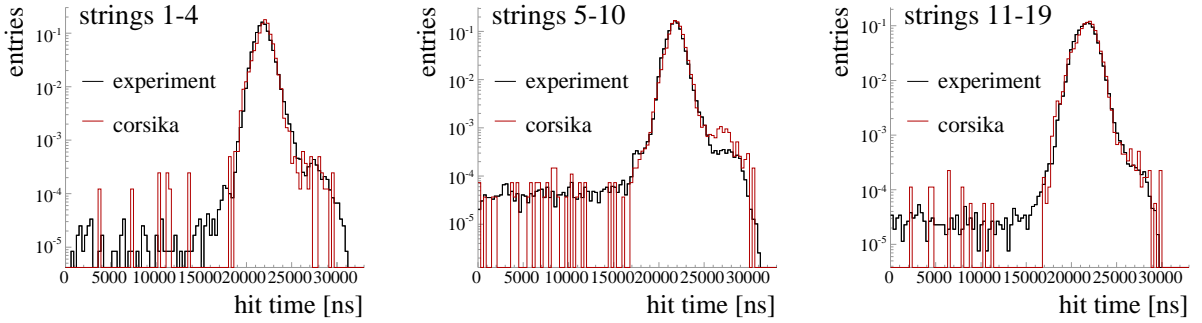


**Figure C.27** – Time distributions of first hits in each OM which passes the standard OM selection and the OM selection described in section C.3 for strings 1-4 (left), strings 5-10 (middle), and strings 10-19 (right). Hit cleaning as described in section 7.3.2 (hit cleaning for the iterative likelihood reconstruction) is applied. except for the time window cleaning (17000-25000 ns).

out OMs below a certain depth to assess the light deposition in the detector via the hit multiplicity or related observables.

In contrast to observables that are sensitive to the light deposition, and hence the *amount* of hits registered during an event, the likelihood reconstruction relies primarily on the *timing* of the first hit in each OM. That is, the OM selection applied for track reconstructions must establish good agreement in the timing distribution of the first hits, rather than in the hit multiplicity. In general, the OM selection should be as tight as necessary (in order to ensure an accurate description of experimental data by the simulation) and as loose as possible (in order to maximize the information provided to the reconstruction algorithm). In particular, the spatial volume covered by the OMs that are actually being used should be as large as possible, in order to pinpoint the track location at distinct points in space which are maximally spatially separated.

Since the hit times of first hits in all OMs agree well for both optically and electrically read-out OMs and for OMs at shallow depths, we include all OMs which pass the standard OM selection and the OM selection described in sections C.2.2 and C.3. Figure C.27 shows the timing distribution of the first hit in each OM which passes the *level 2* hit cleaning as defined in Table 7.2.1, except for the time window cleaning. OMs listed in Table 27 as well as OMs located on string 13 are excluded. Hits within the time window between 17000 and 25000 ns are used for the likelihood reconstruction. In this time window, hit times of simulated and experimental data agree well.

The inclusion of electrically read-out OMs and OMs at depths above  $z = 100$  m yields slightly better agreement between experimental and simulated data with respect to the reconstructed zenith angles. Figure C.28 compares the reconstructed zenith angles obtained from an iterative likelihood reconstruction using electrically and optically read-out channels over the full depth range to the zenith angles obtained from a likelihood reconstruction that uses only hits from optically read-out channels below  $z = 100$  m. Simulated and experimental data agree well for both reconstructions, but the agreement is slightly better for the reconstruction obtained with the larger OM set. Using the larger OM set also reduces the amount of hits reconstructed atmospheric muons in both experimental and simulated data.

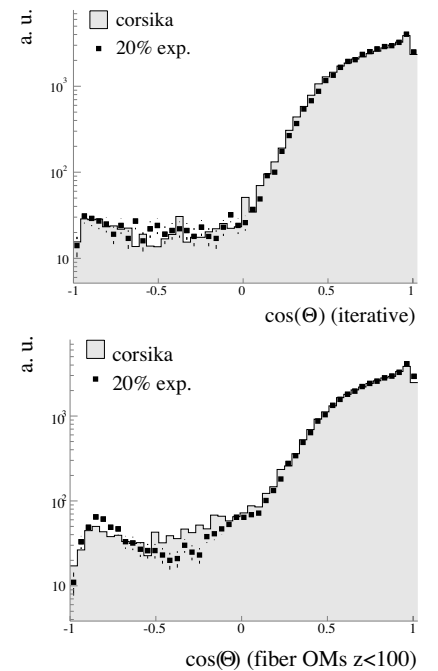


**Figure C.28** – Cosine of the zenith angle reconstructed with hits from all OMs which pass the standard OM selection and the OM selection described in section C.3 (top) and with hits only from optically read-out OMs at depths below  $z = 100$  m (bottom). The distributions were taken after applying *cut # 6* described in section 7.3.3.

## D Cut optimization using the Model Rejection Factor and limit calculation

The main objective of the AMANDA and IceCube experiments is to confirm or falsify yet undiscovered phenomena like cosmic neutrinos or, in this case, magnetic monopoles. Because the expected event rates from these phenomena are small, most AMANDA-II analyses are optimized with respect to the so-called *Model Rejection Factor* [201]: Final cuts are placed such that the most stringent constraint on a certain theoretical model is expected.

For this analysis, we optimize the final cuts such that we expect the minimum possible upper bound on an isotropic flux of monopoles at the location of the detector at 90% confidence level.

### D.1 Hypotheses Testing

After performing the Monte Carlo simulation and developing selection criteria, the mean number of signal events,  $\langle n_s \rangle$ , expected from the new phenomenon and the mean number of background events,  $\langle n_b \rangle$ , are known. We consider the case that they are Poisson distributed.

If  $x$  denotes the total number of events in a data sample (where it is not known, whether the sample consists of pure background events or of a combination of signal *and* background events), two alternative hypotheses can be formulated in terms of its probability distribution:

- $H_0$  :  $x$  is Poisson distributed with parameter  $\mu = \langle n_s \rangle + \langle n_b \rangle$ , following the probability distribution

$$f_0(x) = P(x | \mu) = \frac{(\langle n_s \rangle + \langle n_b \rangle)^x}{x!} e^{-(\langle n_s \rangle + \langle n_b \rangle)}, \quad (57)$$

corresponding to presence, of signal events and

- $H_1$  :  $x$  is Poisson distributed with parameter  $\mu = \langle n_b \rangle$ , as

$$f_1(x) = P(x | \mu) = \frac{\langle n_b \rangle^x}{x!} e^{-\langle n_b \rangle}, \quad (58)$$

corresponding to absence of signal events.

A critical number of events,  $n_0$ , can be defined, dividing all possible values of  $x$  in a rejection and a acceptance region of  $H_0$ . The value  $n_0$  is usually chosen with respect to the error probability:

$$\alpha \stackrel{!}{=} \sum_{x=0}^{n_0} f_0(x), \quad (59)$$

giving the probability of incorrect rejection of  $H_0$ , or, in other words, the probability of taking a new phenomenon to be absent, while it exists. The quantity  $1 - \alpha$  is called *significance level* of the test. The other type of error that can occur is given by

$$\beta = \sum_{x=n_0+1}^{\infty} f_1(x). \quad (60)$$

It describes the probability of taking the phenomenon to be present, while it is absent.

## D.2 Constructing Confidence Belts

Measuring the observable  $x$  means to measure a quantity that is supposed to be Poisson distributed with unknown “true” parameter  $\mu_t$ . For any hypothetical value  $\mu$  we can find the critical value  $n_0$  below which the corresponding null hypothesis  $H_0$  would be rejected at significance level  $1 - \alpha$  from

$$P(x > n_0(\mu) \mid \mu) \stackrel{!}{=} 1 - \alpha. \quad (61)$$

However, there is some ambiguity in choosing the acceptance region as a left bounded interval. One could also choose an interval  $[x_1, x_2]$  such that

$$P(x_1(\mu) < x < x_2(\mu) \mid \mu) = 1 - \alpha. \quad (62)$$

The boundaries  $x_1$  and  $x_2$  can be chosen arbitrarily, as long as the interval fulfills the significance condition (62). Additional criteria are thus needed to give a straight definition. One possible criterion is to choose *central intervals* such that the excluded tail on either side is  $\alpha/2$ . However, this choice can prove problematic in cases of small signals, because the rejection region may extent to negative, *i.e.*, unphysical values. Feldman and Cousins [175] therefore developed a more general *ordering scheme*, giving a unique rule, which values to include in the acceptance interval. This ordering is based on the ratio of likelihoods

$$R = P(x \mid \mu) / P(x \mid \mu_{\text{best}}), \quad (63)$$

where  $P(x \mid \mu)$  is the likelihood for obtaining  $x$  given the actual mean  $\mu$  and  $P(x \mid \mu_{\text{best}})$  is the likelihood for obtaining  $x$  given the best-fit physically allowed mean. Values of  $x$  are added in the acceptance interval for a given  $\mu$  in decreasing order of  $R$ , until the sum of all  $P(x \mid \mu)$  meets or exceeds the desired significance. The set of the acceptance intervals for all possible  $\mu$ 's is called a *confidence belt*. A schematic sketch of such a confidence belt construction is shown in figure D.1.

If we now assume a measurement of  $x$  had yielded a particular value  $x_0$ , we can determine a set of possible  $\mu$  with the property

$$P(\mu_1 < \mu < \mu_2) = 1 - \alpha, \quad (64)$$

where the boundaries  $\mu_1$  and  $\mu_2$  are a function of the measured  $x_0$ . From figure D.1 we can see that the condition

$$\mu_1(x_0) < \mu_0 < \mu_2(x_0) \quad (65)$$

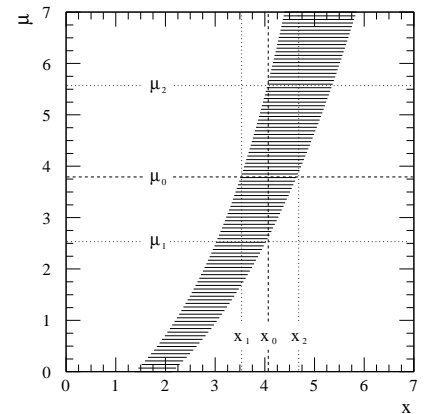


**Figure D.1** – Generic confidence belt construction. The full horizontal line segments indicate the acceptance intervals for each hypothetical  $\mu$ . Considering one particular choice  $\mu_0$ , we can see that  $\mu_0$  lies in the interval  $[\mu_1, \mu_2]$  exactly when  $x_0$  lies in the interval  $[x_1, x_2]$ . From [46].

is valid for an arbitrary  $\mu_0$  *exactly* when [202]

$$x_1(\mu_0) < x_0 < x_2(\mu_0). \quad (66)$$

The above relation is true for *any* choice of  $\mu_0$ , and thus also for the true value  $\mu_t$ . We can therefore give the probability of obtaining an interval  $[\mu_1, \mu_2]$  that includes  $\mu_t$ , namely:

$$P(\mu_1(x_0) < \mu_t < \mu_2(x_0)) = P(x_1 < x_0 < x_2) = 1 - \alpha. \quad (67)$$

$1 - \alpha$  is called *confidence level* of the given interval.

### D.3 The Average Upper Limit

Feldman and Cousins [175] proposed to quantify the sensitivity of an experiment independently of experimental data by calculating the *average* upper limit at a certain confidence level,  $\bar{\mu}$ , that would be obtained in absence of signal.

Assuming that the background is exactly known, the number of measured events  $x$  will behave according to equation (58), *i.e.*, in an ensemble of identical experiments, a particular result  $x_0$  would occur in a relative fraction  $P(x_0 | \langle n_b \rangle)$ . Since every  $x_0$  corresponds to exactly one upper limit, we can calculate an average upper limit by summing over all possible outcomes, weighted by their Poisson probability of occurrence (for the case that the ordering scheme results in a two-sided confidence interval, one uses the upper end  $\mu_2$  of the interval):

$$\bar{\mu} = \sum_{x_0=0}^{\infty} \mu(x_0) \frac{\langle n_b \rangle^{x_0}}{x_0!} e^{-\langle n_b \rangle}. \quad (68)$$

The average upper limit gives a quantification of the experimental sensitivity<sup>53</sup>, in that it gives the *most probable limit* the experiment would obtain in the case of no true signal. One could therefore also speak of a *limit expectation*. The average upper limit is given in absolute numbers of events and is, at that stage, model independent.

### D.4 The Model Rejection Factor

The average upper limit  $\bar{\mu}$  tells us that the experiment is capable to constrain any hypothetical signal that corresponds to a signal expectation of  $\langle n_s \rangle = \bar{\mu}$  at the required confidence level.

We can further quantify the sensitivity with respect to a particular hypothetical signal (or “model”) using the ratio of predicted signal events to average upper limit (the so-called *Model Rejection Factor*)

$$MRF = \frac{\langle n_s \rangle}{\bar{\mu}}. \quad (69)$$

A large *MRF* implies a large signal to background ratio, and hence a good sensitivity.

<sup>53</sup>Feldman and Cousins explicitly called this quantity the *sensitivity* of the experiment

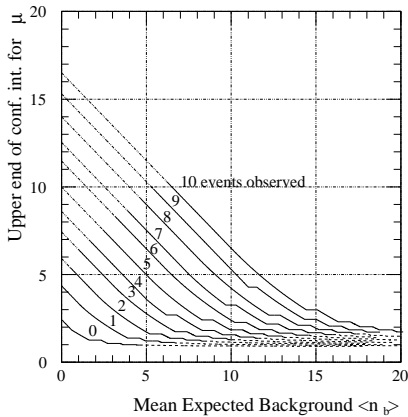


**Figure D.2** – Upper end  $\mu_2$  of a 90% confidence level intervals according to Feldman and Cousins for an unknown Poissonian signal mean  $\mu$  and mean expected background  $\langle n_b \rangle$ . Each curve corresponds to a hypothetical experimental observation  $x_0$ . Dotted lines at the upper left ends indicate regions where  $\mu_1$  is non-zero, dashed lines indicate regions where the number of obtaining  $x_0$  (or fewer) has fallen below 1%. From [175].

Following [201], we use the *MRF* for cut optimization. The optimization procedure works as follows. For the final cut parameter, we calculate  $\bar{\mu}$  from the number of remaining simulated background events  $\langle n_b \rangle$  and the number of remaining signal events  $\langle n_s \rangle$  predicted by the signal hypothesis. In our case, the underlying signal hypothesis is an isotropic flux of relativistic magnetic monopoles at the detector. The cut is placed where the *MRF* reaches its maximum.

The *MRF* corresponds to a certain flux strength, the (average) upper flux limit ( $\Phi_{C.L.}$ ), which is calculated by scaling the simulated flux ( $\Phi_{\text{simulated}}$ ) with  $MRF^{-1}$ . Expressed in terms of the flux upper limit, the optimum cut position is found by minimizing

$$\Phi_{C.L.} = \frac{\Phi_{\text{simulated}}}{MRF} \stackrel{!}{=} \text{min}. \quad (70)$$

## D.5 Confidence belt construction in presence of systematic uncertainties

After placing the final cut and unblinding the data, we observe a certain number of events  $x_0$  remaining in the final data set, and we place a limit on the flux of magnetic monopoles by comparing  $x_0$  to the number of expected background events. If the background and the monopole detection efficiency were exactly known, the limit calculation would reduce to the construction of a confidence belt as described above. In reality however, there the number of expected signal and background events ( $\langle n_s \rangle$  and  $\langle n_b \rangle$ ) are determined with Monte Carlo simulations, and are therefore subject to statistical and systematic uncertainties.

The uncertainties in the expected event rates translate into an uncertainty in the probability distributions that enter the calculation of the acceptance region for a given  $\mu$ . In order to take these uncertainties into account, the Poisson probability  $P(x | \mu = \langle n_s \rangle + \langle n_b \rangle)$  is replaced with an integral over possible true but unknown event rates  $n_b$  and  $n_s$  [176]:

$$\hat{P}(x|\mu) = \int_0^\infty \int_0^\infty P(x|n_s + n_b) w_b(n_b) w_s(n_s) dn_b dn_s. \quad (71)$$

The probability density functions  $w_b$  and  $w_s$  parameterize the uncertainties in background and signal expectation respectively. The shape of the functions can only be hypothesized. For this analysis, we assume Gaussian errors, so that the functions take the form

$$w_b(n_b) = \frac{1}{\sqrt{2\pi}\sigma_b} \exp\left(-\frac{(n_b - \langle n_b \rangle)^2}{2\sigma_b^2}\right) \quad (72)$$

$$w_s(n_s) = \frac{1}{\sqrt{2\pi}\sigma_s} \exp\left(-\frac{(n_s - \langle n_s \rangle)^2}{2\sigma_s^2}\right). \quad (73)$$

The widths of the distributions,  $\sigma_b$  and  $\sigma_s$ , would ideally be assessed by varying parameters in the simulation chain, and comparing the resulting event rates with the ones obtained with the standard simulation set up. For this analysis, this approach is impracticable, due to the CPU requirement of the simulations. So, these parameters can at best be estimated. Following the various AMANDA-II analyses that aim at constraining the flux of neutrinos of ultra high energies [178, 168, 179], we establish an estimate based on systematic studies undertaken for analyses that focus on neutrino detection in the TeV energy range (see chapter 10).

With the adopted values for  $\sigma_b$  and  $\sigma_s$ , the integral of equation 71 is fully defined, and the confidence belt can be constructed using the likelihood ratio ordering scheme described in section D.2. For the necessary computations, we use the program *POLE* (*POissonian Limit Estimator*) [203, 204] which provides a ready-to-use implementation of the algorithm described above.

## E Event #4731980

One event in the 20% data set stands out due to an extremely high light yield, while the reconstructed zenith angle is close to the horizon. The event was recorded in run #490 on day 260. Its event identification number is 4731980.

Event #4731980 was first noticed as an extreme outlier in the distribution of a light yield criterion used for the search for down-going monopoles (*cut d.2*, see section 9.1). The respective cut parameter (shown in Figure E.1 in semi-logarithmic representation) is a linear combination of the number of hits, the duration of the event, and the reconstructed zenith angle.

During the event, total of 2722 hits was recorded; 750 of these hits occurred in those OMs which are used to measure the light deposition (optically read out OMs below a depth of  $z = 100$  m). This is the highest hit multiplicity observed in the entire data set. The brightest event observed in the 80% data set after unblinding (event #484694) yielded a total of 2208 hits, 691 of which were recorded in the OMs used in this analysis.

Event #4731980 is reconstructed with a zenith angle of  $83.1^\circ$ , much closer to the horizon than the brightest event from the 80% data set (event #484694, which was reconstructed with a zenith angle of  $61.7^\circ$ ). Atmospheric muon bundles entering the detector at such flat zenith angles are not expected to deposit as much light as observed. Figure E.2 (page 136) shows the zenith angle dependency of some observables sensitive to the light yield (amplitude sum, number of hit OMs, total number of hits) for the 20% experimental data set and simulated atmospheric muon background before application of the final cut.

Visual inspection of the event signature and the event’s *fingerprint* (see appendix B and section 4.8.2) revealed no pathological features. The *fingerprint* of event #4731980 is shown in Figure E.3. Leading edge times recorded in individual strings show a rather hyperbolic structure, as expected for nearly horizontal events with many delayed photons. For the electrically read-out strings, (channel numbers smaller than 302), this structures appears to be washed out. This is a result of the the overflow of most channels (for the electrically read-out channels, earlier edges are discarded in favor of later ones if the TDC buffer is filled with 16 edges, see section 4.4.2). The leading edge time distribution in string 17 (this string located above the main detection volume and is normally not used for analysis purposes, see section 4.2) appears featureless. One may take this as in indication for the hits being of electronic origin. On the other hand, the hits on string 17 occur substantially later than the hits detected in the main detection volume (as it would be expected for photon hits several hundred meters away from the light source), and the photon arrival times might have been randomized by multiple scattering.

The values of the nine *flare indicators* (see appendix B) for event #4731980 are listed in Table 28. Two indicators (**flare\_induc\_B10** and **flare\_induc\_1119**) have undefined values, because the “normalization constants” which are required for their calculation are valid only over a limited channel multiplicity range (see [134]). Three indicators take values greater than one: **flare\_only\_adc**, **flare\_nch\_dead**, and **flare\_short\_M**. Two of these indicators (**flare\_nch\_dead** and **flare\_short\_M**) were identified as unsuitable for high energy analy-

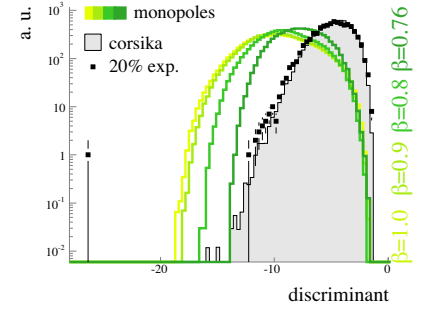


**Figure E.1** – Fisher discriminant used in *cut d.2*. Event #4731980 shows up as an extreme outlier.

(1) <b>flare_only_adc</b>	2.18
(2) <b>flare_missing_ch</b>	0.0003
(3) <b>flare_nch_dead</b>	5.71
(4) <b>flare_short_M</b>	2.71
(5) <b>flare_short_H</b>	0.18
(6) <b>flare_long_noise</b>	0.3
(7) <b>flare_long_missing</b>	0
(8) <b>flare_induc_B10</b>	undef.
(9) <b>flare_induc_1119</b>	undef.

**Table 28** – Values of the nine *flare indicators* for event #4731980 (see appendix B for an explanation of the indicators).

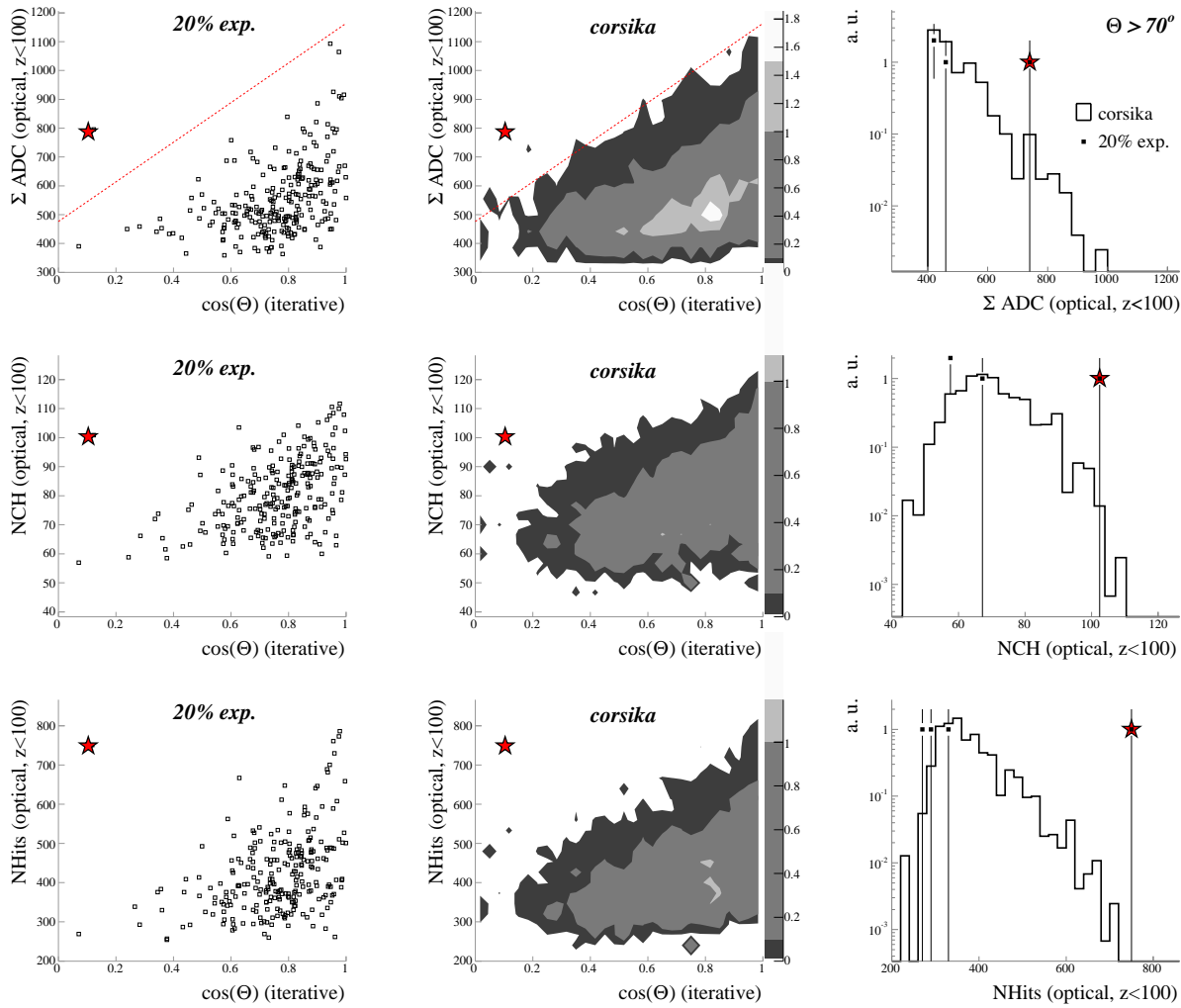


**Figure E.2** – Observables sensitive to the light yield: Amplitude sum ( $\Sigma \text{ADC}_{\text{optical}}^{z < 100}$ , top row), number of hit OMs ( $\text{NCH}_{\text{optical}}^{z < 100}$ , middle row), and hit multiplicity ( $\text{NHits}_{\text{optical}}^{z < 100}$ , bottom row). Shown are the dependencies of the three observables on cosine of the reconstructed zenith angle for 20% of the experimental data set (left column) and simulated atmospheric muon background (middle column) before the application of the final cut (the final cut in the  $\Sigma \text{ADC}_{\text{optical}}^{z < 100}$ - $\cos \Theta$ -plane is marked by the red lines in the top-row plots). The right column shows the one-dimensional distribution of the three observables for simulated atmospheric muon background (open histograms) and 20% experimental data (black markers) for events which were reconstructed with zenith angles greater than  $70^\circ$ . In this angular region, the 20% experimental data set comprises four events. For three of the four events, the light yield is consistent with predictions from the background simulation. One event (event #4731980, marked as a red star in each of the plots) lies in a region where, dependent on the observable, the background expectation has fallen below  $10^{-1}$  to  $< 10^{-3}$  events.

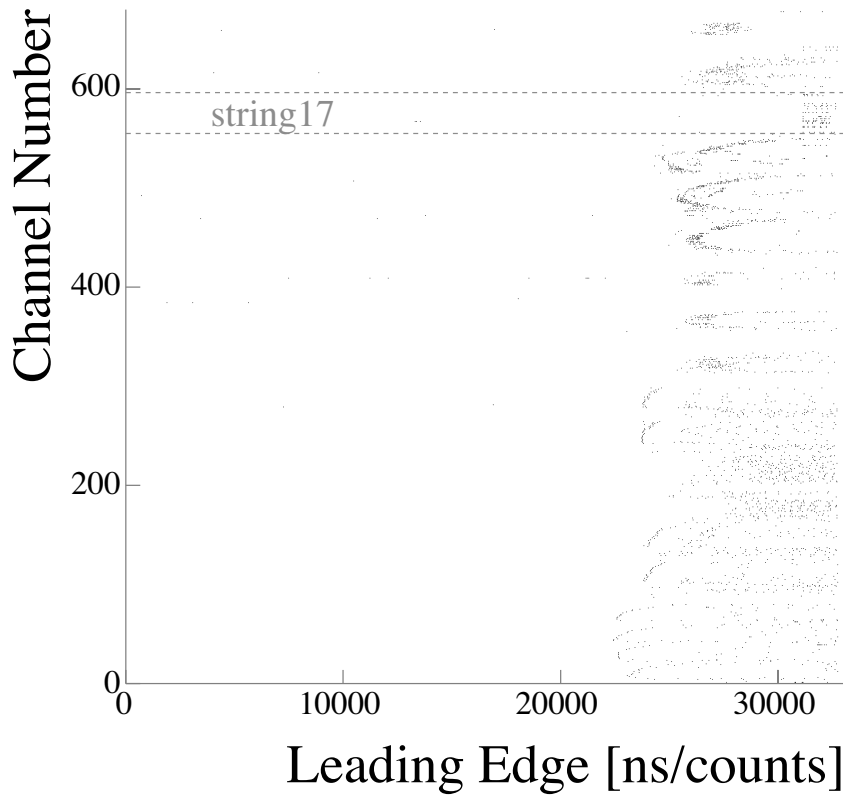


Figure E.3 – The *fingerprint* (OM number versus uncalibrated leading edge times) for event #4731980.

ses, because they were found to be correlated to light deposition [205].<sup>54</sup> If these two indicators are not considered, the largest value observed is `flare_only_adc`=2.18, which lies within the range of indicator values expected for particle induced events.<sup>55</sup>

Figure E.4 shows a snapshot of event #4731980 in the event display. The signature exposes no obvious characteristics of an instrumental effect. The hit pattern suggest a spherical light emission as expected from Cherenkov emissions induced by electromagnetic or hadronic cascades of extremely high energy. Although the hit pattern does not resemble the track-like signature expected for monopole signals, it was decided to leave the event in the data set. An alternative approach would have been to try to develop criteria to eliminate high energy cascade-like events. At this point of the analysis however, the event was considered a potential candidate for a ultra-high energy (UHE) neutrino interaction. If the unblinding had revealed indications for a UHE neutrino flux at a measurable level, monopole search above the horizon would have been proven impossible (due to

<sup>54</sup>The behavior of flare indicators in events with high light yield was studied using events triggered by the light pulses from a nitrogen laser of varying intensity [205]. The indicators `flare_nch_dead` and `flare_short_M` were correlated to the amount of light released in the detector, taking values as high as 10 (`flare_nch_dead`) and 9 (`flare_short_M`) for laser pulses at highest intensities. The enhanced values are probably due to a large amount of cross talk. The probability for a pulse to induce cross talk in an adjacent cable rises with the pulse amplitude. The indicators `flare_nch_dead` and `flare_short_M` are sensitive to cross-talk, as they are related to the amount of hits observed in otherwise “dead” channels and the amount of hits with unusually short TOT in OMs read out via twisted-pair cable respectively.

<sup>55</sup>The considered data set comprises 889 events. According to equation (55) in appendix B, the indicator value above which we expect *less* than one particle induced event is `flare_only_adc`= $\log_{10}(889) = 2.9$ .

the irreducible background of extraterrestrial neutrinos), and this analysis would have turned into a UHE neutrino detection, although not initially intended.

Only after completion of this analysis (unblinding yielded no additional UHE neutrino candidates), event #4731980 was finally identified as a detector artifact. Motivated by the observation of event #4731980 in this analysis, the highest multiplicity events in data sets taken after 2000 were selected and visually inspected [206]. Ten of the inspected events were nearly identical copies of event #4731980. Figure E.5 shows snapshots of three of the ten instances that were found.

The origin this class of events is still unknown. Vertex reconstructions [160] applied to the hit patterns of the ten events suggest a light deposition in the detector close to OM #531, located on string 16. It seems very likely that an electronics component in OM #531 or in a neighboring OM is damaged.<sup>56</sup> In contrast to its neighbors, OM #531 contains an artificial light source, an UV LED flasher board. The LED flasher boards, prototypes of the flasher boards that were later deployed with the IceCube Digital Optical Modules (DOMs), are the brightest light sources that were deployed within the AMANDA detector. Unfortunately, no instance of an event triggered by firing the LEDs in OM #531 could be found in archived calibration data. The flasher boards on string 16 were never used for calibration (they were mainly deployed for test purposes regarding the DOM development) and existing data from these flasher runs were not archived with the standard calibration data [207].

According to the developers of the LED flasher boards, an unintentionally release of light is impossible, even if parts of hardware were damaged [208]. As of this writing, the eleven background events still lack an explanation. So far, no additional instances of the signature have been observed.

---

<sup>56</sup>OM #531 did not pass the standard OM selection criteria for the year 2000, but it was considered functional during the following years. Neighboring OMs were considered functional over all years, including 2000.

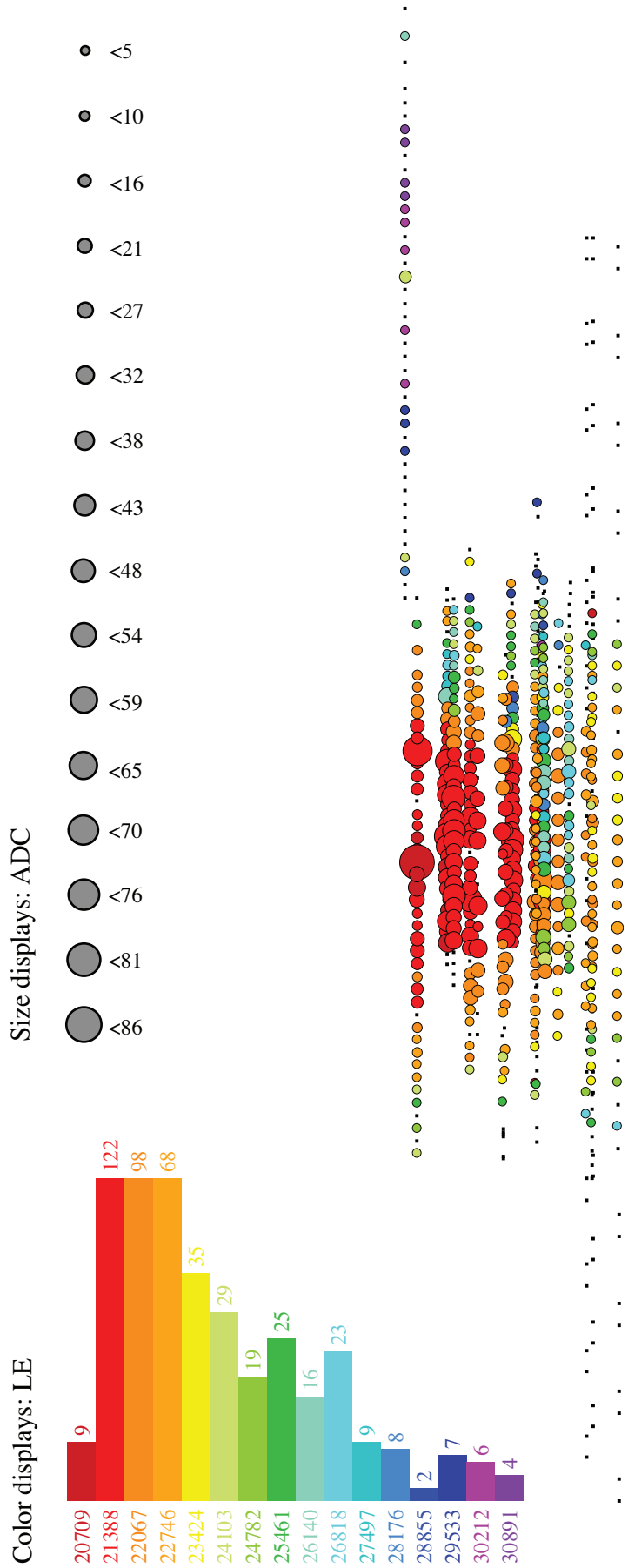


**Figure E.4** – Event #4731980 in the event display. For a better exposure of the time flow, only first hits in each OM are displayed.

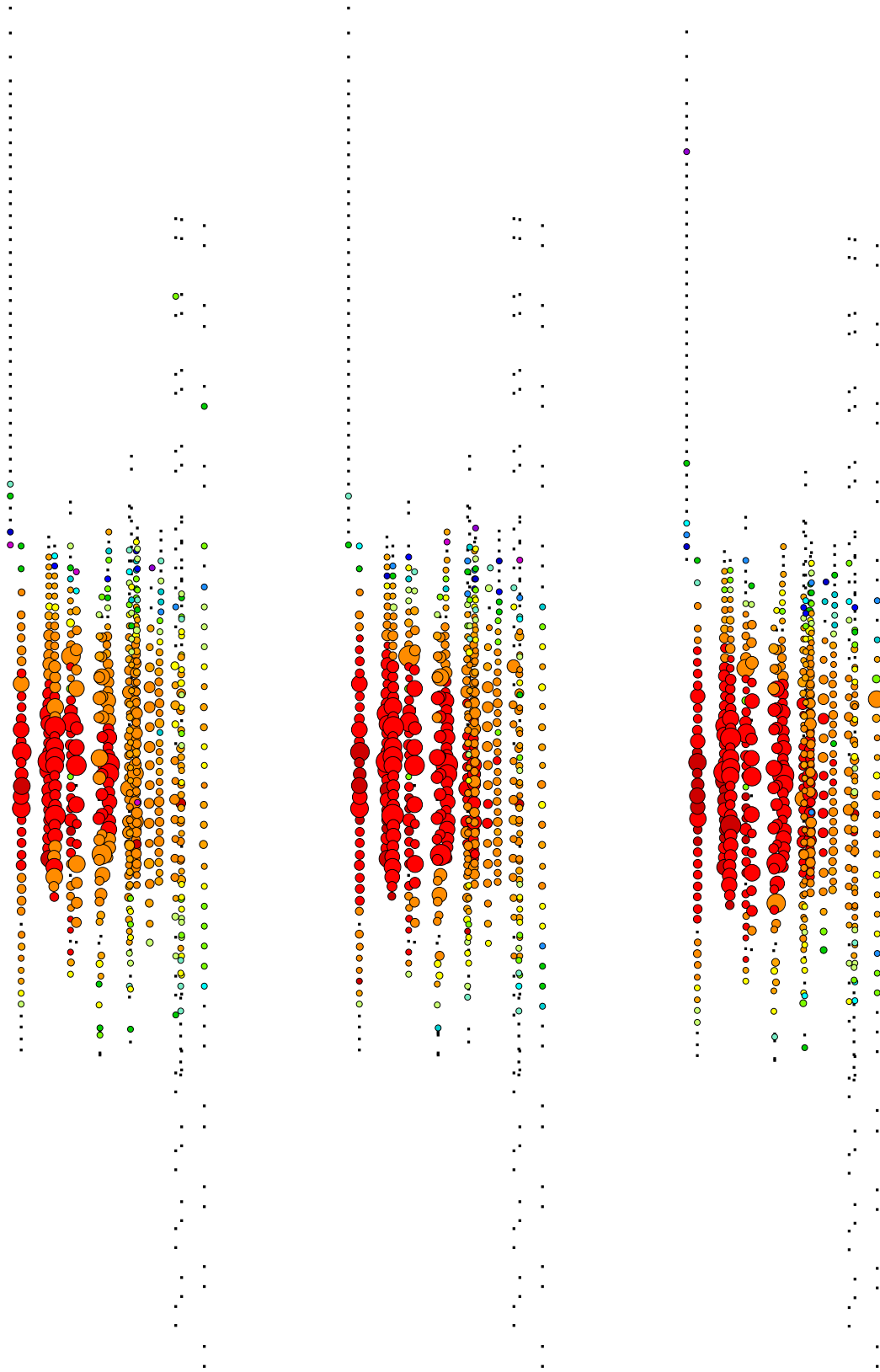


**Figure E.5** – Examples of event signatures that are nearly identical to the signature of event #4731980. Event #845896 (left), event #960804, and event #3725389 were recorded during the year 2003.

## F Primary cosmic ray composition and energy spectra used for the background simulation

The primary cosmic ray spectrum and composition used for the simulations of the atmospheric background muons in most AMANDA and IceCube analyses is the *poly-gonato* model (see section 5.3.2). Within the *poly-gonato* model, trans-iron elements (nuclear charge  $Z > 26$ ) play an important role at high energies. Figure F.1 shows the contribution of different mass groups to the all-particle spectrum. At energies above  $10^{7.5}$  GeV  $\approx 3.3 \times 10^7$  GeV, elements with  $Z > 27$  contribute more than 10% to the all-particle flux. As mentioned in section 5.3, the simulation of these heavy elements is not supported by the simulation package CORSIKA, and hence their contribution is missing in the background simulation.

Above a certain energy threshold, the lack of heavy elements in the atmospheric muon simulation must become apparent. Figure F.2 shows the energy spectrum of simulated cosmic ray primaries for background events which remain after the application of *cut # d.2* (see section 9.1). The energy distribution peaks around  $3 \times 10^7$  GeV.

At this selection level, a deficit of simulated background events with high light deposition is indeed observed. Figure F.3 shows the distribution of the Fisher discriminant that was used in *cut # d.2*. The left panel of the figure shows a comparison of the distributions (*after applying cut 2.d*) observed in 20% experimental data (black markers) and the atmospheric muon background simulated using the *poly-gonato* model (open histogram). The deficit of simulated events becomes apparent for values of the discriminant smaller than  $\sim 10$  (a small value of the discriminant corresponds to events with a high light yield, and hence to a large primary energy). The right panel of Figure F.3 shows the correlation of the discriminant with energy of the cosmic ray primary. As expected, the region in which we observe an excess of experimental events corresponds to primary energies greater than  $\sim 10^{7.5}$  GeV.

A similar excess of experimental events is also observed in other observables sensitive to light deposition. Figure F.4 shows the distributions of the amplitude sum ( $\Sigma \text{ADC}_{\text{optical}}^{z < 100}$ ), the hit multiplicity ( $\text{NHits}_{\text{optical}}^{z < 100}$ ), and the number of hit channels ( $\text{NCH}_{\text{optical}}^{z < 100}$ ) for 20% of the experimental data and simulated atmospheric muon background (top row), and the correlation of these three observables to the primary energy (bottom row).

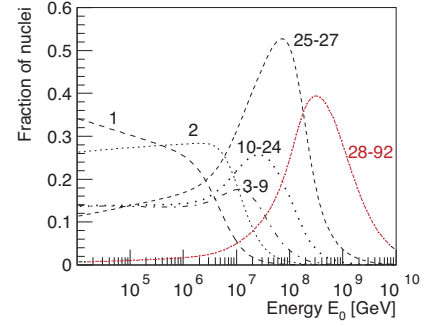


**Figure F.1** – Energy dependence of the relative contribution from different mass groups of galactic cosmic rays to the all-particle flux according to the *poly-gonato* model. The *poly-gonato* model does not account for extragalactic cosmic rays, which are believed to dominate the flux at highest energies.

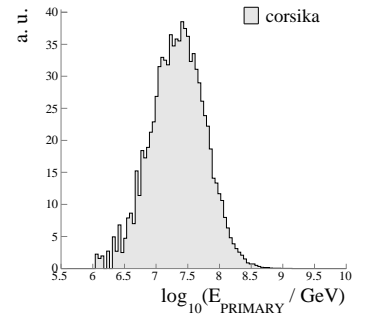


**Figure F.2** – The primary energy spectrum after application of *cut # d.2*.

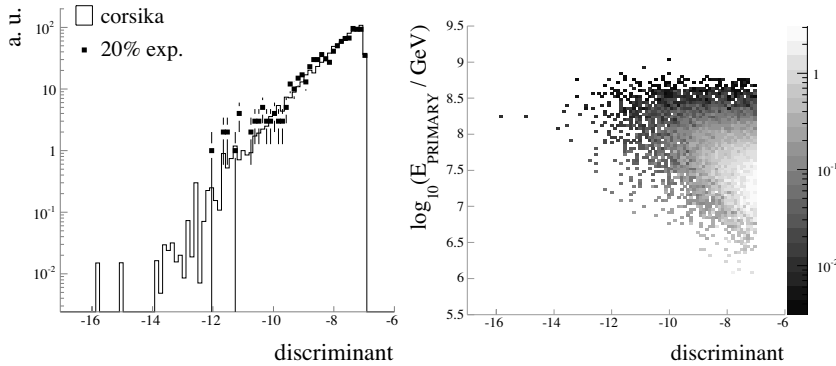


**Figure F.3** – Distribution of the Fisher discriminant used as cut parameter in *cut # d.2* for 20% experimental data compared to the background simulation (left) and the correlation of the discriminant with primary energy (right).

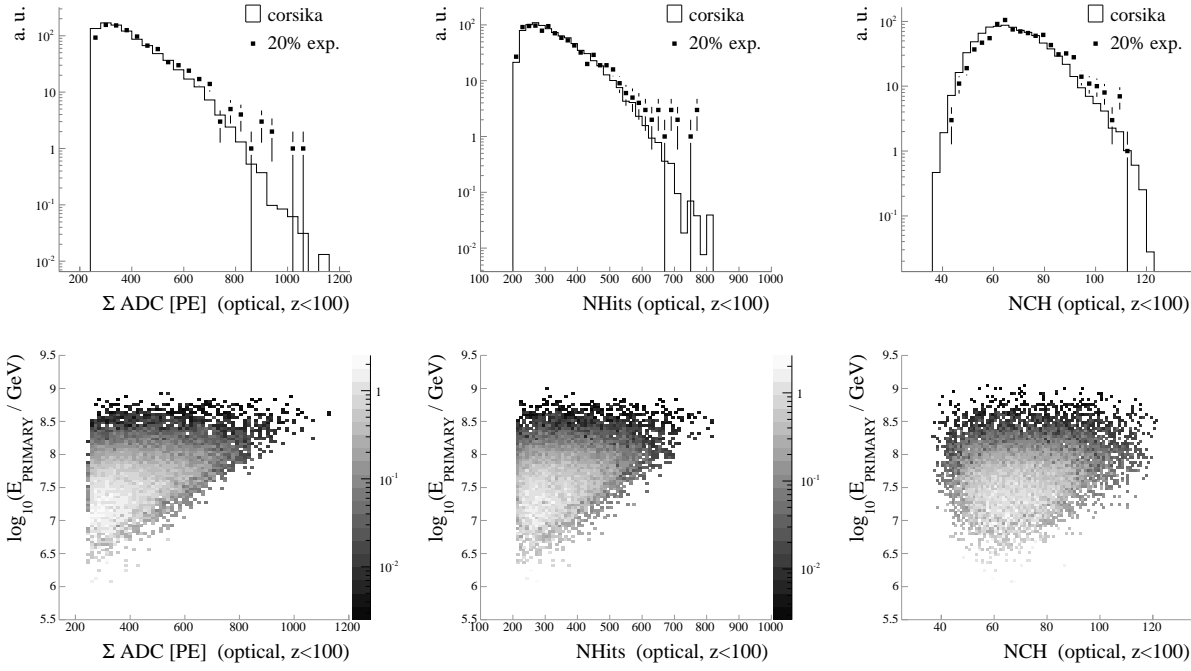


**Figure F.4** – Observables sensitive to the light yield:  $\Sigma \text{ADC}_{\text{optical}}^{z<100}$  (left),  $\text{NHits}_{\text{optical}}^{z<100}$  (middle), and  $\text{NCH}_{\text{optical}}^{z<100}$  (right). The panels in the top row show the one-dimensional distributions of these three observables for 20% experimental data (black markers) and background simulation using the *poly-gonato* model (open histograms) after application of *cut # d.2* (see section 9.1). The panels in the bottom row show the correlation of these three observables with the energy of the initial cosmic ray primary.

The distributions of experimental and simulated data disagree in the region where the energies of the simulated cosmic ray primaries exceed  $\sim 10^{7.5}$  GeV.

The *poly-gonato*-model obviously does not provide a sufficient description of the atmospheric muon background at highest energies if trans-iron elements are discarded in the CORSIKA simulation. The *two-component* model in contrast, can provide a more accurate description because it models the all-particle flux over the full energy range with only two elements, proton and iron primaries. Figure F.5 compares the primary energy spectra for events remaining after *cut # d.2*, simulated with *poly-gonato* model and the *two-component* model respectively. For the event sample simulated with the *poly-gonato* model the event rate drops off more rapidly with primary energy.

The presence of additional high energy primary particles in the *two-component* sample affects the distributions of key observables used in this analysis. Figure F.6 shows a comparison between the *poly-gonato* and the *two-component* model for the three observables  $\Sigma \text{ADC}_{\text{optical}}^{z<100}$ ,  $\text{NHits}_{\text{optical}}^{z<100}$ , and  $\text{NCH}_{\text{optical}}^{z<100}$ . For all three observables, the *two-component* model is in better agreement with experimental data.

Generally, we must conclude that for monopole searches above the horizon, or other searches for signals whose prime distinctive feature is a high light yield (and which consequently have an extremely high energy threshold), the standard approach for background simulation (using the *poly-gonato* model discarding trans-iron elements) is unfeasible. Apart from the *poly-gonato* model, the *two-component* model is, to the knowledge of the author, presently the only available model that provides a straight parame-

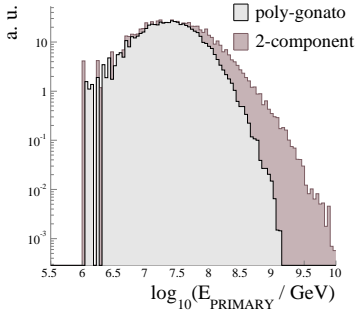


**Figure F.5** – Primary energy spectra for background samples simulated with the *poly-gonato* model (grey) and the *two-component* model (light purple) after applying *cut # d.2* (see section 9.1).

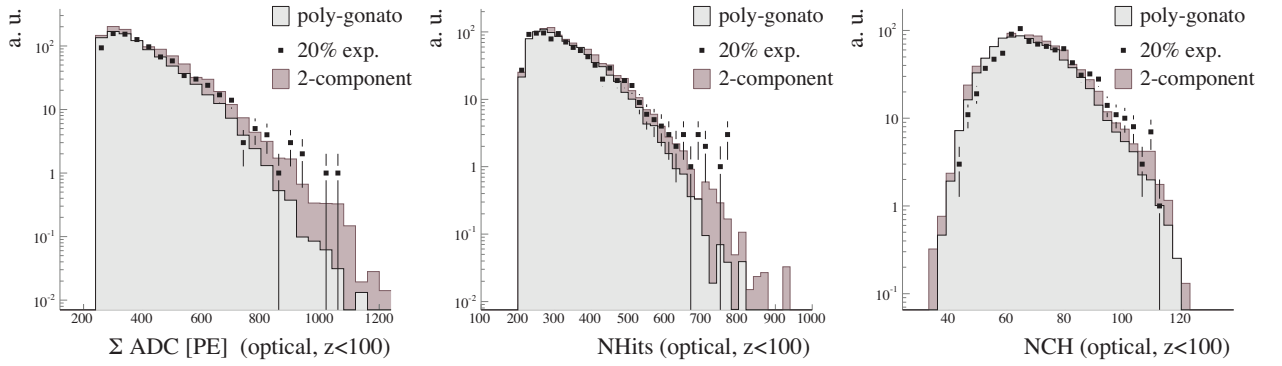


**Figure F.6** – Distributions of  $\Sigma \text{ADC}_{\text{optical}}^{z < 100}$  (left),  $\text{NHits}_{\text{optical}}^{z < 100}$  (middle), and  $\text{NCH}_{\text{optical}}^{z < 100}$  (right) for simulated atmospheric muon background using the *poly-gonato* model (light grey histograms) and the *two-component* model (light purple histograms), compared to 20% of the experimental data set (black markers).

terization of the energy spectra of individual elements in cosmic radiation. Although the *two-component* model drastically simplifies known facts (using only two elements to describe the all-particle spectrum<sup>57</sup>), it is capable to describe the cosmic-ray induced muon background in AMANDA-II up to the final level of this analysis reasonably well.

At the final analysis level, the improvements achieved by using the *two-component* model instead of the standard approach becomes obvious. Figure F.7 shows the number of background events predicted by both models as a function of the final cut value (one of the key quantities used for cut optimization). The predictions from the *two-component* and the *poly-gonato* model for the number of background events to remain after unblinding differ by almost an order of magnitude: The *two-component* model predicts 2.6 events, while the *poly-gonato* model predicts 0.3 events after imposing the final cut.

It should be emphasized that the problems of standard background simulation to reproduce experimental data at highest energies is not due to the *poly-gonato* model itself, but due to the limitations in the simulation package CORSIKA. Since the *complete* model cannot be simulated, it remains unknown whether or not the *poly-gonato* model is in agreement with AMANDA data.

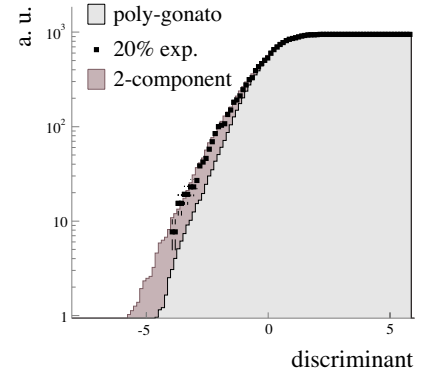


**Figure F.7** – Number of background events in the final data set predicted by the *two-component* model (light purple) and the *poly-gonato* model (light grey) as a function of the position of the final cut on the Fisher discriminant (see section 9.2). Optimum sensitivity is achieved by requiring the discriminant to be smaller -4.7. Experimental data (events from the 20% data set, scaled to the livetime of the 80% initially blind data set) are shown for comparison (black markers). For the sake of clarity, the single “outlier event” present in the 20% data set (event #4731980, see section 9.1 and appendix E) is not included in the distribution.

<sup>57</sup>A more recent analysis of data taken by the KASCADE experiment [151] aims at measuring the energy spectra of five primary mass groups [82]. The analysis technique is similar to the one used for the *two-component* model, but the model uses five primary elements (protons, helium, carbon, silicon, and iron) to approximate the all particle flux, instead of only protons and iron. Reference [82] does not yet give straight parameterizations of the energy spectra because, according to the authors, the analysis is limited by uncertainties in the presently available cosmic ray interactions models.

## References

- [1] J. C. Maxwell. A Dynamical Theory of the Electromagnetic Field. *Philosophical Transactions of the Royal Society of London*, 155:459–512, 1865.
- [2] E. Amaldi et al. Search for Dirac magnetic poles. CERN-63-13.
- [3] Paul A. M. Dirac. Quantised Singularities in the Electromagnetic Field. *Proc. Roy. Soc. A*, 133:60–72, 1931.
- [4] John Preskill. Magnetic monopoles. *Ann. Rev. Nucl. Part. Sci.*, 34:461–530, 1984.
- [5] J. M. Figuera-O’Farrill. Electromagnetic Duality for Children. Lectures on electromagnetic duality, University of Edinburgh, 1998.
- [6] A. Zee. *Quantum Field Theory in a Nutshell*. Princeton University Press, 2003.
- [7] Y. Aharonov and D. Bohm. Significance of electromagnetic potentials in the quantum theory. *Phys. Rev.*, 115:485–491, 1959.
- [8] H. Georgi and S. L. Glashow. Unity of all elementary particle forces. *Phys. Rev. Lett.*, 32:438–441, 1974.
- [9] Gerard ’tHooft. Magnetic Monopoles in Unified Gauge Theories. *Nucl. Phys. B*, 79:276–284, 1974.
- [10] Alexander M. Polyakov. Particle spectrum in quantum field theory. *JETP Lett.*, 20:194–195, 1974.
- [11] E. J. Weinberg. Monopoles and Grand Unification. Invited talk given at Monopole ’83 Conf., Ann Arbor, MI, Oct 6-9, 1983.
- [12] G. Boerner. *The early universe*. Springer Verlag, 1988.
- [13] H. Georgi, H. R. Quinn, and S. Weinberg. Hierarchy of interactions in unified gauge theories. *Phys. Rev. Lett.*, 33:451–454, 1974.
- [14] M. Daniel, G. Lazarides, and Q. Shafi. SU(5) monopoles, magnetic symmetry and confinement. *Nucl. Phys.*, B170:156, 1980.
- [15] George Lazarides, C. Panagiotakopoulos, and Q. Shafi. Magnetic monopoles from superstring models. *Phys. Rev. Lett.*, 58:1707, 1987.
- [16] P. H. Frampton and T. W. Kephart. Higgs sector and proton decay in SU(15) grand unification. *Phys. Rev.*, D42:3892–3894, 1990.
- [17] P. H. Frampton and B.-H. Lee. SU(15) grand unification. *Phys. Rev. Lett.*, 64:619, 1990.
- [18] T. W. Kephart and Q. Shafi. Family unification, exotic states and magnetic monopoles. *Phys. Lett.*, B520:313–316, 2001.
- [19] S. F. King and Q. Shafi. Minimal supersymmetric SU(4) x SU(2)L x SU(2)R. *Phys. Lett.*, B422:135–140, 1998.
- [20] A. D. Linde. Phase transitions in gauge theories and cosmology. *Rept. Prog. Phys.*, 42:389, 1979.
- [21] E. W. Kolb and M. S. Turner. *The Early Universe*. Addison Wesley, 1993.

- [22] T. W. B. Kibble. Topology of cosmic domains and strings. *J. Phys.*, A9:1387–1398, 1976.
- [23] A. H. Guth. The inflationary universe: A possible solution to the horizon and flatness problems. *Phys. Rev.*, D23:347–356, 1981.
- [24] A. D. Linde. A new inflationary universe scenario: A possible solution of the horizon, flatness, homogeneity, isotropy and primordial monopole problems. *Phys. Lett.*, B108:389–393, 1982.
- [25] John P. Preskill. Cosmological production of superheavy magnetic monopoles. *Phys. Rev. Lett.*, 43:1365, 1979.
- [26] G. Lazarides, C. Panagiotakopoulos, and Q. Shafi. Magnetic monopoles from superstring models. *Phys. Rev. Lett.*, 58:1707, 1987.
- [27] W. Collins and M. S. Turner. Thermal production of superheavy magnetic monopoles in the new inflationary-universe scenario. *Phys. Rev. D*, 29(10):2158–2161, May 1984.
- [28] M. S. Turner. Thermal production of superheavy magnetic monopoles in the early universe. *Phys. Lett.*, B115:95, 1982.
- [29] P. J. Steinhardt. Progress and Prospects for the Inflationary Universe. Invited talk given at Monopole '83 Conf., Ann Arbor, MI, Oct 6-9, 1983.
- [30] S. Dar, Q. Shafi, and A. Sil. Flux of primordial monopoles. *Phys. Rev.*, D74:035013, 2006.
- [31] Q. Shafi and V. N. Senoguz. Coleman-Weinberg potential in good agreement with WMAP. *Phys. Rev.*, D73:127301, 2006.
- [32] D. V. Nanopoulos, K. A. Olive, M. Srednicki, and K. Tamvakis. Gauge hierarchy generation and cosmology in locally supersymmetric guts. *Phys. Lett.*, B124:171, 1983.
- [33] S. D. Wick, T. W. Kephart, T. J. Weiler, and P. L. Biermann. Signatures for a cosmic flux of magnetic monopoles. *Astropart. Phys.*, 18:663–687, 2003.
- [34] E. Huguet and P. Peter. Bound states in monopoles: Sources for UHECR? *Astropart. Phys.*, 12:277–289, 2000.
- [35] R. Beck, A. Brandenburg, D. Moss, A. Shukurov, and D. Sokoloff. Galactic Magnetism: Recent developments and perspectives. *Ann. Rev. Astron. Astrophys.*, 34:155–206, 1996.
- [36] P. P. Kronberg, P. Biermann, and F. R. Schwab. The continuum radio structure of the nucleus of M82. *Astrophys. J.*, 246:751–760, June 1981.
- [37] K. I. Kellermann and I. I. K Pauliny-Toth. Compact radio sources. *Ann. Rev. Astron. Astrophys.*, 19:373–410, 1981.
- [38] T. A. Ensslin, P. L. Biermann, P. P. Kronberg, and X.-P. Wu. Cosmic ray protons and magnetic fields in clusters of galaxies and their cosmological consequences. *Astrophys. J.*, 477:560, 1997.
- [39] D. Ryu, H. Kang, and P. L. Biermann. Cosmic magnetic fields in large scale filaments and sheets. 1998.

- [40] E. N. Parker. The Generation of Magnetic Fields in Astrophysical Bodies II: The Galactic Field. *Astrophys. J.*, 134:255, 1971.
- [41] M. S. Turner, E. N. Parker, and T. J. Bogdan. Magnetic monopoles and the survival of galactic magnetic fields. *Phys. Rev.*, D26:1296, 1982.
- [42] L. P. Gamberg and K. A. Milton. Dual quantum electrodynamics: Dyon dyon and charge monopole scattering in a high-energy approximation. *Phys. Rev.*, D61:075013, 2000.
- [43] S. P. Ahlen. Theoretical and experimental aspects of the energy loss of relativistic heavily ionizing particles. *Rev. Mod. Phys.*, 52:121–173, 1980.
- [44] H. Bethe. Zur Theorie des Durchgangs schneller Korpuskularstrahlen durch Materie. *Annalen der Physik*, 397:325–400, 1930.
- [45] D. H. Perkins. *Introduction to High Energy Particle Physics*. Addison - Wesley, 1987.
- [46] W. M. Yao et al. Review of particle physics. *J. Phys.*, G33:1–1232, 2006.
- [47] S. D. Wick, T. W. Kephart, T. J. Weiler, and P. L. Biermann. Signatures for a Cosmic Flux of Magnetic Monopoles. *VAND-TH*, (99-12), 1999.
- [48] P. A. Cherenkov. Visible Radiation Produced by Electrons Moving in a Medium with Velocities Exceeding that of Light. *Phys. Rev. Lett.*, 52:378, 1937.
- [49] D. R. Tompkins. Total Energy Loss and Cherenkov Emission from Monopoles. *Phys. Rev. B*, 138(1):248–250, 1965.
- [50] J. R. Ellis. Testing GUTs: Where do monopoles fit? Invited talk given at Magnetic Monopole Workshop, Racine, Wis., Oct 14-17, 1982.
- [51] C. G. Callan. Disappearing Dyons. *Phys. Rev.*, D25:2141, 1982.
- [52] V. A. Rubakov. Adler-Bell-Jackiw Anomaly and Fermion Number Breaking in the Presence of a Magnetic Monopole. *Nucl. Phys.*, B203:311–348, 1982.
- [53] V. A. Rubakov. Monopole catalysis of proton decay. *Rept. Prog. Phys.*, 51:189–241, 1988.
- [54] J. Arafune and M. Fukugita. Velocity dependent factors for the Rubakov process for slowly moving magnetic monopoles in matter. *Phys. Rev. Lett.*, 50:1901, 1983.
- [55] S. Errede. Experimental limits on monopole catalysis of nucleon decay. Invited talk given at Monopole '83 Conf., Ann Arbor, MI, Oct 6-9, 1983.
- [56] D. E. Groom. In search of the supermassive magnetic monopole. *Phys. Rept.*, 140:323, 1986.
- [57] M. Ambrosio et al. The MACRO detector at Gran Sasso. *Nucl. Instrum. Meth.*, A486:663–707, 2002.

- [58] M. Ambrosio et al. Final results of magnetic monopole searches with the MACRO experiment. *Eur. Phys. J.*, C25:511–522, 2002.
- [59] E. W. Kolb, S. A. Colgate, and J. A. Harvey. Monopole catalysis of nucleon decay in neutron stars. *Phys. Rev. Lett.*, 49:1373, 1982.
- [60] S. Dimopoulos, J. Preskill, and F. Wilczek. Catalyzed nucleon decay in neutron stars. *Phys. Lett.*, B119:320, 1982.
- [61] P. B. Price and M. H. Salamon. Search for supermassive magnetic monopoles using Mica crystals. *Phys. Rev. Lett.*, 56:1226–1229, 1986.
- [62] S. Orito et al. Search for supermassive relics with a 2000- $m^2$  array of plastic track detectors. *Phys. Rev. Lett.*, 66(15):1951–1954, Apr 1991.
- [63] Y. F. Novoseltsev et al. A search for massive magnetic monopoles at the Baksan Underground Scintillation Telescope (BUST). *Nucl. Phys. Proc. Suppl.*, 151:337–340, 2006.
- [64] E. Andres et al. Observation of high-energy neutrinos using Cherenkov detectors embedded deep in Antarctic ice. *Nature*, 410:441–443, 2001.
- [65] V. Aynutdinov et al. Search for a diffuse flux of high-energy extraterrestrial neutrinos with the NT200 neutrino telescope. *Astropart. Phys.*, 25:140–150, 2006.
- [66] T. Stolarczyk. Antares first muons with the first line. *Nucl. Phys. Proc. Suppl.*, 165:188–195, 2007.
- [67] J. Ahrens et al. Sensitivity of the IceCube detector to astrophysical sources of high energy muon neutrinos. *Astropart. Phys.*, 20:507–532, 2004.
- [68] A. Achterberg et al. First year performance of the IceCube neutrino telescope. *Astropart. Phys.*, 26:155–173, 2006.
- [69] E. G. Anassontzis et al. Towers and KM3NeT. *Nucl. Instrum. Meth.*, A567:538–544, 2006.
- [70] P. Piattelli. Status of NEMO. *Nucl. Phys. Proc. Suppl.*, 165:172–180, 2007.
- [71] T. K. Gaisser. *Particle astrophysics with high energy neutrinos*. Cambridge University Press, 1992.
- [72] M. Nagano and A. A. Watson. Observations and implications of the ultrahigh-energy cosmic rays. *Reviews of Modern Physics*, 72:689–732, July 2000.
- [73] T. K. Gaisser. Outstanding Problems in Particle Astrophysics. In M. M. Shapiro, T. Stanev, and J. P. Wefel, editors, *Neutrinos and Explosive Events in the Universe*, pages 3–+, January 2005.
- [74] M. Nagano et al. Energy spectrum of primary cosmic rays above  $10^{17}$  eV determined from the extensive air shower experiment at Akeno. *J. Phys.*, G18:423–442, 1992.
- [75] D. J. Bird et al. Evidence for correlated changes in the spectrum and composition of cosmic rays at extremely high-energies. *Phys. Rev. Lett.*, 71:3401–3404, 1993.

- [76] M. A. Lawrence, R. J. O. Reid, and A. A. Watson. The Cosmic ray energy spectrum above  $4 \times 10^{17}$  eV as measured by the Haverah Park array. *J. Phys.*, G17:733–757, 1991.
- [77] E. Fermi. On the Origin of Cosmic Radiation. *Phys. Rev.*, 75:1169–1174, 1949.
- [78] E. Fermi. Galactic magnetic fields and the origin of cosmic radiation. *Astrophysical Journal*, 119:1–6, 1954.
- [79] B. Wiebel-Sooth, P. L. Biermann, and H. Meyer. Cosmic rays. VII. Individual element spectra: prediction and data. *Astron. Astrophys.*, 330:389–398, February 1998.
- [80] E. G. Berezhko. Maximum energy of cosmic rays accelerated by supernova shocks. *Astroparticle Physics*, 5:367–378, October 1996.
- [81] P. O. Lagage and C. J. Cesarsky. The maximum energy of cosmic rays accelerated by supernova shocks. *Astron. Astrophys.*, 125:249–257, September 1983.
- [82] T. Antoni et al. KASCADE measurements of energy spectra for elemental groups of cosmic rays: Results and open problems. *Astropart. Phys.*, 24:1–25, 2005.
- [83] K. Greisen. End to the cosmic ray spectrum ? *Phys. Rev. Lett.*, 16:748, 1966.
- [84] J. R. Hoerandel. On the knee in the energy spectrum of cosmic rays. *Astropart. Phys.*, 19:193–220, 2003.
- [85] J. R. Hoerandel. Cosmic-ray composition and its relation to shock acceleration by supernova remnants. *ArXiv Astrophysics e-prints*, February 2007.
- [86] A. M. Hillas. Cosmic Rays: Recent Progress and some Current Questions. *ArXiv Astrophysics e-prints*, July 2006.
- [87] A. M. Hillas. TOPICAL REVIEW: Can diffusive shock acceleration in supernova remnants account for high-energy galactic cosmic rays? *Journal of Physics G Nuclear Physics*, 31:95–+, May 2005.
- [88] A. Atoyan and C. D. Dermer. High Energy Cosmic Rays from Local GRBs. *Journal of Physics Conference Series*, 47:92–101, October 2006.
- [89] V. S. Berezhinsky and S. I. Grigor'eva. A bump in the ultrahigh-energy cosmic ray spectrum. *Astron. Astrophys.*, 199:1–12, 1988.
- [90] V. Berezhinsky, A. Z. Gazizov, and S. I. Grigor'eva. Dip in UHECR spectrum as signature of proton interaction with CMB [rapid communication]. *Physics Letters B*, 612:147–153, April 2005.
- [91] C. H. V. Wiebusch. *The Detection of Faint Light in Deep Underwater Neutrino Telescopes*. PhD thesis, Rheinisch Westfälische Technische Hochschule Aachen, Germany, December 1995. PITHA 95/37.
- [92] M. Thunman, G. Ingelman, and P. Gondolo. Charm Production and High Energy Atmospheric Muon and Neutrino Fluxes. *Astropart. Phys.*, 5:309–332, 1996.

- [93] M. Ackermann. *Searches for signals from cosmic point-like sources of high energy neutrinos in 5 years of AMANDA-II data*. PhD thesis, Humboldt-Universität zu Berlin, 2006.
- [94] J. G. Learned and K. Mannheim. High-Energy Neutrino Astrophysics. *Annual Reviews of Nuclear Science*, 2000.
- [95] D. Chirkin and W. Rhode. Muon Monte Carlo: A New high precision tool for muon propagation through matter. AMANDA Internal Report 20010802, 2001.
- [96] R. M. Sternheimer and R. F. Peierls. General expression for the density effect for the ionization loss of charged particles. *Phys. Rev. B*, 3(11):3681–3692, Jun 1971.
- [97] Y. Kazama. Electric and Magnetic Dipole Moments of the Bound System of a Dirac Particle and a Fixed Magnetic Monopole. *Phys. Rev.*, D16:3078, 1977.
- [98] J. Derkaoui et al. Energy losses of magnetic monopoles and of dyons in the earth. *Astropart. Phys.*, 9:173–183, 1998.
- [99] M. Ackermann et al. Search for Ultra High-Energy Neutrinos with AMANDA-II. *Astrophys. J.*, 675:1014, 2008.
- [100] M. Ambrosio et al. Search for nucleon decays induced by GUT magnetic monopoles with the MACRO experiment. *Eur. Phys. J.*, C26:163–172, 2002.
- [101] A. Pohl and D. Hardtke. Subrelativistic particle searches with the AMANDA-II detector. In *Proc. 30th ICRC, Merida, Mexico*, 2007.
- [102] V. Aynutdinov et al. Search for relativistic magnetic monopoles with the Baikal neutrino telescope NT200. In *Proc. 29th ICRC, Pune, India*, 2005.
- [103] P. Niessen and C. Spiering. Search for relativistic magnetic monopoles with the AMANDA detector. In *Proc. 27th ICRC, Hamburg, Germany*, 2001.
- [104] J.-S. Ricol. *Etude de la détection de monopôles magnétiques au sein du futur télescope à neutrinos Antares et caractérisation des performances du traitement des impulsions des photomultiplicateurs*. PhD thesis, Université de la Méditerranée Aix-Marseille II, 2002.
- [105] B. A. P. van Rens. *Detection of Magnetic Monopoles below the Cherenkov Limit*. PhD thesis, Universiteit van Amsterdam, 2006.
- [106] B. A. P. van Rens. Detection of magnetic monopoles with the antares detector. *Phys. Atom. Nucl.*, 69:1908–1913, 2006.
- [107] T. Kajita et al. Search for nucleon decays catalyzed by magnetic monopoles. *J. Phys. Soc. Jap.*, 54:4065–4068, 1985.
- [108] R. Becker-Szendy et al. New magnetic monopole flux limits from the IMB proton decay detector. *Phys. Rev.*, D49:2169–2173, 1994.
- [109] I. A. Belolaptikov et al. The Baikal underwater neutrino telescope: Design, performance, and first results. *Astropart. Phys.*, 7:263–282, 1997.

- [110] K. Woschnagg and P. B. Price. Temperature dependence of absorption in at 532 nm. *Appl. Opt.*, 40:2496, 2001.
- [111] A. Achterberg et al. Five years of searches for point sources of astrophysical neutrinos with the AMANDA-II neutrino telescope. *Phys. Rev.*, D75:102001, 2007.
- [112] J. A. Aguilar et al. Transmission of light in deep sea water at the site of the antares neutrino telescope. *Astropart. Phys.*, 23:131–155, 2005.
- [113] Per Askebjør et al. Optical properties of deep ice at the south pole: Absorption. *Appl. Opt.*, 36:4168–4180, 1997.
- [114] M. Ackermann et al. Optical properties of deep glacial ice at the South Pole. *J. Geophys. Res.*, 111:D13203, 2006.
- [115] Y. D. He and P. B. Price. Remote sensing of dust in deep ice at the South Pole. *J. Geophys. Res.*, 103:17041, 1998.
- [116] S. L. Miller. Clathrate hydrates of air in Antarctic ice. *Science*, 165:489–490, 1969.
- [117] T. Uchida, W. Shimada, T. Hondoh, S. Mae, and N. I. Barkov. Refractive-index measurements of natural air-hydrate crystals in an Antarctic ice sheet. *Appl. Opt.*, 34:5746–5749, 1995.
- [118] J. Lunberg. Photonics. Talk given at the AMANDA/IceCube collaboration meeting, Berkeley, 2005.
- [119] T. Schmidt. *Aufbau und Funktionsnachweis eines optischen Moduls mit optisch analoger Pulsübertragung für den AMANDA-II- und den ICECUBE-Detektor*. PhD thesis, Humboldt-Universität zu Berlin, 2002.
- [120] A. Karle. Monte Carlo Simulation of photon transport and detection in deep ice: muons and cascades. In *Simulation and Analysis Methods for Large Neutrino Telescopes*. DESY Zeuthen, Germany, 1998. DESY-PROC-1999-01.
- [121] A. Karle et al. Analog optical transmission of fast photomultiplier pulses over distances of 2-km. *Nucl. Instrum. Meth.*, A387:274–277, 1997.
- [122] I. J. Taboada Fermin. *Search for High Energy Neutrino Induced Cascades with the AMANDA-B10 Detector*. PhD thesis, University of Pennsylvania, 2002.
- [123] C. H. V. Wiebusch. Private communication, 2007.
- [124] P. Lindahl. Investigation and Timing Properties and Possibilities of Analogue Pulse Detection for a Detector Channel of the Neutrino telescope AMANDA. Master's thesis, Uppsala University, 1997.
- [125] A. Biron. *Search for Atmospheric Muon Neutrinos and Extraterrestrial Neutrino Point Sources in the 1997 AMANDA-B10 Data*. PhD thesis, Humboldt-Universität zu Berlin, 2002.
- [126] J. Ahrens et al. Calibration and survey of AMANDA with the SPASE detectors. *Nucl. Instrum. Meth.*, A522:347–359, 2004.

- [127] P. Miočinovič. *Muon energy reconstruction in the Antarctic Muon And Neutrino Detector Array*. PhD thesis, University of California, Berkeley, 2001.
- [128] S. Hundertmark. *Simulation und Analyse von Myonereignissen im Amanda-B4-Neutrino teleskop*. PhD thesis, Humboldt-Universität zu Berlin, Mathematisch-Naturwissenschaftliche Fakultät, 1999.
- [129] M. Ackermann. Activities in Desy to study systematic effects of AMANDA data analysis. Talk given at the IceCube collaboration Meeting, Imperial College, London, UK, September 2005.
- [130] P. H. Barrett, L. M. Bollinger, G. Cocconi, Y. Eisenberg, and K. Greisen. Interpretation of cosmic-ray measurements far underground. *Rev. Mod. Phys.*, 24(3):133–178, Jul 1952.
- [131] M. Ambrosio et al. Seasonal variations in the underground muon intensity as seen by MACRO. *Astropart. Phys.*, 7:109–124, 1997.
- [132] J. Ahrens. Ein webbasiertes Überwachungssystem für das AMANDA Neutrino teleskop. Diploma Thesis, Johannes-Gutenberg Universität, Mainz, 2001.
- [133] M. Ribordy. AMANDA-II/2000 data statistics, OM selection and retriggering procedure. AMANDA Internal Report 20020601, 2002.
- [134] A. Pohl. A Statistical Tool for Finding Non-Particle Events from the AMANDA Neutrino Telescope. Licentiatexamen, Uppsala Universitet, 2004.
- [135] C. H. V. Wiebusch and R. Wischnewski. Proposal to measure an X-talk map for AMANDA-II: T0 calibration and beyond. AMANDA Internal Report 20001102, 2000.
- [136] A. Achterberg et al. Multiyear search for a diffuse flux of muon neutrinos with AMANDA-II. *Phys. rev. D*, 76:042008, 2007.
- [137] A. Karle. Hole ice studies with YAK data/MC. <http://icecube.berkeley.edu/kurt/interstring/hole-ice/yak.html>, 1998.
- [138] K. W. Woschnagg. The Interesting Hole-Ice Properties Page. <http://icecube.berkeley.edu/kurt/interstring/hole-ice/>.
- [139] S. Hundertmark. Vertical Ice Properties for the AMANDA-Simulation. AMANDA Internal Report 20001001, 2000.
- [140] J. Lundberg et al. Light tracking for glaciers and oceans: Scattering and absorption in heterogeneous media with Photonics. *Nucl. Instrum. Meth.*, A581:619–631, 2007.
- [141] G. C. Hill, A. Karle, P. Desiati, and K. W. Woschnagg. Evidence for insufficient absorption in the AMANDA Monte Carlo. <http://icecube.wisc.edu/~ghill/absorption/absorption2.html>, 2003.
- [142] A. Bouchta, J. Jacobsen, P. Miočinovič, P. Steffen, O. Streicher, S. Tilav, and C. H. V. Wiebusch. F2000 AMANDA offline format – An ASCII data format for handling data and MC events. User’s Guide, 2001.
- [143] O. Streicher and C. H. V. Wiebusch. RDMC – A library for processing neutrino telescope data and MC files. User’s Guide, 1998.

- [144] CERN Application Software Group. GEANT Detector Description and Simulation Tool. Cern Program Long Writeup W5013.
- [145] C. H. V. Wiebusch. GEN 3.0 – Generators for events in Neutrino telescopes. User’s Guide, 1998.
- [146] B. Christy. The Search for Relativistic Magnetic Monopoles. Candidacy Paper, University of Maryland, 2007.
- [147] S. Hundertmark. The Grapefruit realease of Amasim. <http://www.physto.se/~amanda/amasim/grapefruit/grapefruit.html>, 2003.
- [148] D. Heck et al. CORSIKA: A Monte Carlo Code to Simulate Extensive Air Showers. Technical Report 6019, Forschungszentrum Karlsruhe, 1998.
- [149] R. Engel et al. Test of hadronic interaction models with data from the Pierre Auger Observatory. In *Proc. 30th ICRC, Merida, Mexico*, 2007.
- [150] R. Glasstetter et al. Analysis of Electron and Muon Size Spectra of EAS. In *Proc. 26th ICRC, Salt Lake City, USA*, 1999.
- [151] T. Antoni et al. The Cosmic ray experiment KASCADE. *Nucl. Instrum. Meth.*, A513:490–510, 2003.
- [152] D. Chirkin and W. Rhode. Muon Monte Carlo: A New high precision tool for muon propagation through matter. In *Proc. 27th ICRC, Hamburg, Germany*, 2001.
- [153] D. Boersma et al. Sieglinde. <http://internal.icecube.wisc.edu/amanda/software/sieglinde/>, 2002.
- [154] R. Brun and F. Rademakers. Root – an object oriented data-analysis framework. <http://root.cern.ch/root>, 1995.
- [155] C. Walck. Live and Dead-time Analysis. <http://www.physto.se/~walck/amanda/livedead/>.
- [156] T. Hauschild. *Search for Cosmic Point Sources of High Energy Neutrinos with the AMANDA-II Detector*. PhD thesis, Humboldt-Universität zu Berlin, 2004.
- [157] J. R. Klein and A. Roodman. Blind analysis in nuclear and particle physics. *Ann. Rev. Nucl. Part. Sci.*, 55:141–163, 2005.
- [158] R. A. Fisher. The use of multiple measurements in taxonomic problems. *Annals Eugen.*, 7:179–188, 1936.
- [159] K. Futunaga. *Introduction to Statistical Pattern Recognition*. Morgan Kaufmann, Academic Press, 1990.
- [160] J. Ahrens et al. Muon track reconstruction and data selection techniques in AMANDA. *Nucl. Instrum. Meth.*, A524:169–194, 2004.
- [161] D. Pandel. Measurment of Water and Detector Parameters and Reconstruction of Muons to Energies of 100 TeV with the Baikal Neutrino Telescope NT-72. Diploma Thesis, Humboldt Universität, Berlin, 1996.
- [162] G. Japaridze and M. Ribordy. Photon arrival time distribution convoluted to a Gaussian time measurement uncertainty. AMANDA Internal Report 20031201, 2003.

- [163] W. H. Press et al. *Numerical Recipes in FORTRAN*. Cambridge University Press, Cambridge, 1992.
- [164] R. Brun and F. James. The minimization package. <http://root.cern.ch/root/html/TMinuit>, 2000.
- [165] R. Lang. Search for Point Sources of High-Energy Neutrinos with the AMANDA Detector. Diploma thesis, Faculty of Sciences, University of Ulm, 2005.
- [166] V. J. Stenger. Track fitting for DUMAND-II Octagon Array. External Report HDC-1-90, University of Hawaii at Manoa, Hawaii, USA, 1990.
- [167] H. Wissing. Monopole Search with AMANDA-II. Talk given at the AMANDA/IceCube collaboration meeting, Madison, 2003.
- [168] L. M. Gerhardt. *The Search for Ultra-High Energy Neutrinos with AMANDA-II*. PhD thesis, University of California, Irvine, 2007.
- [169] M. P. Kowalski. *Search for Neutrino-Induced Cascades with the AMANDA-II Detector*. PhD thesis, Humboldt-Universität zu Berlin, 2004.
- [170] P. Gondolo, G. Ingelman, and M. Thunman. Charm production and high energy atmospheric muon and neutrino fluxes. *Astropart. Phys.*, 5:309–332, 1996.
- [171] L. V. Volkova and G. T. Zatsepin. Uncertainties in prompt atmospheric neutrino flux calculations. *Phys. Lett.*, B462:211–216, 1999.
- [172] C. G. S. Costa, F. Halzen, and C. Salles. Prompt TeV-PeV atmospheric neutrino window. *Phys. Rev. D*, 66(11):113002, Dec 2002.
- [173] R. Gandhi and S. Panda. Probing the cosmic ray ‘knee’ and very high energy prompt muon and neutrino fluxes via underground muons. *JCAP*, 0607:011, 2006.
- [174] M. Gaug, P. Niessen, and C. H. V. Wiebusch. Investigations on Smoothness observables. AMANDA internal report 20000201, 2000.
- [175] G. M. Feldman and R. D. Cousins. Unified approach to the classical statistical analysis of small signals. *Physical Review D*, 57(7):3873, 1998.
- [176] J. Conrad, O. Botner, A. Hallgren, and C. Perez de los Heros. Including systematic uncertainties in confidence interval construction for Poisson statistics. *Phys. Rev.*, D67:012002, 2003.
- [177] A. Biron and H. Wissing. Impact of Varied OM Sensitivities on the AMANDA-B10 Analysis. AMANDA Internal Report 20001202, 2000.
- [178] C. Wiedemann. *A Search for Ultra-High Energy Neutrinos with AMANDA-II*. PhD thesis, Stockholm University, 2007.
- [179] J. Lundberg. UHE Unblinding Request. [http://www.physto.se/~johan/uhe/uhe\\_0304\\_ub-request\\_jan19\\_2008.pdf](http://www.physto.se/~johan/uhe/uhe_0304_ub-request_jan19_2008.pdf), 2008.
- [180] M. Ackermann et al. Flux limits on ultra high energy neutrinos with AMANDA-B10. *Astropart. Phys.*, 22:339–353, 2005.

- [181] B. Christy, A. Olivas, and D. Hardtke. Exotic particles searches with IceCube. Prepared for 30th International Cosmic Ray Conference (ICRC 2007), Merida, Yucatan, Mexico, 3-11 Jul 2007.
- [182] H. Wissing. Detection of Cosmic Muon-Neutrinos with ICECUBE. Diploma Thesis, Humboldt Universität zu Berlin, 2001.
- [183] A. Bouchta. Seasonal variation of the muon flux seen by AMANDA. In *Proc. 26th ICRC, Salt Lake City, USA*, volume 2, pages 108–111, 1999.
- [184] Antarctic Meteorological Research Center. <ftp://ice.ssec.wisc.edu/pub/southpole/radiosonde/>.
- [185] P. A. Newman and E. R. Nash. The Unusual Southern hemisphere Stratosphere Winter of 2002. *J. Atmos. Sci.*, 62:614–628, 2005.
- [186] J. L’Ecuyer and D. W. J. Thompson. Annular Modes Website. <http://www.atmos.colostate.edu/ao/ResPapers/SouthHem.html>.
- [187] C. Varotsos. The southern hemisphere ozone hole split. *Environmental Science and Pollution Research*, 9:375, 2002.
- [188] International Union of Pure and Applied Chemistry (IUPAC). Gold Book. <http://goldbook.iupac.org/D01827.html>.
- [189] National Aeronautics and Space Administration (NASA). Unusually small Antarctic ozone hole this year attributed to exceptionally strong stratospheric weather systems. <http://www.gsfc.nasa.gov/topstory/20020926ozonehole.html>, September 2002.
- [190] National Oceanic & Atmospheric Administration (NOAA). Earth System Research Laboratory, Physical Sciences Division. <http://www.cdc.noaa.gov/PublicData/>.
- [191] H. Wissing. Flare variables in high-multiplicity events. <http://www-zeuthen.desy.de/~hwissing/resources/flares/>, 2005.
- [192] A. Pohl, A. Hallgren, and H. Wissing. Private communications, 2005.
- [193] L. Gerhardt. The Search for Ultra High Energy (UHE) Neutrinos with AMANDA-II for 2000. <http://www.ps.uci.edu/~gerhard/uhe/uhe.html>, 2006.
- [194] A. Hallgren, A. Pohl, L. Gerhardt, and H. Wissing. Private communication, 2005.
- [195] T. R. DeYoung. *Observation of Atmospheric Muon Neutrinos with AMANDA*. PhD thesis, University of Wisconsin, Madison, 2001.
- [196] H. Wissing. What is wrong with string 13? <http://www-zeuthen.desy.de/~hwissing/resources/string13/>, 2006.
- [197] D. J. Boersma and T. Hauschild. private communication, 2005.
- [198] K. W. Woschnagg. Ice Properties Systematics. Talk given at the AMANDA/IceCube Spring Collaboration meeting, Madison, 2007.
- [199] S. Hundertmark. Experiment vs. Simulation – Comparison with 2003 AMANDA data. <http://www.physto.se/~hundert/icecube/comp2003/main.html>, 2007.

- [200] M. Walter. Comparison of Relative Sensitivities of AMANDA OM's for 2003. [http://www-zeuthen.desy.de/~walter/OM\\_sensitivity/2003\\_withStockholm\\_comparison\\_OM\\_sens/om\\_rel\\_sens\\_03-03s.html](http://www-zeuthen.desy.de/~walter/OM_sensitivity/2003_withStockholm_comparison_OM_sens/om_rel_sens_03-03s.html), 2007.
- [201] G. C. Hill and K. Rawlins. Unbiased cut selection for optimal upper limits in neutrino detectors: The model rejection potential technique. *Astropart. Phys.*, 19:393–402, 2003.
- [202] J. Neyman. Outline of a theory of statistical estimation based upon the classical theory of probability. *Phil. Trans. Roy. Soc. London, Series A 236*, page 333, 1937.
- [203] J. Conrad. Calculation of Confidence intervals with systematic uncertainties. <http://www3.tsl.uu.se/~conrad/pole.html>, 2003.
- [204] F. Tegenfeldt and J. Conrad. On Bayesian Treatment of Systematic Uncertainties in Confidence Interval Calculations. *Nucl. Instrum. Meth. A*, 539:407, 2005.
- [205] L. Gerhardt. Flare Variables for Laser Runs. [http://www.ps.uci.edu/~gerhardt/uhe/laser\\_flare.html](http://www.ps.uci.edu/~gerhardt/uhe/laser_flare.html), 2006.
- [206] L. Gerhardt, A. Silvestri, C. Wiedemann, and H. Wissing. private communication, 2006.
- [207] P. Miočinovič, K. Woschnagg, and H. Wissing. private communication, 2006.
- [208] G. Przybylski and H. Wissing. private communication, 2006.
- [209] J. R. Hörandel, N. N. Kalmykov, and A. V. Timokhin. The end of the galactic cosmic-ray energy spectrum - a phenomenological view. *Journal of Physics Conference Series*, 47:132–141, October 2006.



# Acknowledgments

This document was made possible by years of support and assistance of many people. Christopher Wiebusch gave me the opportunity to complete this work at the RWTH Aachen. I would like to thank him for taking over the responsibility for my thesis, for his continuous support over the last years, for sharing his expert knowledge about AMANDA with me, for giving me both freedom and advice at the right times, and not least, for his optimism and confidence in my work, which always motivated me to tackle the numerous obstacles I encountered over the course of a challenging analysis. Christian Spiering coached my work on both AMANDA and IceCube over several years at DESY. I thank him for introducing me to neutrino astrophysics and the scientific community, for his scientific advice, for many instructive discussions about monopoles and their detection, and also for giving me the chance to go to the South Pole, which was an important work experience as much as a great adventure. I thank Francis Halzen, Albrecht Karle, and Teresa Montaruli for inviting me to Madison, where I spent several months in pleasant and fruitful collaboration with the members of the IceCube group at UW.

Numerous of my colleagues at DESY, UW, and RWTH, and many collaborators in other institutions on both sides of the Atlantic have contributed to this work. Peter Nießen, the pioneer monopole hunter in AMANDA, was always ready to help with all sorts of technicalities. His familiarity with each and every piece of software used in AMANDA was tremendously valuable for accommodating monopoles in the simulation and analysis software. David Boersma, the main developer of the *Sieglinde* analysis package, put lots of effort in designing a framework flexible enough to permit “exotic” analyses. He patiently answered countless questions and helped me with putting my ideas into practice. Stephan Hundertmark, Paolo Desiati, and Markus Ackermann, the authors of the detector simulation and the standard scripts for Monte Carlo mass production and data filtering, were always ready to provide the information that I needed to get the monopole processing up and running. I have also benefited from exchanging ideas and experience with Lisa Gerhard and Christin Wiedemann, the UHE neutrino hunters.

A number of collaborators have given valuable feedback to this work. I thank the *Exotics Working Group* and its convener David Hardtke for reviewing the analysis and for encouragement and support with putting forward the unblinding proposal. Special thanks go to my fellow monopolist Arvid Pohl, the inventor of the *flare checker*, and his advisor Allan Hallgren, for detailed discussions on flare handling. David Boersma and Teresa Montaruli were the official referees for my analysis, and I would like to thank them for their careful reviews and also for their kind words and compliments, which meant a lot to me.

I am grateful to many members of the AMANDA/IceCube collaboration who contributed to this work by teaching me things, exchanging ideas, sharing knowledge, being responsible and responsive coworkers, or by just being pleasurable colleagues and friends. I thank my fellow grad students, post-docs, and the scientific staff at DESY, UW, and RWTH for providing a friendly and cooperative work environment. Much of my skills in data analysis, programming, batch processing *etc.* is the result of constant exchange and cooperation with my colleagues and regular feedback during group meetings. At the South Pole, it was a pleasure to work with Thomas Feser, Wolfgang Wagner, and Karl Heinz Becker, and I would like to thank them for teaching me a lot about hardware, DAQ, and software. I thank Kurt Woschnagg for always being responsive to all my questions about ice properties and calibration, and for his assistance with tracking down information about OM # 531. I am also grateful for his excellent feedback and help during the finalization of the IceCube performance paper. Torsten Schmidt never hesitates to share his seemingly endless knowledge about OMs, DOMs, and anything that is connected to them via cable or fiber, and I enjoyed many hardware lessons over a mate tea or a cocktail in Berlin Friedrichshain. Troy Straszheim taught me C++ in all its magnificence and splendor, and I would like to thank him for the countless hours we spent in Berlin bars scribbling code snippets on paper napkins and coasters. I would like to thank Stefan Schlenstedt for always having an open ear for everything related to this work and for his advice regarding both physics and physicists. The computing requirements of this work often needed extra attention from the user support, and I do not want to miss to thank the staff in the computing centers at DESY, UW, and RWTH for their patience, cooperativeness, and their assistance with large scale data processing, archiving, and transfers.

Schließlich möchte ich meiner Familie und allen meinen Freunden danken, die so geduldig alle Höhen und Tiefen diese Projekts mit mir geteilt haben.



Lebenslauf:

**Persönliche Daten:**

Name:	Wissing
Vorname:	Henrike
Geburtsdatum:	26. 05. 1974
Geburtsort:	Hattingen
Staatsangehörigkeit:	deutsch

**Qualifikationen:**

1993	Abitur
1994 - 1996	Studium der Physik, Universität Dortmund
1996	Vordiplom Physik
1996 - 2001	Studium der Physik, Humboldt Universität zu Berlin
2001	Diplom Physik
2002	Beginn der Promotion, Humboldt Universität zu Berlin
ab 2006	Promotion, RWTH Aachen